Modelling turbulent flows in the natural convection regime using hybrid RANS- LES approaches

Puneeth Bikkanahally Muni Reddy

THÈSE

UNIVERSITÉ DE PAU ET DES PAYS DE L'ADOUR

École doctorale des sciences exactes et leurs applications

Présentée et soutenue publiquement

le 21 decembre 2023 par

Puneeth BIKKANAHALLY MUNI REDDY

pour l'obtention du grade de

DOCTEUR

de l'Université de Pau et des Pays de l'Adour

SPÉCIALITÉ: MÉCANIQUE DES FLUIDES

MODÉLISATION DES ÉCOULEMENTS TURBULENTS EN RÉGIME DE CONVECTION NATURELLE PAR APPROCHES HYBRIDES RANS-LES

MODELLING TURBULENT FLOWS IN THE NATURAL CONVECTION REGIME USING HYBRID RANS-LES APPROACHES

Directeur de thèse:

Dr. Rémi MANCEAU

COMPOSITION DU JURY

Dr. Shia-Hui PENG	Swedish Defence Research Agency (FOI)	Rapporteur
Dr. Emmanuel LAROCHE	ONERA, Toulouse	Rapporteur
Dr. Didier SAURY	Université de Poitiers	Examinateur
Dr. Sylvain SERRA	Université de Pau et des Pays de l'Adour	Examinateur
Dr. Rémi MANCEAU	Université de Pau et des Pays de l'Adour	Membre

UNIVERSITÉ DE PAU ET DES PAYS DE L'ADOUR

Acknowledgements

Completing this doctoral thesis has been a journey marked by numerous challenges, triumphs, and invaluable support from many individuals whom I would like to acknowledge with deep appreciation.

First and foremost, I am profoundly grateful to my advisor, Dr. Rémi MANCEAU, whose invaluable guidance, patience, and continued motivation have been the cornerstone of this endeavour. His insightful feedback, encouragement, and dedication have shaped not only the direction of this research but also my growth as a researcher.

My heartfelt thanks also goes out to my colleagues (past and present) at team CAGIRE who are exceptionally kind and made my integration within the team seem like a breeze. I have them to thank also for my much improved grasp of the French language. Along the same vein, I express my sincere gratitude to the staff and researchers at LMAP for their support and for providing a conducive environment for my studies. Furthermore, thanks to my peers of the MONACO_2025 project and thanks in particular to Saad and Vladimir whose work has directly played a role in my research.

I extend my heartfelt thanks to the members of the jury for their thorough feedback, constructive criticism, and insightful discussions. Special thanks to Dr. Shia-Hui PENG and Dr. Emmanuel LAROCHE for their detailed review of the manuscript.

I am indebted to the developers of Code Saturne for creating and maintaining such an excellent tool for CFD research. Furthermore, I would like to thank the developers of the myriad of open-source tools that have made my research a more pleasant experience.

On a more personal note, I am deeply thankful to my family for their unconditional love,

encouragement, and understanding throughout this journey. Their unwavering support has been my anchor during moments of uncertainty and challenge.

I will forever be grateful for the friendships, both old and new, I have had throughout this journey. Every kind word said, moment shared, and memories made have had an impact and encouraged me to do better. Special thanks to the international community of students and researchers who have made my stay at Pau memorable.

Finally, I would like to acknowledge the financial support provided by Agence nationale de la recherche (ANR), which enabled me to pursue this research. Thanks also to MCIA and GENCI-IDRIS (Grant 2019-A0072A10980) computing clusters for the resources provided to carry out this work.

To Harish.

Résumé

La présente thèse est consacrée au développement et à la validation de modèles de turbulence pour les écoulements de convection naturelle. Les écoulements affectés par la flottabilité jouent un rôle important dans de nombreuses applications industrielles et environnementales, par exemple dans les secteurs des deux partenaires industriels; EDF : pour la conception des centrales nucléaires et le Groupe PSA : pour la conception de l'espace sous le capot des automobiles. Afin d'éviter des expériences coûteuses et de permettre une conception et un développement rapides, il est essentiel d'utiliser des modèles CFD efficaces, robustes et précis pour simuler de tels écoulements. La thèse représente la conclusion du projet MONACO_2025 (MOdelling NAtural COnvection 2025) visant à développer une gamme de modèles de turbulence tenant compte de la flottabilité.

La recherche et le développement dans le contexte industriel sont toujours dominés par l'utilisation de modèles RANS, en particulier l'utilisation de modèles de viscosité turbulente du premier ordre en raison de leur coût de calcul abordable. Dans cette perspective, la première partie des développements de modèles est axée sur la stratégie RANS. En s'appuyant sur le modèle de viscosité turbulente sensibilisé à la flottabilité (Full buoyancy extension (FBE)) précédemment développé dans le cadre du projet MONACO_2025, les performances de ces modèles sont évaluées dans des cas test pertinents pour l'industrie, tels que celui de la convection naturelle dans une cavité carrée différentiellement chauffée (differentially heated cavity (DHC)) à un nombre de Rayleigh élevé de 10^{11}. Deux modèles sont évalués, à savoir le $k\omega$-SST and BL-v^2/k, qui sont très pertinents pour le secteur industriel. Les modèles RANS sensibilisés à la flottabilité, initialement développés dans

l'écoulement vertical en canal différentiellement chauffée, montrent des améliorations significatives dans la prédiction des profils de vitesse moyenne grâce à l'amélioration du bilan de quantité de mouvement. Dans le cas du DHC carré, où les simulations sont en mode URANS en raison de la présence de mouvements résolus, les améliorations sont marginales mais cohérentes. Une attention particulière est accordée à la formulation des termes sources dans l'équation du taux de dissipation spécifique, , du modèle $k\omega$-SST lorsque l'on considère les effets de la stratification. La reformulation conduit à une correction du comportement de la viscosité turbulente dans la région centrale stratifiée de la DHC carré.

Un objectif important du projet MONACO_2025 est le développement de modèles capables de prédire des phénomènes instationnaires. À cet égard, les modèles hybrides RANS/LES offrent une stratégie de simulation à coût raisonnable tout en conservant la capacité de capturer les informations nécessaires dans les écoulements instationnaires. Ainsi, la deuxième partie de la thèse se concentre sur l'extension du modèle HTLES précédemment développé pour les écoulements isothermes aux écoulements de convection naturelle. Le modèle HTLES $k\omega$-SST est sensibilisé aux effets de flottabilité par la mise en uvre FBE pour aider le modèle RANS de la standard. Le comportement du modèle est évalué dans DHC carrée, ce qui a conduit au développement d'une nouvelle fonction de protection, appelée fonction de protection elliptique, visant à rendre le modèle plus robuste et à réduire l'influence de l'empirisme. Il est intéressant de noter que, bien que les améliorations apportées par FBE soient marginales, elles sont conservées lorsqu'elles sont incorporées dans le modèle HTLES par rapport au modèle HTLES avec une fermeture de viscosité turbulente standard. Enfin, les modèles RANS et HTLES sont comparés à des simulations LES haute-fidélité pour démontrer le potentiel de la méthode HTLES dans la prédiction de phénomènes dépendant du temps tout en maintenant les coûts de calcul à un niveau bas.

Abstract

The present thesis is devoted to the development and validation of turbulence models for natural convection flows. Flows driven solely by buoyancy effects, i.e., density variations occurring in the fluid medium caused by the presence of temperature gradients, are termed as /natural convection flows/. Buoyancy affected flows play an important role in many industrial and environmental applications, for instance, in the sectors of the two industrial partners; EDF: for the design of nuclear power plants and PSA Group: for the design of under-hood space of auto-mobiles. In order to avoid expensive experiments and promote rapid design and development, it is quintessential to employ efficient, robust, and accurate CFD models to simulate such flows. The thesis represents the conclusion of the project MONACO_2025 (MOdelling NAtural COnvection 2025) aimed at developing a range of turbulence models accounting for buoyancy.

Research and development in the industrial context is still dominated by the use of RANS models, in particular the use of first order eddy-viscosity models thanks to their affordability. To that end, the first part of model developments are focussed on the RANS strategy. Building up on the buoyancy sensitised eddy-viscosity model (Full buoyancy extension (FBE)) previously developed as part of the MONACO_2025 project, the performance of these models is assessed in industry relevant test case such as that of natural convection in a square differentially heated cavity (DHC) at a high Rayleigh number of 10^{11}. Two models are assessed, namely the $k\omega$-SST and BL-v^2/k, which are highly relevant to the industrial sector. The buoyancy sensitised RANS models, initially developed in the vertical differentially heated channel flow show significant improvements in the prediction of the

mean velocity profiles thanks to the improved momentum balance. In the case of square DHC, where the simulations are in URANS mode due to the presence of resolved motion even in refined grids, the improvements are marginal but consistent. A particular attention is paid to the formulation of the source terms in the specific dissipation rate equation, ω, of the $k\omega$-SST model when considering the effects of stratification. The reformulation leads to a correction in the behaviour of turbulent viscosity in the stratified core region of the square DHC.

An important objective of the MONACO_2025 project is the development of models able to predict time-dependent phenomena. In this regards, hybrid RANS/LES models offer a cost-effective simulation strategy while retaining the ability to capture the necessary unsteady flow information. As such, the second part of the thesis focusses on the extension of the HTLES (Hybrid Temporal Large Eddy Simulation) model previously developed for isothermal flows to natural convection flows. The $k\omega$-SST HTLES model is sensitised to buoyancy effects through the implementation of the FBE to aid the underlying RANS model. The behaviour of the model is assessed in the square DHC leading to the development of a new shielding function called the elliptic shielding function aimed at making the model more robust and reduce the influence of empiricism. Interestingly enough, although the improvements from the FBE are marginal, these improvements are retained when incorporated in the HTLES model as compared to the HTLES model with a standard eddy-viscosity closure. Finally, the RANS and HTLES models are compared against high-fidelity LES simulations to showcase the potential of the HTLES method in the prediction of time-dependent phenomena while keeping the computational costs low.

Glossary

ADM Approximate Deconvolution Model.

AFM Algebraic Flux Model.

ASM Algebraic Stress Model.

CFD Computational Fluid Dynamics.

DDES Delayed DES.

DES Detached Eddy Simulation.

DFM Differential Flux Model.

DHC Differentially heated cavity.

DIT Decaying Isotropic turbulence.

DNS Direct Numerical Simulation.

EB-AFM Elliptic Blending - Algebraic Flux Model.

EB-DFM Elliptic Blending - Differential Flux Model.

FBE Full Buoyancy Extended Model.

GGDH Generalised Gradient Diffusion Hypothesis.

GIS Grid Induced Separation.

HTLES Hybrid Temporal LES.

ICC Internal Consistency Constraint.

IDDES Improved DDES.

LES Large Eddy Simulation.

MSD Modelled Stress Depletion.

PITM Partially Integrated Transport Model.

RANS Reynolds Averaged Navier-Stokes.

RSM Reynolds-Stress model.

SGDH Simple Gradient Diffusion Hypothesis.

SOLU Second Order Linear Upwind.

SSM Scale Similarity Model.

TADM Temporal Approximate Deconvolution Model.

TPITM Temporal PITM.

URANS Unsteady RANS.

VCF (Differentially heated) Vertical channel flow.

WALE Wall-Adapting Local Eddy-Viscosity Model.

Mathematical operators

$A \propto B$ Navier-Stokes operator.

δ_{ij} Kronecker delta.

$\frac{\partial^2 A}{\partial B^2}$ second order partial derivative of A w.r.t B.

$\frac{\partial A}{\partial B}$ partial derivative of A w.r.t B.

$\frac{DA}{DB}$ total derivative of A w.r.t B.

$\frac{D^2 A}{DB^2}$ second order total derivative of A w.r.t B.

$\mathcal{N}$ Navier-Stokes operator.

Latin symbols

A Aspect ratio of the cavity ($= L_x/L_y$).

C_K Kolmogorov constant.

C_d Dynamic Smagorinsky model co-efficient.

C_{ij} Cross-stress tensor.

C_s Proportionality constant in the Smagorinsky model.

E energy spectrum.

Gr Grashoff number.

L_{ij} Leonard tensor.

Pr Prandtl number.

R_{ij} Reynolds stress tensor.

R_{ij} two point velocity correlation.

Ra Rayleigh number.

Re Reynolds number.

S_{ij} Strain-rate tensor.

U_i i^{th} component of velocity.

U_s Sweeping velocity.

$\mathcal{D}^P$ Pressure diffusion term.

$\mathcal{D}^T$ Turbulent diffusion term.

$\mathcal{D}^\nu$ Viscous diffusion term.

$\mathcal{F}_i$ External force.

$\mathcal{G}$ Buoyancy production term.

$\mathcal{P}$ Production term.

b_{ij} anisotropy tensor.

g_i Gravity vector.

k Turbulent kinetic energy.

Greek symbols

Δ filter width.

Φ mean quantity = $\overline{\Phi^*}$.

Φ_{ij} velocity spectrum.

Π Pressure-Strain rate correlation/redistribution term.

Greek symbols

Θ Temperature.

α parameter of the elliptic equation.

α thermal diffusivity.

α_t turbulent diffusivity.

β co-efficient of thermal expansion.

μ dynamic viscosity.

ν kinematic viscosity.

ν_t turbulent viscosity.

ω frequency.

ω specific dissipation rate.

ϕ fluctuating quantity.

ϕ^* instantaneous quantity.

ρ Density.

τ_{ij} Deviatoric stress tensor.

ε Dissipation term.

$\widetilde{\phi}$ filtered quantity.

Contents

Chapter 1.

Introduction

1.1. Context

Fluid motion observed in nature is, most often, turbulent. Likewise, this holds true in engineering applications. The ubiquity of turbulence has driven many researchers to define the phenomena. To this day, there doesn't exist an accurate definition of turbulence. However, turbulent flows can be characterised sufficiently based on some features they present in contrast to laminar flows. These features, although inter-linked, can be listed as follows due to the importance of the roles they play in engineering applications.

- Turbulence is **chaotic**

  Turbulent flows are chaotic and unpredictable. As such, predicting the motion of turbulent flows is near impossible. Turbulence can be triggered by various perturbations, be it due to boundary conditions, initial conditions, and/or external forces acting on the fluid. In particular, the flow fields are highly sensitive to initial conditions, such dynamical systems were extensively studied by Lorenz (1963).

- Turbulence is **diffusive**

  An important characteristic for many engineering applications, turbulence increases mixing and heat transfer.

- Turbulence is **three-dimensional**

  Turbulent flows present non-zero vorticity in the 3 directions, which plays an important role in the dynamics of the flow.

- Turbulence is composed of **multiple scales**

  A large range of length and time scales can be observed in turbulent flows. Energy cascades from the large scales to the small scales where it is dissipated into heat by the viscous forces, a notion first introduced by Richardson (1922).

Given the complex nature of turbulent flows and their importance in environmental and industrial applications, it is imperative for the sake of design and development process to have the ability to study and understand the impact of turbulent motion arising in a variety of scenarios. Historically, researchers and engineers relied solely on experiments to understand and predict fluid flows. Although experiments provide highly reliable data, the process is extremely expensive since experimental setups are difficult to build and just as difficult to modify if a different configuration of the design is necessary.

In the wake of the digital era, computer-based simulations have become one of the main strategies employed in the prediction of turbulent flows. The study and development of numerical methods and mathematical models to simulate fluid flows using computational power is termed as *Computational Fluid Dynamics (CFD)*. CFD offers a significant advantage, compared to experiments, in that the design and development process is greatly simplified thanks to the ease with which various iterations of a design can be simulated computationally at a fraction of the cost. In the present day, experiments and CFD are used in conjunction with each other such that experiments still play an important role in validating the CFD results predominantly in academic research.

The CFD toolkit comprises a range of strategies for simulating turbulent flows whereby the equations governing fluid motion are simulated at various levels of approximation, such as:

- *Direct numerical simulation (DNS)*, which represents the most straightforward form

of simulation where the governing equations are solved without any approximations

- *Large eddy simulation (LES)*, where only the large energy containing scales are directly computed while the small scales are modelled through mathematical approximations
- *Reynolds averaged Navier-Stokes (RANS)*, where the mean motions are computed and the effect of the instantaneous motions are approximated through a wide variety of mathematical models
- Hybrid RANS/LES, where some regions of the fluid domain are computed using RANS while the other regions are computed using LES

The study and development of the aforementioned mathematical approximations/models is termed as *turbulence modelling*. Of the strategies mentioned above, RANS methods are predominantly employed in the industrial context since DNS and LES are impractical for complex geometries owing to their high computational costs. Hybrid RANS/LES strategies are some of the more recent methodologies to be developed which aim to retain cost-effectiveness by using RANS in regions where detailed description of turbulent dynamics is not necessary while still having the ability to directly simulate the large scales, akin to LES, in select regions of the fluid domain.

In the present thesis, turbulence models are developed for the express purpose of simulating flows driven by buoyancy. Fluid flows that are solely driven by density variations, in the presence of gravity, occurring in the fluid medium due to temperature gradients or varying species concentrations are called buoyancy driven flows. This thesis represents the conclusion of the project Modelling Natural Convection 2025 (MONACO_2025), funded by the *Agence nationale de la recherche (ANR-17-CE06-0005-01)*, which is aimed at developing a range of turbulence models accounting for buoyancy. The goal of the MONACO_2025 project is to combine efforts from two distinct industrial sectors to address the challenge of simulating unsteady, turbulent flows influenced by buoyancy effects. This collaborative effort involves two academic partners: the Department of Applied Mathematics at the

University of Pau/CNRS (LMAP), more specifically the Inria project-team CAGIRE and the Pprime Institute of CNRS/ENSMA/University of Poitiers (PPRIME), involved in the fields of turbulence modelling and experimental studies, respectively. Additionally, it includes the R&D departments of two industrial partners, the Peugeot S.A. group (now Stellantis) and the Électricité de France (EDF) group, prominent players in the automotive and energy production industries, respectively.

Industrial context: The industrial context of the MONACO_2025 project and the present thesis by extension is two-pronged, with one part relating to the design of automobiles and the second relating to the design of nuclear reactors.

- **Automotive sector** :

  One of the key issues faced by th Stellantis group is that of designing the engine compartment. It encompasses a complex assembly of over 3,600 individual components, each subject to temperature monitoring to ensure both the efficiency and safety of the vehicle. Furthermore, it contributes to approximately 5 to 8% of the overall aerodynamic drag and associated CO2 emissions. The dimensioning of the compartment involves a delicate balance between aerodynamics and thermal considerations, a balance that is validated through a series of on-road tests involving steady-speed segments and stationary phases (such as that encountered at red lights, toll booths, and in traffic congestion). While CFD is routinely employed for forced convection simulations (as illustrated in Figure 1.1), state-of-the-art turbulence models used in industrial codes currently fall short in accurately reproducing flows dominated by natural convection during stationary phases, characterised by a Rayleigh number of the order of 10^{10}. As a result, the design process still heavily relies on costly, full-scale wind tunnel experiments. Overcoming this technical challenge is imperative, particularly in light of the Stellantis group's ambition to transition to a full digital design of their vehicles in the 2025 horizon, so as to solely utilise CFD in the design and development process.

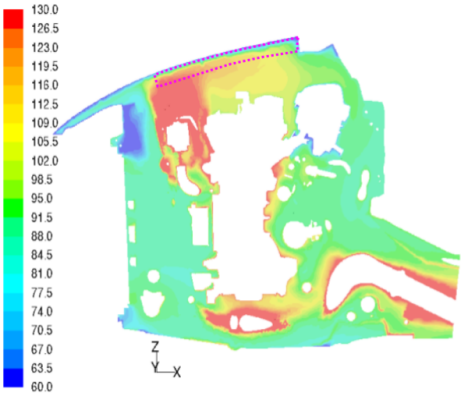

Figure 1.1.: Cross-section of an underhood compartment, showing mean temperature computations in the forced convection regime (Jameel, 2020).

- **Energy production sector** :

  Natural convection regimes pose a significant challenge in the nuclear industry. Addressing physical phenomena (Figure 1.2) such as thermal shocks, stratification, erosion, and boiling necessitates precise predictions of both the flow and temperature fields. Enhancing models for turbulent heat transfer is paramount for nuclear reactor design which involves scenarios with high Rayleigh numbers, typically falling within the range of $[10^8, 10^{12}]$. Especially in the post-Fukushima era, there has since been a concerted effort towards the development of passive reactor cooling systems which offer higher degree of safety as compared to active systems. The design of these components requires robust and accurate simulation tools to ensure that the components are reliably designed in accordance with nuclear safety standards. Historically, the nuclear industry mainly relied on the use of *system codes* where entire power plants are simulated by simplifying individual components into pipe segments using empirical relations, however, such one-dimensional approximations lack the necessary information regarding flow dynamics. Nowadays, EDF has been a pioneer in developing an open-source CFD code, named *code_saturne* (Archambeau et al., 2004), for three-dimensional CFD simulations of components relating to nuclear reactor safety. The main goal of the MONACO_2025 project is thus to develop turbulence

modelling strategies with the ability to simulate unsteady turbulent flows and as a first step, disseminate the models through code_saturne.

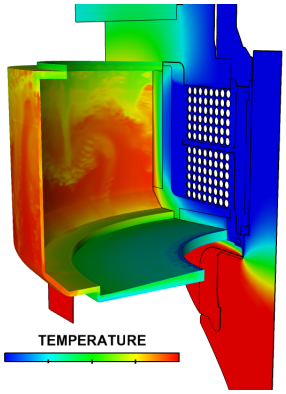

Figure 1.2.: Temperature field in a thermal barrier of a nuclear Reactor Cooling Pump - source MONACO_2025[1]

Research context: In regards to the research context, the main problem to overcome for turbulence modelling, in particular relating to industrial applications, is to strike a good balance between accuracy and computational cost. As mentioned previously, although LES resolves a large part of the flow dynamics, it is generally impractical due to the high computational costs for the large Reynolds/Rayleigh numbers of industrial configurations. On the other hand, RANS modelling for buoyant flows have experienced significant improvements over the past decade (Dehoux et al., 2017; Dehoux, 2012). Such models, which are of the *Reynolds-stress model (RSM)* family, are not standard in the commercial codes used by the industry due to their complexity and the higher standards of robustness demanded by the industry. In this regard, RANS models of the eddy-viscosity genre sensitised to buoyancy effects are developed so as to facilitate rapid dissemination to industrial codes. Furthermore, the main objective of the MONACO_2025 project is the development of hybrid RANS/LES models for buoyant flows so as to lift the technical barrier of computing unsteady natural convection flows in industry relevant test cases. The industrial constraints restricting the use of LES render the use of hybrid strategies very attractive due to the considerable

[1] `https://team.inria.fr/cagire/monaco-2025/`

alleviation of computational cost resulting from the reduction in mesh size by a large factor of 100 (Manceau, 2018). With the RANS models sensitised to buoyancy effects serving as the underlying closure, the aim is to develop hybrid strategies that are able to improve on the mean statistics obtained from the RANS models while being able to predict the unsteady phenomena in select regions of interest in natural convection flows.

1.2. Contributions of the present thesis

Inline with the objectives of the MONACO_2025 project, this thesis focuses on two aspects of turbulence modelling for natural convection flows:

1. development of industry relevant RANS models based on the eddy-viscosity approach sensitised to buoyancy effects

2. development of a hybrid RANS/LES approach for natural convection flows based on temporal filtering, using these buoyancy sensitised RANS models as the underlying closure

The work carried out in the present thesis are seeded by the works of Jameel (2020) and Duffal (2020).

- **RANS models sensitised to buoyancy effects**:
  This work is in the continuity of the thesis of Jameel (2020) who developed a buoyancy extended strategy for eddy-viscosity models allowing better accountability of buoyancy effects in the $k\omega$-SST and BL-v^2/k models. In the present thesis, for the case of the $k\omega$-SST model, the consequences of the blending between $k-\varepsilon$ and $k-\omega$ models on the buoyancy source terms in the transport equation for specific dissipation rate, ω, are revisited and the formulation is corrected. Following which, the models are integrated in code_saturne and compared against the standard models, generally available in industrial codes, in the vertical channel flow test case of Kis et al. (2014)

at $Gr = 3 \times 10^6$. A further validation study is carried out using the benchmark DNS database of a square differentially heated cavity at $Ra = 10^{11}$ (Sebilleau, 2016; Sebilleau et al., 2018). This test case is particularly interesting due to the fact that the physics encountered is highly relevant to the industrial partners of the MONACO_2025 project.

- **Development of hybrid RANS/LES model for natural convection flows**:
  The work of Duffal (2020) further developed/reformulated the HTLES model of (Manceau, 2018) for isothermal flows. This new formulation is developed for natural convection flows in the present thesis. The $k\omega$-SST model is hybridised such that the base RANS models still retain their sensitisation to buoyancy effects. Following the implementation of these modifications in code_saturne, the validation study carried out focusses highly on the square DHC (Sebilleau, 2016; Sebilleau et al., 2018) since the test case presents a high level of turbulence at $Ra = 10^{11}$. The issues regarding the HTLES model behaviour in the cavity cases are resolved leading to the development of a new shielding function necessitating the addition of an elliptic equation to the HTLES formulation.

  Finally, high fidelity LES simulations of the square DHC are carried out in order to evaluate the performance of the HTLES model and the RANS models sensitised to buoyancy.

1.3. Guide to the manuscript

Chapter 1 serves to present the general context and introduces the reader to the problem faced by the industry in regards to simulation of unsteady natural convection flows. In that regard, the MONACO_2025 project is introduced and the goals of the project are defined which are integral to the present thesis as it represents the conclusive step of the project.

Chapter 2 of the thesis focuses on the bibliographic study relating to the simulation

of turbulent flows. A review of the various simulation techniques used for the study and modelling of turbulent flows is presented w.r.t isothermal flows. Additionally the chapter serves to introduce the notation which is used throughout the thesis.

Chapter 3 focusses on the bibliographic study of natural convection flows. This short chapter is used to highlight the influence of buoyancy on the various transport equations in a clear and concise manner.

Chapter 4 details the RANS approaches developed as part of the MONACO_2025 project. In continuity with the work of Jameel (2020), the development of the full buoyancy extended model (FBE) is presented along with further developments and validation studies carried out in the present thesis.

Chapter 5 details the hybrid approaches developed as part of the MONACO_2025 project. The HTLES model developed for isothermal flows by Duffal (2020) is further developed in the context of buoyancy affected flows and validated using the square differentially heated cavity of Sebilleau et al. (2018). The chapter also provides an assessment of the RANS and HTLES models in comparison to high fidelity LES.

Chapter 6 concludes the work carried out in the present thesis. Conclusions are drawn from the principal results of the thesis and recommendations for future work are provided in the context of both academia and industry.

Finally, appendices A and B provide a quick overview of further results generated during the course of the thesis. **Appendix A** focuses on the high fidelity LES of square DHC with a comparison of the different models employed. **Appendix B** entails the results obtained for the rectangular differentially heated cavity of (F. Trias et al., 2010a,b) using the models previously validated for square DHC.

Chapter 2.

Simulating turbulent flows

2.1. Introduction

This chapter serves to establish the bibliographic study relating to the simulation of turbulent flows. The concepts and ideas used in the various strategies for simulating turbulent flows are established by building up on the governing equations and defining some statistical quantities relating to the physics of the flow. A review of the turbulence models is then presented in 4 parts, namely:

- Direct numerical simulation (DNS)
- Large eddy simulation (LES) models
- Reynolds averaged Navier-Stokes (RANS) models
- Hybrid RANS/LES models

The chapter also provides a means to introduce the notation which is used throughout the rest of the thesis.

2.2. Governing equations

The velocity and pressure fields of a fluid in motion are given by the so called Navier-Stokes equations. Using a Cartesian coordinate system and Einstein's notations, implying summation over repeated indices, we can write the Navier-Stokes equations as follows:

- Continuity equation

$$\frac{D\rho}{Dt} = \frac{\partial \rho}{\partial t} + \frac{\partial \rho u_i^*}{\partial x_i} = 0 \tag{2.1}$$

- Momentum equation

$$\frac{\partial \rho u_i^*}{\partial t} + \frac{\partial \rho u_i^* u_j^*}{\partial x_j} = -\frac{\partial p^*}{\partial x_i} + \frac{\partial \tau_{ij}}{\partial x_j} + \mathcal{F}_i \tag{2.2}$$

The equations above describe the conservation of mass and momentum, respectively, for the instantaneous velocity and pressure fields. The system of equations requires initial and boundary conditions. The additional term, $\mathcal{F}_i$, accounts for forces acting on the fluid volume other than the pressure gradient. The stresses undergone by the fluid volume are represented by the **deviatoric stress tensor**, τ_{ij},

$$\tau_{ij} = \mu \left(\frac{\partial u_i^*}{\partial x_j} + \frac{\partial u_j^*}{\partial x_i} - \frac{2}{3} \frac{\partial u_k^*}{\partial x_k} \right) \tag{2.3}$$

In the present thesis, we will work under the hypothesis of an incompressible flow, i.e. constant density flows with buoyancy forces respected by the Boussinesq approximation. In this case the continuity equation produces the condition that the velocity field must be *divergence-free*. Thus for an incompressible flow, the Navier-Stokes equations write:

- Continuity equation

$$\begin{aligned} \frac{D\rho}{Dt} &= \frac{\partial \rho}{\partial t} + \cancelto{0}{u_i^* \frac{\partial \rho}{\partial x_i}} + \rho \frac{\partial u_i^*}{\partial x_i} = 0 \\ \frac{\partial u_i^*}{\partial x_i} &= 0 \end{aligned} \tag{2.4}$$

- Momentum equation

$$\underbrace{\frac{\partial u_i^*}{\partial t}}_{\text{Unsteady}} + \underbrace{u_j^* \frac{\partial u_i^*}{\partial x_j}}_{\text{Convection}} = - \underbrace{\frac{1}{\rho} \frac{\partial p^*}{\partial x_i}}_{\text{Pressure}} + \underbrace{\nu \frac{\partial^2 u_i^*}{\partial x_j \partial x_j}}_{\text{Diffusion}} + \underbrace{\mathcal{F}_i}_{\text{External forces}} \tag{2.5}$$

The crux of the problem leading to a flow becoming turbulent arises from the quadratic convection term on the left-hand side of equation Equation (2.5). The flow becomes turbulent when the convective term grows larger than the diffusive term. Meaning, the inertial forces dominate the viscous forces. The non-dimensional number called Reynolds number, defined as the ratio between these forces, is used as a measure for the level of turbulence in a fluid flow.

Consider a flow with characteristic velocity U and a characteristic length (e.g. prescribed by the geometry) L, then the convective term can be estimated as U^2/L and the diffusive term as $\nu U/L^2$. The Reynolds number can then be written as:

$$Re_L = \frac{UL}{\nu} \tag{2.6}$$

2.3. Scales in turbulent flows

The existence of various scales, spatial and temporal, has been used to characterise turbulence for as long as it has been studied. Such characterisations originated in a qualitative sense before researchers established fundamental theories that led to their quantification. This section provides some context in view of both the qualitative and quantitative aspects

of the scales presented by turbulent flows so as to form a basis for the introduction of the turbulence models described later.

2.3.1. Energy Cascade

Consider a flow at high Reynolds number, such that the characteristic scale LU is large in comparison with the viscous scales. Under such considerations, Richardson (1922) introduced the notion of the energy cascade whereby introducing fundamental concepts/mechanisms of turbulent flows.

1. Turbulence is comprised of *eddies* of various sizes
2. Large eddies are created by the mean flow driven by forces acting on the fluid
3. Large eddies are characterised by length and velocity scales of the order of the characteristic scales L and U, respectively
4. Large eddies break up into smaller eddies in an inviscid manner
5. Smaller eddies further break down in to even smaller eddies until the effects of molecular viscosity dissipate the energy into heat

The notion of *energy-cascade* creates a basis for understanding the mechanisms involved in the transfer of energy in a turbulent fluid. However, it is prudent to quantify such scales of import.

2.3.2. Energy spectra and Kolmogorov hypothesis

The random nature of turbulence lends itself to be studied under a statistical lens thus allowing us to extract meaningful data. Consider a random data series representing the fluctuations of velocity, $u_i = u_i^* - U_i$, where the mean value is subtracted from the instantaneous velocity signal. One can obtain quantities, by processing the signal using statistical operations, that correlate to the physics of the flow. The mean value is an example

of a first-order statistical quantity. Higher-order quantities can be derived describing the scales of turbulent flows. Two such techniques most commonly employed are the *velocity correlation function* and the *energy spectrum*.

The velocity correlation function in space and time is given by (see Pope, 2000; Sagaut et al., 2006; Tennekes et al., 1972) Equation (2.7). It describes the extent to which the velocity at two points, in space or time, are related.

$$R_{ij}(r) = \overline{u_i(\boldsymbol{x},t)u_j(\boldsymbol{x}+\boldsymbol{r},t)} \qquad R_{ij}(\tau) = \overline{u_i(\boldsymbol{x},t)u_j(\boldsymbol{x},t+\tau)} \tag{2.7}$$

The Fourier transform of the velocity correlations give the velocity spectrum in wave-number space (assuming homogeneity) or frequency space (assuming stationarity).

$$\Phi_{ij}(\kappa) = \frac{1}{2\pi}\iiint_{-\infty}^{\infty} R_{ij}(\boldsymbol{r})e^{-i\kappa\boldsymbol{r}}d\boldsymbol{r} \qquad \Phi_{ij}(\omega) = \frac{1}{2\pi}\int_{-\infty}^{\infty} R_{ij}(\tau)e^{-i\omega\tau}d\tau \tag{2.8}$$

The diagonal elements of the correlation function, R_{ii} at a given point in space/time, and its spectra, Φ_{ii} at a given wave-number, represent the kinetic energy such that,

$$R_{ii}(0) = \overline{u_i u_i} = \iiint_{-\infty}^{\infty} \Phi_{ii}(\boldsymbol{\kappa})d\boldsymbol{\kappa} \tag{2.9}$$

Integrating $\Phi_{ii}(\boldsymbol{\kappa})$ over a sphere, $\mathcal{S}$, of radius $||\boldsymbol{\kappa}||$ in the equation above eliminates the directional information and the quantity thus obtained is the *energy spectrum*,

$$E(\kappa) = \frac{1}{2}\oint \Phi(\kappa)d\mathcal{S} \qquad E(\omega) = \frac{1}{2}\Phi(\omega) \tag{2.10}$$

where the factor $1/2$ is introduced so that the integral of the energy spectrum exactly equals the kinetic energy.

The velocity correlation function (Equation (2.7)) and the velocity spectrum (Equation (2.8)) are Fourier transform pairs. The pairs in spatial domain provide directional

information about the velocity through their dependence on $\boldsymbol{r}$ and $\boldsymbol{\kappa}$ allowing to define length scales. While the pairs in the time domain allow to define time scales dictating the flow. Similarly, the energy spectrum is the Fourier transform pair of the *autocorrelation function* (= $R_{ii}(r)$ or = $R_{ii}(\tau)$). The study of energy spectra allows one to discern critical details of the flow such as the scales at which energy is induced/dissipated in the flow and subsequently the interactions between the eddies at these scales.

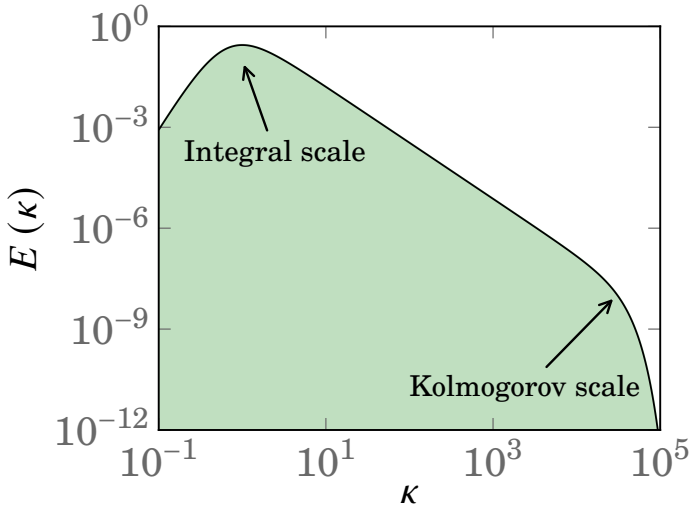

Figure 2.1.: Energy spectra

With the knowledge of the quantities above, several important turbulent scales can be quantified and visualised. Figure 2.1 shows an idealised energy spectra of the velocity fluctuations in wave-number space. Lower wave-numbers represent the large scales in physical space and conversely larger wave-numbers represent the smaller scales.

1. **Energy production range**

   The energy production range is the range where the spectrum rises until it reaches a peak, indicating the infusion of energy from the forces driving the flow. The scales in this range are anisotropic due to the fact that they are created and affected by external forces/boundary conditions. Furthermore, as the wave-number increases the spectrum decreases suggesting that the most energy containing eddies lie in the

large-scales. The largest scale at which the energy transfers to smaller scales is called the *Integral length scale* (L), which is defined as

$$L \equiv \frac{2\pi}{\kappa_L} \equiv \frac{1}{\overline{u^2}} \int_0^\infty R(r)dr \tag{2.11}$$

Similarly, the integral time scale is defined as,

$$T \equiv \frac{2\pi}{\omega_L} \equiv \frac{1}{\overline{u^2}} \int_0^\infty R(\tau)d\tau \tag{2.12}$$

2. **Dissipative range**

   The dissipative range is the range of the spectrum where the scales are small enough that the viscous effects are dominant leading to the conversion of energy in the vortical structures of the flow to heat. A. Kolmogorov (1941) proposed hypotheses describing the behaviour of the small scales. The first hypothesis states that, *given a turbulent flow of sufficiently high Reynolds number, there exists a universal equilibrium range where the statistics of the scales are determined by the viscosity, ν, and the dissipation rate, ε.* On the basis of this hypothesis, the length, time, and velocity scales can be created for the small scales,

$$\eta = \left(\nu^3/\varepsilon\right)^{1/4} \qquad \tau = (\nu/\varepsilon)^{1/2} \qquad u_\eta = (\varepsilon\nu)^{1/4} \tag{2.13}$$

   The Reynolds number of this range shows the balance between the convective scales and dissipative scales,

$$Re_\eta = \frac{u_\eta \eta}{\nu} = 1 \tag{2.14}$$

3. **Inertial range**

   The inertial range is the range of the spectrum that lies between the production and

dissipative ranges $L \gg l \gg \eta$, given a large enough separation between the largest and smallest scales, i.e., $L/\eta \gg 1$. A. Kolmogorov (1941) in his second hypothesis states, *given a turbulent flow of sufficiently high Reynolds number, statistically the motions in this scale have a universal form determined uniquely by the dissipation rate, ε.* This hypothesis suggests that the transfer of energy from the Integral scales to the Kolmogorov scales happens without loss due to molecular viscosity and is fixed at ε. The transfer of energy from the large scales can be estimated as $\varepsilon \approx U^3/L$ and Equation (2.13) gives us $\varepsilon = u_\eta^3/\eta$, equating these relations and some further algebra allows us to quantify the separation between the large and small scales as

$$\frac{L}{\eta} = Re_L^{3/4} \tag{2.15}$$

2.4. DNS

Of the various simulation strategies developed and made available for the study and understanding of turbulent flows, Direct numerical simulations (DNS) are conceptually the most straight forward. The DNS approach entails directly solving the Navier-Stokes equations using an appropriately discretised mesh and an accurate numerical scheme. As such, the mesh should be fine enough to resolve the length and time scales down to the Kolmogorov scales. Evidently, DNS eliminates the need for any models to be used to approximate the flow field and provides us with highly precise information regarding the underlying physics.

Equation (2.15) provides the means to estimate the cost of a DNS simulation (see Sagaut et al., 2006). Considering the smallest mesh size to be of the order of η, for a DNS simulation in 3-dimensions,

$$N_{xyz} = \left(\frac{L_x}{\eta}\right)\left(\frac{L_y}{\eta}\right)\left(\frac{L_z}{\eta}\right) \approx Re_L^{9/4} \tag{2.16}$$

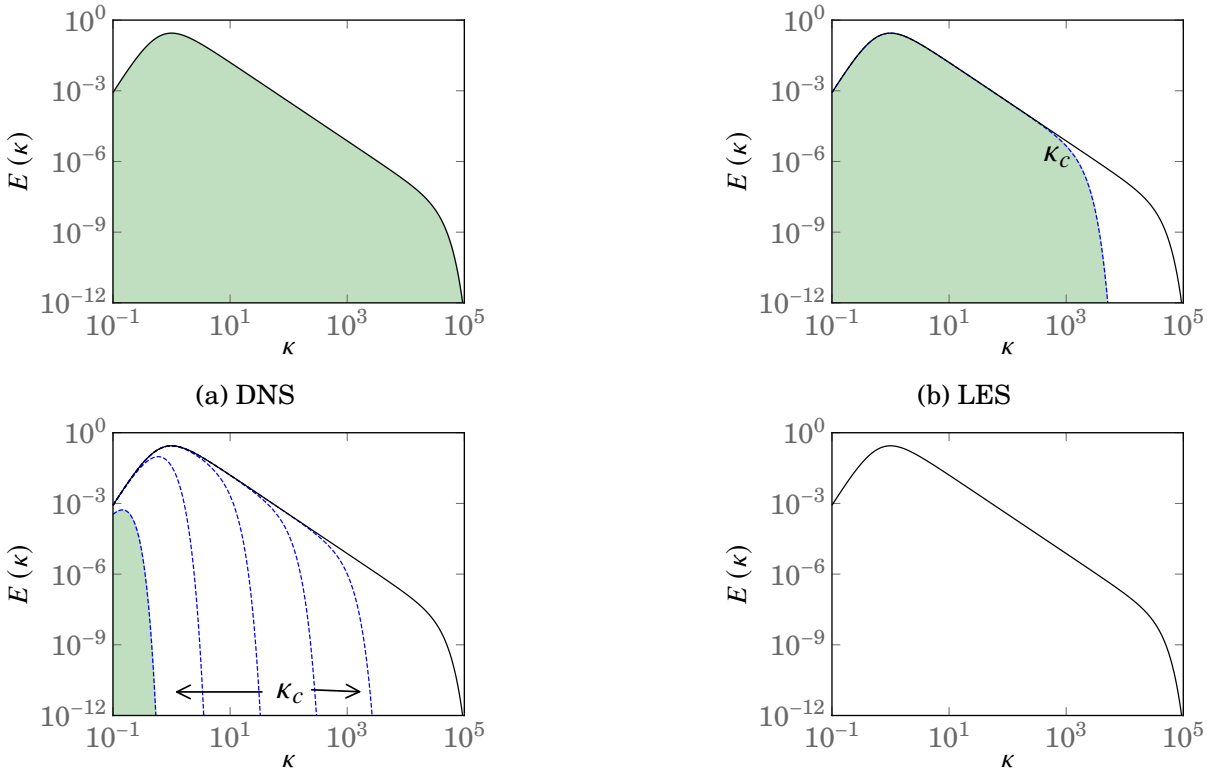

(a) DNS

(b) LES

(c) Hybrid RANS/LES

(d) RANS

Figure 2.2.: Resolved and Modelled scales of various methods (green fill: Resolved scales)

Furthermore, an estimation on the amount of time-steps, Δt, necessary to simulate one eddy turn-over can be accounted for, the distance traversed by a fluid particle should be less than η within one time-step.

$$N_t \approx \frac{T}{\Delta t} \approx \frac{T}{\eta/U} \approx \frac{T}{L/U} Re_L^{3/4} = Re_L^{3/4} \tag{2.17}$$

Due to the stringent criteria needed for a successful DNS, it remains inaccessible for turbulent flows encountered in the industry. For instance, to date the highest Reynolds number reached using DNS is $Re_b = 125000$ ($Re_\tau \approx 5200$) for the simulation of turbulent channel flow by Lee et al. (2015). Such a simulation was achieved at very high costs. Upwards of 1.2×10^{11} mesh points were needed to sufficiently resolve all the scales of turbulence. In addition, the authors developed a new scalable turbulence DNS code optimised for use in

super-computing facilities using up to a million computational cores.

Although these drawbacks make it impossible for DNS to be used at the industry level, it does not diminish the importance of studies conducted using DNS for academic test cases such as the channel flow above. There are advantages to developing DNS databases such as,

- gaining in depth knowledge of the physics of turbulence
- providing a benchmark for validation
- aid in the development of turbulence models

Given that turbulence is encountered in a majority of industrial flows, it is imperative to be able to simulate turbulent flows. Additionally, it is also not feasible to develop experimental facilities for a wide range of reasons. For these reasons, researchers and engineers turn to modelling turbulent flows. Two main techniques exist for modelling turbulence, namely,

- Large Eddy Simulations (LES)
- Reynolds Averaged Navier-Stokes (RANS)

2.5. Filtering approach - LES

The main restriction of using DNS is the need for a highly refined grid in order to capture the smallest scales of turbulence. The idea behind LES, as the name suggests, is to resolve the energy containing eddies and use models to approximate the small scales. This is achieved by applying a low-pass filter to the variables in the flow field in spectral-space which manifests as a cut-off length/time scale in physical space. Figure 2.2 shows an ideal representation of the separation of scales achieved using the filtering approach, such that,

$$\begin{aligned} \phi^* &= \widetilde{\Phi} + \phi' \\ \underbrace{\phi^*}_{\text{instantaneous}} &= \underbrace{\widetilde{\phi^*}}_{\text{resolved}} + \underbrace{(\phi^* - \widetilde{\phi^*})}_{\text{unresolved}} \end{aligned} \tag{2.18}$$

Equation (2.19) shows a general spatio-temporal filter (Kampé de Feriet, 1952), which can be applied either in the spatial-domain or the time-domain.

$$\widetilde{\Phi}(\mathbf{x},t) = \widetilde{\phi^*}(\mathbf{x},t) = \int_{\mathcal{D}} \int_{-\infty}^{t} \mathcal{G}\left(\mathbf{x},\mathbf{x}',t,t'\right) \phi^*\left(\mathbf{x}',t'\right) d\mathbf{x}' \mathrm{d}t' = \mathcal{G} \star \phi^* \tag{2.19}$$

where $\mathcal{G}$ is the convolution kernel defined in the spatio-temporal domain. In order to obtain a filtered form of the Navier-Stokes equations, the filtering operator must satisfy the following properties:

1. **Conservation of constants**

$$\widetilde{a} = a \Rightarrow \int_{\mathcal{D}} \int_{-\infty}^{t} \mathcal{G}\left(\mathbf{x},\mathbf{x}',t,t'\right) d\mathbf{x}' \mathrm{d}t' = 1 \tag{2.20}$$

2. **Linearity**

$$\widetilde{\phi + \psi} = \widetilde{\phi} + \widetilde{\psi} \tag{2.21}$$

3. **Commutation with derivatives**

$$\widetilde{\frac{\partial \phi}{\partial s}} = \frac{\partial \widetilde{\phi}}{\partial s}, \quad s = \mathbf{x} \text{ or } t \tag{2.22}$$

Filters defined as homogenous verify the above properties readily.

However, they cannot be used as is due to problems arising from defining filters on bounded domains as well as using varying filter widths. In practice, filtering operations are implicit in nature, where the filtering operation originates from the numerical scheme and the filter width is defined as the cube-root of the cell volume. This means that the filtering operation

can be quite inhomogeneous in nature. This results in the introduction of commutation errors from the derivatives. Evidently, it is then not possible to define the effective filter for the simulation leading to difficulties in modelling the sub-grid scales. However, these commutation errors introduced are considered to be negligible in practice. Several workarounds exist to tackle this problem, as explained in Sagaut (2006) for example, in order to extend the definitions of filters to bounded domains and with varying filter widths. Additionally, the choice of the numerical scheme can induce dissipative effects damping the resolution of higher wave-numbers/frequencies.

It is also important to note that excepting the Sharp cut-off/Spectral filter, the classical filters presented in the following sections are not idempotent in contrast to the Reynolds averaging operator, i.e.,

$$\widetilde{\widetilde{\phi^*}} = \mathcal{G} \star \mathcal{G} \star \phi^* \neq \widetilde{\phi^*} \tag{2.23}$$

$$\widetilde{\phi'} = \mathcal{G} \star (1 - \mathcal{G}) \star \phi^* \neq 0 \tag{2.24}$$

2.5.1. Spatial filters

The general expression for spatial filtering is as follows,

$$\widetilde{\phi^*}(x,t) = \mathcal{G} \star \phi^* = \int_{-\infty}^{+\infty} \mathcal{G}(x - x', t)\phi^*(x', t)dx' \tag{2.25}$$

Some classical filters used for spatial scale separation are presented below for a 1-dimensional case with the filter width , Δ.

Table 2.1.: Spatial filters

Filter	Kernel, $\mathcal{G}_\Delta$	Transfer function, $\widehat{\mathcal{G}}_\Delta$
Top-hat	$\frac{1}{\Delta}\mathcal{H}(\frac{\Delta}{2} - \lvert x - x'\rvert)$	$\frac{\sin(\kappa\Delta/2)}{\kappa\Delta/2}$
Gaussian	$(\frac{6}{\pi\Delta^2})^{1/2} \exp(\frac{-6\lvert x-x'\rvert^2}{\Delta^2})$	$\exp(\frac{-\Delta^2\kappa^2}{24})$
Spectral/Sharp cut-off	$\frac{\sin(\pi r/\Delta)}{\pi r}$	$\mathcal{H}(\pi/\Delta - \lvert\kappa\rvert)$

$\mathcal{H}$ being the *Heavyside* function.

2.5.2. Temporal filters

The general expression for temporal filtering is as follows,

$$\widetilde{\phi^*}(x,t) = \mathcal{G} \star \phi^* = \int_{-\infty}^{+\infty} \mathcal{G}(x, t'-t)\phi^*(x,t')dt' \tag{2.26}$$

An additional condition for a filter to be applicable to the time-domain is that it should be *causal*. The causality constraint necessitates that,

$$\mathcal{G}(t'-t) = 0 \quad \text{for } t' > t$$

Notably Pruett et al. (2003) have defined such filters in their work on temporal-LES, for example,

Table 2.2.: Temporal filters

Filter	Kernel, G_Δ	Transfer function, $\widehat{G}_\Delta$
Exponential	$\frac{1}{\Delta_T}\exp(\frac{\lvert t-t'\rvert}{\Delta_T})$	$\frac{1}{1+i\omega\Delta_T}$
Heavyside	$\frac{1}{\Delta_T}\mathcal{H}(\lvert t-t'\rvert+\Delta_T)$	$\frac{1-\exp(-i\omega\Delta_T)}{i\omega\Delta_T}$

where $\mathcal{H}$ is the *Heavyside* function.

2.5.3. Filtered Navier-Stokes equations

The filtered form of the Navier-Stokes equations are presented here assuming that the filter commutes with the derivative operators. It can be noted that the divergence-free condition is satisfied by the filtered equations. Additionally, filtering the momentum equation leads to the appearance of a sub-filter stress term that needs to be modelled. Since the filtering operation is not idempotent, further algebra is necessary to clearly define the forms of the convective term and the sub-filter stress term in momentum equation as demonstrated in Equation (2.28).

$$\frac{\partial \widetilde{U}_i}{\partial x_i} = 0, \text{ where } \widetilde{U}_i = \widetilde{u}_i^* \tag{2.27}$$

$$\frac{\partial \widetilde{U}_i}{\partial t} + \widetilde{U}_j \frac{\partial \widetilde{U}_i}{\partial x_j} = -\frac{1}{\rho}\frac{\partial \widetilde{P}}{\partial x_i} + \nu \frac{\partial^2 \widetilde{U}_i}{\partial x_j \partial x_j} - \frac{\partial \tau_{ij}^{\text{sfs}}}{\partial x_j} \tag{2.28}$$

- **Leonard's Decomposition of the non-linear term**

$$\begin{aligned}
\widetilde{u_i^* u_j^*} &= \widetilde{\widetilde{U}_i \widetilde{U}_j} + \underbrace{\widetilde{\widetilde{U}_i u_j'} + \widetilde{u_i' \widetilde{U}_j}}_{C_{ij}} + \underbrace{\widetilde{u_i' u_j'}}_{R_{ij}} \\
\widetilde{u_i^* u_j^*} &= \widetilde{U}_i \widetilde{U}_j + \underbrace{\widetilde{\widetilde{U}_i \widetilde{U}_j} - \widetilde{U}_i \widetilde{U}_j}_{L_{ij}} + C_{ij} + R_{ij} \\
\tau_{ij}^{\text{sfs}} &= \widetilde{u_i^* u_j^*} - \widetilde{U}_i \widetilde{U}_j \\
\tau_{ij}^{\text{sfs}} &= L_{ij} + C_{ij} + R_{ij}
\end{aligned} \tag{2.29}$$

Close attention needs to be paid to the way the non-linear term is decomposed. Using the relation $u_i^* = \widetilde{U}_i + u_i'$, one arrives at the 1st step in Equation (2.29), called a double decomposition (Sagaut, 2006). The Cross-stress tensor, C_{ij}, represents interactions between the resolved and the unresolved scales. The Reynolds stress tensor, R_{ij}, represents the interaction between the unresolved scales. However, the term $\widetilde{\widetilde{U}_i \widetilde{U}_j}$ poses a problem due to the presence of a second filtering operator which is expensive to compute directly. Leonard (1975) in his decomposition suggested further steps in order to alleviate this problem thus arriving at the final form shown in Equation (2.29) allowing us to write the momentum equation in the form shown in Equation (2.28). The resulting additional term called the Leonard tensor, L_{ij}, represents the interactions among the resolved scales of the simulation.

2.5.4. Spatial sub-filter scale modelling

All that remains is to model the sub-filter scale tensor, τ_{ij}^{sfs}, in order to account for the dissipation of energy at the unresolved scales. Indeed, it has to be noted that LES can be used without the use of an explicit sub-filter scale model. This is called the Implicit LES approach, which is based on using a dissipative numerical scheme and the assumption that the action of numerical dissipation on the unresolved scales is representative of an explicit model. However, sub-filter scale models remain by far the more extensively studied and used. A multitude of models exist based on various methods of interpretation such as,

1. Turbulent viscosity models
2. Scale similarity models
3. Models based on the deconvolution of filtered quantities
4. and others...

An exhaustive list can be found in the work of Sagaut (2006).

We shall focus on the description of ***Turbulent viscosity models***. The idea behind these models is to represent the sub-filter stresses as a diffusive term.

$$\tau_{ij}^{\text{sfs}} - \frac{1}{3}\tau_{kk}^{\text{sfs}} = -2\nu_{\text{sfs}}\widetilde{S}_{ij} \tag{2.30}$$

The deviatoric part of the stresses are modelled using the linear eddy-viscosity, where the residual stresses are related to the filtered strain rate $\widetilde{S}_{ij} = 1/2(\partial\widetilde{U}_i/\partial x_j + \partial\widetilde{U}_j/\partial x_i)$. Note that the isotropic part, τ_{kk}, is absorbed as a modified pressure term leaving the deviatoric part to be modelled explicitly.

1. **Smagorinsky model**: (Smagorinsky, 1963) proposed an eddy-viscosity model for the closure problem of the sub-filter stresses by analogy to the mixing-length model, where the sub-filter viscosity is modelled as,

$$\nu_{\text{sfs}} = l_s^2 \widetilde{\mathcal{S}} = C_s^2 \widetilde{\Delta}^2 \widetilde{\mathcal{S}}, \qquad \widetilde{\mathcal{S}} = \sqrt{2 \widetilde{S}_{ij} \widetilde{S}_{ij}} \tag{2.31}$$

where $\widetilde{\mathcal{S}}$ is the characteristic filtered rate of strain, l_s is the Smagorinsky length scale. The length scale l_s is taken to be proportional to the filter width, $\widetilde{\Delta}$, resulting in the proportionality constant, C_s which needs to be calibrated.

Considering a high Reynolds number flow in the case of a homogeneous isotropic turbulence such that the integral length scale is much larger than the cut-off filter width, $L \gg \widetilde{\Delta}$, the *local equilibrium hypothesis* gives us that the mean injected energy is cascaded without loss and is balanced by the dissipation.

In the case of an eddy viscosity model, the rate of production is given by,

$$P = 2\nu_{\text{sfs}} \widetilde{S}_{ij} \widetilde{S}_{ij} = \nu_{\text{sfs}} \widetilde{\mathcal{S}}^2 \tag{2.32}$$

$$\varepsilon = \overline{\mathcal{P}}_{\text{sfs}} = \overline{\nu_{\text{sfs}} \widetilde{\mathcal{S}}^2} = l_s^2 \overline{\widetilde{\mathcal{S}}^3} \tag{2.33}$$

Under the hypothesis of a sharp spectral filter with the cut-off wave-number, $\kappa_c = \pi / \widetilde{\Delta}$, in the inertial range, $\overline{\widetilde{\mathcal{S}}^2}$ can be estimated using the Kolmogorov energy spectrum, such that

$$\overline{\widetilde{\mathcal{S}}^2} = \overline{2 \widetilde{S}_{ij} \widetilde{S}_{ij}} = \frac{3}{2} \pi^{4/3} C_K \varepsilon^{2/3} \widetilde{\Delta}^{-4/3} \tag{2.34}$$

Combining equations Equations (2.31), (2.33) and (2.34),

$$\frac{l_s^2}{\widetilde{\Delta}^2} = \frac{\overline{\widetilde{\mathcal{S}}^2}^{3/2}}{\overline{\widetilde{\mathcal{S}}^3}} \left(\frac{2}{3\pi^{4/3} C_K} \right)^{3/2}, \tag{2.35}$$

finally, in accordance with the analysis of Lilly (1967) we use the approximation

$\overline{\widetilde{\mathcal{S}}^2}^{3/2} = \overline{\widetilde{\mathcal{S}}^3}$, giving us

$$C_s = \frac{l_s}{\widetilde{\Delta}} = \frac{1}{\pi}\left(\frac{2}{3C_K}\right)^{3/4} \approx 0.18 \tag{2.36}$$

It is important to note that this constant **is not really a constant** but rather an arbitrary coefficient whose value is dependent on a number of factors such as,

- *Type of flow*:

  $C_s \simeq 0.18 - 0.2$ for isotropic turbulence

  $C_s \simeq 0.065 - 0.1$ for channel-flows

  Additionally, strong deviations of flow characteristics from the hypotheses used to derive the model yield unsatisfactory results.

- *Reynolds number*: For laminar flows, where the residual stresses are essentially zero, a non-zero value of C_s results in non-zero sub-filter viscosity when the resolved velocity gradients are non-zero, thus leading to incorrect results.

In practice the value of C_s is calibrated to improve the results of the computation either in an empirical fashion or by the introduction of additional damping functions to account for near wall effects.

2. **Dynamic Smagorinsky Model**: Germano et al. (1991) proposed a model aimed at replacing the Smagorinsky constant, C_s, universally applied to a flow field, by computing the model coefficient dynamically C_d as a function of the local state of the flow at simulation time. The core idea of this new model is the introduction of an additional test-filter ($\langle\cdot\rangle$) with a filter width $\langle\Delta\rangle \simeq 2\widetilde{\Delta}$, so that the information obtained from sampling the smallest resolved scales using the test-filter can be used to model the unresolved sub-filter scales $\left(< \widetilde{\Delta}\right)$.

   The extension of the decomposition of velocity with the application of the test-filter writes,

$$u^* = \widetilde{U} + u' = \langle \widetilde{U} \rangle + \left(\widetilde{U} - \langle \widetilde{U} \rangle \right) + u' \tag{2.37}$$

Furthermore, the residuals stresses are to be defined based on the two levels of filtering, i.e., the sub-filter unresolved scales $\left(\tau_{ij}^{\text{sfs}} \right)$ and the sub-test-filter scales $\left(T_{ij}^{\text{sfs}} \right)$.

$$\tau_{ij}^{\text{sfs}} = \widetilde{u_i^* u_j^*} - \widetilde{U}_i \widetilde{U}_j \tag{2.38}$$

$$T_{ij}^{\text{sfs}} = \langle \widetilde{U_i U_j} \rangle - \langle \widetilde{U}_i \rangle \langle \widetilde{U}_j \rangle \tag{2.39}$$

Finally using the Germano identity (Germano, 1992), one can represent the Leonard stress tensor fully in terms of known the resolved field, $\widetilde{U}$, such that,

$$\mathcal{L}_{ij} = T_{ij}^{\text{sfs}} - \tau_{ij}^{\text{sfs}} = \langle \widetilde{U}_i \widetilde{U}_j \rangle - \langle \widetilde{U}_i \rangle \langle \widetilde{U}_j \rangle \tag{2.40}$$

Introducing the Smagorinsky model as is for both τ_{ij}^{sfs} and T_{ij}^{sfs} assuming that the same co-efficient can be used for both filtering levels, the deviatoric parts can be written as such,

$$\tau_{ij} - \frac{1}{3}\tau_{kk} = -2C_d \widetilde{\Delta}^2 \widetilde{\mathcal{S}} \widetilde{S}_{ij} \tag{2.41}$$

$$T_{ij} - \frac{1}{3}T_{kk} = -2C_d \langle \widetilde{\Delta} \rangle^2 \langle \widetilde{\mathcal{S}} \rangle \langle \widetilde{S}_{ij} \rangle \tag{2.42}$$

the above relations allow us to write the deviatoric part of the Leonard stress tensor,

$$\mathcal{L}_{ij} - \frac{1}{3}\mathcal{L}_{kk} = -C_d \left(2\widetilde{\Delta}^2 \langle \widetilde{\mathcal{S}} \widetilde{S}_{ij} \rangle - 2\langle \widetilde{\Delta} \rangle^2 \langle \widetilde{\mathcal{S}} \rangle \langle \widetilde{S}_{ij} \rangle \right) = C_d M_{ij} \tag{2.43}$$

The dynamic Smagorinsky co-efficient can be computed using the relation above since both $\mathcal{L}_{ij}$ and M_{ij} can be determined in terms of the resolved velocity field. However, such a solution to the co-efficient is tensorial in nature. In order to determine a single value, originally Germano et al. (1991) proposed contracting the Leonard tensor using the strain rate tensor, $\widetilde{S}_{ij}$. But this method fails if $\widetilde{S}_{ij}$ is zero. Lilly (1992) further proposed a modification whereby the co-efficient is determined by a least-squares method giving the solution to be

$$C_d = \frac{M_{ij}\mathcal{L}_{ij}}{M_{kl}M_{kl}} \tag{2.44}$$

The co-efficient above can have negative values and a zero denominator, both of which would lead to instabilities in the computation. In order to increase the numerical stability, a suitable averaging operation is introduced,

$$C_d = \frac{\overline{M_{ij}\mathcal{L}_{ij}}}{\overline{M_{kl}M_{kl}}} \tag{2.45}$$

3. **Wall-Adapting Local Eddy-Viscosity Model (WALE)**: One of the downfalls of eddy-viscosity models is the incorrect behaviour in the near-wall regions resulting in extraneous damping of fluctuations. Nicoud et al. (1999) introduced the WALE model to recover the proper near-wall scaling $\left(\nu_{\text{sfs}} \propto y^3\right)$, where y is the distance to the wall. The model is written as follows,

$$\nu_{\text{sfs}} = C_w^2 \widetilde{\Delta}^2 \frac{\left(\mathcal{S}_{ij}^d \mathcal{S}_{ij}^d\right)^{3/2}}{\left(\widetilde{S}_{ij}\widetilde{S}_{ij}\right)^{5/2} + \left(\mathcal{S}_{ij}^d \mathcal{S}_{ij}^d\right)^{5/4}}, \tag{2.46}$$

with $C_w = 0.55 - 0.6$ and

$$\mathcal{S}_{ij}^d = \widetilde{S}_{ik}\widetilde{S}_{kj} + \widetilde{\Omega}_{ik}\widetilde{\Omega}_{kj} - \frac{1}{3}\delta_{ij}\left(\widetilde{S}_{mn}\widetilde{S}_{mn} - \widetilde{\Omega}_{mn}\widetilde{\Omega}_{mn}\right), \tag{2.47}$$

is the traceless symmetric part of the square of the velocity gradient tensor. In addition to recovering the correct asymptotic behaviour at the wall, this model takes into account both the strain and rotation rates of the turbulent structures.

2.5.5. Temporal sub-filter scale modelling

Temporal LES has received attention recently due mainly to the works of Pruett (2000) and Pruett et al. (2003, 2006), particularly considering *Eulerian Time-Domain Filtering*. To note, they developed the *Temporal Approximate Deconvolution model (TADM)*, based on the Approximate Deconvolution model (ADM) of Stolz et al. (1999) and the *Temporal Scale Similarity model (TSSM)* based on the Scale Similarity model (SSM) of Bardina et al. (1980).

TADM approach relies on modelling the exact residual stress, τ_{ij}^{sfs}, using the de-convoluted velocity which approximates the unfiltered velocity. This is achieved through a repeated application of linear deconvolution, i.e., through the use of truncated Taylor series expansion of the inverse filter operator. Furthermore, the TADM approach is a generalised form of the TSSM approach with TSSM being the zeroth-order deconvolution of the TADM method akin to their spatially filtered counterparts (ADM and SSM).

2.6. Statistical approach - RANS

Due to the chaotic character of the system, the velocity field of a turbulent flow can be considered as *random*, in the sense that it does not posses a unique value when measured N-times under the same set of conditions. In case of laminar flows the velocity field can be predicted to a high degree of certainty either experimentally or numerically using the Navier-Stokes equations. In the case of turbulent flows, we can only aim to characterise the flow fields based on statistical quantities such as the *mean*, *variance*, and further higher order moments.

Under these considerations, a random field at a point in space and time, can be decomposed

into its mean and fluctuations; such a decomposition is called the *Reynolds decomposition*. For any arbitrary quantity ϕ^*, we have the Reynolds decomposition as follows,

$$\begin{aligned} \phi^* &= \Phi + \phi \\ \underbrace{\phi^*}_{\text{instantaneous}} &= \underbrace{\overline{\phi^*}}_{\text{mean}} + \underbrace{(\phi^* - \overline{\phi^*})}_{\text{fluctuations}} \end{aligned} \tag{2.48}$$

Generally, the averaging operator in turbulence is defined as the *Ensemble average*. For a quantity measured N-times over N-realisations of an experiment carried out under a similar set of conditions, the ensemble average is given by,

$$\overline{\phi^*}(\mathbf{x}, t) = \Phi(\mathbf{x}, t) = \lim_{N \to \infty} \frac{1}{N} \sum_{n=1}^{N} \phi_n^*(\mathbf{x}, t) \tag{2.49}$$

However, in practice it is not feasible to repeat experiments/computations as many times. Hence it is convenient to express the average in different forms, under certain hypotheses, which allow for easier measurement of statistical quantities.

- For *statistically stationary flows* where the statistic quantities are independent of time, $\overline{\phi^*}(\mathbf{x}, t) = \overline{\phi^*}(\mathbf{x})$, evoking the *ergodicity hypothesis* (Monin et al., 1971), the ensemble average is equivalent to the temporal average

$$\overline{\phi^*}(\mathbf{x}) = \Phi(\mathbf{x}) = \lim_{T \to \infty} \frac{1}{T} \int_0^T \phi^*(\mathbf{x}, t) dt \tag{2.50}$$

- For *statistically homogeneous flows* in one or more spatial directions, the statistical quantities are independent of their location in the domain. Here for instance in the x-direction $\overline{\phi^*}(x, y, z, t) = \overline{\phi^*}(y, z, t)$, again evoking the *ergodicity hypothesis* (Monin et al., 1971), and the ensemble average is equivalent to the spatial average in the homogeneous direction

$$\overline{\phi^*}(y, z, t) = \Phi(y, z, t) = \lim_{L \to \infty} \frac{1}{L} \int_0^L \phi^*(x, y, z, t) dx \tag{2.51}$$

An averaging operator allowing for Reynolds decomposition has to have the following properties,

- Conservation of constants

$$\overline{a} = a \tag{2.52}$$

- Linearity

$$\begin{aligned} \overline{a\phi^*} &= a\overline{\phi^*} \\ \overline{\phi^* + \psi^*} &= \overline{\phi^*} + \overline{\psi^*} \end{aligned} \tag{2.53}$$

- Commutation with derivatives

$$\overline{\frac{\partial \phi^*}{\partial s}} = \frac{\partial \overline{\phi^*}}{\partial s}, \quad s = \mathbf{x} \text{ or } t \tag{2.54}$$

Additionally, the mean obtained with the averaging operator implies that the random variables are evenly distributed around the mean and that it is not a variable in itself, such that, $\overline{\overline{\phi^*}} = \overline{\phi^*}$, further implying that the fluctuations are centred exactly at zero, $\overline{\phi} = 0$.

2.6.1. Reynolds averaged NS

Applying the Reynolds decomposition to the incompressible Navier-Stokes equations (Equations (2.4) and (2.5)) and using the properties listed above for the Reynolds averaging operators, we obtain the *Reynolds Averaged Navier-Stokes (RANS)* equations.

- Continuity equation

$$\frac{\partial U_i}{\partial x_i} = 0 \tag{2.55}$$

- Momentum equation

$$\frac{\partial U_i}{\partial t} + U_j \frac{\partial U_i}{\partial x_j} = -\frac{1}{\rho}\frac{\partial P}{\partial x_i} + \nu \frac{\partial^2 U_i}{\partial x_j \partial x_j} - \frac{\partial \overline{u_i u_j}}{\partial x_j} \tag{2.56}$$

It can be noted that the incompressibility condition of a *divergence-free* velocity holds for the RANS equations too. The additional term appearing at the right-hand side of the equation, $\overline{u_i u_j}$, is called the Reynolds stress. It is termed as a stress because its influence on the mean flow is akin to that of the stresses exerted due to molecular forces by the viscous term. The Reynolds stresses are additional unknowns that need to be accounted for if one has to solve the mean equations of motion. Since it is a symmetric tensor, there are 6 unknowns introduced in total and with only 4 equations the system of equations are *undetermined*. This problem is often referred to as the ***Turbulence Closure Problem***.

Researchers have devised multiple ways of tackling the closure problem, ranging from the *Mixing length model* (Prandtl, 1925) to models based on directly solving the Reynolds stress transport equation.

2.6.2. Transport equations for second order moments

In order to close the system of equations, it is prudent to understand the nature of the Reynolds stress term. The obvious starting point would be to study the transport equations for Reynolds stresses. Defining a Navier-Stokes operator, $\mathcal{N}(u_i^*)$ (Wilcox, 2006), where

$$\mathcal{N}(u_i^*) = \frac{\partial u_i^*}{\partial t} + \frac{\partial u_k^* u_i^*}{\partial x_k} + \frac{1}{\rho}\frac{\partial p^*}{\partial x_i} - \nu \frac{\partial^2 u_i^*}{\partial x_k \partial x_k}, \tag{2.57}$$

the transport equation for Reynolds stresses can be derived as,

$$\overline{u_i \mathcal{N}(u_j^*) + u_j \mathcal{N}(u_i^*)} = 0 \tag{2.58}$$

Finally, the Reynolds stress equation can be written as follows,

$$\begin{aligned}\frac{\partial \overline{u_i u_j}}{\partial t} + U_k \frac{\partial \overline{u_i u_j}}{\partial x_k} = &- \left. \overline{u_i u_k} \frac{\partial U_j}{\partial x_k} - \overline{u_j u_k} \frac{\partial U_i}{\partial x_k} \right\} \mathcal{P}_{ij} \\ &+ \left. \nu \frac{\partial^2 \overline{u_i u_j}}{\partial x_k x_k} \right\} \mathcal{D}^{\nu}_{ij} \\ &- \left. \frac{\partial \overline{u_i u_j u_k}}{\partial x_k} \right\} \mathcal{D}^{T}_{ij} \\ &- \left. \frac{1}{\rho} \frac{\partial}{\partial x_k} \left(\overline{u_i p} \delta_{jk} + \overline{u_j p} \delta_{ik} \right) \right\} \mathcal{D}^{P}_{ij} \\ &+ \left. \overline{\frac{p}{\rho} \left(\frac{\partial u_i}{\partial x_j} + \frac{\partial u_j}{\partial x_i} \right)} \right\} \Pi_{ij} \\ &- \left. 2\nu \overline{\frac{\partial u_i}{\partial x_k} \frac{\partial u_j}{\partial x_k}} \right\} \varepsilon_{ij}\end{aligned} \tag{2.59}$$

- $\mathcal{P}_{ij}$: Production term
- $\mathcal{D}^{\nu}_{ij}$: Viscous diffusion
- $\mathcal{D}^{T}_{ij}$: Turbulent diffusion
- $\mathcal{D}^{P}_{ij}$: Pressure diffusion
- Π_{ij} : Pressure-Strain rate correlation/redistribution term
- ε_{ij} : Dissipation term

2.6.3. Second order closure models - Reynolds stress models

Equation (2.59) produces terms of two kinds. The first kind (namely, $\mathcal{P}_{ij}$ and $\mathcal{D}^{\nu}_{ij}$) which can be directly evaluated from the mean flow. The second kind (namely, $\mathcal{D}^{T}_{ij}$, $\mathcal{D}^{P}_{ij}$, Π_{ij}, and ε_{ij}) which are functions of higher-moments that are impossible to be evaluated with the information available from the simulations. In an effort to simplify the Navier-Stokes equations through the averaging process, the inevitable appearance of such terms further compounds the turbulence closure problem. Since further deriving transport equations for

the unknown terms **will** lead to the appearance of higher and higher order moments, these terms are modelled in lieu of being evaluated.

Turbulent diffusion term, $\mathcal{D}_{ij}^{T}$

A common approach to modelling the triple correlation in the turbulent diffusion term is based on the *gradient diffusion hypothesis*. Relating the triple correlation to the tensor of rank three obtained from the gradient of the Reynolds stresses gives,

$$\overline{u_i u_j u_k} \propto \frac{\partial \overline{u_i u_j}}{\partial x_k} \tag{2.60}$$

Introducing a proportionality constant, C_s, and the missing dimensional factor of $length^2/time$ two forms of models can be formed using,

- *Simple gradient diffusion hypothesis (SGDH)*

$$\overline{u_i u_j u_k} = -C_s \frac{k^2}{\varepsilon} \frac{\partial \overline{u_i u_j}}{\partial x_k}, \tag{2.61}$$

  where the model constant is taken to be, $C_s \approx 0.11$.

- *Generalised gradient diffusion hypothesis (GGDH)*

$$\overline{u_i u_j u_k} = -C_s \frac{k}{\varepsilon} \overline{u_k u_l} \frac{\partial \overline{u_i u_j}}{\partial x_l}, \tag{2.62}$$

  where the model constant is taken to be, $C_s \approx 0.22$.

Models of a more complex nature have been explored by researchers, however, it is generally noted that this term is not of critical importance and the above models are satisfactory.

Pressure diffusion term, $\mathcal{D}_{ij}^{P}$

Pressure fluctuations in a flow are quite difficult to measure accurately in experiments. With the advent of DNS, highly resolved databases were used to study the effects of the pressure diffusion term. These terms were found to have negligible influence in many cases and hence can be neglected in turbulence models. Actually, the pressure diffusion term is generally modelled as part of the turbulence diffusion term, $\mathcal{D}_{ij}^{T}$, using a gradient diffusion hypothesis such that the calibration of the constant, C_s, also accounts for the pressure diffusion term.

Pressure-Strain rate correlation term, Π_{ij}

Unlike the pressure diffusion terms, the pressure strain-rate correlation term plays a major role in many cases of study and is found to be of the same order as the production term. Moreover, the correlations within the term are not measurable and thus has received a great deal of attention by turbulence modellers to predict its behaviour through various means. The separation of the pressure terms in the Reynolds stress equation is such that this correlation term is *traceless* and hence does not aid in the production of kinetic energy. Its effects are rather to redistribute energy among the various components of the Reynolds stress and therefore it is also called the *redistribution term*.

The Poisson equation for pressure gives insights into understanding the effects of pressure fluctuations on the flow field. Taking the divergence of the Navier-Stokes equations, applying the Reynolds decomposition, and using the incompressibility constraint gives the Poisson equation for pressure fluctuations as,

$$\frac{1}{\rho}\frac{\partial^2 p}{\partial x_j \partial x_j} = \underbrace{-\frac{\partial^2}{\partial x_i \partial x_j}\left(u_i u_j - \overline{u_i u_j}\right)}_{\text{slow-term}} \quad \underbrace{-2\frac{\partial U_i}{\partial x_j}\frac{\partial u_j}{\partial x_i}}_{\text{rapid-term}} \tag{2.63}$$

The second term on the right-hand side is directly influenced by changes in the mean strain-rate and hence called the *rapid-term*. On the contrary, the first term which is

indirectly affected by the mean strain-rate is called the *slow-term*. The solution of Equation (2.63), obtained by using Green's theorem to integrating over the flow domain, gives the pressure fluctuation at a given point. Essentially, this allows to build the redistribution term to be written in terms of the slow-term and rapid-term.

$$\Pi_{ij} = \Pi^s_{ij} + \Pi^r_{ij} \tag{2.64}$$

Π^s_{ij} and Π^r_{ij} can be modelled as either linear or non-linear relations of the Reynolds stresses. One such model most commonly used is the Speziale, Sarkar, and Gatski (SSG) model (Speziale et al., 1991), it is written as follows,

$$\Pi^s_{ij} = -C_1 \varepsilon b_{ij} + C_2 \varepsilon \left(b_{ik} b_{kj} - \frac{1}{3} b_{mn} b_{mn} \delta_{ij} \right) \tag{2.65}$$

$$\Pi^r_{ij} = -C_1^* \mathcal{P} b_{ij} + \left(C_3 - C_3^* \sqrt{II} \right) k S_{ij} + C_4 k \left(b_{ik} S_{kj} + S_{ik} b_{kj} - \frac{2}{3} b_{mn} S_{mn} \delta_{ij} \right) + C_5 k \left(b_{ik} \Omega_{kj} + \Omega_{ik} b_{kj} \right), \tag{2.66}$$

where $\mathcal{P} = 1/2 \mathcal{P}_{kk}$, $II = b_{ij} b_{ij}$ is the second tensor invariant of the anisotropy tensor $b_{ij} = \frac{\overline{u_i u_j}}{2k} - \frac{1}{3}\delta_{ij}$, S_{ij} and Ω_{ij} are the symmetric and anti-symmetric strain-rate tensors, and $C_{...}$ are the constants to be calibrated.

Dissipation term, ε_{ij}

This term represents the transformations of mechanical energy to heat due to viscous effects. One of the common approaches is the use of the Kolmogorov hypothesis of local isotropy since dissipation occurs at the small scales,

$$\varepsilon_{ij} = \frac{2}{3} \varepsilon \delta_{ij}, \quad \varepsilon = \nu \overline{\frac{\partial u_i}{\partial x_j} \frac{\partial u_i}{\partial x_j}} \tag{2.67}$$

The solution for ε is obtained by solving a transport equation.

2.6.4. First order closure models - Eddy-viscosity models

One of the most popular strategies of modelling the unknown correlation terms in the RANS momentum equations is by relation to a *turbulent eddy viscosity*. This is achieved through a Boussinesq relationship between the second order moments and the mean strain rate tensor, called as the linear eddy viscosity models. The Boussinesq relationship is a direct analogy to the viscous stress relation for an incompressible Newtonian fluid,

$$\overline{u_i u_j} = \frac{2}{3}k\delta_{ij} - 2\nu_t S_{ij}, \qquad k = \frac{\overline{u_i u_i}}{2} \text{ and } S_{ij} = \frac{1}{2}\left(\frac{\partial U_i}{\partial x_j} + \frac{\partial U_i}{\partial x_j}\right) \tag{2.68}$$

The RANS momentum equation can be formulated such that the diffusive term is now represented by an effective viscosity, $\nu + \nu_t$

$$\frac{\partial U_i}{\partial t} + U_j\frac{\partial U_i}{\partial x_j} = -\frac{1}{\rho}\frac{\partial P^\star}{\partial x_i} + \frac{\partial}{\partial x_j}\left((\nu + \nu_t)\frac{\partial U_i}{\partial x_j}\right) \tag{2.69}$$

where the isotropic part of the Reynolds stress is absorbed into the hydrodynamic pressure, $P^\star = P + \rho 2k/3$.

Further sub-levels of modelling exist within the linear eddy-viscosity modelling framework, however, particular focus is given to models of the *two-equation* family. In essence, the turbulent length and velocity scales necessary to predict the effects of the Reynolds stresses are gathered using transport equations for simpler quantities such as *kinetic energy*, k, in combination with either the *dissipation rate*, ε, or the *specific dissipation-rate (dissipation rate per unit kinetic energy)*, $\omega \propto \varepsilon/k$. The unknown turbulent viscosity term in the eddy-viscosity formulation of the RANS equations, Equation (2.69), is dimensionally $length^2/time$.

$$\nu_t \propto \underbrace{k^{1/2}}_{\substack{\text{velocity}\\ \text{scale}}} \quad \underbrace{\ell}_{\substack{\text{length}\\ \text{scale}}} \tag{2.70}$$

Transport equation for turbulent kinetic energy

$$\begin{aligned}\frac{\partial k}{\partial t} + U_j \frac{\partial k}{\partial x_j} = &\underbrace{-\overline{u_i u_j}\frac{\partial U_i}{\partial x_j}}_{\mathcal{P}} - \underbrace{\frac{1}{\rho}\frac{\partial}{\partial x_j}\left(\overline{p u_j}\right)}_{\mathcal{D}^P} - \underbrace{\frac{\partial}{\partial x_j}\left(\frac{1}{2}\overline{u_i u_i u_j}\right)}_{\mathcal{D}^T} \\ &+ \underbrace{\nu\frac{\partial^2 k}{\partial x_j \partial x_j}}_{\mathcal{D}^\nu} - \underbrace{\nu\overline{\frac{\partial u_i}{\partial x_j}\frac{\partial u_i}{\partial x_j}}}_{\varepsilon}\end{aligned} \tag{2.71}$$

As done before for the Reynolds stress equation, the terms $\mathcal{D}^P$ and $\mathcal{D}^T$ need modelling. A similar approach is used wherein the pressure and turbulent diffusion terms are combined and modelled under the simple gradient diffusion hypothesis.

$$\frac{1}{\rho}\overline{p u_j} + \frac{1}{2}\overline{u_i u_i u_j} = -\frac{\nu_t}{\sigma_k}\frac{\partial k}{\partial x_j}, \tag{2.72}$$

where σ_k is the Prandtl number for diffusion and is considered to be a constant for incompressible flows. In order to fully close the equations, a length scale, ℓ, and a model for the dissipation rate, ε, needs to be specified.

$k-\varepsilon$ based models

Modelling the dissipation rate, ε, is not a simple matter. An approach using the exact transport equation leads to much too complex correlations that require further closure approximations if attempted through a strictly mathematical sense. Researchers have instead opted to follow a more phenomenological approach based on physical reasoning.

The role of dissipation rate can be seen as a representation of the energy transferred from the large-scales (see Kolmogorov's second hypothesis) in contrast to its representation in Equation (2.71) as the dissipation of small-scales due to processes in the dissipative

range. For high-reynolds number flows, the transfer of energy from the large scales can be estimated as,

$$\varepsilon \propto k^{3/2}/\ell, \quad \varepsilon \propto k/\tau \tag{2.73}$$

This subtle reasoning is the basis for the transport equation of dissipation rate to be derived empirically based on the transport equation for turbulent kinetic energy.

Standard $k-\varepsilon$ model Jones et al. (1972) developed the $k-\varepsilon$ model with further work to refine the model coefficients by Launder et al. (1974), the *Standard $k-\varepsilon$ model* is written as follows,

$$\nu_t = C_\mu \underbrace{k^{1/2}}_{\substack{\text{velocity}\\ \text{scale}}} \underbrace{k^{3/2}/\varepsilon}_{\substack{\text{length}\\ \text{scale}}} = C_\mu k^2/\varepsilon, \tag{2.74}$$

where the model coefficient, $C_\mu = 0.09$, is calibrated empirically through the analysis of turbulent boundary layers (see Hanjalic et al. (2011) and Pope (2000)).

$$\frac{\partial k}{\partial t} + U_j \frac{\partial k}{\partial x_j} = \underbrace{2\nu_t S_{ij} S_{ij}}_{\mathcal{P}_k} + \frac{\partial}{\partial x_j}\left[\left(\nu + \frac{\nu_t}{\sigma_k}\right)\frac{\partial k}{\partial x_j}\right] - \varepsilon \tag{2.75}$$

$$\frac{\partial \varepsilon}{\partial t} + U_j \frac{\partial \varepsilon}{\partial x_j} = C_{\varepsilon 1}\frac{\varepsilon}{k}\mathcal{P}_k + \frac{\partial}{\partial x_j}\left[\left(\nu + \frac{\nu_t}{\sigma_\varepsilon}\right)\frac{\partial \varepsilon}{\partial x_j}\right] - C_{\varepsilon 2}\frac{\varepsilon^2}{k} \tag{2.76}$$

Equation (2.71) is rewritten using Equation (2.72) and the linear eddy-viscosity hypothesis (Equation (2.68)), $\mathcal{P}_k = -\left(\frac{2}{3}k\delta_{ij} - 2\nu_t S_{ij}\right)\frac{\partial U_i}{\partial x_j} = 2\nu_t S_{ij} S_{ij}$. The dissipation rate equation is written empirically in relation to the transport equation for turbulent kinetic energy as $\varepsilon \sim k/\tau$. The model coefficients are as follows,

C_μ	C_{ε_1}	C_{ε_2}	σ_k	σ_ε
0.09	1.44	1.92	1.0	1.3

BL-v^2/k model When the $k-\varepsilon$ model is used in the context of wall-bounded flows, the formulation of turbulent eddy-viscosity poses issues. In the presence of a solid boundary, the wall normal shear-stress, u_2^2, experiences a damping effect due to the so called wall-blocking effect. The present formulation of the turbulent viscosity stems from the high-Reynolds number flow assumption wherein the velocity and length scales were descriptive of an inviscid isotropic transfer of energy from the large scales to the small scales. As such, $\nu_t = C_\mu k^2/\varepsilon$ does not account for anisotropy resulting from the damping of u_2^2, leading to an over-prediction of turbulent viscosity. One possible solution to this problem is to augment the eddy-viscosity formulation with a *'damping function'*, f_μ, such that $\nu_t = C_\mu f_\mu k^2/\varepsilon$. The damping function is generally a function of the wall-distance aiming to imitate the reduction of turbulent viscosity. This solution, however, is very empirical and not universally applicable. Additionally, singularities appear at the wall in the destruction term of the dissipation rate equation, $C_{\varepsilon_2}\varepsilon^2/k$, where ε is finite while $k \to 0$.

Durbin (1991) proposed a more physics based alternative approach, the so called v^2-f model based on the $k-\varepsilon$ model. Here, an additional scalar transport equation is solved for the wall-normal fluctuations, v^2. It should be noted that even though the v^2 equation is presented as the solution to wall-normal fluctuations, since it is introduced through the framework of turbulent eddy-viscosity models, it is a scalar characterising turbulence and indeed independent of the coordinate system. Durbin (1991) observed that the wall-blocking effect can be modelled through a simplified elliptic pressure-strain model.

$$f - L^2\nabla^2 f = f_h \tag{2.77}$$

where f_h is the solution in the homogeneous case far from the walls. The elliptic relaxation equation (Equation (2.77)) is used in the v^2 transport equation to sensitize for wall-blocking effects. The turbulent eddy-viscosity can now be modified to obtain the correct behaviour in the near-wall regions as,

$$\nu_t = C_\mu v^2 \mathcal{T}, \quad \text{with } C_\mu \sim 0.2 \tag{2.78}$$

Unfortunately, the model suffers from numerical stiffness due to the wall boundary conditions for f. Since its introduction, vast amounts of developments and modifications have been made to the $v^2 - f$ model in an attempt to improve its stability. The most recent attempt to improve the model is the BL-v^2/k model by Billard et al. (2012).

Developments of the BL-v^2/k model

1. Following the work of Laurence et al. (2005) to improve the robustness of the $v^2 - f$ model, Billard et al. (2012) replace the additional scalar transport term by v^2/k. This allows the boundary condition for the elliptic relaxation equation to be set to 0 at the wall, thus alleviating the problems coming from the wall boundary conditions for f.

2. An elliptic relaxation equation (Equation (2.88)) akin to the Elliptic Blending Reynolds Stress Model (EBRSM) of Manceau et al. (2002) is used to provide a blending function, α. α is 0 at the wall and goes to 1 far from the walls. This allows for a more *code-friendly* formulation of the model as the terms can be regrouped using the blending function.

3. Similar to Durbin (1991), the length and time scales are appropriately modified so that in the near wall region they are limited to the Kolmogorov scales. Furthermore, the length and time scales are of the form $\sqrt{L^2 + \eta^2}$ (Equation (2.89)) for better transition between the Integral and Kolmogorov scales. The introduction of such a time scale in the dissipation rate equation obviates the singularity at the wall and aids in improving the numerical stability of the model.

4. Several improvements are focused on the reformulation of the dissipation term in the kinetic energy equation. The dissipation term is decomposed as in Jakirlic et al. (2002), aiming at separating the homogeneous and inhomogeneous contributions to the dissipation rate and a transport equation is solved for ε_h.

$$\varepsilon = \varepsilon_h + E + \frac{\nu}{2}\frac{\partial^2 k}{\partial x_j \partial x_j} \tag{2.79}$$

The term E, (Equation (2.84)), first proposed by Jones et al. (1972) and used in the dissipation rate equation, is an inhomogeneous low-Reynolds number correction used to account for the increased production of dissipation in the buffer layer providing improvements in the near-wall predictions. Through a change of variables, Billard et al. (2012) introduced this formulation implicitly in the kinetic energy equation thus avoiding numerical stability issues. Additionally, the viscous diffusion terms are halved in all the transport equations to have proper near-wall balances of the source terms, due to the decomposition Equation (2.79).

5. Billard et al. (2012), by studying a channel flow, found it necessary to reduce the coefficient, C_{ε_2}, in the defect layer in order to maintain the balance $\mathcal{D}_k^T = \varepsilon$. This balance comes from the fact that at the centre of the channel the velocity gradient decreases (hence $\mathcal{P}$) and turbulence is maintained due to the turbulent transport terms. Following the work of Parneix et al. (1996), the C_{ε_2} coefficient is written as in Equation (2.85).

Finally, the model is written as below.

$$v_t = C_\mu \varphi k \min\left(T, T_{\text{lim}}\right) \tag{2.80}$$

$$\frac{\partial k}{\partial t} + U_j \frac{\partial k}{\partial x_j} = \mathcal{P} + \frac{\partial}{\partial x_j}\left[\left(\frac{v}{2} + \frac{v_t}{\sigma_k}\right)\frac{\partial k}{\partial x_j}\right] - \varepsilon_h - E \tag{2.81}$$

$$\frac{\partial \varepsilon_h}{\partial t} + U_j \frac{\partial \varepsilon_h}{\partial x_j} = \frac{C_{\varepsilon_1}\mathcal{P} - C^*_{\varepsilon_2}\varepsilon_h}{T} + \frac{\partial}{\partial x_j}\left[\left(\frac{v}{2} + \frac{v_t}{\sigma_{\varepsilon_h}}\right)\frac{\partial \varepsilon_h}{\partial x_j}\right] \tag{2.82}$$

$$\frac{\partial \varphi}{\partial t} + U_j \frac{\partial \varphi}{\partial x_j} = -\frac{\varphi}{k}\mathcal{P} + \frac{\partial}{\partial x_j}\left[\left(\frac{\nu}{2} + \frac{\nu_t}{\sigma_\varphi}\right)\frac{\partial \varphi}{\partial x_j}\right] + \frac{2}{k}\frac{\nu_t}{\sigma_k}\frac{\partial \varphi}{\partial x_j}\frac{\partial k}{\partial x_j} + f \tag{2.83}$$

$$E = C_{\varepsilon_3}(1-\alpha)^3 \times \frac{k}{\varepsilon_h} 2\nu\nu_t \left(\frac{\partial^2 U_i}{\partial x_k x_j}\right)\left(\frac{\partial^2 U_i}{\partial x_k x_j}\right) \tag{2.84}$$

$$C^*_{\varepsilon_2} = C_{\varepsilon_2} + \alpha^3 \left(C_{\varepsilon_4} - C_{\varepsilon_2}\right) \tanh\left(\left|\frac{1}{\varepsilon_h}\frac{\partial}{\partial x_j}\left(\frac{\nu_t}{\sigma_k}\frac{\partial k}{\partial x_j}\right)\right|^{3/2}\right) \tag{2.85}$$

$$f = \left(1-\alpha^3\right) f_w + \alpha^3 f_h \tag{2.86}$$

$$f_w = -\frac{\varepsilon_h}{2}\frac{\varphi}{k} \quad \text{and} \quad f_h = -\frac{1}{T}\left(C_1 - 1 + C_2\frac{\mathcal{P}}{\varepsilon_h}\right)\left(\varphi - \frac{2}{3}\right) \tag{2.87}$$

$$\alpha - L^2\nabla^2\alpha = 1 \tag{2.88}$$

$$L = \sqrt{C_L^2\left(\frac{k^3}{\varepsilon_h^2} + C_\eta^2\frac{\nu^{3/2}}{\varepsilon_h^{1/2}}\right)}; \quad T = \sqrt{\frac{k^2}{\varepsilon_h^2} + C_T^2\frac{\nu}{\varepsilon_h}}; \quad T_{lim} = \frac{0.6}{\sqrt{6}C_\mu\varphi\sqrt{S_{ij}S_{ij}}} \tag{2.89}$$

C_μ	C_T	C_L	C_η	C_1	C_2	C_{ε_1}	C_{ε_2}	C_{ε_3}	C_{ε_4}	σ_k	σ_ε	σ_φ
0.09	4.0	0.164	75	1.7	0.9	1.44	1.83	2.3	0.4	1.0	1.5	1.0

$k-\omega$ based models

As discussed before, in order to close the system of equations for RANS, ν_t needs to be specified with a velocity scale and a length scale. Unlike the velocity scale which can be obtained directly from the kinetic energy as $k^{1/2}$, the length scale needs another turbulence characterising quantity such as ε in the $k-\varepsilon$ model. Numerous options have been explored by researchers for this second quantity. Another popular choice is the *dissipation rate per unit kinetic energy*, ω, first introduced by A. N. Kolmogorov (1942) conceptually. The $k-\omega$ model has seen many developments over time with the model proposed by Wilcox (1988)

being the most widely studied. Here the dissipation term in the kinetic energy equation is replaced by $\varepsilon = C_\mu k\omega$ and the transport equation for ω is derived in a phenomenological manner as seen for ε (Equation (2.76)).

$$\nu_t = \underbrace{k^{1/2}}_{\substack{\text{velocity}\\ \text{scale}}} \quad \underbrace{k^{1/2}/\omega}_{\substack{\text{length}\\ \text{scale}}} = k/\omega, \tag{2.90}$$

$$\frac{\partial k}{\partial t} + U_j \frac{\partial k}{\partial x_j} = \underbrace{2\nu_t S_{ij} S_{ij}}_{\mathcal{P}_k} + \frac{\partial}{\partial x_j}\left[\left(\nu + \frac{\nu_t}{\sigma_k}\right)\frac{\partial k}{\partial x_j}\right] - C_\mu k\omega \tag{2.91}$$

$$\frac{\partial \omega}{\partial t} + U_j \frac{\partial \omega}{\partial x_j} = \gamma \frac{\omega}{k}\mathcal{P}_k + \frac{\partial}{\partial x_j}\left[\left(\nu + \frac{\nu_t}{\sigma_\omega}\right)\frac{\partial \omega}{\partial x_j}\right] - \beta\omega^2 \tag{2.92}$$

$$\gamma = \frac{\beta}{C_\mu} - \frac{\sigma_\omega \kappa^2}{\sqrt{C_\mu}} \tag{2.93}$$

C_μ	κ	β	σ_k	σ_ω
0.09	0.41	0.075	2.0	2.0

Thanks to the use of ω to close the system, the model is integrable down to the wall with the proper boundary conditions for ω and also improves predictions in free shear flows, adverse pressure gradient boundary layers, and strongly separated flows (Wilcox, 2006). However, it was found that the use of $k-\omega$ model in the free-stream was too sensitive to the inlet boundary conditions imposed on ω.

As a remedy to this problem Menter (1994) proposed the $k-\omega$ SST model, which effectively combines the $k-\varepsilon$ and $k-\omega$ models through the use of a blending function, F_1. The blending function is designed in such a way as for the model to be in $k-\varepsilon$ mode far from the walls and in $k-\omega$ mode in the near-wall regions, thus combining the advantages of both the models. To achieve this, Menter (1994) derived the transport equation for the specific dissipation rate through a change of variable, $\varepsilon = C_\mu k\omega$, in the transport equations for the $k-\varepsilon$ model (Equations (2.75) and (2.76)). This procedure produces an additional cross-diffusion term,

$C\mathcal{D}$, as compared to the original $k-\omega$ model (Equation (2.92)).

$$\frac{\partial \omega}{\partial t} + U_j \frac{\partial \omega}{\partial x_j} = \underbrace{\gamma_\omega \frac{\omega}{k} \mathcal{P}_k}_{\mathcal{P}_\omega} + \frac{\partial}{\partial x_j}\left[\left(\nu + \frac{\nu_t}{\sigma_\omega}\right)\frac{\partial \omega}{\partial x_j}\right] - \beta_\omega \omega^2 + \underbrace{2(1-F_1)\frac{\nu_t}{\sigma_\omega}\frac{1}{k}\frac{\partial \omega}{\partial x_j}\frac{\partial k}{\partial x_j}}_{C\mathcal{D}} \tag{2.94}$$

The constants in the $k-\omega$ SST model are consequently varied to match the active model with the use of the blending function, such that

$$\phi = F_1 \phi_1 + (1 - F_1)\phi_2 \tag{2.95}$$

$$F_1 = \begin{cases} 1, & k-\omega \text{ mode: near-wall} \\ 0, & k-\varepsilon \text{ mode: far-wall} \end{cases} \tag{2.96}$$

Further improvements to the model were carried out in the work of Menter (1994).

- The production to dissipation ratio in adverse pressure gradient flows is large. With the use of the Boussinesq relationship, this leads to an overprediction of the Reynolds stresses in boundary layers. Noting that two-equation models fail in this aspect since they do not account for the transport of turbulent shear stress, $\overline{uv}$, Menter (1994) proposed a modification to the eddy-viscosity formulation. Upon review of previous works, Bradshaw's assumption for computing the Reynolds stresses is opted for, wherein the shear stress is proportional to the turbulent kinetic energy $\overline{uv} = a_1 k$, with a_1 a constant. The eddy-viscosity under this assumption is rewritten as follows,

$$\nu_t = \frac{a_1 k}{\max(a_1 \omega; \mathcal{S} F_2)} = \begin{cases} k/\omega \text{ when } \mathcal{S} < \omega \text{ or } F_2 = 0 \\ k/\mathcal{S} F_2 \end{cases} \tag{2.97}$$

  The second blending function is 1 for boundary layer flows and 0 for free-shear flows.

As noted by the author, this change in the formulation of the turbulent eddy-viscosity consequently means that the production term in the specific dissipation rate equation is rewritten in terms of ν_t instead of the factor ω/k.

- In Menter et al. (2003a), a production limiter is introduced in order to limit the overestimation of the production term in the turbulent kinetic energy equation in stagnation regions. The limit placed ensures that the production does not exceed 10 times the dissipation term.

$$\mathcal{P}_k = min\left(\nu_t \mathcal{S}^2, 10 C_\mu k\omega\right) \tag{2.98}$$

The full $k-\omega$ SST model is written as follows,

$$\nu_t = \frac{a_1 k}{\max\left(a_1\omega; SF_2\right)} \tag{2.99}$$

$$\frac{\partial k}{\partial t} + U_j\frac{\partial k}{\partial x_j} = \mathcal{P}_k + \frac{\partial}{\partial x_j}\left[\left(\nu + \frac{\nu_t}{\sigma_k}\right)\frac{\partial k}{\partial x_j}\right] - C_\mu k\omega \tag{2.100}$$

$$\frac{\partial \omega}{\partial t} + U_j\frac{\partial \omega}{\partial x_j} = \frac{\gamma_\omega}{\nu_t}\mathcal{P}_k + \frac{\partial}{\partial x_j}\left[\left(\nu + \frac{\nu_t}{\sigma_\omega}\right)\frac{\partial \omega}{\partial x_j}\right] - \beta_\omega\omega^2 + 2(1-F_1)\frac{\nu_t}{\sigma_{\omega 2}}\frac{1}{k}\frac{\partial \omega}{\partial x_j}\frac{\partial k}{\partial x_j} \tag{2.101}$$

$$\gamma_1 = \frac{\beta_{\omega_1}}{C_\mu} - \frac{\sigma_{\omega_1}\kappa^2}{\sqrt{C_\mu}} \quad ; \quad \gamma_2 = \frac{\beta_{\omega_2}}{C_\mu} - \frac{\sigma_{\omega_2}\kappa^2}{\sqrt{C_\mu}} \tag{2.102}$$

$$F_1 = \tanh\left[arg_1^4\right]; \quad \arg_1 = \min\left[\max\left[\frac{k^{1/2}}{C_\mu\omega d_w}; \frac{500\nu}{\omega d_w^2}\right]; \frac{4\rho k}{\sigma_{\omega 2} CD_{k\omega} d_w^2}\right] \tag{2.103}$$

$$F_2 = \tanh\left[\arg_2^2\right]; \quad \arg_2 = \max\left[\frac{2k^{1/2}}{C_\mu\omega d_w}; \frac{500v}{\omega d_w^2}\right] \tag{2.104}$$

$$CD_{k\omega} = \max\left[2\rho\frac{1}{\sigma_{\omega 2}}\frac{\partial k}{\partial x_j}\frac{\partial \omega}{\partial x_j}; 10^{-20}\right] \tag{2.105}$$

C_μ	κ	a_1	σ_k	$\sigma_{\omega 1}$	$\sigma_{\omega 2}$	$\beta_{\omega 1}$	$\beta_{\omega 2}$
0.09	0.41	0.31	1.0/0.85	2.0	1.0/0.856	0.075	0.0828

2.7. Hybrid RANS/LES models

2.7.1. Motivations for Hybrid RANS/LES methods

Hybrid RANS/LES approaches aim to form a middle ground between the limit of RANS on the lower end of cost/physics resolution to LES on the higher end. For various practical engineering reasons the motivations for the exploration of such methods are inspired by the field of applied aerodynamics. Industrial practice to solve flows around complex geometries is to employ Unsteady RANS (URANS) strategies. Solving flows which are inherently unsteady, say due to the presence of unsteady boundary conditions or periodic motions, using RANS with a time-stepping algorithm allows to capture the unsteadiness of the mean motions. Numerous studies have shown URANS predictions to be reasonably accurate when there exist sufficient scale separation between the unsteady mean motions and the turbulence scales that are modelled (see Sagaut et al. (2006) for discussions and examples). On the other hand, LES solutions provide appreciably more information that helps engineers in the design process. However, the grid resolution required to resolve the boundary layers is just as appreciably high in comparison to URANS. Furthermore, it is not always necessary to have highly resolved information in all regions of the flow and the use of LES cannot be justified as RANS simulations would perform sufficiently. Although computational power available for simulations has increased significantly over time, it remains impractical to perform LES simulations for complex geometries.

In view of the advantages and disadvantages of both RANS and LES methods, hybrid models are an attempt at combining as best as possible the advantages of both approaches

while diminishing the disadvantages. For example, solving the near-wall regions with RANS allows to evade too fine grids needed by LES in these regions. At the same time, switching to LES far from the walls would allow for the extraction of highly resolved information without the need for refined grids. A successful blend of these models is therefore highly beneficial for industrial applications.

One point of contention between the RANS and LES models is that they fundamentally deal with very different length and time scales. The scales describing the turbulent viscosity for RANS are derived primarily through the mean quantities computed at runtime. The various constants appearing in the equations characterising turbulence are carefully calibrated in order to have fairly accurate predictions in a variety of cases. LES simulations on the other hand resolve a large range of scales up to the limit defined by the filter width with the unresolved scales generally requiring simple models. This is a hurdle that needs to be passed when considering hybridisation of RANS and LES.

2.7.2. Types of Hybrid models

The approach to blending RANS and LES models within a simulation can be broadly classified into 2 categories (Sagaut et al., 2006), namely, *Zonal* and *Global* Hybrid RANS/LES methods.

Zonal methods

The principle of this approach is to divide the fluid domain into pre-defined zones of interest within which either a purely RANS or purely LES model is used. The interface between the RANS and LES zones is therefore discontinuous. The challenge in using zonal methods is the correct definition of boundary conditions at these interfaces. Since the scales resolved in RANS/URANS are extremely different as compared to LES, the missing spectral information needs to be provided in a RANS $\rightarrow$ LES interface; while the turbulent viscosity needs to be reconstructed in a LES $\rightarrow$ RANS interface.

For a RANS → LES interface, the solution of the RANS calculation is insufficient to estimate the resolved quantities to be inputted to the LES zone. Various *enrichment* techniques have been developed to tackle this issue (see Sagaut et al., 2006) but it remains an open question still, as the techniques are dependent on the test cases studied and lack generality. On the contrary, at a LES → RANS interface the high frequencies corresponding to the turbulent fluctuations are generally removed through the use of averaging operators and depending on the location of the RANS region (either downstream or upstream), additional source terms are introduced to aid in the computation of the turbulent viscosity.

One of the major drawbacks of this method is that it is *a priori* not always clear or possible to define the zones of RANS or LES in an effective manner, especially when considering industrial test cases. In contrast, presuming the interfaces are well defined, it is to be noted that the explicit separation of RANS and LES zones has the advantage that any suitable model of RANS/LES can be used at the designated zones without having to contend with the difference in the forms of the RANS/LES equations.

Global methods

The principle of *global* or *non-zonal* approaches is to use a single set of equations that blend the RANS and LES models in a continuous fashion. Unlike the *zonal methods*, *global approaches* switch from RANS to LES and vice-versa by comparing the turbulence scales from the RANS solution with the filter-width chosen for LES. Generally, RANS models are used close to the wall boundaries and LES away from the walls. The modelled (unresolved) scales need to be reduced away from the walls to allow for the fluctuations to grow such that the LES model will be able to provide unsteady information accurately. The functions defined to control this switch essentially work by modifying the eddy-viscosity of the RANS model thereby reducing the modelled energy. As such, there exists a certain level of empiricism when implementing the switch from a statistically averaged model to a scale resolving model.

A point of contention with global methods is that of the overlap area between RANS and LES modes where the continuous switch happens. This region gives rise to the so-called *'grey area'* problem where the model is neither in RANS mode or LES mode explicitly. Several solutions have been envisaged by researchers to evade this issue, such as, the use of shielding functions (Spalart et al., 2006) to control the rate and region of transition or the use of forcing (Piomelli et al., 2003) to develop resolved scales rapidly, etc...

Paving way to a more rigorous description and reduced empiricism, it has been shown that global methods can be interpreted as a filtering approach with a varying cut-off filter width (Manceau, 2018; Schiestel et al., 2005). On the other hand, Sagaut et al. (2006) interpret global methods as multiresolution methods, where resolved fluctuations are created or destroyed based on the levels of eddy-viscosity in LES and RANS regions respectively. Through this point of view, levels of eddy-viscosity are said to be modified due to the switch in the filtering operations observed in RANS and LES modes, called as an *effective filter*. With the above perspectives in mind, a set of prerequisites need to be considered for the development of a *global hybrid RANS/LES model*.

- *Consistency of the filtering operation*: The effective filter acting on the flow field should conform to the following:

  1. In the limit where the cut-off wavenumber/frequency of the effective filter tends to 0, i.e. $\kappa_c \to 0$ or $\omega_c \to 0$, such that none of the turbulence scales are resolved — the model should revert to a RANS closure where the flow field is equivalent to a statistically averaged field. The implication clearly being that in this limit all the turbulence scales are modelled.

$$U = \overline{u^*} = \lim_{\kappa_c | \omega_c \to 0} \widetilde{u^*}$$

  2. In the limit where the cut-off wavenumber/frequency of the effective filter is greater than the smallest resolved scales (highest wavenumber/frequency) i.e.,

$\kappa_c \to \infty$ or $\omega_c \to \infty$, the turbulent eddy-viscosity must be reduced by the model such that the resolved spectra tending toward to that of a DNS/LES shall be recovered. The implication clearly being that in this limit all the turbulence scales up to the cut-off are resolved as accurately as possible.

$$u^* = \lim_{\kappa_c | \omega_c \to \infty} \widetilde{u^*}$$

These properties are not valid in all cases and certain hypotheses, such as homogeneity and statistical stationarity, are called upon when justifying their use in the models.

- *Form similarity (Homomorphism) of the averaged and filtered equations*: Using a consistent filtering operator, as described previously, is only a first step whereby the filtered quantities can be justifiably represented in both the RANS and LES limits. Owing to the use of a single set of equations for both the RANS and LES modes, another important condition the transport equations themselves have to meet is that of *form similarity* — the terms of the transport equations in both RANS and LES modes should correspond to one another.

  This is readily seen for the continuity (Equation (2.27) and Equation (2.55)) and momentum equations (Equation (2.28) and Equation (2.56)). The sub-filter stresses for the LES equations are retrieved by invoking the *averaging invariance* property demonstrated by Germano (1992).

  – **Averaging Invariance of turbulence equations**

    Defining a general set of central moments such that,

$$\tau_{ij} = \tau(u_i^*, u_j^*) = \left\langle u_i^* u_j^* \right\rangle - \left\langle u_i^* \right\rangle \left\langle u_j^* \right\rangle \tag{2.106}$$

$$\tau_{ijk} = \tau(u_i^*, u_j^*, u_k^*) = \left\langle u_i^* u_j^* u_k^* \right\rangle - \left\langle u_i^* \right\rangle \left\langle u_j^* \right\rangle \left\langle u_k^* \right\rangle - \left\langle u_i^* \right\rangle \tau(u_j^*, u_k^*) - \left\langle u_j^* \right\rangle \tau(u_k^*, u_i^*) - \left\langle u_k^* \right\rangle \tau(u_i^*, u_j^*) \tag{2.107}$$

where $\langle \cdot \rangle$, is a generic filter which is (i) linear and constant-preserving, (ii) commutes with space and time derivatives, and (iii) consistent (see above). The transport equation for the sub-filter stress can be written as follows,

$$\frac{\partial \tau_{ij}^{\text{sfs}}}{\partial t} + \widetilde{U}_k \frac{\partial \tau_{ij}^{\text{sfs}}}{\partial x_k} = -\tau_{ik}^{\text{sfs}} \frac{\partial \tilde{U}_j}{\partial x_k} - \tau_{jk}^{\text{sfs}} \frac{\partial \widetilde{U}_i}{\partial x_k} - \frac{\partial \tau \left(u_i^*, u_j^*, u_k^* \right)}{\partial x_k} + \nu \frac{\partial^2 \tau_{ij}^{\text{sfs}}}{\partial x_k \partial x_k} - \frac{1}{\rho} \tau \left(u_i^*, \frac{\partial p^*}{\partial x_j} \right) - \frac{1}{\rho} \tau \left(u_j^*, \frac{\partial p^*}{\partial x_i} \right) - 2\nu\tau \left(\frac{\partial u_i^*}{\partial x_k}, \frac{\partial u_j^*}{\partial x_k} \right). \tag{2.108}$$

It can be seen that this equation (Equation (2.108)) and the Reynolds stress equation (Equation (2.59)) are formally similar.

2.7.3. Hybrid RANS/LES models with spatial filtering

Detached Eddy Simulation (DES)

First derived by (Spalart et al., 1997), the *detached eddy simulation* method was motivated by the need for capturing the physics regarding the flow structures around geometries of interest in aeronautics (external flows) such as detached aerofoils, nacelles, landing gears, and vortex generators. Such geometries are of low aspect ratios generating eddies of a similar scale which are separated from the boundary layer and thus do not require an extremely fine grid to obtain resolved structures. The authors classify turbulent structures as **attached**, eddies within a boundary layer, and **detached**, those outside of the boundary layer. RANS models calibrated for *thin shear flows* tend to misrepresent the physics in regions of massive separation far from the boundary layer and URANS solutions are limited to the accuracy of the model itself even with sufficient grid refinement. To satisfy the

need for resolving 3D turbulent eddies, the idea of DES is to use a RANS model for the attached eddies, while resolving the scales using LES for the detached eddies within a single formulation of equations, with the switch between the two being continuous (non-zonal).

The original formulation is made using the *one-equation Spalart-Allmaras (S-A) model* (Spalart et al., 1992), where the transport equation for turbulent viscosity is solved to determine the turbulent scales. (Travin et al., 2000) generalised the formulation such that a DES model can be formulated from any RANS model by modifying the length scale appropriately. Further works led to the *two-equation* forms using $k-\omega$ SST model as the base RANS model owing to its strength in predicting flow separation (Strelets, 2001; Travin et al., 2002).

The mechanism for the switch from RANS to LES is controlled by a hybridisation function, F_{DES}, which involves a comparison between the *length scale* obtained from the scale determining RANS equations and the grid spacing. The general idea of obtaining a DES model from a RANS model involves replacing the RANS length scale l_{RANS} by the new DES length scale l_{DES}. In the case of two-equation models this is achieved by introducing the hybridisation function in the dissipation term of the kinetic energy transport equation leading to a modification of the amount of modelled energy and thereby modifying the turbulent viscosity, ν_{sfs}.

$$\varepsilon_{DES} = F_{DES}\varepsilon_{sfs} = F_{DES}C_{\mu}k\omega, \text{ where, } F_{DES} = \max\left[1, \frac{k^{3/2}/\varepsilon_{sfs}}{C_{DES}\Delta}\right] \tag{2.109}$$

$$\frac{\partial k}{\partial t} + U_j\frac{\partial k}{\partial x_j} = 2\nu_{sfs}S_{ij}S_{ij} + \frac{\partial}{\partial x_j}\left[\left(\nu + \frac{\nu_{sfs}}{\sigma_k}\right)\frac{\partial k}{\partial x_j}\right] - \underbrace{F_{DES}C_{\mu}k\omega}_{\varepsilon_{DES}} \tag{2.110}$$

Given a mesh, the DES model switches from RANS to LES and vice-versa depending on the grid refinement. A coarse grid would drive the model towards a fully RANS mode since $k^{3/2}/\varepsilon_{sfs} \leq C_{DES}\Delta$ and thus $\varepsilon_{DES} = \varepsilon_{sfs}$. With a refined grid where Δ is sufficiently fine to resolve the turbulent scales, the model would switch to LES ($F_{DES} > 1$ thus increasing

dissipation) leading to resolved structures as a consequence of the diminished turbulent viscosity [$\nu_{sfs} \approx k_{sfs}/\omega_{sfs} = C_\mu k_{sfs}^2/\varepsilon_{sfs}$]. In LES mode, the resolved energy increases, however, since the modelled energy is killed by an increase in dissipation, ε_{DES}, due to an increase in F_{DES}, the total energy is conserved.

The coefficient C_{DES} is calibrated in decaying homogeneous isotropic turbulence in purely LES mode in order to find the optimum value. The procedure, as noted by the authors (Travin et al., 2002), depends on various factors such as the RANS closure model used and the differencing scheme employed due to the variations in numerical dissipation of the schemes. In addition, Friess et al. (2015) derived an *equivalent-DES* based on the $k-\varepsilon$ model and showed that C_{DES} is also a function of the grid size and as such needs to be computed as a function of the *effective filter*. Δ is the grid spacing defined as $\Delta = \max[\Delta_x, \Delta_y, \Delta_z]$. This form was chosen over others such as $\Delta = (\Delta_x \Delta_y \Delta_z)^{1/3}$ so that the model would not go to LES mode in the areas of thin boundary layers.

The DES method is one of the older methods of hybrid simulations to have been developed and thus has seen various improvements over the years. Of note, researchers have identified and formulated solutions to tackle the problems arising due to the mesh and also improve the treatment of the boundary layer.

- Delayed DES (DDES) method: Spalart et al. (2006) noted that when the grid is *ambiguous*, that is when a grid is refined (but not enough for performing a good LES) the model switches to LES too close to the solid boundary leading to the phenomenon termed as *"grid induced separation (GIS)"*. In order to avoid this problem, the authors implemented a delay function for the LES mode to be activated, such a function is now come to be known as a *shielding function*. The shielding function enforces the RANS mode in attached boundary layers irrespective of the grid.

- Improved DDES (IDDES) method: Shur et al. (2008) proposed the model combining the capabilities of DDES and WMLES, i.e., it makes it possible to switch to LES in attached boundary layer at some distance from the wall. The authors introduced

improvements in the definitions of Δ and the shielding function to resolve the issues of *log-layer mismatch* while retaining the improvements provided by the DDES method.

Partially integrated Transport Model (PITM)

The PITM methodology, developed by Schiestel et al. (2005) and Chaouat et al. (cite: 2005), was proposed as a means of bridging the gap between RANS and LES formulations grounded on firm theoretical foundations. The core idea is to deduce a set of sub-grid scale equations whereby the amount of modelled and resolved energy can be regulated allowing for a switch between RANS and LES strategies. The seamless switching is achieved by dynamically modifying the co-efficient of the dissipation term in the transport equation for turbulent dissipation rate, ε_{sfs}.

The method allows for the derivation of a sub-grid scale model based on any RANS (statistical) model using partial spectral integration (Schiestel, 1987) on a turbulence spectrum split through filtering operations (see Figure 2.3).

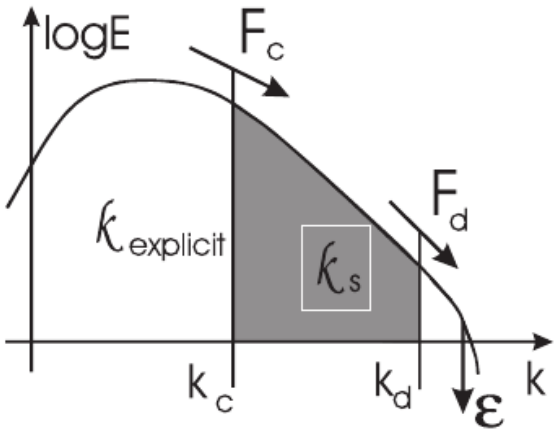

Figure 2.3.: Sketch of spectral portioning for filtered turbulence (from Schiestel et al. (2005))

The spectrum is divided as such:

- Resolved scales $[0, \kappa_c]$, where κ_c is the cut-off wavenumber of the filtering operation

- Modelled scales $[\kappa_c, \kappa_d]$, where κ_d is the wavenumber at which the spectrum is split
- Dissipative scales $[\kappa_d, \infty[$

The energy flux between the different ranges of scales is then:

- F_c : Energy transferred from the resolved to the modelled scales, representative of the modelled production, $\mathcal{P}_m$
- F_d : Energy transferred from the modelled scales to the dissipative scales equivalent to the rate of dissipation, ε, assuming equillibrium at small scales

The dissipative scales are defined such that the net energy contribution to the total energy from these scales is negligible. This necessitates that κ_d is sufficiently large to be outside of the inertial region of the spectrum, hence, $F_d = \varepsilon \approx \varepsilon_{sfs}$. In order to dynamically control κ_d, it is defined as follows,

$$\kappa_d = \kappa_c + \zeta \frac{\varepsilon_m}{k_m^{3/2}} \tag{2.111}$$

where ζ is sufficiently large to maintain a large separation between the resolved and dissipative scales. To note, the large separation in scales also entails that the dissipation of energy due to resolved scales is negligible ($\varepsilon_r = 0$).

Under the hypothesis of *homogeneous anisotropic turbulence*, the transport equation for the dissipation term is derived by partial integration of the transport equation for the energy spectrum:

$$\frac{\partial E}{\partial t} = -\Lambda_{ij} A_{ij} + \mathcal{T} - 2\nu\kappa^2 E \tag{2.112}$$

where Λ_{ij} is the mean velocity gradient, A_{ij} is the spherical mean of the spectral tensor of velocity correlations, $\mathcal{T}$ is the rate of energy transfer due to wave-number interactions, and the last term on the RHS being the viscous dissipation. Upon integrating the spectral energy transport equation over the wave-number ranges, the authors (Schiestel et al., 2005)

derived sub-grid model equations similar to that of $k-\varepsilon$ model. A more generalised sub-grid stress model presented in Chaouat et al. (2005) writes,

$$k_m t = \mathcal{P}_m - \varepsilon_m \tag{2.113}$$

$$\varepsilon_m t = C_{\varepsilon 1}\frac{\varepsilon_m}{k_m}\mathcal{P}_m - \underbrace{(C_{\varepsilon 1} + r(C_{\varepsilon 2} - C_{\varepsilon 1}))}_{C^*_{\varepsilon 2}}\frac{\varepsilon_m^2}{k_m} \tag{2.114}$$

The term C_2^* provides for the transposition of the turbulence model from RANS to LES. C_2^* is dependent on the energy ratio r ($= k_m/k$). To note the behaviour of the new coefficient in the different regimes:

- in RANS mode ($\kappa_c \to 0$) : $C^*_{\varepsilon 2} \to C_{\varepsilon 2}$ since $r = 1$ as $k_m = k$.
- in LES mode $r < 1$ and thus $C^*_{\varepsilon 2} < C_{\varepsilon 2}$, so the destruction term in the dissipation rate equation reduces thus increasing the dissipation rate and consequently killing the modelled energy and the turbulent viscosity thereby allowing for the resolved fluctuations to develop.

The energy ratio is estimated using the Kolmogorov hypothesis of the equilibrium Eulerian spectrum (A. Kolmogorov, 1941),

$$E(\kappa) = C_K \varepsilon^{2/3}\kappa^{-5/3}, \tag{2.115}$$

supposing that the cut-off wave-number is placed in the inertial zone of the spectrum, such that

$$r = \frac{k_m}{k} = \frac{1}{k}\int_{\kappa_c}^{\infty} E(\kappa)d\kappa = \frac{3}{2}C_K\left(\kappa_c\frac{k^{3/2}}{\varepsilon}\right)^{-2/3} \tag{2.116}$$

The subgrid scale turbulent viscosity is estimated using the Heisenberg hypothesis (Hinze

et al., 1975),

$$\nu_m = C_\kappa \int_{\kappa_c}^{\infty} \kappa^{-3/2} E(\kappa)^{1/2} d\kappa = \frac{3}{4} C_\kappa C_K^{1/2} \varepsilon^{1/3} \kappa_c^{-4/3} = C_\mu \frac{k_m^2}{\varepsilon}, \tag{2.117}$$

where $C_\mu = \frac{1}{3} C_\kappa C_K^{-3/2}$. Furthermore, Chaouat et al. (2009) demonstrate the limiting behaviour of the sub-grid viscosity under local equilibrium, $\mathcal{P}_m = \varepsilon_m = \varepsilon$, to be equivalent to the Smagorinsky model with a cut-off wave-number $\kappa_c = \pi/\Delta$,

$$\nu_m = \frac{1}{\pi^2} \left(\frac{3 C_K}{2} \right)^3 C_\mu^{3/2} \Delta^2 \left[2 \widetilde{\overline{S}_{ij}} \widetilde{\overline{S}_{ij}} \right]^{1/2} \tag{2.118}$$

2.7.4. Hybrid RANS/LES models with temporal filtering

Temporal filtering allows for a highly consistent definition between the whole spectrum of DNS, LES, and RANS formulations. As noted previously, certain hypothesis are called up on in order to satisfy the consistency constraint while designing a hybrid RANS/LES model. In this regard, temporal filtering approaches offer a consistent formalism while requiring less stringent hypotheses as shown by Fadai-Ghotbi et al. (2010b) and Manceau (2018).

For the filtering operation to be consistent with the RANS limit and satisfy the *Ergodicity hypothesis*,

- a spatial filter can be used strictly only for ***homogeneous flows***,
- a temporal filter can be used for ***statistically stationary inhomogeneous flows***.

As such the use of a temporal filtering approach allows for a wider range of flows to be considered which is valuable for industrial applications.

In contrast to the advantages of the use of temporal filters, considerations need to be made in regards to their invariance properties. One of the challenges encountered in the use of Eulerian time-domain filters is that of **Galilean invariance**. Speziale (1987) raised the issue that a temporal filter of the form $\mathcal{G}(x, x', t, t') = \mathcal{G}_{\Delta_T}(t, t')\, \delta(x, x')$, does not satisfy the Galilean invariance property. For spatial filtering, the transformations are Galilean

invariant (Speziale, 1987), i.e., $\widetilde{U}_i^{\bullet} = \widetilde{U}_i - v_i$, where $\widetilde{U}_i^{\bullet}$ is the frame of reference translated by v_i.

This is not the case for temporal filtering, i.e., $\widetilde{U}_i^{\bullet} \neq \widetilde{U}_i - v_i$. Fadai-Ghotbi et al. (2010b) introduced a generalised filter of the form,

$$\widetilde{u}^{*}(\mathbf{x}, t) = \iint \mathcal{G}\left(\mathbf{x}' - \xi\left(\mathbf{x}, t' - t\right), t' - t\right) \mathbf{u}^{*}\left(\mathbf{x}', t'\right) \mathrm{d}\mathbf{x}' \mathrm{d}t',$$

where the kernel is,

$$\mathcal{G}\left(\mathbf{x}' - \xi\left(\mathbf{x}, t' - t\right), t' - t\right) = \delta\left(\mathbf{x}' - \xi\left(\mathbf{x}, t' - t\right)\right) G_{\Delta_T}\left(t' - t\right).$$

By defining the parameter, ξ, as

$$\boldsymbol{\xi}(\mathbf{x}, t' - t) = \mathbf{x} + \mathbf{V}_{\mathrm{ref}}(t' - t),$$

with V_{ref} being the uniform motion of the application point of the filter, Fadai-Ghotbi et al. (2010b) demonstrated that Galilean invariance is preserved. Such a filter, called the *uniform temporal filter* (Manceau, 2018), ensures that the filtering operation is in accordance with the RANS limit as the filter width goes to infinity.

Temporal-PITM

As a further step, Fadai-Ghotbi et al. (2010b) used the *uniform temporal filter* to develop a hybrid RANS/LES model based on the PITM approach. Owing to its strong theoretical foundations based on spectral splitting, the PITM methodology presents as a solid basis up on which the *Temporal PITM (TPITM)* was developed. The TPITM model is derived in a manner similar to PITM, however, thanks to the use of the uniform temporal filter, the less stringent hypothesis of *inhomogenous statistically stationary turbulence* is employed leading to a much broader range of application.

The temporal Eulerian spectrum, E_T, is divided into 3 zones, namely,

- Resolved scales $[0, \omega c]$, where ωc is the cut-off frequency of the filtering operation
- Modelled scales $[\omega c, \omega d]$, where ωd is the frequency at which the spectrum is split
- Dissipative scales $[\omega d, \infty[$

Further integrating the transport equation for the spectrum, E_T, over the defined ranges of frequency, the system of equations for the sub-filter energy, k_{sfs}, and the dissipation, ε_{sfs}, are obtained. The hybridisation function, $C^*_{\varepsilon 2}$ obtained in this case is identical to that of the spatially filtered PITM. The sub-grid scale turbulent viscosity is estimated also using the Heisenberg hypothesis.

$$C^*_{\varepsilon 2} = C_{\varepsilon 1} + r(C_{\varepsilon 2} - C_{\varepsilon 1}) \tag{2.119}$$

The cut-off frequency, ω_c, is in the inertial range of the Kolmogorov spectrum. Since the Kolmogorov spectrum is defined for the spatial domain, in order to define the energy ratio, r, for TPITM the Kolmogorov spectrum has to be reformulated in the time domain. A relationship between the spatial and temporal Kolmogorov spectrum can be established based on the analysis of Tennekes (1975) who proposed a dispersion relation such that,

$$\omega = U_s \kappa, \text{ with, } U_s = U + \gamma\sqrt{k} \tag{2.120}$$

where U_s is the *sweeping velocity* representing the advection of the small eddies by the large eddies, U is the magnitude of the mean velocity which is characteristic to the large scale motions, and γ is a constant. The equilibrium Eulerian spectrum can now be defined in the time-domain as,

$$E(\omega) = C_K \varepsilon^{2/3} U_s^{2/3} \omega^{-5/3}, \tag{2.121}$$

Fadai-Ghotbi et al. (2010b) in considering the case where the mean velocity is 0, giving the dispersion relation, $\omega_c = \kappa_c\sqrt{k}$ with $U_s = \sqrt{k}$, found the energy ratio as,

$$r = \frac{k_m}{k} = \frac{3}{2} C_K \left(\kappa_c \frac{k^{3/2}}{\varepsilon}\right)^{-2/3} = \frac{3}{2} C_K \left(\omega_c \frac{k}{\varepsilon}\right)^{-2/3} \tag{2.122}$$

Finally, similar to the PITM model, the sub-filter scale turbulent viscosity is estimated using the Heisenberg hypothesis (Hinze et al., 1975) as,

$$\nu_m = C_\mu \frac{k_m^2}{\varepsilon}. \tag{2.123}$$

2.8. Summary of the chapter

The chapter provided an overview of the physics and modelling of turbulent flows. The concepts relating to the energy spectrum and the scales presented in fluid turbulence are detailed. Following this the turbulence models relevant/applied to the thesis are described in detail including the description of the transport equations used to model the turbulent scales. A general description of Hybrid RANS/LES methods is provided ending with notes on the development of the Temporal-PITM model, which paves way to the development of the Hybrid temporal LES (HTLES) model as will be detailed in Chapter 5.

Chapter 3.

Natural Convection flows

3.1. Introduction

Following the mathematical formulation for isothermal flows as described in the previous chapter, the present chapter focuses on the description of the governing equations, simulation strategies and closure models specifically for the case of turbulent flows with natural convection. The choice of separating the descriptions for isothermal and natural convection flows was made so as to highlight the influence of buoyancy on the various transport equations discussed in a clear and concise manner.

3.2. Governing equations

Natural convection flows are solely driven by density variations occurring in the fluid medium due to temperature gradients or varying species concentrations. In the presence of gravity such a buoyant force acting on the fluid writes,

$$\mathcal{F} = \rho g_i$$

where g_i is the gravity vector, leading to the additional term in the momentum equation,

$$\frac{\partial u_i^*}{\partial t} + u_j^* \frac{\partial u_i^*}{\partial x_j} = -\frac{1}{\rho}\frac{\partial p^*}{\partial x_i} + \nu \frac{\partial^2 u_i^*}{\partial x_j \partial x_j} + \underbrace{\rho g_i}_{\text{Buoyant force}} \tag{3.1}$$

Given *small temperature differences*, the variations in density are accounted for using the *Boussinesq approximation*. The Boussinesq approximation entails the following assumptions,

1. Except for the variation of density **in the buoyancy term of the momentum equation**, all other variations in the properties of the fluid due to temperature are neglected.

2. The variation in density, due to temperature differences, can be expanded in a Taylor series expansion around a reference temperature unique to the whole flow field, Θ_0. Given an instantaneous temperature field, θ^*, density as a function of θ^* can be written as,

$$\rho(\theta^*) = \rho_0 + \left.\frac{\partial \rho}{\partial \theta^*}\right|_{\Theta_0} (\theta^* - \Theta_0) + O(\theta^* - \Theta_0)^2 \tag{3.2}$$

   where the terms of O^2 and higher are truncated leaving us with a linear relationship between density and temperature. The coefficient of thermal expansion, β, is defined as,

$$\beta = -\frac{1}{\rho_0}\frac{\partial \rho}{\partial \theta^*} \tag{3.3}$$

   Combining Equation (3.3) with Equation (3.2) the linear relationship between the density and temperature can be written as,

$$\rho(\theta^*) = \rho_0 \left[1 - \beta(\theta^* - \Theta_0)\right] \tag{3.4}$$

In considering the Boussinesq approximation and the assumptions implied therein, the transport equations governing the incompressible fluid flow in natural convection systems are written as follows,

- Continuity equation

$$\frac{\partial u_i^*}{\partial x_i} = 0 \tag{3.5}$$

- Momentum equation

$$\frac{\partial u_i^*}{\partial t} + u_j^* \frac{\partial u_i^*}{\partial x_j} = -\frac{1}{\rho_0}\frac{\partial p^*}{\partial x_i} + \nu \frac{\partial^2 u_i^*}{\partial x_j \partial x_j} - \underbrace{\beta g_i (\theta^* - \Theta_0)}_{\text{Buoyant force}} \tag{3.6}$$

- Energy equation

$$\frac{\partial \theta^*}{\partial t} + u_j^* \frac{\partial \theta^*}{\partial x_j} = \alpha \frac{\partial^2 \theta^*}{\partial x_j \partial x_j} \tag{3.7}$$

  where α is the scalar diffusivity.

3.3. Characteristic scales and dimensionless numbers

Similar to the definition of the Reynolds number which is used to characterise turbulence in forced flows, characteristic scales can be chosen to normalise the $\mathcal{NS}$-equations so as to obtain non-dimensional numbers more focused towards describing natural convection flows.

The choice of the characteristic length scale, L, is straightforward as it is prescribed by the geometry itself. The temperature scale can be obtained just as easily from the imposed boundary conditions and is generally taken to be the difference between two boundaries, be it two walls or a wall and the ambient, such that $\Delta\Theta = \Theta_H - \Theta_C$. The velocity scale concerning natural convection flows, however, is another matter. For example, in forced flows the velocity is imposed as an inflow condition and can serve as the characteristic velocity scale. In natural convection flows, the velocity is a result of the buoyant driving force and hence needs to be chosen based on dimensional grounds such as ν/L or α/L. Based on these choices, dimensionless variables (ϕ) in relation to their dimensional counterparts

($\phi^\star$) are written as follows:

$$x_i = \frac{x_i^\star}{L} \quad ; \quad u_i = \frac{u_i^\star L}{\nu} \quad ; \quad t = \frac{t^\star \nu}{L^2} \quad ; \quad \theta = \frac{\theta^\star - \Theta_0}{\Delta\Theta} \quad ; \quad p = \frac{p^\star L^2}{\rho_0 \nu^2} \tag{3.8}$$

In considering these non-dimensional variables, the momentum and energy equations write:

$$\frac{\partial u_i}{\partial t} + u_j \frac{\partial u_i}{\partial x_j} = -\frac{\partial p}{\partial x_i} + \frac{\partial^2 u_i}{\partial x_j \partial x_j} - Gr\theta \frac{g_i}{g} \tag{3.9}$$

where $g_i/g = (-1, 0, 0)$, if x is the vertical direction, and

$$\frac{\partial \theta}{\partial t} + u_j \frac{\partial \theta}{\partial x_j} = \frac{1}{Pr} \frac{\partial^2 \theta}{\partial x_j \partial x_j}. \tag{3.10}$$

The above exercise leads to the appearance of two non-dimensional numbers namely: the Grashoff number (Gr) and the Prandtl number (Pr). Gr and Pr, assuming the Boussinesq approximation, fully characterise the behaviour of a buoyancy driven flow and are defined as follows:

$$Gr = \frac{\beta g \Delta\Theta L^3}{\nu^2} \quad ; \quad Pr = \frac{\nu}{\alpha} \tag{3.11}$$

The Grashoff number is the ratio of the buoyancy and viscous forces. It can be interpreted as a counterpart of the Reynolds number for natural convection flows as,

$$Gr = \frac{\beta g \Delta\Theta L^3}{\nu^2} = \beta g \Delta\Theta L \frac{L^2}{\nu^2} = u_{buo}^2 \frac{L^2}{\nu^2} = Re_{buo}^2 \tag{3.12}$$

where $u_{buo} = \sqrt{\beta g \Delta\Theta L}$ can be recognised as a characteristic buoyant velocity.

The product of Gr and Pr gives rise to the Rayleigh number, Ra, which is often used to describe buoyant flows. The Rayleigh number is interpreted as the ratio of the time scales of thermal transport due to diffusion and convection,

$$Ra = \frac{\text{time scale of diffusive transport}}{\text{time scale of convective transport}} = \frac{L^2/\alpha}{\nu/u_{buo}^2} \tag{3.13}$$

Ra thus describes the level of turbulence in natural convection flows with the flow being more turbulent with increasing Ra numbers.

3.4. DNS

Direct numerical simulations of natural convection flows are few and far between in comparison to their use in the study of forced isothermal flows. Of the natural convection configurations studied academically, *differentially heated vertical channel* and the *Rayleigh-Benard convection* cases are of the simplest form. These two cases differ in that the former has the gravity vector parallel to the walls while the latter has the gravity vector perpendicular to the walls. Therefore, they represent two extreme ends of the spectrum of natural convection flows. However, both the cases are homogeneous in two directions and the flow statistics only depend on the wall-normal direction which makes them a popular choice to study using DNS due to the reduced cost of computation. For more complex configurations and/or high Rayleigh number flows, DNS is even rarer and becoming accessible only recently due to the increased availability of computational power. In this thesis, DNS databases are used as a benchmarking tool to analyse the performance of the models developed. These test cases are discussed and illustrated at the end of this chapter.

3.5. Filtering approach - LES

Large eddy simulations remained one of the major simulation strategies used to understand natural convection flows at higher Ra until recently, especially for differentially heated cavity flows (Bosshard et al., 2013; Dehbi et al., 2014; Peng et al., 2000; Peng et al., 2001, 2002; Sergent et al., 2003; Sergent et al., 2013; Zhang et al., 2014). This section briefly describes the sub-filter scale modelling related to natural convection flows found in the literature. The filtered equations rewritten in regards to natural convection flows are as follows,

$$\frac{\partial \widetilde{U}_i}{\partial x_i} = 0 \tag{3.14}$$

$$\frac{\partial \widetilde{U}_i}{\partial t} + \widetilde{U}_j \frac{\partial \widetilde{U}_i}{\partial x_j} = -\frac{1}{\rho_0}\frac{\partial \widetilde{P}}{\partial x_i} + \nu \frac{\partial^2 \widetilde{U}_i}{\partial x_j \partial x_j} - \frac{\partial \tau_{ij}^{\text{sfs}}}{\partial x_j} - \beta g_i \left(\widetilde{\Theta} - \Theta_0\right) \tag{3.15}$$

$$\frac{\partial \widetilde{\Theta}}{\partial t} + \widetilde{U}_j \frac{\partial \widetilde{\Theta}}{\partial x_j} = \alpha \frac{\partial^2 \widetilde{\Theta}}{\partial x_j \partial x_j} - \frac{\partial \tau_{i\theta}^{\text{sfs}}}{\partial x_j} \tag{3.16}$$

The sub-filter heat flux appearing on the right-hand side of Equation (3.16), represents the effect of unresolved scales on the resolved scales akin to the sub-filter stress tensor. This term needs to be modelled and is defined analogous to the sub-filter stress employing Leonard's decomposition (triple decomposition),

$$\begin{aligned}
\widetilde{u_i^* \theta^*} &= \widetilde{\widetilde{U}_i \widetilde{\Theta}} + \underbrace{\widetilde{\widetilde{U}_i \theta'} + \widetilde{u_i' \widetilde{\Theta}}}_{C_{i\theta}} + \underbrace{\widetilde{u_i' \theta'}}_{R_\theta} \\
&= \widetilde{U}_i \widetilde{\Theta} + \underbrace{\widetilde{\widetilde{U}_i \widetilde{\Theta}} - \widetilde{U}_i \widetilde{\Theta}}_{L_{i\theta}} + C_{i\theta} + R_{i\theta} \\
&= \widetilde{U}_i \widetilde{\Theta} + L_{i\theta} + C_{i\theta} + R_{i\theta} \\
&= \widetilde{U}_i \widetilde{\Theta} + \tau_{i\theta}^{\text{sfs}}
\end{aligned} \tag{3.17}$$

$$\text{with } \tau_{i\theta}^{\text{sfs}} = \widetilde{u_i^* \theta^*} - \widetilde{U}_i \widetilde{\Theta} \tag{3.18}$$

3.5.1. Sub-filter scale modelling

Due to the complexities arising from the coupling of momentum and scalar transport in natural convection flows, modelling the sub-filter scales is difficult. The most common approach is to invoke the *Reynolds analogy*, relating the sub-filter diffusivity to the sub-filter viscosity through a sub-filter scale turbulent Prandtl number. Written for the Smagorinsky

model,

$$\alpha_{\text{sfs}} = \frac{\nu_{\text{sfs}}}{Pr_{\text{sfs}}} = \frac{C_s^2}{Pr_{\text{sfs}}}\widetilde{\Delta}^2\widetilde{\mathcal{S}}, \qquad \widetilde{\mathcal{S}} = \sqrt{2\widetilde{S}_{ij}\widetilde{S}_{ij}} \tag{3.19}$$

where Pr_{sfs} is the sub-filter scale Prandtl number. The sub-filter heat fluxes are then computed using the Simple gradient diffusion hypothesis,

$$\tau_{i\theta}^{\text{sfs}} = -\alpha_{\text{sfs}}\frac{\partial\widetilde{\Theta}}{\partial x_i} \tag{3.20}$$

Attempts have been made to improve the models with reasonable success. To note, the work of Eidson (1985), in Rayleigh-Bernard cases, to sensitize the time scale in $\nu_{\text{sfs}} \propto \Delta^2/T$ to include the effects of buoyancy production. Following which, Peng et al. (2002) further improved the model in addition to using the dynamic procedure of Germano et al. (1991). Sergent et al. (2003) developed a *local sub-grid diffusivity model* which does not rely on the Reynolds analogy and computed ν_{sfs} and α_{sfs} independently.

However, these models have not been implemented in codes aimed at the industry, which remain reliant on the Reynolds analogy. This entails the use of a constant value for the sub-filter scale turbulent Prandtl number = 0.4 as suggested by Eidson (1985). To note, the performance of various LES models in cubical cavities have been assessed in recent works of Kumar et al. (2016) and Clifford et al. (2020).

In the present thesis, LES simulations have been performed for the Square differentially heated cavity to compare with the results of both the RANS and Hybrid RANS/LES models developed.

3.6. Statistical approach - RANS

The aim of this section is to establish the theoretical foundations for the development of RANS models sensitised to buoyancy which will be discussed in the next chapter. The RANS equations governing the mean flow in natural convection systems write,

- Continuity equation

$$\frac{\partial U_i}{\partial x_i} = 0 \tag{3.21}$$

- Momentum equation

$$\frac{\partial U_i}{\partial t} + U_j \frac{\partial U_i}{\partial x_j} = -\frac{1}{\rho_0}\frac{\partial P}{\partial x_i} + \nu \frac{\partial^2 U_i}{\partial x_j \partial x_j} - \frac{\partial \overline{u_i u_j}}{\partial x_j} - \beta g_i \left(\Theta - \Theta_0\right) \tag{3.22}$$

- Energy equation

$$\frac{\partial \Theta}{\partial t} + U_j \frac{\partial \Theta}{\partial x_j} = \alpha \frac{\partial^2 \Theta}{\partial x_j \partial x_j} - \frac{\partial \overline{u_i \theta}}{\partial x_j} \tag{3.23}$$

In addition to solving for the Reynolds stress in order to close the system of equations, 3 more unknowns are introduced in the form of turbulent heat fluxes, $\overline{u_i\theta}$. As before, the transport equations for these two quantities need to be solved which increases the computational cost or they need to be modelled with an aim to reduce errors introduced therein.

3.6.1. Transport equations for Reynolds stresses

As in the case of isothermal flows presented in Chapter 2, the nature of these terms can be better understood by studying their transport equations. Modifying the Navier-Stokes operator to account for the source term, $\mathcal{N}(u^*)$ is rewritten as follows,

$$\mathcal{N}(u_i^*) = \frac{\partial u_i^*}{\partial t} + \frac{\partial u_k^* u_i^*}{\partial x_k} + \frac{1}{\rho_0}\frac{\partial p^*}{\partial x_i} - \nu \frac{\partial^2 u_i^*}{\partial x_k \partial x_k} - \beta g_i(\theta^* - \Theta_0), \tag{3.24}$$

$$\overline{u_i \mathcal{N}(u_j^*) + u_j \mathcal{N}(u_i^*)} = 0 \tag{3.25}$$

The transport equation for the Reynolds stress is now derived with the addition of the buoyancy term in the Navier-Stokes operator. Owing to the coupling between the momentum

and heat transfer in purely buoyancy driven flows, additional terms appear in the Reynolds stress equation.

$$\frac{\partial \overline{u_i u_j}}{\partial t} + U_k \frac{\partial \overline{u_i u_j}}{\partial x_k} = \mathcal{P}_{ij} + \mathcal{D}^{\nu}_{ij} - \mathcal{D}^{T}_{ij} - \mathcal{D}^{P}_{ij} - \varepsilon_{ij} + \Pi^{*}_{ij} \underbrace{- \beta \left(g_i \overline{u_j \theta} + g_j \overline{u_i \theta} \right)}_{\mathcal{G}_{ij}} \tag{3.26}$$

The last two terms,

- $\mathcal{G}_{ij}$: Buoyancy production term
- Π^{*}_{ij} : Pressure-Strain rate correlation/redistribution term

are added/modified due to the effects of buoyancy. The buoyancy production term depends on the solution of the transport equation or the model chosen for the prediction of turbulent heat fluxes.

Pressure-Strain rate correlation term, Π^{*}_{ij}

Without the effects of an additional force on the fluid such as the buoyancy force, the modelling of Π_{ij} was briefly noted in Chapter 2. In the case of natural convection flows, the Poisson equation for the pressure fluctuations writes,

$$\frac{1}{\rho_0} \frac{\partial^2 p}{\partial x_j \partial x_j} = \underbrace{- \frac{\partial^2}{\partial x_i \partial x_j} \left(u_i u_j - \overline{u_i u_j} \right)}_{\text{slow-term}} \quad \underbrace{-2 \frac{\partial U_i}{\partial x_j} \frac{\partial u_j}{\partial x_i}}_{\text{rapid-term}} \quad \underbrace{-\beta \frac{\partial \theta}{\partial x_i} g_i}_{\text{buoyant term}} \tag{3.27}$$

Using Green's theorem to integrate over the fluid domain to obtain the fluctuating pressure and multiplying with $\left(\partial u_i / \partial x_j + \partial u_j / \partial x_i \right)$, the Pressure-Strain correlation term can be written as,

$$\begin{aligned}\Pi^*_{ij} &= \Pi^s_{ij} + \Pi^r_{ij} + \Pi^\theta_{ij} \\ &= \Pi_{ij} + \Pi^\theta_{ij}\end{aligned} \tag{3.28}$$

The buoyant term, Π^θ_{ij}, in the pressure-strain rate correlation acts to reduce the anisotropy of production due to buoyancy in a similar manner to that of the rapid term, Π^r_{ij}, which reduces the anisotropy of stress production. This term is generally modelled using the isotropisation of production strategy of Gibson et al. (1976) and Naot (1970), which writes,

$$\Pi^\theta_{ij} = -C\left(\mathcal{G}_{ij} - \frac{1}{3}\mathcal{G}_{kk}\delta_{ij}\right) \tag{3.29}$$

The constant, C, is usually taken to be in the range of 0.5 and 0.6. Further elaborate models based on tensorial expansions exist, as for Π^r_{ij}, described in Hanjalic et al. (2011) for instance.

3.6.2. Transport equations for the turbulent kinetic energy

The transport equation for the turbulent kinetic energy involves an additional production term due to buoyancy which requires solving/modelling the turbulent heat flux terms.

$$\frac{\partial k}{\partial t} + U_j\frac{\partial k}{\partial x_j} = \mathcal{P} - \mathcal{D}^P - \mathcal{D}^T + \mathcal{D}^\nu - \varepsilon \underbrace{-\beta g_i \overline{u_i\theta}}_{\mathcal{G}} \tag{3.30}$$

The additional production term due to buoyancy, $\mathcal{G}$ is given by,

$$\mathcal{G} = \frac{1}{2}\mathcal{G}_{kk},$$

3.6.3. Transport equation for turbulent heat fluxes

The Reynolds averaging procedure produces three additional unknowns in the thermal transport equation, namely the turbulent heat fluxes. Defining an operator, $\mathcal{N}(\theta^*)$,

$$\mathcal{N}(\theta^*) = \frac{\partial \theta^*}{\partial t} + \frac{\partial u_k \theta^*}{\partial x_k} - \alpha \frac{\partial^2 \theta^*}{\partial x_k \partial x_k} \tag{3.31}$$

the transport equation is derived through the operation below,

$$\overline{u_i \mathcal{N}(\theta^*) + \theta \mathcal{N}(u_i^*)} = 0 \tag{3.32}$$

Following some algebraic manipulations the transport equation writes,

$$\begin{aligned}
\frac{\partial \overline{u_i\theta}}{\partial t} + U_k \frac{\partial \overline{u_i\theta}}{\partial x_k} = & - \left(\overline{u_i u_j} \frac{\partial \Theta}{\partial x_j} + \overline{u_j \theta} \frac{\partial U_i}{\partial x_j} \right) \quad \Big\} \mathcal{P}_{i\theta} = \mathcal{P}_{i\theta}^{\Theta} + \mathcal{P}_{i\theta}^{U} \\
& - \beta g_i \overline{\theta\theta} \quad \Big\} \mathcal{G}_{i\theta} \\
& + \left(\overline{\frac{p}{\rho_0} \frac{\partial \theta}{\partial x_i}} \right) \quad \Big\} \Pi_{i\theta} \\
& - (\alpha + \nu) \overline{\frac{\partial \theta}{\partial x_k} \frac{\partial u_i}{\partial x_k}} \quad \Big\} \varepsilon_{i\theta} \\
& + \frac{\partial}{\partial x_k} \left(\alpha u_i \overline{\frac{\partial \theta}{\partial x_k}} \right) + \frac{\partial}{\partial x_k} \left(\nu \theta \overline{\frac{\partial u_i}{\partial x_k}} \right) \quad \Big\} \mathcal{D}_{i\theta}^{\nu+\alpha} \\
& - \frac{1}{\rho_0} \left(\overline{\frac{\partial p \theta}{\partial x_i}} \right) \quad \Big\} \mathcal{D}_{i\theta}^{P} \\
& + \overline{\frac{\partial \theta u_i u_k}{\partial x_k}} \quad \Big\} \mathcal{D}_{i\theta}^{T}
\end{aligned} \tag{3.33}$$

- $\mathcal{P}_{i\theta}$: Production due to mean temperature and velocity gradients
- $\mathcal{G}_{i\theta}$: Production due to buoyancy
- $\Pi_{i\theta}$: Pressure redistribution term
- $\varepsilon_{i\theta}$: Dissipation term
- $\mathcal{D}_{i\theta}^{\nu+\alpha}$: Molecular diffusion

- $\mathcal{D}_{i\theta}^{P}$: Pressure diffusion
- $\mathcal{D}_{i\theta}^{T}$: Turbulent diffusion

The production terms can be computed exactly, given an additional transport term for the thermal variance is solved. The rest of the terms need to be modelled.

The pressure redistribution term can be separated using the Poisson equation for pressure. Multiplying Equation (3.27) by $\frac{\partial \theta}{\partial x_i}$ and integrating over the domain using Green's theorem, the redistribution term can be written as,

$$\Pi_{i\theta} = \Pi_{i\theta}^{s} + \Pi_{i\theta}^{r} + \Pi_{i\theta}^{\theta} \tag{3.34}$$

These terms can be modelled in a similar fashion to their Reynolds stress counterparts, either using linear or non-linear relations. The *basic model* of Hanjalic et al. (2011) is one such linear model where,

- The *slow-term* is formulated similar to the return-to-isotropy model of Rotta (1951)
- The *rapid-term* is formulated using the isotropisation of production strategy
- The *buoyant-term* is modelled analogous to rapid-term using the isotropisation of production model

The linear model writes,

$$\Pi_{i\theta} = -C_{\theta 1}\frac{1}{\tau}\overline{u_i\theta} + C_{\theta 2}\overline{u_j\theta}\frac{\partial U_i}{\partial x_j} + C_{\theta 3}\beta g_i\overline{\theta\theta} \tag{3.35}$$

Since the dissipation occurs at small scales where the hypothesis of isotropy holds, the dissipation term is rendered null.

$$\varepsilon_{i\theta} = 0 \tag{3.36}$$

The turbulent diffusion and pressure diffusion terms are modelled using the General gradient diffusion hypothesis (GGDH) of (Daly et al., 1970).

$$D_{i\theta}^{T} + D_{i\theta}^{P} = \frac{\partial}{\partial x_k}\left(C_\theta \frac{k}{\varepsilon}\overline{u_k u_l}\frac{\partial \overline{u_i\theta}}{\partial x_l}\right) \tag{3.37}$$

Dol et al. (1997) proposed the following model for the molecular diffusion term,

$$D_{i\theta}^{\nu+\alpha} = \frac{\partial}{\partial x_k}\left(\frac{\nu+\alpha}{2}\frac{\partial \overline{u_i\theta}}{\partial x_k}\right) - \frac{1}{2}(\alpha-\nu)\overline{\theta\frac{\partial^2 u_i}{\partial x_k^2}} + \frac{1}{2}(\alpha-\nu)\overline{u_i\frac{\partial^2\theta}{\partial x_k^2}} \tag{3.38}$$

where the last two terms are generally neglected giving,

$$D_{i\theta}^{\nu+\alpha} = \frac{\partial}{\partial x_k}\left(\frac{\nu+\alpha}{2}\frac{\partial \overline{u_i\theta}}{\partial x_k}\right) \tag{3.39}$$

These models in combination to solve for the transport equation of turbulent heat fluxes form the so called *Differential flux model (DFM)* . Use of more complex closures for the terms above generates a whole family of DFMs (see for instance, the works of Dehoux et al. (2017)).

3.6.4. Transport equation for the temperature variance

Applying the procedure as seen before for the transport equations of Reynolds stress and turbulent heat fluxes, the transport equation for temperature variance is obtained as shown below.

$$\mathcal{N}(\theta^*) = \frac{\partial\theta^*}{\partial t} + \frac{\partial u_k\theta^*}{\partial x_k} - \alpha\frac{\partial^2\theta^*}{\partial x_k\partial x_k} \tag{3.40}$$

$$\overline{\theta\mathcal{N}(\theta^*)} = 0 \tag{3.41}$$

$$\begin{aligned}\frac{\partial\overline{\theta\theta}}{\partial t}+U_k\frac{\partial\overline{\theta\theta}}{\partial x_k} = &-2\left(\overline{\theta u_k}\frac{\partial\Theta}{\partial x_k}\right) \quad \Big\} \mathcal{P}_{\theta\theta}\\ &-2\alpha\overline{\frac{\partial\theta}{\partial x_k}\frac{\partial\theta}{\partial x_k}} \quad \Big\} \varepsilon_{\theta\theta}\\ &+\alpha\frac{\partial^2\overline{\theta\theta}}{\partial x_k\partial x_k} \quad \Big\} \mathcal{D}^{\alpha}_{\theta\theta}\\ &+\frac{\partial\overline{\theta\theta u_k}}{\partial x_k} \quad \Big\} \mathcal{D}^{T}_{\theta\theta}\end{aligned} \tag{3.42}$$

- $\mathcal{P}_{\theta\theta}$: Production due to mean temperature gradient
- $\mathcal{D}^{\alpha}_{\theta\theta}$: Thermal diffusion
- $\mathcal{D}^{T}_{\theta\theta}$: Turbulent diffusion
- $\varepsilon_{\theta\theta}$: Dissipation term

The transport equation for the temperature variance is presented here for posterity. Since this thesis will not be dealing with the computation of this term, discussion on the aspects of its term-by-term modelling have been foregone.

3.6.5. Algebraic models for second order moments

Solving the full set of transport equations for the second moments undeniably provides better results when compared to simpler models such as those obtained by the eddy viscosity/diffusivity methods. However, solving these sets of coupled equations leads to complexities either due to numerics or due the geometry in the case of industrial applications. Launder (1975) and Rodi (1976) proposed truncated forms of the differential equations for the second moments, leading to algebraic expressions which significantly reduce computational cost and complexity. The assumptions necessary for such a truncation are much less restrictive in comparison to the eddy viscosity/diffusivity relations. The truncation to obtain such

algebraic models is based on two hypothesis, the *weak-equilibrium hypothesis* and the *strong-equilibrium hypothesis*.

The weak-equilibrium hypothesis states that anisotropy in the flow does not vary or varies slowly along the streamlines. Further assuming the hypothesis holds for the other differential terms in the transport equation for second moments, namely the diffusion terms, one can write,

$$\left(\frac{D}{Dt} - \mathcal{D}\right) b_{ij} = 0 \tag{3.43}$$

where, $b_{ij} = \frac{\overline{u_i u_j}}{2k} - \frac{1}{3}\delta_{ij}$ is the anisotropy tensor.

$$\frac{D\overline{u_i u_j}}{Dt} - \mathcal{D}_{ij} = \frac{\overline{u_i u_j}}{k}\left(\frac{Dk}{Dt} - \mathcal{D}_k\right) \tag{3.44}$$

$$\mathcal{P}_{ij} + \mathcal{G}_{ij} + \Pi_{ij} - \varepsilon_{ij} = \frac{\overline{u_i u_j}}{k}\left(\mathcal{P} + \mathcal{G} - \varepsilon\right) \tag{3.45}$$

Substituting the *basic model* (Hanjalic et al., 2011; Pope, 2000) for the pressure scrambling term, the Reynolds stresses are obtained in algebraic form as follows,

$$\overline{u_i u_j} = \frac{2}{3}k\delta_{ij} + \frac{k}{\varepsilon}\left[\frac{1 - C_2}{C_1 + \frac{(\mathcal{P}+\mathcal{G})}{\varepsilon} - 1}\left(\mathcal{P}_{ij} - \frac{2}{3}\mathcal{P}\delta_{ij}\right) + \frac{1 - C_3}{C_1 + \frac{(\mathcal{P}+\mathcal{G})}{\varepsilon} - 1}\left(\mathcal{G}_{ij} - \frac{2}{3}\mathcal{G}\delta_{ij}\right)\right] \tag{3.46}$$

To further simplify the relation, we employ the *strong-equilibrium hypothesis*. The strong-equilibrium hypothesis states that production of energy is balanced by the dissipation.

$$\mathcal{P} + \mathcal{G} = \varepsilon \tag{3.47}$$

Finally, the truncated algebraic model for the reynolds stresses called the *Algebraic Stress*

model (ASM) is obtained as,

$$\overline{u_i u_j} = \frac{2}{3}k\delta_{ij} + \frac{k}{\varepsilon}\left[\frac{1-C_2}{C_1}\left(\mathcal{P}_{ij} - \frac{2}{3}\mathcal{P}\delta_{ij}\right) + \frac{1-C_3}{C_1}\left(\mathcal{G}_{ij} - \frac{2}{3}\mathcal{G}\delta_{ij}\right)\right] \tag{3.48}$$

Table 3.1.: Constants for the ASM

C_1	C_2	C_3
1.8	0.6	0.6

The same procedure can be applied to the anisotropy vector of the turbulent heat fluxes. Hanjalic (2002) also proposed such a model and Dol et al. (1997) formalised the model by laying down the fundamental theory for the algebraic model for turbulent heat fluxes. The model derived by the truncation of DFM to an algebraic form is called the *Algebraic flux model (AFM)*.

From the weak-equilibrium hypothesis one can write,

$$\left(\frac{D}{Dt} - \mathcal{D}\right)\left[\frac{\overline{u_i\theta}}{\left(\overline{\theta\theta}k\right)^{1/2}}\right] = 0 \tag{3.49}$$

$$\begin{aligned}\frac{D\overline{u_i\theta}}{Dt} - \mathcal{D}_{i\theta} &= \frac{\overline{u_i\theta}}{\left(\overline{\theta\theta}k\right)^{1/2}}\left[\frac{D}{Dt}\left(\left(\overline{\theta\theta}k\right)^{1/2}\right) - \mathcal{D}\left(\overline{\theta\theta}k\right)^{1/2}\right] \\ &= \frac{1}{2}\overline{u_i\theta}\left[\frac{1}{\overline{\theta\theta}}\underbrace{\left(\frac{D\overline{\theta\theta}}{Dt} - \mathcal{D}_{\theta\theta}\right)}_{\mathcal{P}_{\theta\theta}-\varepsilon_{\theta\theta}} + \underbrace{\frac{1}{k}\left(\frac{Dk}{Dt} - \mathcal{D}_k\right)}_{\mathcal{P}+\mathcal{G}-\varepsilon}\right]\end{aligned} \tag{3.50}$$

$$\mathcal{P}_{i\theta} + \mathcal{G}_{i\theta} + \Pi_{i\theta} - \varepsilon_{i\theta} = \frac{\overline{u_i\theta}}{2}\left[\frac{1}{k}\left(\mathcal{P}+\mathcal{G}-\varepsilon\right) + \frac{1}{\overline{\theta\theta}}\left(\mathcal{P}_{\theta\theta}-\varepsilon_{\theta\theta}\right)\right] \tag{3.51}$$

The *basic-model* for the pressure scrambling term is employed once more. Note that

$\varepsilon_{i\theta} = 0$ due to the local isotropy assumption. Further simplifying with the use of the *strong-equilibrium hypothesis*, $\mathcal{P} + \mathcal{G} = \varepsilon$ and $\mathcal{P}_{\theta\theta} = \varepsilon_{\theta\theta}$, one obtains the Algebraic flux model shown below.

$$\overline{u_i\theta} = -C_\theta \tau \left((1 - C_{\theta 2}) \, \overline{u_i u_j} \frac{\partial \Theta}{\partial x_j} + (1 - C_{\theta 2}) \, \overline{u_j \theta} \frac{\partial U_i}{\partial x_j} + (1 - C_{\theta 3}) \, \beta g_i \overline{\theta^2} \right) \tag{3.52}$$

where $C_\theta = C'_\theta / C_{\theta 1}$. C'_θ is equal to 1 from the derivation of the model, however researchers have calibrated its value aiming to improve the predictions of the AFM.

3.6.6. Generalised gradient diffusion hypothesis (GGDH)

This hypothesis suggested by Daly et al. (1970) to model the triple correlations in the turbulent diffusion terms, was employed by Ince et al. (1989) to model the turbulent heat fluxes. It can be regarded as a further truncation of the Algebraic flux model where only the term containing thermal production, $\mathcal{P}^{\Theta}_{i\theta}$ is retained. The GGDH model writes,

$$\overline{u_i\theta} = -C_\theta \tau \overline{u_i u_j} \frac{\partial \Theta}{\partial x_j} \tag{3.53}$$

where C_θ is in the range 0.2-0.3, τ is the time scale dependent on the choice of the closure model. It is to be noted that this truncation has the advantage of not having to solve an additional transport equation for the temperature variance.

3.6.7. Simple gradient diffusion hypothesis (SGDH)

This hypothesis aptly named for its simplicity is the direct counterpart to the eddy-viscosity approach. The turbulent heat fluxes are approximated using the temperature gradients using an eddy-diffusivity as the proportionality constant. The eddy-diffusivity is related to the eddy-viscosity through the Reynolds analogy. The SGDH model writes,

$$\overline{u_i\theta} = -\alpha_t \frac{\partial \Theta}{\partial x_i} = -\frac{\nu_t}{\mathrm{Pr}_t} \frac{\partial \Theta}{\partial x_i} \tag{3.54}$$

where Pr_t is the turbulent Prandtl number and is usually taken to be in the range of 0.9-1.0. Owing to its simplicity, this is the most commonly employed model in industrial codes.

However it has to be noted that its extended usage belies the fact that in many flow configurations the SGDH model proves to be deficient. The primary issue is that the model assumes the heat flux vector and the temperature gradient are aligned, which is not the case for example in a canonical configuration such as the heated vertical wall. Moreover, lacking any vertical temperature gradients as in the case of a heated vertical wall, the SGDH model predicts zero buoyancy effect on turbulence. Ince et al. (1989) proposed the GGDH model in order to rectify this problem. Hanjalic (2002) noted these deficiencies and has further suggested that the algebraic forms are a minimum level of closure for complex flows.

3.6.8. Buoyancy sensitisation of Eddy-viscosity based models

Some efforts towards the improvement of eddy-viscosity based models to improve the prediction of buoyant flows is to be noted. These efforts are mainly motivated towards the retention of simplicity of the eddy-viscosity models. Davidson (1990) proposed a model where the buoyancy contribution from the ASM is used to sensitise the eddy-viscosity model to account for the anisotropy due to buoyancy production.

$$\overline{u_i u_j} = \frac{2}{3}k\delta_{ij} - \nu_t\left(\frac{\partial U_i}{\partial x_j} + \frac{\partial U_j}{\partial x_i}\right) + \underbrace{\frac{k}{\varepsilon}\frac{1-C_3}{C_1 + \frac{(\mathcal{P}+\mathcal{G})}{\varepsilon} - 1}\left(\mathcal{G}_{ij} - \frac{2}{3}\mathcal{G}\delta_{ij}\right)}_{\text{buoyancy contribution}} \tag{3.55}$$

where the second term in Equation (3.48) is modelled as usual using a turbulent eddy-viscosity.

The GGDH approach was used to model the heat fluxes, which accounts for the additional anisotropy due to buoyancy in the above equation. In his tests using the differentially heated cavity of aspect ratio 5 : 1, the modification showed improvements in decreasing vertical fluctuations and increasing horizontal fluctuations. This is an important flow characteristic

to capture for stably stratified flows where the turbulence in the vertical direction is damped. Another approach followed by Murakami et al. (1996) is that of the use of damping functions to achieve similar goals.

3.7. Academic test cases for natural convection flows

This section describes the test cases considered in the present thesis as benchmark databases for the development and evaluation of the turbulence models for natural convection flows.

3.7.1. Differentially heated vertical channel flow

Figure 3.1 illustrates an infinite vertical channel formed between a hot and a cold wall. Such side-heated flows represent one of the simplest academically studied test cases of natural convection flows aside from the spatially developing vertically heated flat plate. Several DNS databases have been established for this test case over the years including Phillips (1996), Boudjemadi et al. (1997), Versteegh et al. (1999), and Kis et al. (2014). The database of Kis et al. (2014) contains the highest Rayleigh numbers reached in the literature, with the simulation performed at $Ra \approx 2.27 \times 10^7$ (or $Gr = 4.0 \times 10^6$).

The flow is driven solely by the temperature differences between the two walls. The test case presents an anti-symmetric flow, with the flow along the hot wall being directed opposite to the gravity vector, $g_i = \{-1, 0, 0\}$. The test case corresponds to a cavity with an infinite aspect ratio. The flow is periodic in the vertical (x) and transversal (z) directions. As a result the test case does not present any stratification. Such flows are not observed in the real world, however, the above constraints render the configuration to be treated as a one-dimensional problem thus being ideal for model development.

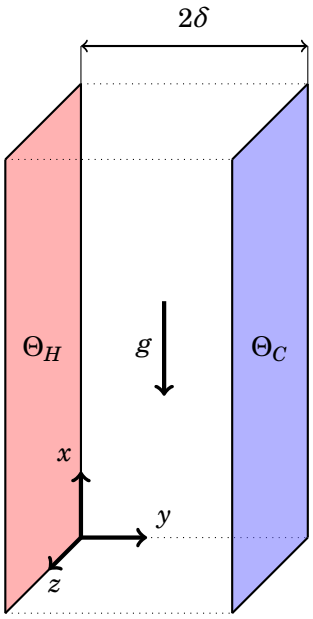

Figure 3.1.: Illustration of Differentially heated vertical channel of Kis et al., 2014

3.7.2. Differentially heated cavity

This section will provide an overview of the *Differentially heated cavities*, which differ from the channel flow presented before through the addition of two additional walls at the top and bottom leading to a very simple geometry. Two cavities are considered for the evaluation of the models developed in the context of this thesis, namely, the Square differentially heated cavity (Figure 3.2a) and the Rectangular differentially heated cavity of aspect ratio 4 (Figure 3.2b). Although the geometry is simple, it belies the fact that these test cases exhibit complex physics of interest which are relevant to industrial applications. Additionally, the flow physics changes significantly depending on the aspect ratio of the cavity and hence a full description of cavity flows not only requires the specification of the Rayleigh, Ra, and Prandtl, Pr, numbers but also the aspect ratio, A.

In regards to the physics presented by cavities, the following characteristics can be noted:

- the flow field presents centrosymmetry
- the flow field is stratified

- the boundary layers between the hot and cold walls are separated by a slowly rotating stratified core
- presence of laminar, transition and turbulent regions
- spatially developing boundary layers
- transition to turbulence due to the appearance of Taylor-Schlichting waves on the vertical boundaries in the case of tall cavities with adiabatic horizontal walls
- ejection of plumes in the case of conductive horizontal walls which trigger transition to turbulence at lower Ra numbers

Historically, due to the complexity of the physics and the necessity for powerful computational resources, there has been a lack of DNS databases for cavities. A large body of early works relating to cavities focused their attention on the identification of the different flow regimes through experimental investigations (Elder, 1965a,b) whereas numerical simulations were still limited to the laminar regime in two-dimensions. Further numerical investigations focusing on the transition mechanisms were conducted by Le Quéré et al. (1998) and Paolucci et al. (1989) to establish the critical Ra for the onset of turbulence. Henkes et al. (1996) performed stability analysis for 3D cases and found that the transition to turbulence occurs at a lower Ra as compared to 2D cases. These studies also highlighted the fact that factors such as the aspect ratio of the cavity and the boundary conditions applied to the top and bottom walls affect the critical Ra significantly. Of note, conductive walls drastically reduce the critical Ra as compared to the case of adiabatic top and bottom walls (Henkes et al., 1996; Xin et al., 2006, 2012).

DNS of rectangular cavities of high aspect ratios have been established for increasingly higher Rayleigh numbers in the last decade (Soria et al. (2004), F. X. Trias et al. (2007), F. Trias et al. (2010b), F. Trias et al. (2010a), Kizildag et al. (2014)). In the present work, for the case of the Rectangular cavity, the database of F. Trias et al. (2010b,a) with an

aspect ratio of $A = 4$ and adiabatic horizontal walls is used as a benchmark, which is an idealisation of the 3-D experimental cavity of Saury et al. (2011).

Square cavities have been studied using LES (Bosshard et al., 2013; Dehbi et al., 2014; Sergent et al., 2013; Zhang et al., 2014) with DNS studies established only in the last decade which includes the works of Sebilleau et al. (2018) and Sergent et al. (2013). Notable experimental studies include the works of Tian et al. (2000a,b) and Ampofo et al. (2003) who performed low turbulence natural convection experiments at $Ra = 1.58 \times 10^9$. Sebilleau et al. (2018) performed DNS simulations using the experimental profiles of Ampofo et al. (2003) as boundary conditions for the horizontal walls in order to compare the statistics between DNS and experiments. In the present work, the square cavity DNS database of Sebilleau et al. (2018) with idealised linear horizontal temperature boundary conditions is used as a benchmark as it provides the highest Ra at 10^{11} with a high level of turbulence.

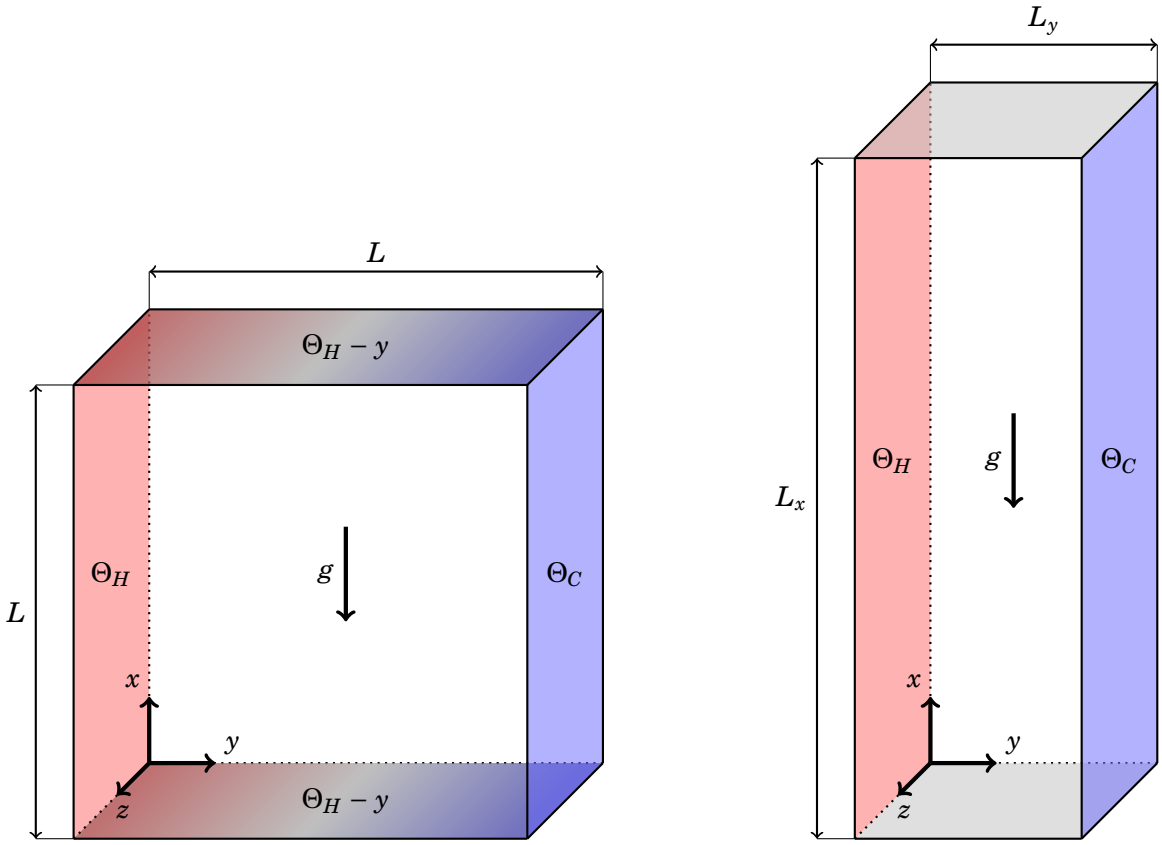

(a) Square cavity of Sebilleau et al., 2018

(b) Rectangular cavity of F. Trias et al., 2010b

Figure 3.2.: Illustrations of the Differentially heated Square and Rectangular cavities

3.7.3. Non-dimensionalisation of governing equations for the computations

This section describes the characteristic scales chosen for the non-dimensionalisation of the governing equations used in the computations. Essentially, the choice is made to use the same characteristic scales as in the works of F. Trias et al. (2010a,b) and Sebilleau et al. (2018). Table 3.2 provides the length scales specific to each of the test cases.

Let $\phi^\star$ represent the dimensional quantities and ϕ the non-dimensional quantities.

Table 3.2.: Choice of characteristic length scales

Test case	Characteristic length scale, L
Differentially heated vertical channel	half channel width, δ
Square differentially heated cavity	cavity height or width, L
Rectangular differentially heated cavity	cavity height, L_x

$$x_i = \frac{x_i^\star}{L} \quad ; \quad u_i = \frac{u_i^\star L}{\alpha\sqrt{Ra}} \quad ; \quad t = \frac{t^\star \alpha\sqrt{Ra}}{L^2} \quad ; \quad \theta = \frac{\theta^\star - \Theta_0}{\Delta\Theta} \quad ; \quad p = \frac{p^\star L^2}{\rho_0 \alpha^2 Ra} \tag{3.56}$$

In considering these non-dimensional variables, the momentum and energy equations write:

$$\frac{\partial u_i}{\partial t} + u_j \frac{\partial u_i}{\partial x_j} = -\frac{\partial p}{\partial x_i} + \frac{Pr}{\sqrt{Ra}} \frac{\partial^2 u_i}{\partial x_j \partial x_j} - Pr\theta \frac{g_i}{g} \tag{3.57}$$

where $g_i/g = (-1, 0, 0)$.

$$\frac{\partial \theta}{\partial t} + u_j \frac{\partial \theta}{\partial x_j} = \frac{1}{\sqrt{Ra}} \frac{\partial^2 \theta}{\partial x_j \partial x_j} \tag{3.58}$$

The variables quantified in the figures and tables in the chapters to follow are non-dimensionalised as described here and any changes to this representation will be done so by explicitly stating that fact.

3.8. Summary of the chapter

This chapter served to describe the mathematical formulation and description of the characteristic scales of natural convection flows. The effects and modifications in the governing and transport equations due to the influence of buoyancy are noted and their modelling using the different strategies is described. The modelling aspects with respect to RANS have been detailed and will serve as a basis for the developments undertaken in the following chapters. Finally the benchmark test cases and their non-dimensionalisation for computations is

noted.

Chapter 4.

RANS modelling of natural convection flows

This work is in the continuity of the thesis of Jameel (2020) who developed a Buoyancy extended strategy for eddy-viscosity models. In the industrial context, the use of the eddy-viscosity model remains prevalent. The aim of the thesis was to improve the predictions of the eddy-viscosity models by sensitising them to the effects of buoyancy. In this chapter, the model will be presented first in the Differentially heated vertical channel flow of Kis et al. (2014), as a validation study. This is followed by an analysis of its performance in a quasi-academic case of the Differentially heated square cavity of Sebilleau et al. (2018). Finally, further improvements carried out in the present thesis in regards to the treatment of source terms in the turbulence equations are presented.

4.1. Baseline performance of RANS models in the Vertical Channel Flow

In this section the baseline performance of RANS models is established. This exercise allows us to clearly understand where models are lacking in terms of their predictions of natural convection flows.

4.1.1. Model formulation

The two-equation models used to compute the turbulence scales and the closures for the Reynolds stress and heat flux terms are recalled here

1. $k\omega$-SST model

$$\nu_t = \frac{a_1 k}{\max\left(a_1\omega; SF_2\right)} \tag{4.1}$$

$$\frac{\partial k}{\partial t} + U_j\frac{\partial k}{\partial x_j} = \mathcal{P} + \mathcal{G} + \frac{\partial}{\partial x_j}\left[\left(\nu + \frac{\nu_t}{\sigma_k}\right)\frac{\partial k}{\partial x_j}\right] - C_\mu k\omega \tag{4.2}$$

$$\frac{D\omega}{Dt} = \frac{\gamma}{\nu_t}\mathcal{P} + \mathcal{G}_\omega^{SST} - \beta\omega^2 + \frac{\partial}{\partial x_j}\left[\left(\nu + \sigma_k\nu_t\right)\frac{\partial\omega}{\partial x_j}\right] + 2(1-F_1)\sigma_{\omega 2}\frac{1}{\omega}\frac{\partial k}{\partial x_i}\frac{\partial\omega}{\partial x_i} \tag{4.3}$$

$$\gamma_1 = \frac{\beta_{\omega_1}}{C_\mu} - \frac{\sigma_{\omega_1}\kappa^2}{\sqrt{C_\mu}} \quad ; \quad \gamma_2 = \frac{\beta_{\omega_2}}{C_\mu} - \frac{\sigma_{\omega_2}\kappa^2}{\sqrt{C_\mu}} \tag{4.4}$$

$$F_1 = \tanh\left[arg_1^4\right]; \quad \arg_1 = \min\left[\max\left[\frac{k^{1/2}}{C_\mu\omega d_w}; \frac{500\nu}{\omega d_w^2}\right]; \frac{4\rho k}{\sigma_{\omega 2} CD_{k\omega} d_w^2}\right] \tag{4.5}$$

$$F_2 = \tanh\left[\arg_2^2\right]; \quad \arg_2 = \max\left[\frac{2k^{1/2}}{C_\mu\omega d_w}; \frac{500v}{\omega d_w^2}\right] \tag{4.6}$$

$$CD_{k\omega} = \max\left[2\rho\frac{1}{\sigma_{\omega 2}}\frac{\partial k}{\partial x_j}\frac{\partial\omega}{\partial x_j}; 10^{-20}\right] \tag{4.7}$$

C_μ	κ	β	σ_k	σ_ω
0.09	0.41	0.075	1.0/0.85	2.0

2. BLv^2/k model

$$v_t = C_\mu \varphi k \min\left(T, T_{\text{lim}}\right) \tag{4.8}$$

$$\frac{\partial k}{\partial t} + U_j \frac{\partial k}{\partial x_j} = \mathcal{P} + \mathcal{G} + \frac{\partial}{\partial x_j}\left[\left(\frac{v}{2} + \frac{v_t}{\sigma_k}\right)\frac{\partial k}{\partial x_j}\right] - \varepsilon_h - E \tag{4.9}$$

$$\frac{\partial \varepsilon_h}{\partial t} + U_j \frac{\partial \varepsilon_h}{\partial x_j} = \frac{C_{\varepsilon_1}(\mathcal{P}+\mathcal{G}) - C^*_{\varepsilon_2}\varepsilon_h}{T} + \frac{\partial}{\partial x_j}\left[\left(\frac{v}{2} + \frac{v_t}{\sigma_{\varepsilon_h}}\right)\frac{\partial \varepsilon_h}{\partial x_j}\right] \tag{4.10}$$

$$\frac{\partial \varphi}{\partial t} + U_j \frac{\partial \varphi}{\partial x_j} = -\frac{\varphi}{k}(\mathcal{P}+\mathcal{G}) + \frac{\partial}{\partial x_j}\left[\left(\frac{\nu}{2} + \frac{\nu_t}{\sigma_\varphi}\right)\frac{\partial \varphi}{\partial x_j}\right] + \frac{2}{k}\frac{\nu_t}{\sigma_k}\frac{\partial \varphi}{\partial x_j}\frac{\partial k}{\partial x_j} + f \tag{4.11}$$

$$E = C_{\varepsilon_3}(1-\alpha)^3 \times \frac{k}{\varepsilon_h} 2 v v_t \left(\frac{\partial^2 U_i}{\partial x_k x_j}\right)\left(\frac{\partial^2 U_i}{\partial x_k x_j}\right) \tag{4.12}$$

$$C^*_{\varepsilon_2} = C_{\varepsilon_2} + \alpha^3\left(C_{\varepsilon_4} - C_{\varepsilon_2}\right)\tanh\left(\left|\frac{1}{\varepsilon_h}\frac{\partial}{\partial x_j}\left(\frac{\nu_t}{\sigma_k}\frac{\partial k}{\partial x_j}\right)\right|^{3/2}\right) \tag{4.13}$$

$$f = \left(1-\alpha^3\right) f_w + \alpha^3 f_h \quad ; \quad \text{where} \quad \alpha - L^2\nabla^2\alpha = 1 \tag{4.14}$$

$$f_w = -\frac{\varepsilon_h}{2}\frac{\varphi}{k} \quad \text{and} \quad f_h = -\frac{1}{T}\left(C_1 - 1 + C_2\frac{(\mathcal{P}+G)}{\varepsilon_h}\right)\left(\varphi - \frac{2}{3}\right) \tag{4.15}$$

$$L = \sqrt{C_L^2\left(\frac{k^3}{\varepsilon_h^2} + C_\eta^2\frac{v^{3/2}}{\varepsilon_h^{1/2}}\right)}; \quad T = \sqrt{\frac{k^2}{\varepsilon_h^2} + C_T^2\frac{v}{\varepsilon_h}}; \quad T_{lim} = \frac{0.6}{\sqrt{6}C_\mu\varphi\sqrt{S_{ij}S_{ij}}} \tag{4.16}$$

C_μ	C_T	C_L	C_η	C_1	C_2	C_{ε_1}	C_{ε_2}	C_{ε_3}	C_{ε_4}	σ_k	σ_ε	σ_φ
0.09	4.0	0.164	75	1.7	0.9	1.44	1.83	2.3	0.4	1.0	1.5	1.0

3. Boussinesq relation for the Reynolds stresses

$$\overline{u_i u_j} = \frac{2}{3}k\delta_{ij} - 2\nu_t S_{ij}, \qquad k = \frac{\overline{u_i u_i}}{2} \text{ and } S_{ij} = \frac{1}{2}\left(\frac{\partial U_i}{\partial x_j} + \frac{\partial U_i}{\partial x_j}\right) \tag{4.17}$$

4. Closures for the turbulent heat fluxes

   - Generalised gradient diffusion hypothesis (GGDH)

$$\overline{u_i\theta} = -C_\theta \tau \overline{u_i u_j}\frac{\partial \Theta}{\partial x_j} \tag{4.18}$$

     Remark: the GGDH model for the heat fluxes is only employed in the transport equations of turbulence quantities and not in the energy equation. This is because the coefficient C_θ is not taken to be a constant but formulated such that in forced convection flows where the buoyancy effects are negligible, the model reverts back to the SGDH formulation (see demonstration in Section 4.2.1).

   - Simple gradient diffusion hypothesis (SGDH)

$$\overline{u_i\theta} = -\alpha_t \frac{\partial \Theta}{\partial x_i} = -\frac{\nu_t}{\mathrm{Pr}_t}\frac{\partial \Theta}{\partial x_i} \tag{4.19}$$

4.1.2. Vertical channel flow

The Vertical differentially heated channel database of Kis et al. (2014) with the highest available Rayleigh number of $Ra = 1.7 \times 10^6$ is used for the baseline study. The test case presents two main regions: a near wall region similar to a boundary layer and a core region of homogeneous shear at the centre of the channel, similar to that of a Couette type flow. As mentioned previously, this test case lends itself well for the purposes of testing turbulence models due to the possibility of analysing it as a one-dimensional problem.

To begin with, it is important to note the consequences of the choice of closure models used for the turbulent heat fluxes particularly for the case of a vertical channel flow which does not present any stratification. Without stratification, the temperature gradient is only present in the direction perpendicular to the gravity vector, g_i.

$$\mathcal{G}_k = -\beta g_i \overline{u_i \theta}, \text{ where } g_i = [-1, 0, 0]. \tag{4.20}$$

With a closure such as SGDH, where the heat flux vector is aligned with the temperature gradient, the buoyancy production term is exactly zero. The kinetic energy production due to buoyancy, $\mathcal{G}_k$, for SGDH writes:

$$\mathcal{G}_k = -\beta g_i \overline{u_i \theta} = \beta \frac{\nu_t}{\mathrm{Pr}_t} \left[g_x \cancelto{0}{\frac{\partial \Theta}{\partial x}} + \cancelto{0}{g_y} \frac{\partial \Theta}{\partial y} + \cancelto{0}{g_z} \frac{\partial \Theta}{\partial z} \right] = 0 \tag{4.21}$$

Whereas in the case of GGDH, the buoyancy production term is non-zero since the anisotropy of turbulence is accounted for such that,

$$\mathcal{G}_k = -\beta g_i \overline{u_i \theta} = \beta g_x C_\theta \tau \overline{u u_j} \frac{\partial \Theta}{\partial x_j} \neq 0 \tag{4.22}$$

This is evidenced clearly in the plots of the production terms seen in Figure 4.1.

Figure 4.2 shows the mean velocity profiles for the $k\omega$-SST and BL-v^2/k model using the SGDH and GGDH closures for the turbulent heat fluxes. For the $k\omega$-SST model, the profiles are overestimated as compared to the DNS data. Accounting for the anisotropy using the GGDH model helps to improve the results significantly, however, the profiles are still over predicted throughout most of the channel. The BL-v^2/k model performs considerably better for both the SGDH and GGDH models. All the profiles predict the peak of the velocity earlier than that of DNS and also do not have the linear variation in the central region as seen in the DNS.

Figure 4.3 shows the mean temperature profiles for the $k\omega$-SST and BL-v^2/k model using

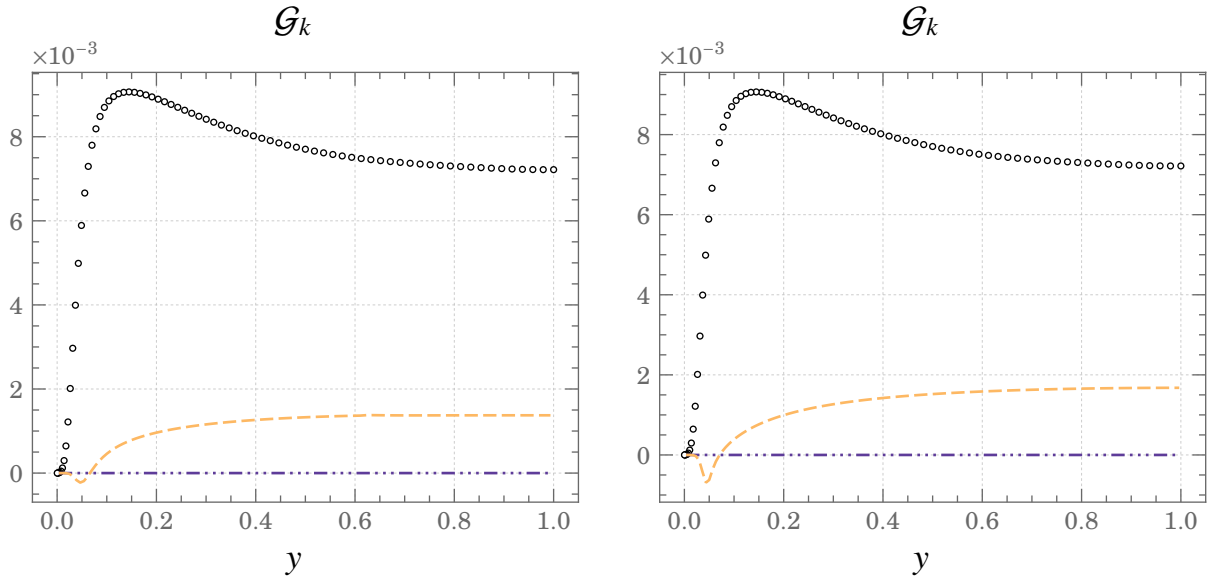

(a) Model: $k\omega$-SST

(b) Model: BL-v^2/k

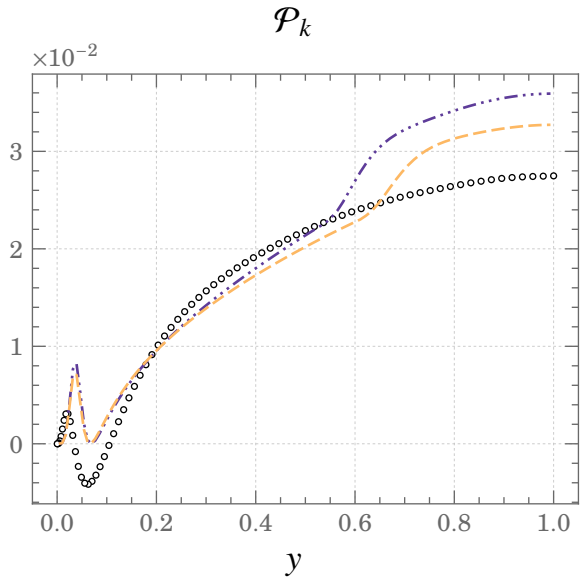

(c) Model: $k\omega$-SST

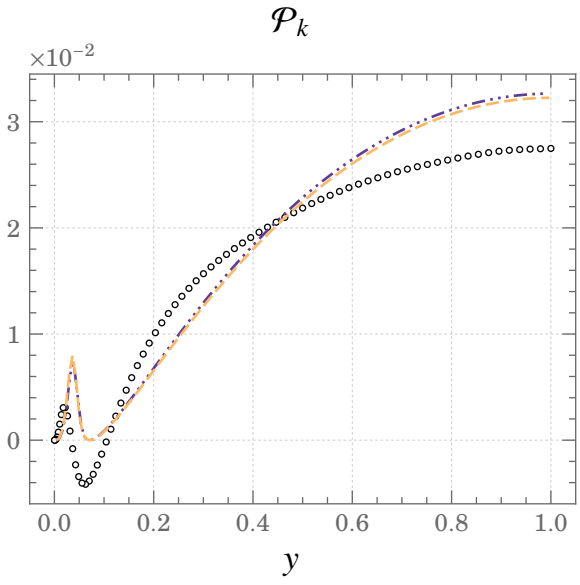

(d) Model: BL-v^2/k

Figure 4.1.: Kinetic energy production, $\mathcal{G}_k$ and $\mathcal{P}_k$ at $Ra \approx 1.7 \times 10^7$ ($Gr = 3 \times 10^6$)
○ ○ ○ *DNS* – – – *GGDH* -·-·- *SGDH*

the SGDH and GGDH closures for the turbulent heat fluxes. Both models over-predict the temperature profile. Although it is not clearly evident for the $k\omega$-SST model (Figure 4.3a), the temperature gradient at the wall is highly under-predicted. The over-prediction of

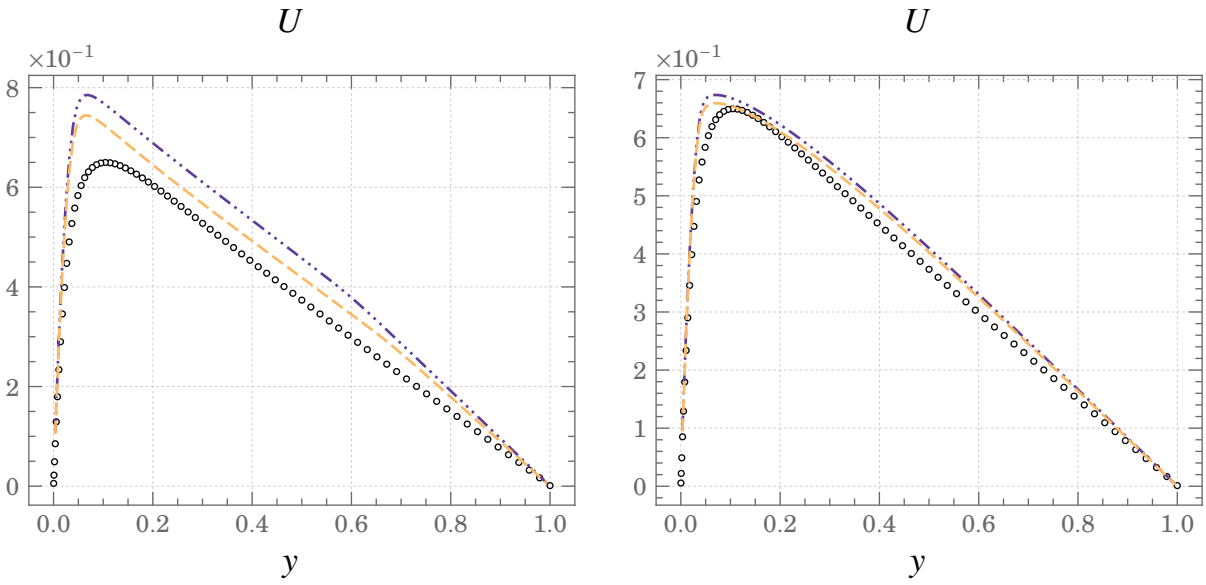

(a) Model: $k\omega$-SST

(b) Model: BL-v^2/k

Figure 4.2.: Mean profiles of Velocity at $Ra \approx 1.7 \times 10^7$ ($Gr = 3 \times 10^6$)
$\circ\ \circ\ \circ$ *DNS* — — *GGDH* -·-·- *SGDH*

temperature is evident in Figure 4.4, where the temperature profiles are normalised with inner wall units. This is due to the friction temperature, θ_τ, being severely under-predicted as shown in Table 4.2a. On the contrary, the BL-v^2/k model shows better agreement with the DNS data close to the wall with a comparatively better prediction of the temperature gradient and hence the friction temperature as shown in Table 4.2b. However, deviation from the DNS profile can be noted around the region corresponding to the peak in the velocity profile. This indicates that the BL-v^2/k model accounts for a strong coupling between the buoyancy force and momentum, especially considering the good prediction achieved for the velocity profile.

Writing the momentum balance, the deficiency in the predictions of these models can be better understood. The time-averaged stream-wise momentum balance writes,

$$0 = \nu \frac{\partial^2 U}{\partial y^2} - \frac{\partial \overline{uv}}{\partial y} + \beta g (\Theta - \theta_0) \tag{4.23}$$

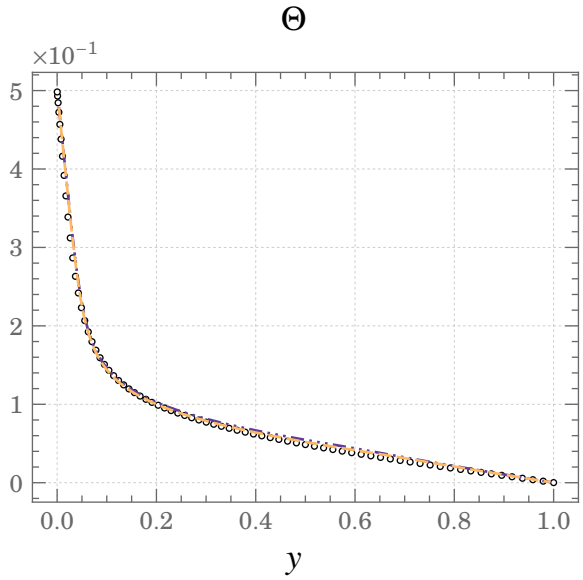

(a) MODEL: $k\omega$-SST

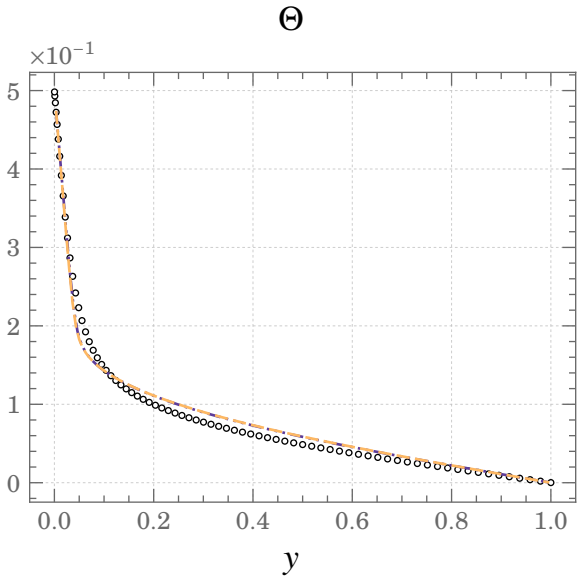

(b) Model: BL-v^2/k

Figure 4.3.: Mean profiles of Temperature at $Ra \approx 1.7 \times 10^7$ ($Gr = 3 \times 10^6$)
○ ○ ○ *DNS* — — — *GGDH* ·-·-· *SGDH*

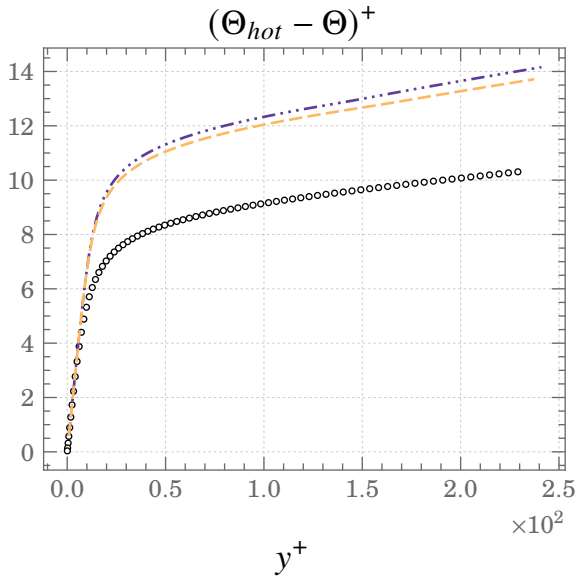

(a) MODEL: $k\omega$-SST

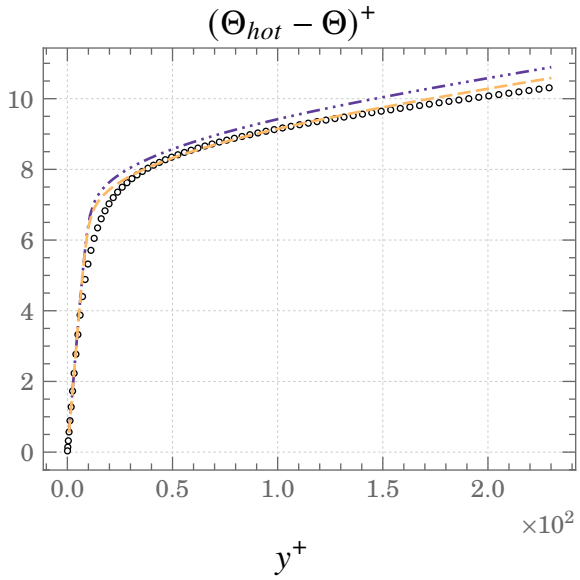

(b) Model: BL-v^2/k

Figure 4.4.: Mean profiles of Temperature normalised with inner wall units at $Ra \approx 1.7 \times 10^7$ ($Gr = 3 \times 10^6$) ○ ○ ○ *DNS* — — — *GGDH* ·-·-· *SGDH*

integrating from the wall up to a distance y,

$$\nu\frac{\partial U}{\partial y} - \rho u_\tau^2 - \overline{uv} + \int_0^y \beta g(\Theta - \theta_0) = 0. \tag{4.24}$$

The equation above shows that the vertical velocity is dependant on the correct prediction of the profiles of shear stress, temperature (buoyancy force), and also on the estimate of the friction velocity. Moreover, these terms balance each other and a misprediction of one can greatly influence the mean profiles.

Model	u_τ	Error(%)
DNS	1.11e-01	-
SGDH	1.18e-01	+6
GGDH	1.16e-01	+4

(a) Model: $k\omega$-SST

Model	u_τ	Error(%)
DNS	1.11e-01	-
SGDH	1.126e-01	+1
GGDH	1.124e-01	+0.8

(b) Model: BL-v^2/k

Table 4.1.: Errors in the estimation of friction velocity, u_τ

Model	θ_τ	Error(%)
DNS	4.85e-02	-
SGDH	3.53e-02	-27
GGDH	3.64e-02	-25

(a) Model: $k\omega$-SST

Model	θ_τ	Error(%)
DNS	4.85e-02	-
SGDH	4.58e-02	-6
GGDH	4.72e-02	-3

(b) Model: BL-v^2/k

Table 4.2.: Errors in the estimation of friction temperature, θ_τ

The turbulent shear stress, $\overline{uv}$, is under predicted over the full range of the channel for the $k\omega$-SST model as seen in Figure 4.5a. The other terms in Equation (4.24) need to compensate for the under prediction of turbulent shear stress. Given the fact that the over-prediction obtained for the temperature profile and thus the buoyancy force further hinders this balance, the momentum balance is compensated primarily due to the higher velocity gradients. As a consequence, the friction velocity is overestimated as seen in Table 4.1a. This culminates in the over-prediction of the velocity profile for the $k\omega$-SST model.

On the other hand, although the turbulent shear stress profile for BLv^2/k model (seen in Figure 4.5b) deviates from the DNS data, it can be noted that the deviations in both the

turbulent shear stress and the temperature profile balance each other — as evidenced by the fact that the velocity profile is predicted well in conjunction with the excellent estimate of the friction velocity as seen in Table 4.1b for both the SGDH and GGDH heat flux closures.

The misprediction of turbulent shear stress is a consequence of using the Bousinessq approximation.

$$\overline{uv} = -\nu_t \frac{\partial U}{\partial y} \tag{4.25}$$

As seen in the profile of turbulent viscosity, ν_t, (Figure 4.7), it is severely underestimated leading to the underestimation of the turbulent shear stress. Furthermore, the under-prediction of turbulent viscosity is a direct consequence of the kinetic energy (Figure 4.6) being under-predicted.

An analysis for the thermal balance can be carried out in similar fashion to the momentum balance just before. Due to periodicity in the stream-wise and transversal directions the temperature varies only in the wall normal direction, leading to the simplification of the temperature transport equation to be analysed as a 1-Dimensional problem as shown below,

$$0 = \alpha \frac{\partial^2 \Theta}{\partial y^2} - \frac{\partial \overline{v\theta}}{\partial y}. \tag{4.26}$$

The above equation shows that the correct prediction of the temperature profile is reliant on the accuracy of the prediction of wall-normal heat flux, $\overline{v\theta}$. As seen in Figure 4.8a, the $k\omega$-SST model largely under-predicts $\overline{v\theta}$. In comparison the BLv^2/k model performs better no doubt thanks to the better formulation of the turbulent viscosity. Integrating Equation (4.26) and normalising with inner wall units, u_τ (friction velocity) and θ_τ (friction temperature) leads to,

$$1 = -\frac{1}{Pr} \frac{\partial \Theta^+}{\partial y^+} + \overline{v\theta}^+. \tag{4.27}$$

Equation (4.27) shows that the heat flux at the wall is balanced by the molecular and turbulent heat fluxes. As seen in Figure 4.9a, when normalised with the inner wall units it is noted that the turbulent heat flux goes to one far from the wall since the molecular

heat flux becomes negligible far from the wall irrespective of the closure model used. More importantly Figure 4.9a highlights the fact that the turbulent heat flux is under-predicted close to the wall. A consequence of the misprediction of the turbulent heat flux is that the friction temperature, i.e., the heat flux at the wall, is severely underestimated, especially in the case of the $k\omega$-SST model. This results in the temperature profile being overestimated by both the models as discussed previously.

In conclusion, the analysis of the performance of the baseline models shows that there is a need to improve the predictions of the turbulent shear stress and the turbulent heat flux. Efforts at the development of such a model, as carried out in the work of Jameel (2020) are presented in the next section.

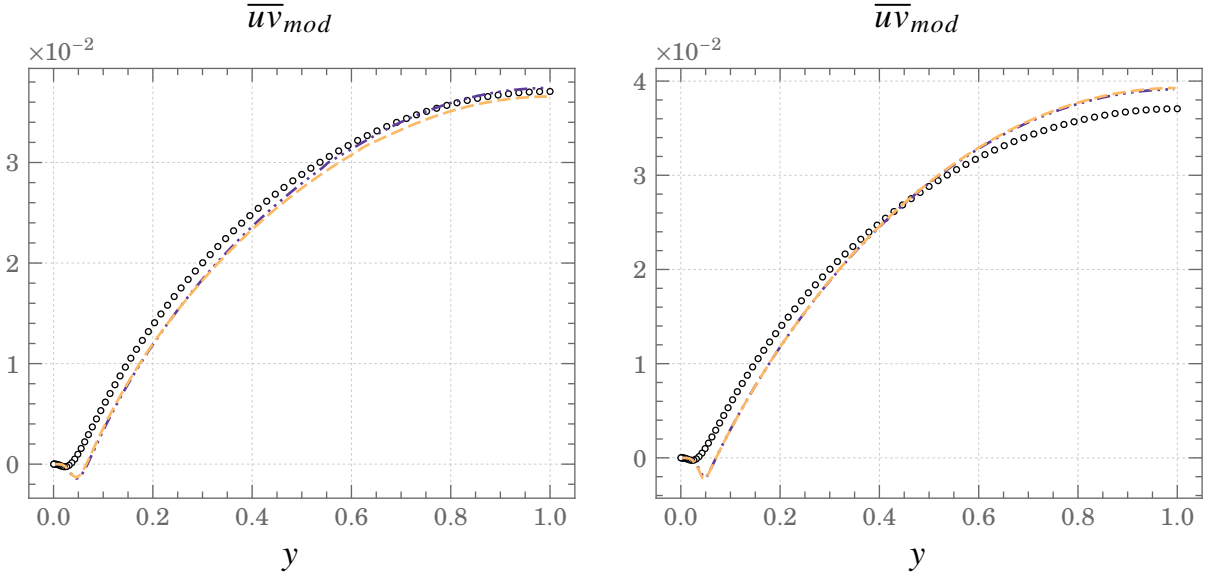

(a) MODEL: $k\omega$-SST

(b) Model: BL-v^2/k

Figure 4.5.: Mean profiles of the turbulent shear stress, $\overline{uv}$

DNS $GGDH$ $SGDH$

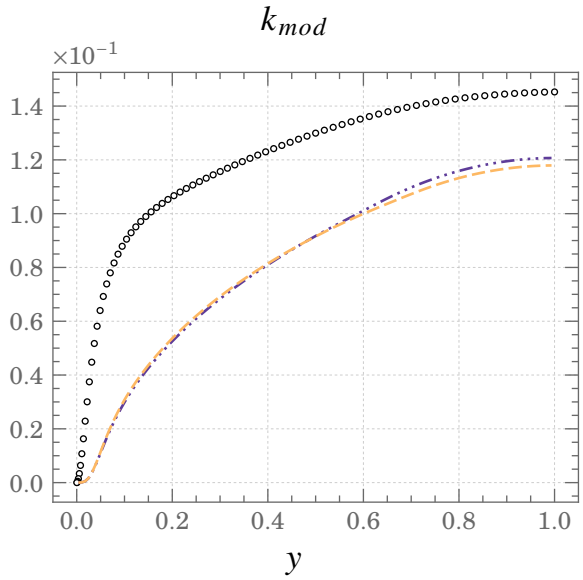

(a) MODEL: $k\omega$-SST

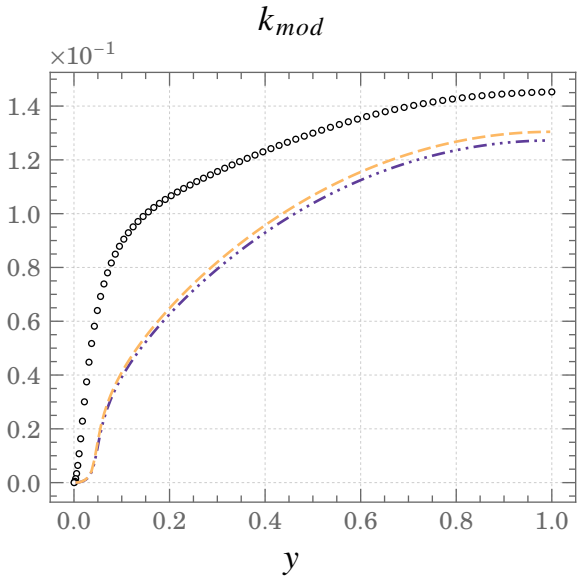

(b) Model: BL-v^2/k

Figure 4.6.: Mean profiles of the turbulent kinetic energy, k
○ ○ ○ *DNS* – – – *GGDH* ·–·–· *SGDH*

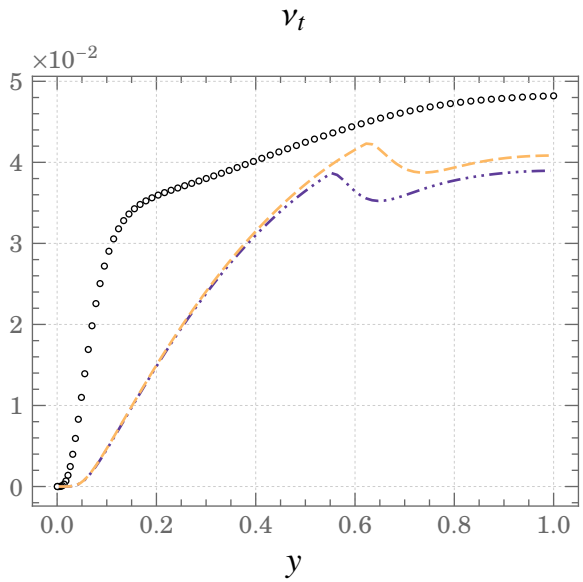

(a) MODEL: $k\omega$-SST

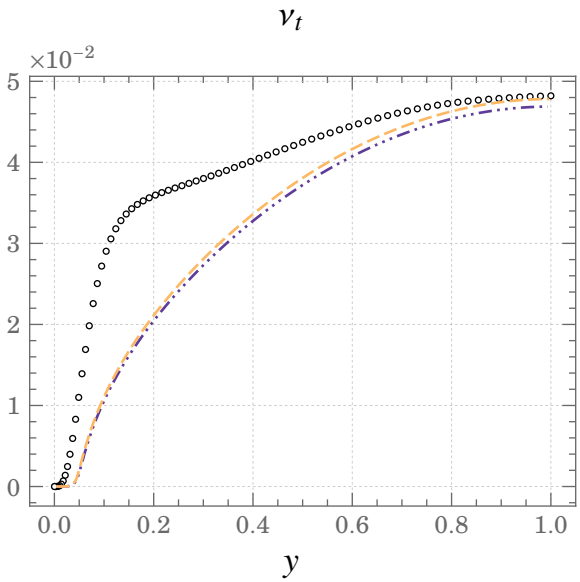

(b) Model: BL-v^2/k

Figure 4.7.: Mean profiles of the turbulent viscosity, ν_t
○ ○ ○ *DNS* – – – *GGDH* ·–·–· *SGDH*

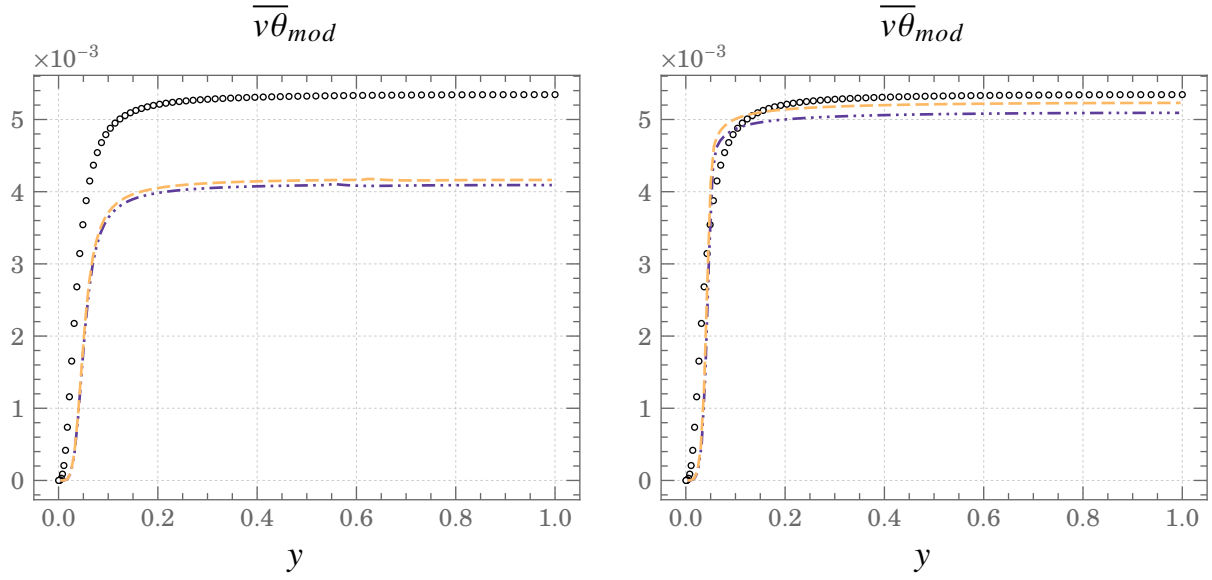

(a) MODEL: $k\omega$-SST (b) Model: BL-v^2/k

Figure 4.8.: Mean profiles of the Wall normal heat flux, $\overline{v\theta}$
$\circ\ \circ\ \circ\ DNS$ $GGDH$ $SGDH$

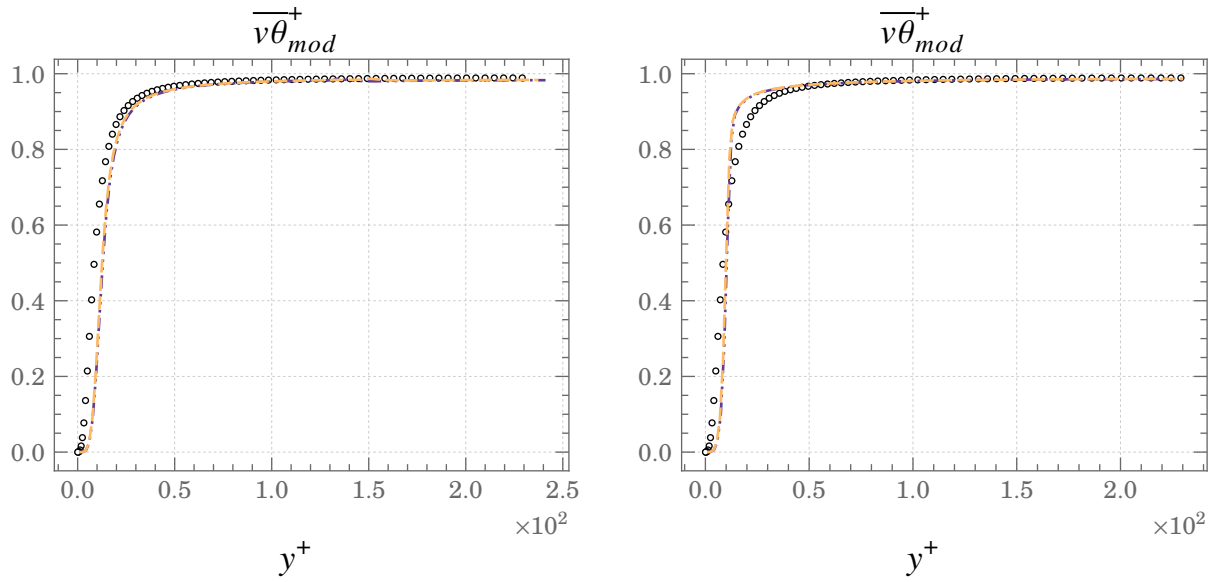

(a) MODEL: $k\omega$-SST (b) Model: BL-v^2/k

Figure 4.9.: Mean profiles of the Wall normal heat flux, $\overline{v\theta}^{+}$
$\circ\ \circ\ \circ\ DNS$ $GGDH$ $SGDH$

4.2. Buoyancy extended model

One of the drawbacks of the eddy-viscosity approach is that the effects of buoyancy production on the Reynolds stresses are not taken in to account. The algebraic relations obtained from truncating the differential equations for the Reynolds stresses clearly contain the buoyancy contribution. Davidson (1990) suggested the use of the buoyancy term from the algebraic model, without the assumption of the strong equilibrium hypothesis, in the eddy-viscosity formulation. In the work of Jameel (2020), the buoyancy term from the ASM, with further simplification using the strong equilibrium hypothesis (see Equation (3.48) in Section 3.6.5), is used as follows,

$$\overline{u_i u_j} = \underbrace{\frac{2}{3}k\delta_{ij} + \tau\left[\frac{1-C_2}{C_1}\left(\mathcal{P}_{ij} - \frac{2}{3}\mathcal{P}\delta_{ij}\right)\right]}_{\text{Standard eddy-viscosity model (STD)}} + \underbrace{\tau\left[\frac{1-C_3}{C_1}\left(\mathcal{G}_{ij} - \frac{2}{3}\mathcal{G}\delta_{ij}\right)\right]}_{\text{Buoyancy contribution (BUO)}} \tag{4.28}$$

Furthermore, the co-efficient of the buoyancy term is reformulated resulting in a single co-efficient, such that

$$\overline{u_i u_j} = \underbrace{\frac{2}{3}k\delta_{ij} - \nu_t\left(\frac{\partial U_i}{\partial x_j} + \frac{\partial U_j}{\partial x_i}\right)}_{STD} + \underbrace{C_\theta^* \tau\left(\mathcal{G}_{ij} - \frac{2}{3}\mathcal{G}\delta_{ij}\right)}_{BUO} \tag{4.29}$$

where C_θ^* is a constant necessitating calibration. Furthermore, the heat fluxes are modelled using the GGDH approach.

$$\overline{u_i\theta} = -C_\theta \tau \overline{u_i u_j}\frac{\partial \Theta}{\partial x_j} \tag{4.30}$$

It is to be noted that the GGDH model now contains the contribution of the buoyancy term in the anisotropic diffusivity.

$$\overline{u_i\theta} = -C_\theta \tau \left(\underbrace{(\overline{u_i u_j})}_{STD} + \underbrace{(\overline{u_i u_j})}_{BUO}\right)\frac{\partial \Theta}{\partial x_j} \tag{4.31}$$

4.2.1. Formulation of C_θ

Jameel (2020) paid special attention to the formulation of the constant, C_θ, in the GGDH model. The idea behind the formulation is to have the buoyancy extended model revert back to the eddy-viscosity model (i.e., noted as STD in the equations above) if and when the influence of buoyancy is negligible. This is achieved through establishing an equivalency between the SGDH and GGDH approaches in the forced convection flow in a channel. The temperature transport is driven solely by the wall-normal heat flux in such cases. Equating the SGDH and GGDH model,

$$\overline{v\theta} = -\alpha_t \frac{\partial \Theta}{\partial y} = -C_\theta \tau \overline{vv} \frac{\partial \Theta}{\partial y} \tag{4.32}$$

From the Bousinessq relationship we get $\overline{vv} = 2k/3$ and with $\alpha_t = \nu_t / Pr_t$, the constraint on C_θ is written in a general form as,

$$C_\theta = \frac{3}{2k} \frac{\nu_t}{Pr_t} \frac{1}{\tau} \tag{4.33}$$

4.2.2. Validation of the buoyancy extended model in the Vertical channel flow

It was seen in Section 4.1 that the baseline models that are prevalently used in industrial codes tend to over-predict both the velocity profiles and the temperature profiles. The root cause of these incorrect predictions, through the analysis of the momentum (Equation (4.23)) and energy balance (Equation (4.26)), were found to be the misprediction of turbulence shear stress, $\overline{uv}$, and turbulent heat flux, $\overline{v\theta}$.

The buoyancy extended model (abbreviated as *FBE* which stands for *Full buoyancy extension*) takes into account additional terms, derived from a simplified form of the Algebraic stress model, in the formulation of the eddy-viscosity approach to combat this issue. The

turbulent shear stress now contains the buoyancy contribution such that,

$$\overline{uv} = -\nu_t \frac{\partial U}{\partial y} + C_\theta^* \tau \beta g \overline{v\theta}. \tag{4.34}$$

Qualitatively Figure 4.10a shows that the turbulent shear stress is markedly improved for the $k\omega$-SST model — far from the wall in particular. The turbulent shear stress for the BLv^2k model is improved closer to the wall and the over-prediction noticed away from the wall helps in improving the gradient of velocity between the velocity peak and the centre of the channel. In both cases the turbulent shear stress is augmented due to the positive buoyancy effect of the additional term. Recalling the momentum balance again,

$$\nu \frac{\partial U}{\partial y} - \rho u_\tau^2 - \overline{uv} + \int_0^y \beta g(\Theta - \theta_0) = 0, \tag{4.35}$$

it can be noted that the improvement in turbulent shear stress contributes in a manner such that compensation from the velocity gradient and the friction velocity is less drastic as compared to the baseline models.

Indeed this can be clearly seen from the velocity profiles in Figure 4.11. For both the $k\omega$-SST and BLv^2k models, the peak velocity is reduced to be more inline with the DNS benchmark. The gradient from the velocity peak towards the centre of the channel is improved, with a vast improvement in the case of the $k\omega$-SST model. Furthermore the near wall gradients are improved as seen from the lowered errors on the estimates of friction velocity in Table 4.3.

The improvement observed in the turbulent shear stress, $\overline{uv}$, can further be tracked to the improvement in the prediction of turbulent viscosity (Figure 4.13) as well. This is a consequence of the improvement of the dynamic and buoyancy production terms in the turbulence scale resolving equations. The dynamic production term is improved upon by the inclusion of the buoyancy term in the turbulent shear stress as shown in Equation (4.34). The use of GGDH closure for the computation of the turbulent heat fluxes further improves

the estimation of the production terms for both the $k\omega$-SST and BLv^2k models as seen in Figure 4.14a.

In regards to the temperature profiles, recalling the thermal balance in the wall-normal direction,

$$0 = \alpha \frac{\partial^2 \Theta}{\partial y^2} - \frac{\partial \overline{v\theta}}{\partial y}, \tag{4.36}$$

improvements are noted for the turbulent heat flux, however leading only to a marginal improvement in the temperature profile (see Figure 4.16). The turbulent heat flux with the GGDH closure accounts for additional buoyancy contribution with the buoyancy extended model such that,

$$\overline{v\theta} = -C_\theta \tau \frac{\partial \Theta}{\partial y} \left(\underbrace{\frac{2}{3}k}_{STD} + \underbrace{\frac{2}{3} C_\theta^* \tau \beta g \overline{u\theta}}_{BUO} \right). \tag{4.37}$$

The extra term helps to improve the turbulent heat flux profile as seen in Figure 4.17, with qualitatively more evident improvements for the BLv^2k model as compared to that of $k\omega$-SST. Furthermore, it can be noted that the buoyancy extended model aids in the estimate of friction temperature as shown in Table 4.4.

In summary, accounting for the effects of buoyancy leads to an improvement of the predictions of mean profiles thanks to improvements in both the momentum and energy balance. Testing these modifications for the industrially relevant RANS models with the aid of an idealised test case such as the vertical differentially heated channel demonstrates that such modifications can provide additional improvements while still retaining the simplicity of eddy-viscosity models.

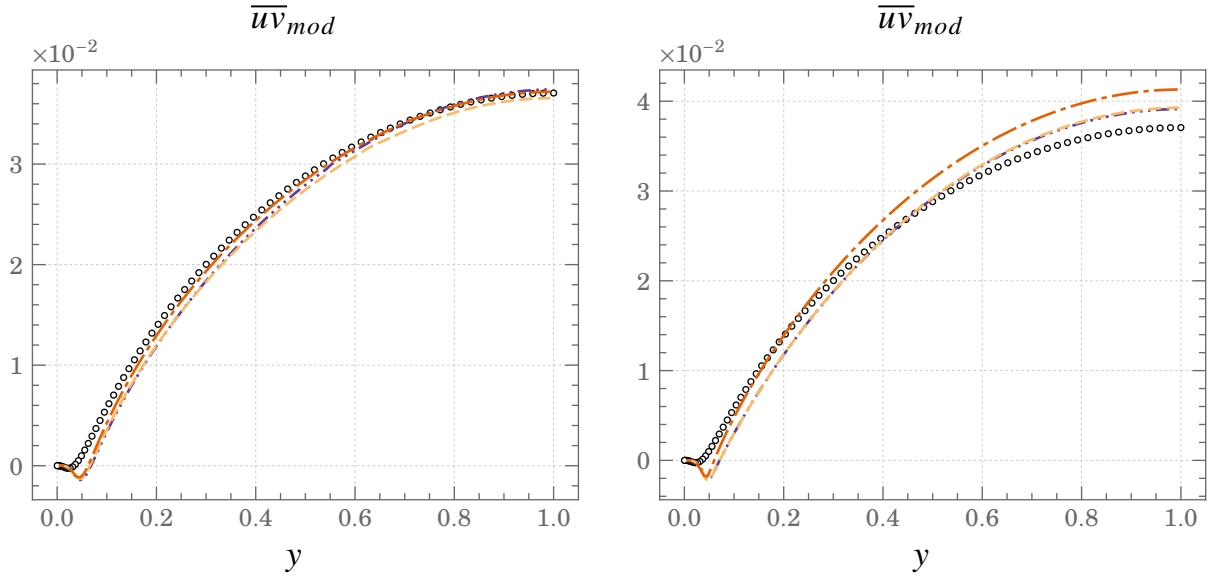

(a) MODEL: $k\omega$-SST (b) Model: BL-v^2/k

Figure 4.10.: Mean profiles of the turbulent shear stress, $\overline{uv}$
$\circ$ $\circ$ $\circ$ *DNS* *FBE* *GGDH* *SGDH*

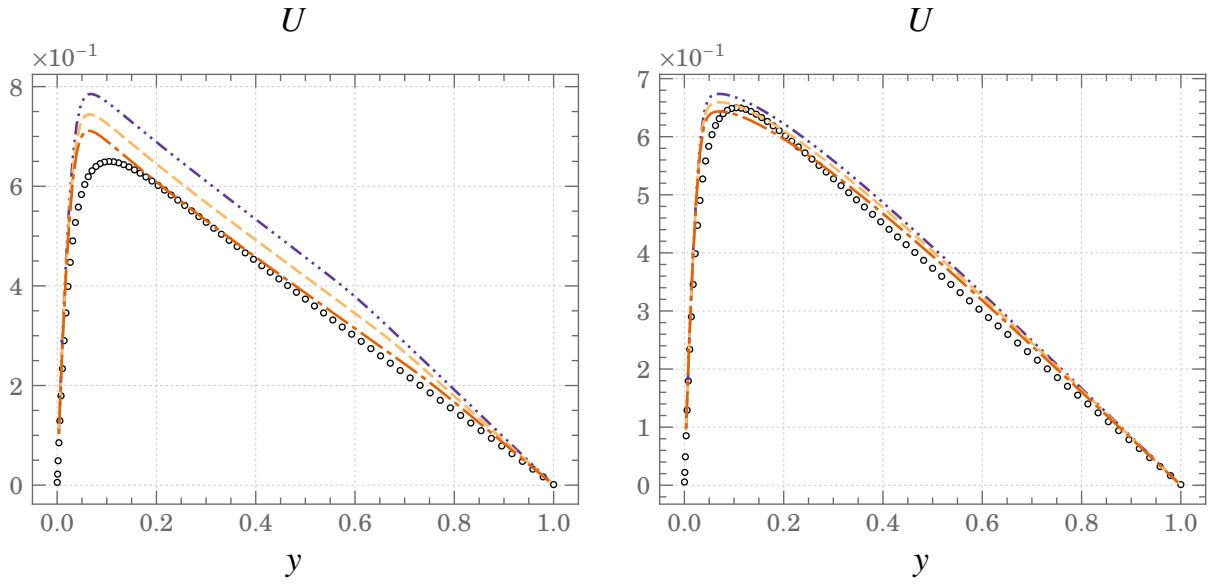

(a) Model: $k\omega$-SST (b) Model: BL-v^2/k

Figure 4.11.: Mean profiles of Velocity at $Ra \approx 1.7 \times 10^7$ ($Gr = 3 \times 10^6$)
$\circ$ $\circ$ $\circ$ *DNS* *FBE* *GGDH* *SGDH*

Model	u_τ	Error(%)
DNS	1.11e-01	-
SGDH	1.18e-01	+6
GGDH	1.16e-01	+4
FBE	1.14e-01	+3

(a) Model: $k\omega$-SST

Model	u_τ	Error(%)
DNS	1.11e-01	-
SGDH	1.126e-01	+1
GGDH	1.124e-01	+0.8
FBE	1.118e-01	+0.4

(b) Model: BL-v^2/k

Table 4.3.: Errors in the estimation of friction velocity, u_τ

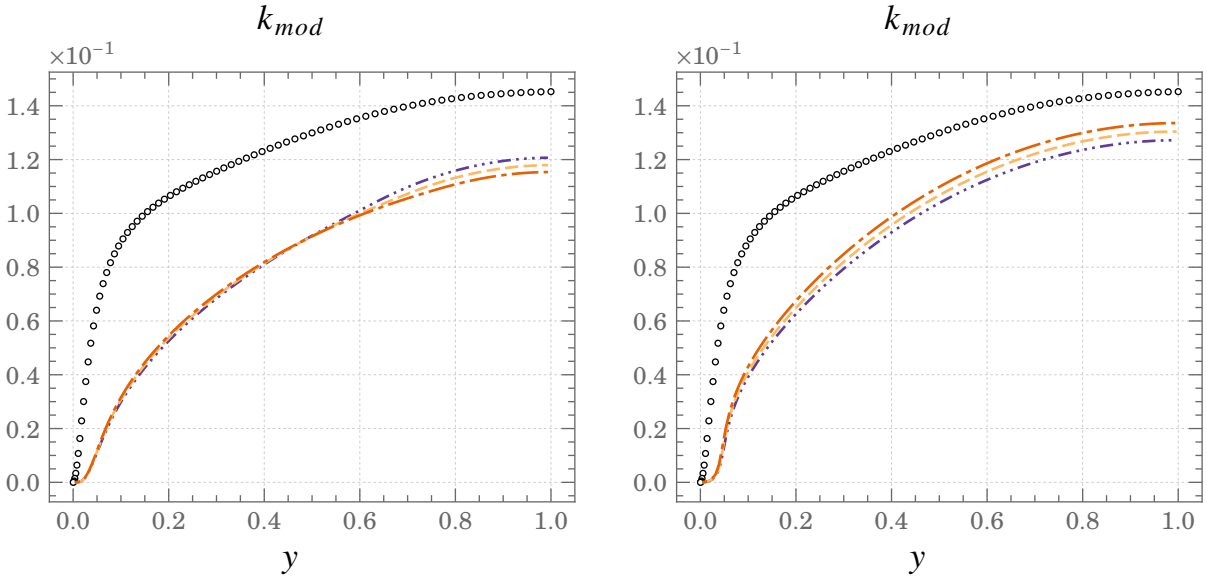

(a) MODEL: $k\omega$-SST

(b) Model: BL-v^2/k

Figure 4.12.: Mean profiles of the turbulent kinetic energy, k

DNS FBE $GGDH$ $SGDH$

Model	θ_τ	Error(%)
DNS	4.85e-02	-
SGDH	3.53e-02	-27
GGDH	3.64e-02	-25
FBE	3.71e-02	-23

(a) Model: $k\omega$-SST

Model	θ_τ	Error(%)
DNS	4.85e-02	-
SGDH	4.58e-02	-6
GGDH	4.72e-02	-3
FBE	4.83e-02	-0.4

(b) Model: BL-v^2/k

Table 4.4.: Errors in the estimation of friction temperature, θ_τ

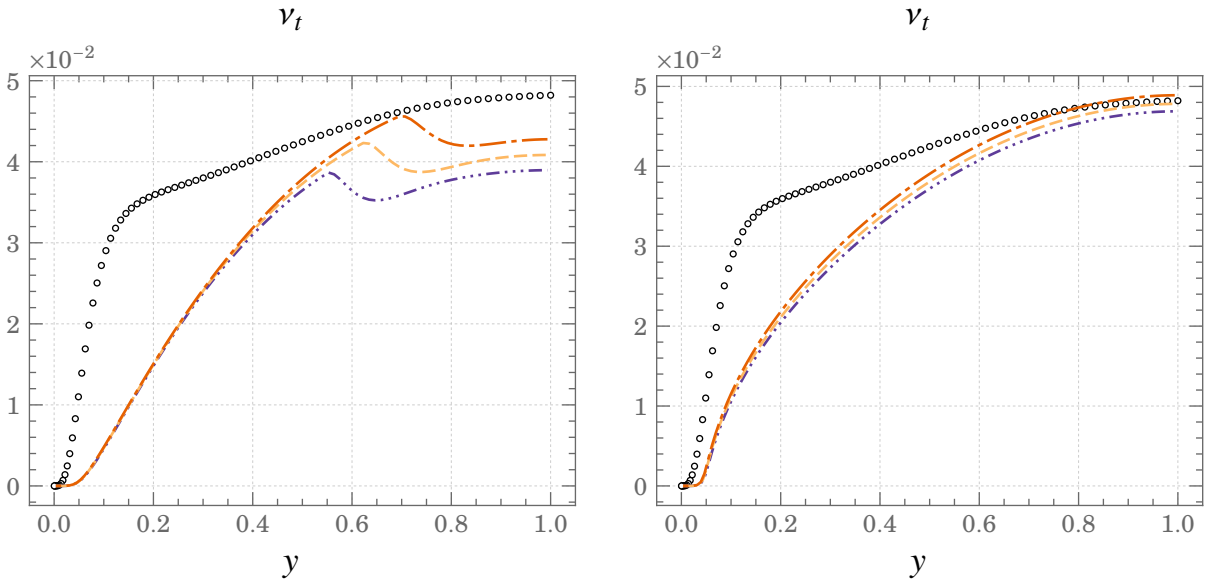

(a) MODEL: $k\omega$-SST (b) Model: BL-v^2/k

Figure 4.13.: Mean profiles of the turbulent viscosity, ν_t
○ ○ ○ *DNS* *FBE* *GGDH* *SGDH*

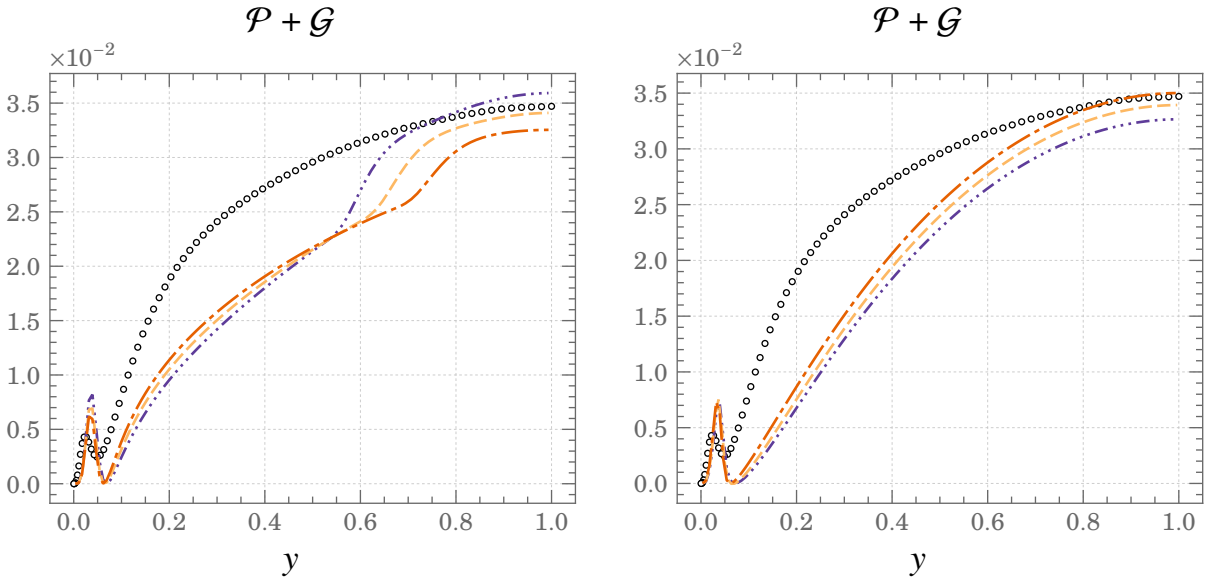

(a) MODEL: $k\omega$-SST (b) Model: BL-v^2/k

Figure 4.14.: Mean profiles of the production terms in the turbulent kinetic energy equation, $\mathcal{P} + \mathcal{G}$ ○ ○ ○ *DNS* *FBE* *GGDH* *SGDH*

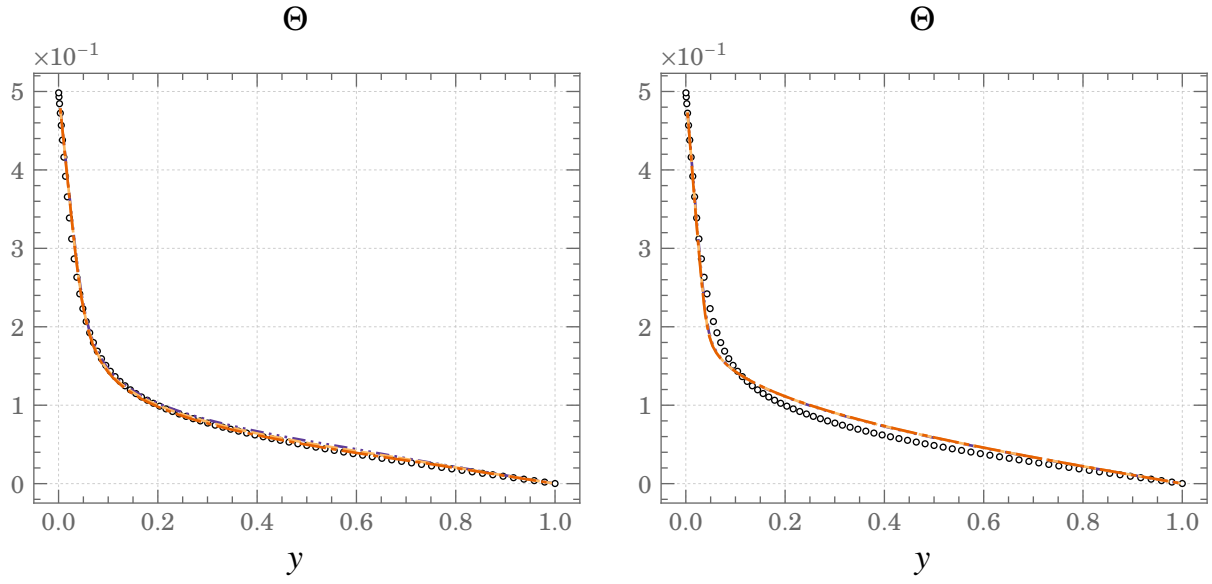

(a) MODEL: $k\omega$-SST (b) Model: BL-v^2/k

Figure 4.15.: Mean profiles of Temperature at $Ra \approx 1.7 \times 10^7$ ($Gr = 3 \times 10^6$)
○ ○ ○ *DNS* *FBE* *GGDH* *SGDH*

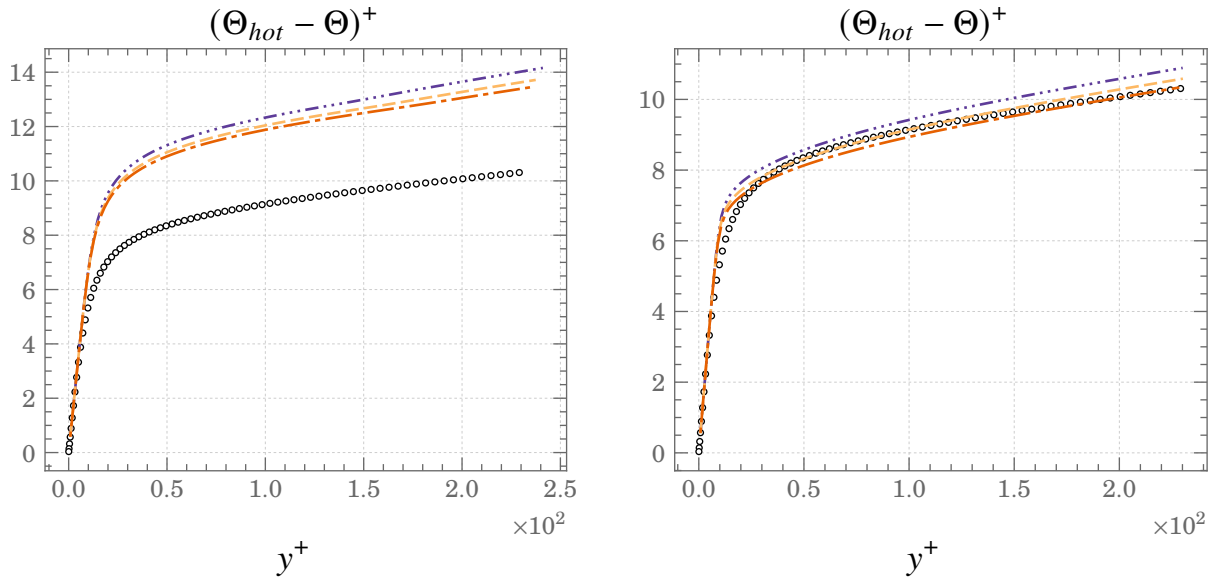

(a) MODEL: $k\omega$-SST (b) Model: BL-v^2/k

Figure 4.16.: Mean profiles of Temperature normalised with inner wall units at $Ra \approx 1.7 \times 10^7$ ($Gr = 3 \times 10^6$)
○ ○ ○ *DNS* *FBE* *GGDH* *SGDH*

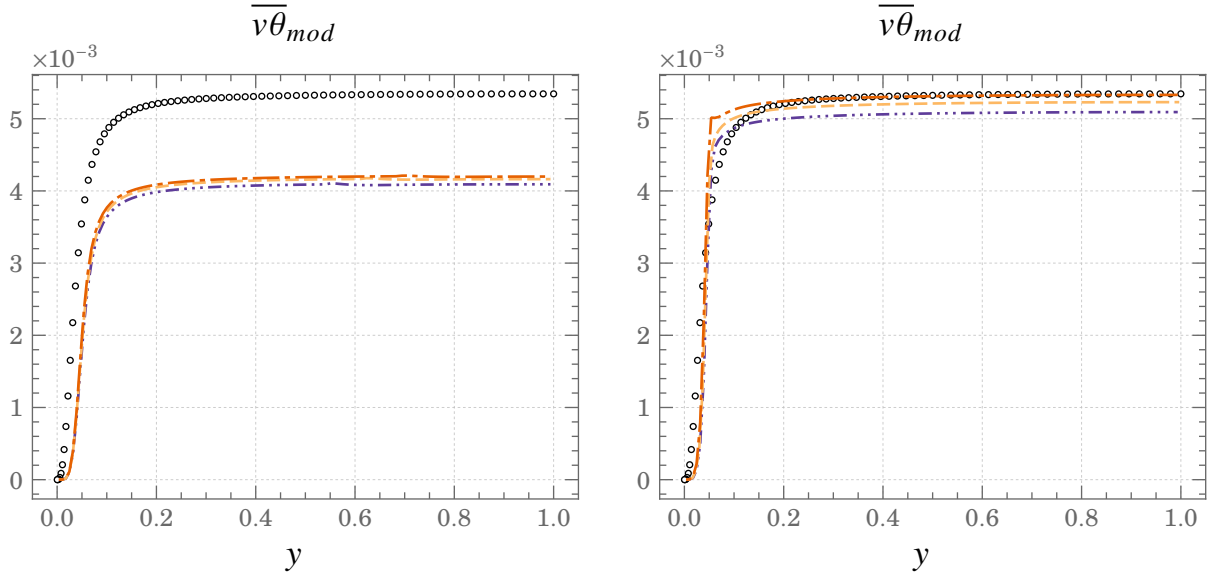

(a) MODEL: $k\omega$-SST

(b) Model: BL-v^2/k

Figure 4.17.: Mean profiles of the Wall normal heat flux, $\overline{v\theta}$

DNS FBE $GGDH$ $SGDH$

4.3. Differentially heated Square cavity

The vertical differentially heated channel served as a demonstrator for the buoyancy modification of eddy-viscosity models thanks to its simplicity whereby the system reduces to a 1-dimensional problem. In this section, these modifications are tested using a more complex configuration of the *square differentially heated cavity* of Sebilleau et al. (2018) at $Ra = 10^{11}$. The study of such a quasi-industrial test case helps to further validate the improvements perceived through the buoyancy extended model (FBE).

4.3.1. Mesh convergence study

A mesh convergence study is carried out in order to eliminate the grid size from being a factor in the results. The RANS simulations using the $k\omega$-SST model are carried out in 2-D with one grid cell in the periodic z-direction. Since the configuration is a square, the grid size in the stream-wise, x, and wall-normal, y, directions are kept the same. In all the cases, the $1st$ grid point is chosen such that the x^+ and y^+ values are lower than 1. Figure 4.18 shows the mean velocity and temperature plots where it can be noted that the increase in grid resolution has a very minimal effect on the profiles. The differences observable near the lower wall of the cavity at $x = 0.1$ of the velocity profile are mainly between the coarsest, 249^2, and the finest, 498^2 grids. At the same cavity height, the differences are significantly less pronounced for the temperature profiles.

Additionally, the simulations present some resolved fluctuations and are technically *Unsteady-RANS (URANS)*. It is therefore interesting to compare a quantity such as the turbulent kinetic energy which is known to be very much dependent on the grid resolution. Observing the plots for modelled and resolved turbulent kinetic energy in Figure 4.19, it can be seen that even the coarsest grid chosen compares well with the finer grids. In view of this comparison, the 332^2 grid was used for the simulations to compare the effects of the buoyancy modifications for this cavity configuration.

Table 4.5.: Grids refined in x and y

Ra	Δ_x^+	Δ_y^+	N_x	N_y	N_z
	< 1	< 1	249	249	1
10^{11}	< 1	< 1	332	332	1
	< 1	< 1	415	415	1
	< 1	< 1	498	498	1

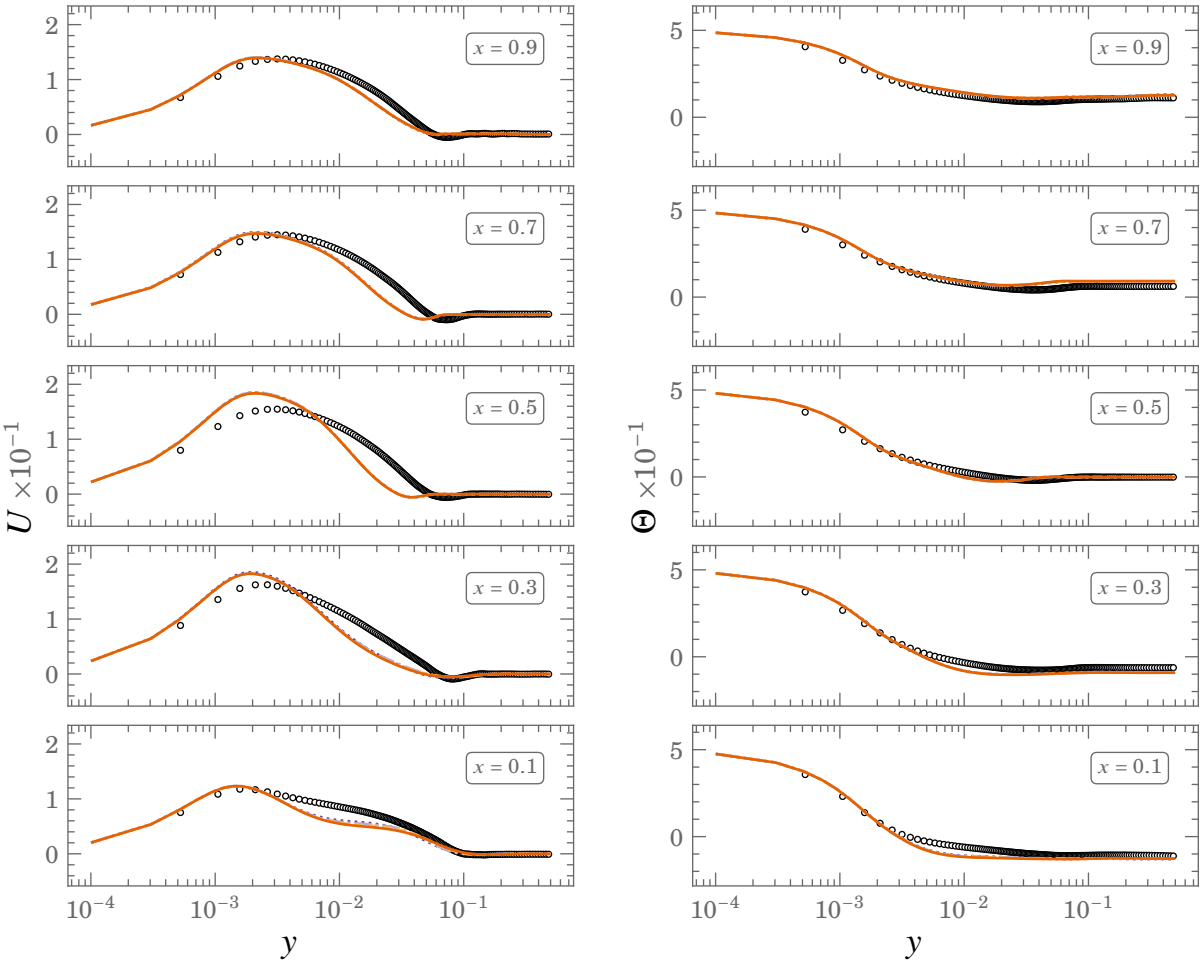

(a) Mean velocity, U

(b) Mean Temperature, Θ

Figure 4.18.: Mean profiles of Velocity and Temperature for various meshes at $Ra \times 10^{11}$
○ ○ ○ ○ DNS ····· 249^2 -·-·-· 332^2 - - - - 415^2 ——— 498^2

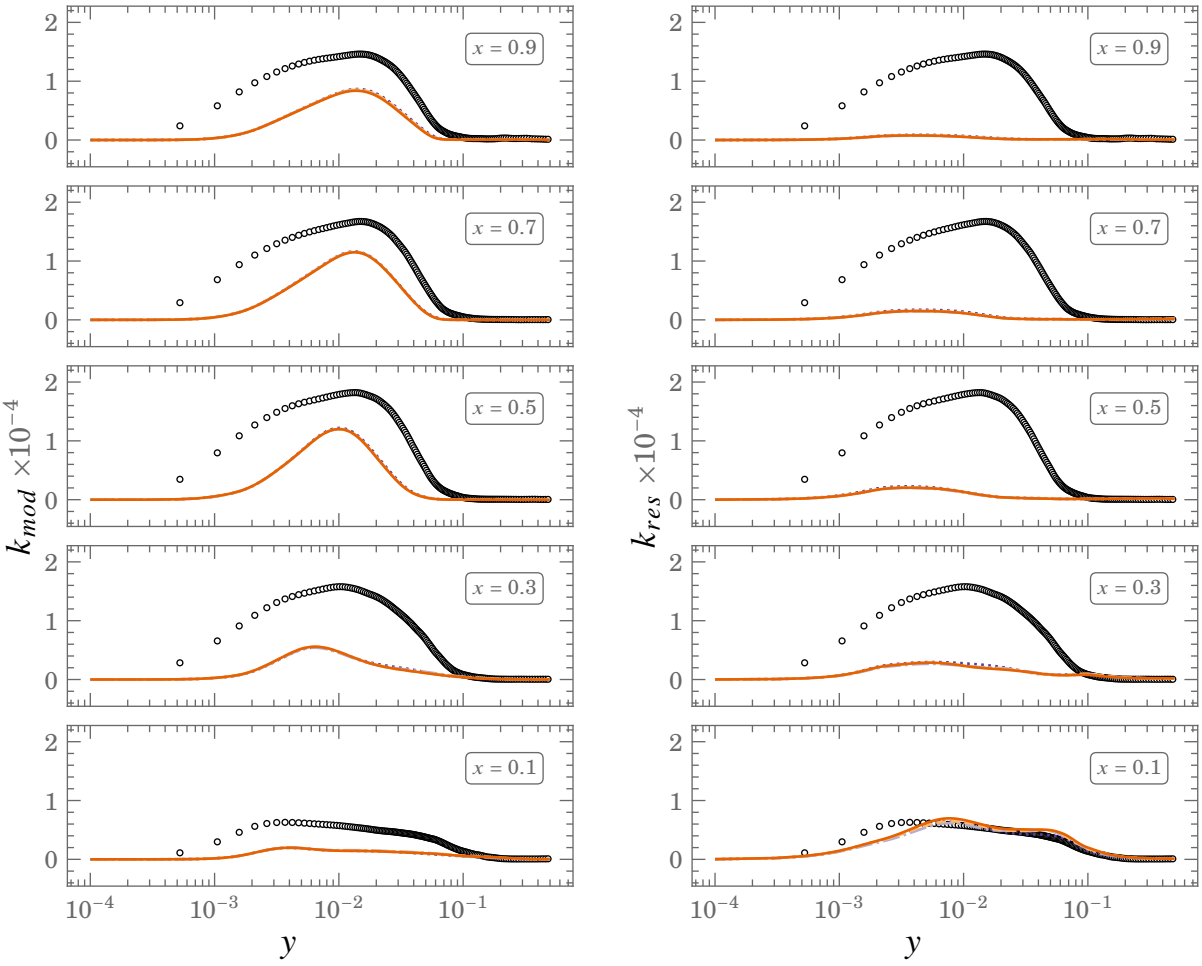

(a) Modelled kinetic energy, k_{mod}

(b) Resolved kinetic energy, k_{res}

Figure 4.19.: Mean profiles of modelled and resolved turbulent kinetic energy for various meshes at $Ra \times 10^{11}$

4.3.2. Performance of the models

The square differentially heated cavity presents a quasi-academic test case owing to the complex physics exhibited. The test case thus proves to be ideal for the comparison of the buoyancy extended model, which is developed with industrial applications in mind. The buoyancy extended model is again compared to the baseline models as seen before. Profiles are plotted at 9 locations along the height of the cavity ranging from $0.1 \leq x \leq 0.9$ up to half the wall-normal direction from the hot wall since the test case presents centrosymmetry.

The mean velocity profiles (Figure 4.21) are over-predicted close to the wall and under-predicted further away from the wall for both $k\omega$-SST and BLv^2/k models. The predictions, however, get better along the height of the cavity towards the top-wall ($x > 0.6$) for both the models. The buoyancy extended model shows marginal but consistent improvements compared to the baseline models. As in the case of the vertical channel flow, the buoyancy extended model provides more corrections to the velocity profile for the $k\omega$-SST model as compared to the BLv^2/k model.

The temperature profiles in Figure 4.22 show that both models overestimate the temperature profile close to the wall. It is interesting to note that at cavity heights $x \leq 0.5$, the temperature profiles are under-predicted towards the centre of the cavity, while at higher cavity heights $x > 0.5$ the temperature profile is over-predicted. At cavity heights $x \leq 0.5$, there exists a crossover point between the models compared and the DNS data which corresponds to the peaks observed in the velocity profiles suggesting a strong coupling of the velocity and temperature fields. This is evidenced by Figure 4.23 and Figure 4.24, where it can be seen that the dynamic production is more dominant towards the top of the cavity while there is a higher contribution of buoyancy production towards the bottom of the cavity. Moreover, the misprediction of the temperature profile near the centre of the cavity can be clearly noticed in Figure 4.20 showing the temperature stratification. The stratification is clearly improved by the buoyancy extended model in the case of $k\omega$-SST for the whole of the cavity. In the case of BLv^2/k, the improvement is seen only at the bottom

half of the cavity while slightly degrading the results in the top half.

In regards to the turbulence quantities, it should be first noted that there is a non-negligible amount of resolved motion in the simulations. This is noticeable in the resolved kinetic energy plots in Figure 4.33. The amount of resolved energy is notably higher for the BLv^2/k model as compared to the $k\omega$-SST, however, it gradually reduces as we move along the height of the cavity. This has an effect on the estimation of the turbulent viscosity and as seen in Figure 4.30, where the turbulent viscosity is under-predicted for both the models since the modelled turbulent kinetic energy is largely under-predicted. As a consequence of this the turbulent shear stress, $\overline{uv}$, is under-predicted as seen in Figure 4.25.

In the case of the buoyancy extended model the predictions of the turbulent heat fluxes play an important role in the overall estimation of turbulent shear stress and consequently the heat fluxes themselves since they are coupled through the use of the GGDH closure. For the $k\omega$-SST model, the buoyancy extension provides noticeable improvements in the predictions of the wall-normal heat flux Figure 4.29. This provides improvements to the profile of $\overline{uv}$. The impact of the buoyancy extension with the BLv^2/k model is very minimal. The buoyancy extension model provides in most cases similar results to that of the GGDH closure. Furthermore, the stream-wise heat flux, $\overline{u\theta}$, is highly under-predicted by both the $k\omega$-SST and BLv^2/k models, irrespective of the heat flux closure used (Figure 4.27). In the bottom half of the cavity the contribution to $\overline{u\theta}$ is majorly due to the resolved motions (Figure 4.28). However these resolved motions are not sustained throughout the height of the cavity which leads to massive under-prediction of $\overline{u\theta}_{tot}$.

Looking at the shear stress profiles in Figure 4.34, it can be noted that the buoyancy extended model provides minor improvements in the bottom half of the cavity ($x \leq 0.6$) while the results remain largely similar for all the heat flux closures near the top of the cavity ($x > 0.6$). Thanks to the better predictions of $\overline{v\theta}$ from the buoyancy extended model in the case of $k\omega$-SST, there is noticeable improvement in the prediction of Nusselt number (Figure 4.35), although the predictions are well underestimated in regards to the DNS. In the case of BLv^2/k, the predictions of the buoyancy extended model are improved compared

to the SGDH closure but remain in line with the predictions of the GGDH closure. The shear stress and Nusselt number plots show that the transition to turbulence for both $k\omega$-SST and BLv^2/k models is around $x = 0.4$ while the DNS data clearly shows that the transition happens around $x = 0.3$.

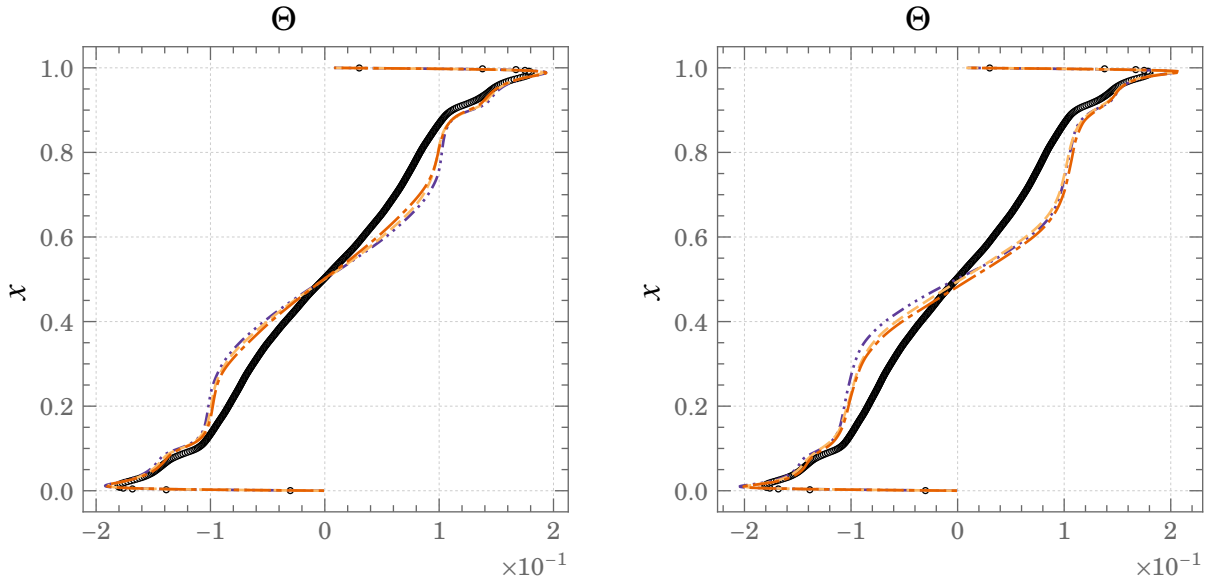

(a) Model: $k\omega$-SST

(b) Model: BL-v^2/k

Figure 4.20.: Profiles of Temperature stratification at $y = 0.5$ for $Ra \times 10^{11}$
○ ○ ○ *DNS* *FBE* *GGDH* *SGDH*

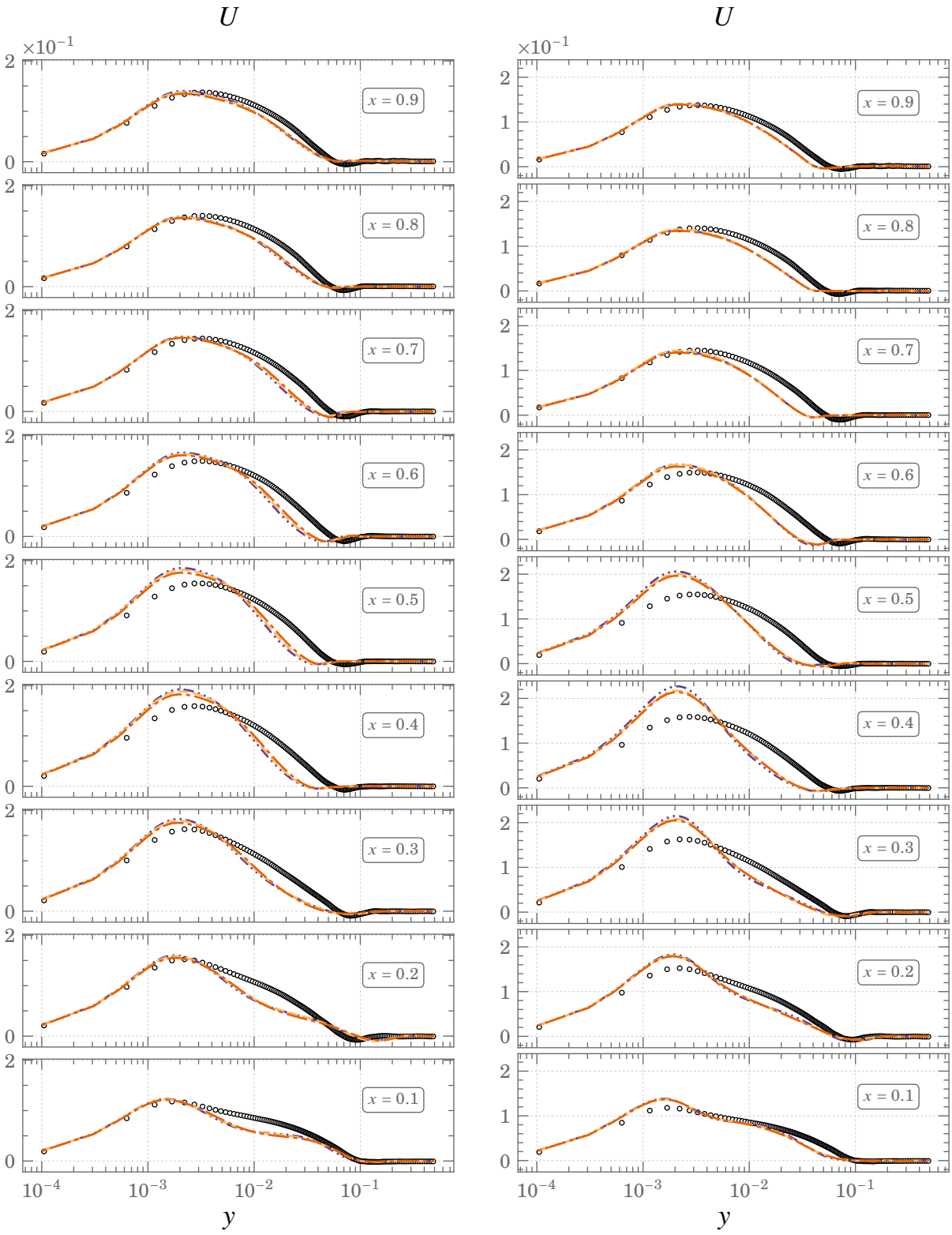

(a) Model: $k\omega$-SST

(b) Model: BL-v^2/k

Figure 4.21.: Mean profiles of Velocity at $Ra \times 10^{11}$

○ ○ ○ *DNS* *FBE* *GGDH* *SGDH*

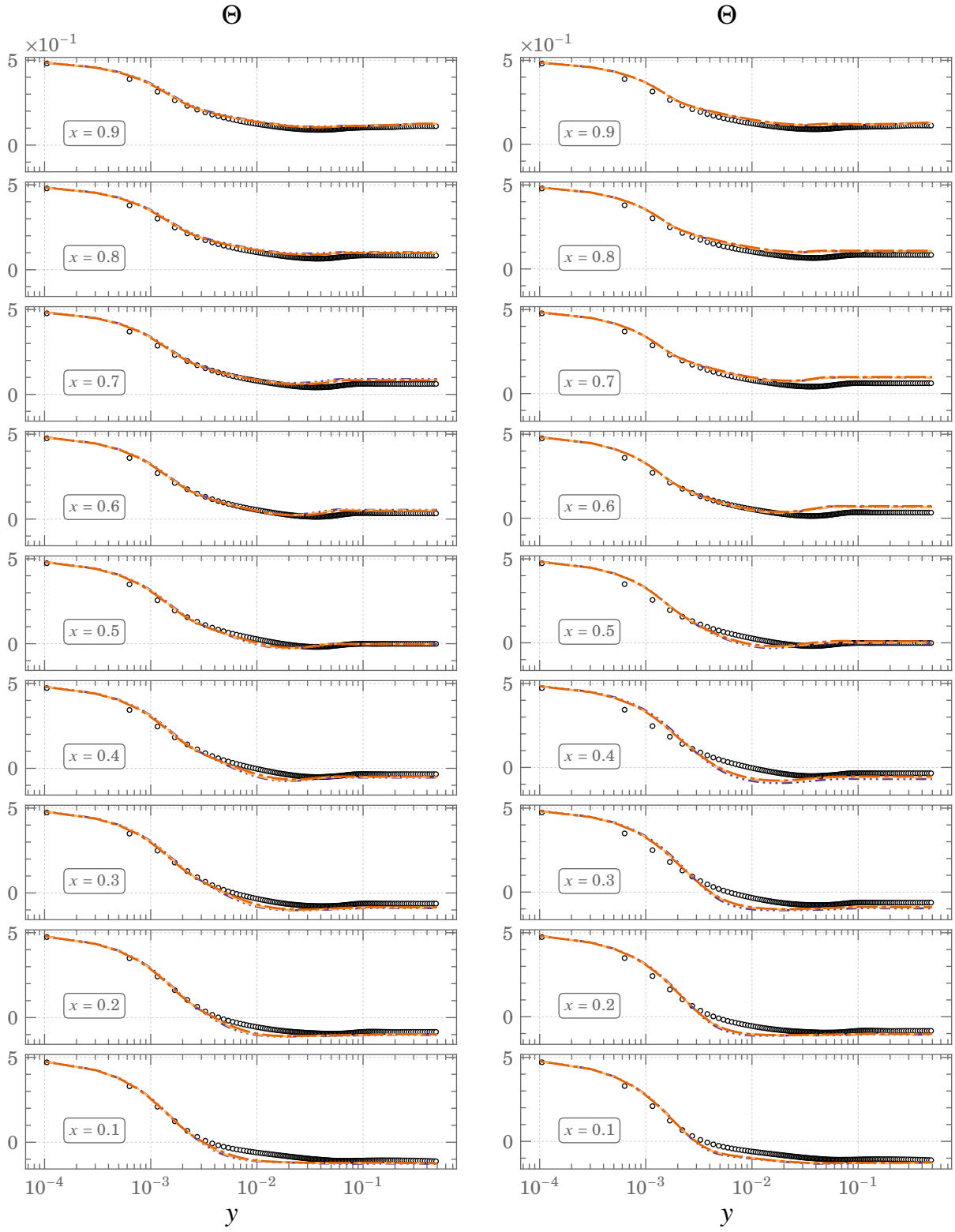

(a) Model: $k\omega$-SST

(b) Model: BL-v^2/k

Figure 4.22.: Mean profiles of Temperature at $Ra \times 10^{11}$

○ ○ ○ *DNS* *FBE* *GGDH* *SGDH*

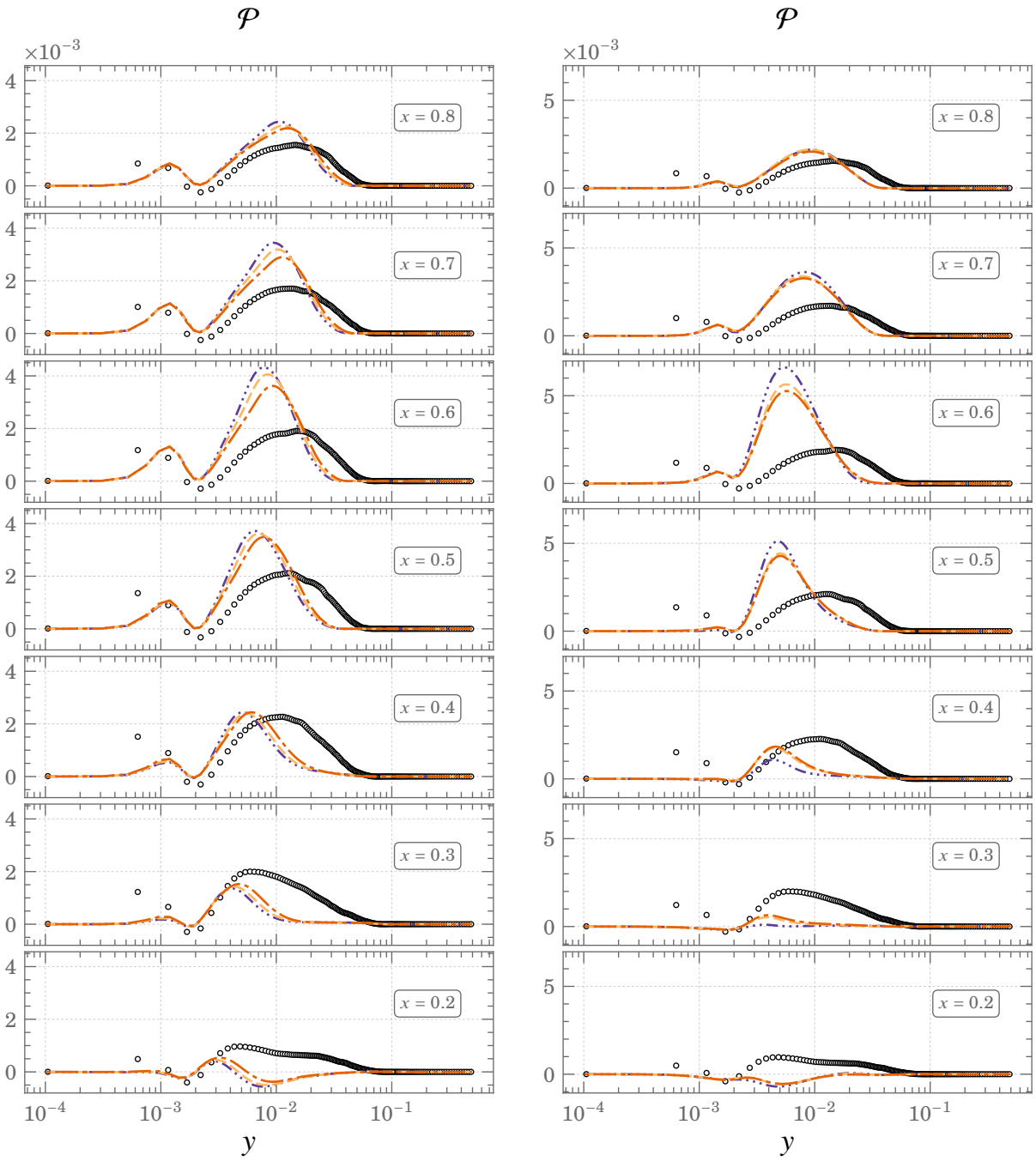

(a) Model: $k\omega$-SST

(b) Model: BL-v^2/k

Figure 4.23.: Dynamic production, $\mathcal{P}$ for $Ra \times 10^{11}$

○ ○ ○ *DNS* *FBE* *GGDH* *SGDH*

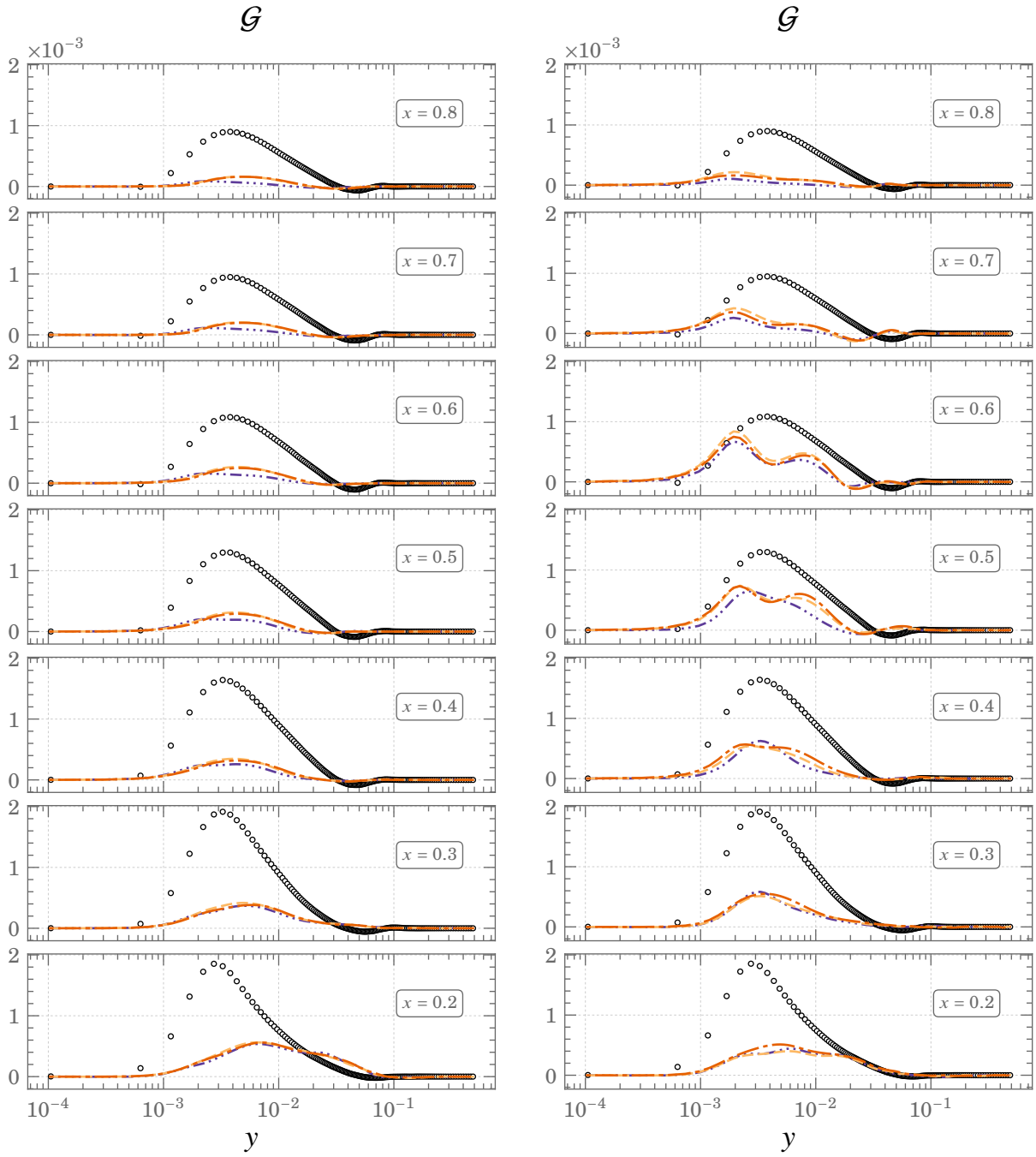

(a) Model: $k\omega$-SST

(b) Model: BL-v^2/k

Figure 4.24.: Buoyancy production, $\mathcal{G}$ for $Ra \times 10^{11}$

$\circ\ \circ\ \circ$ *DNS* — *FBE* — *GGDH* — *SGDH*

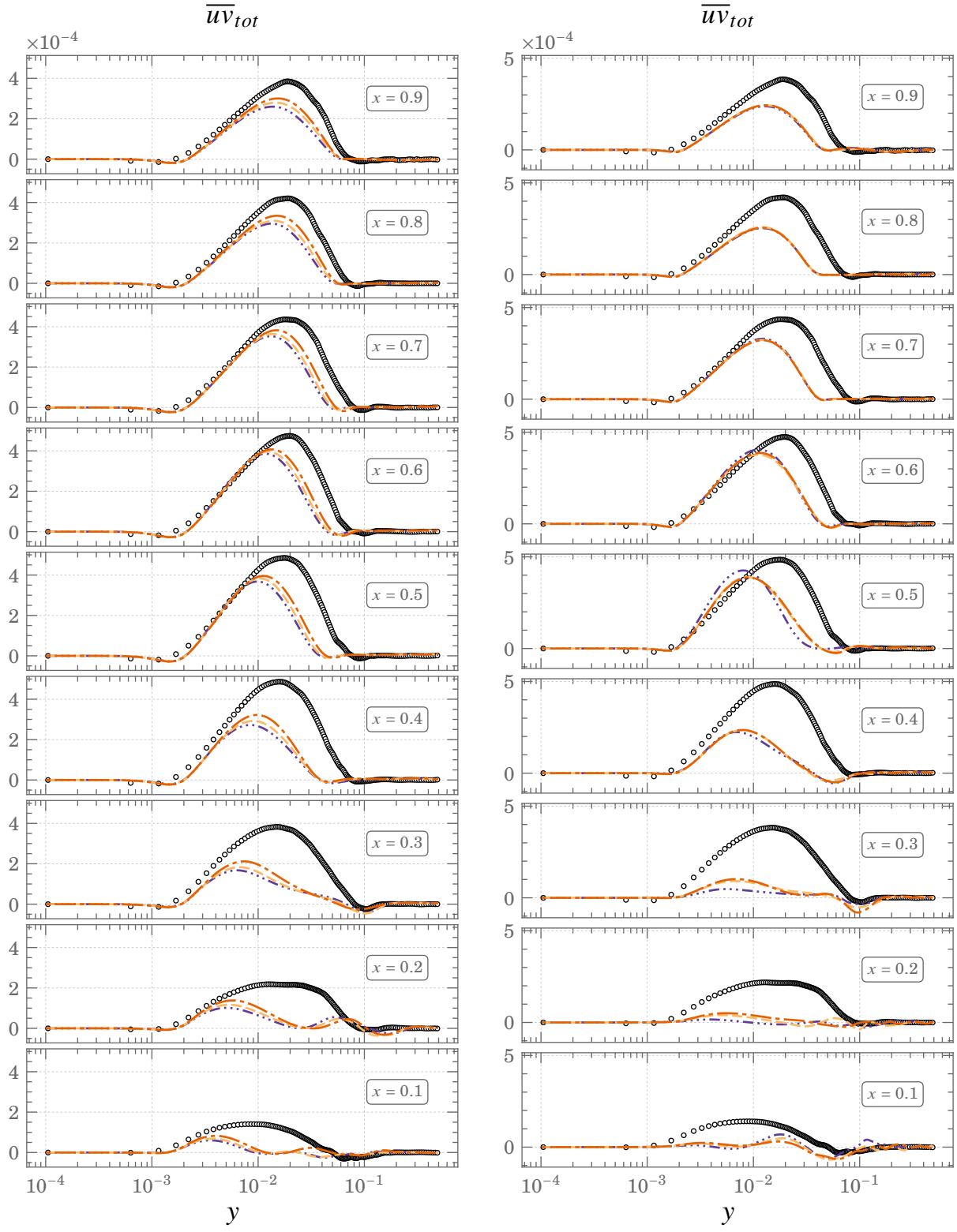

(a) Model: $k\omega$-SST

(b) Model: BL-v^2/k

Figure 4.25.: Mean profiles of $\overline{uv}$ at $Ra \times 10^{11}$

○ ○ ○ *DNS* —·— *FBE* – – – *GGDH* ···· *SGDH*

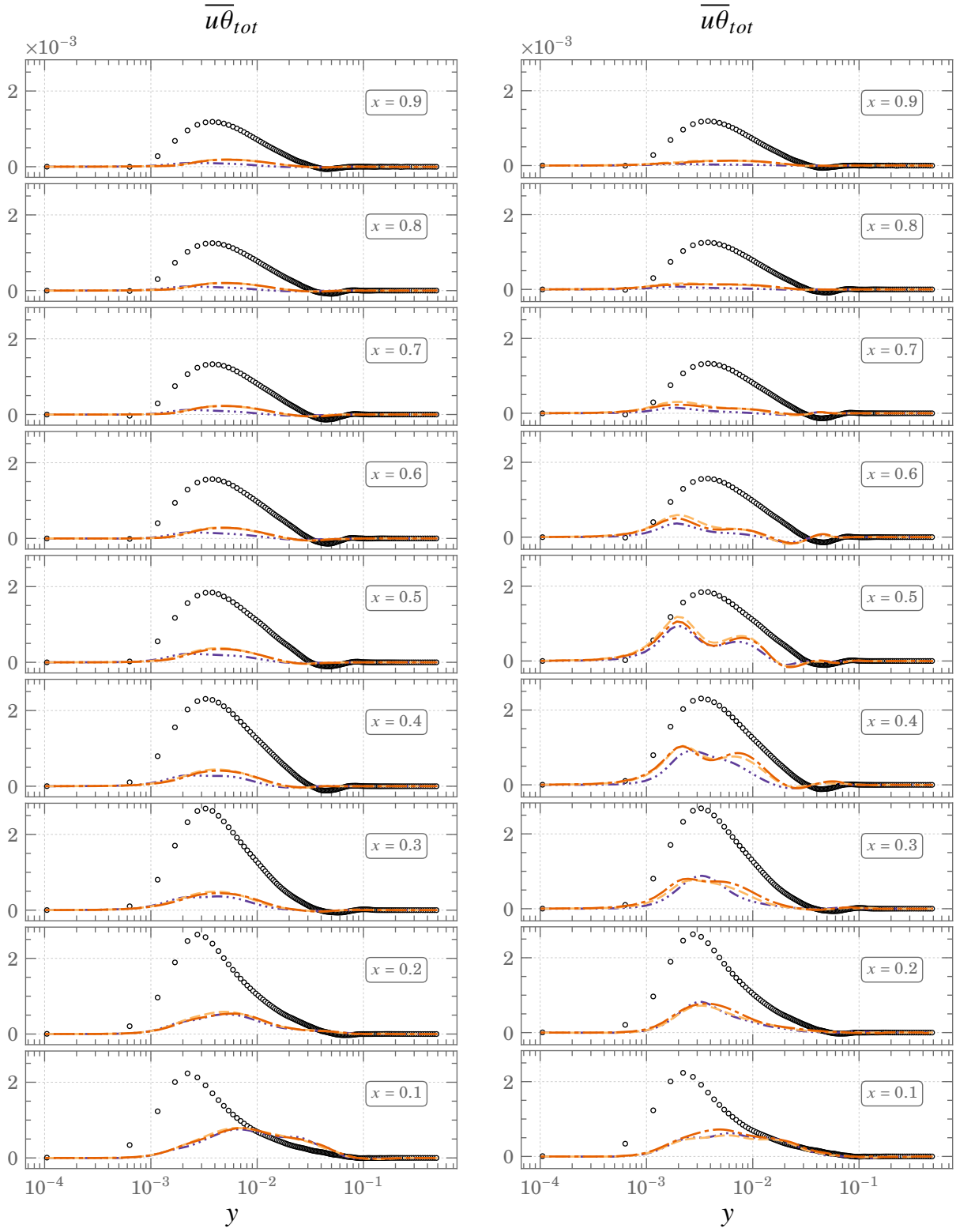

(a) Model: $k\omega$-SST

(b) Model: BL-v^2/k

Figure 4.26.: Mean profiles of $\overline{u\theta}$ at $Ra \times 10^{11}$

$\circ\ \circ\ \circ$ *DNS* — *FBE* — *GGDH* — *SGDH*

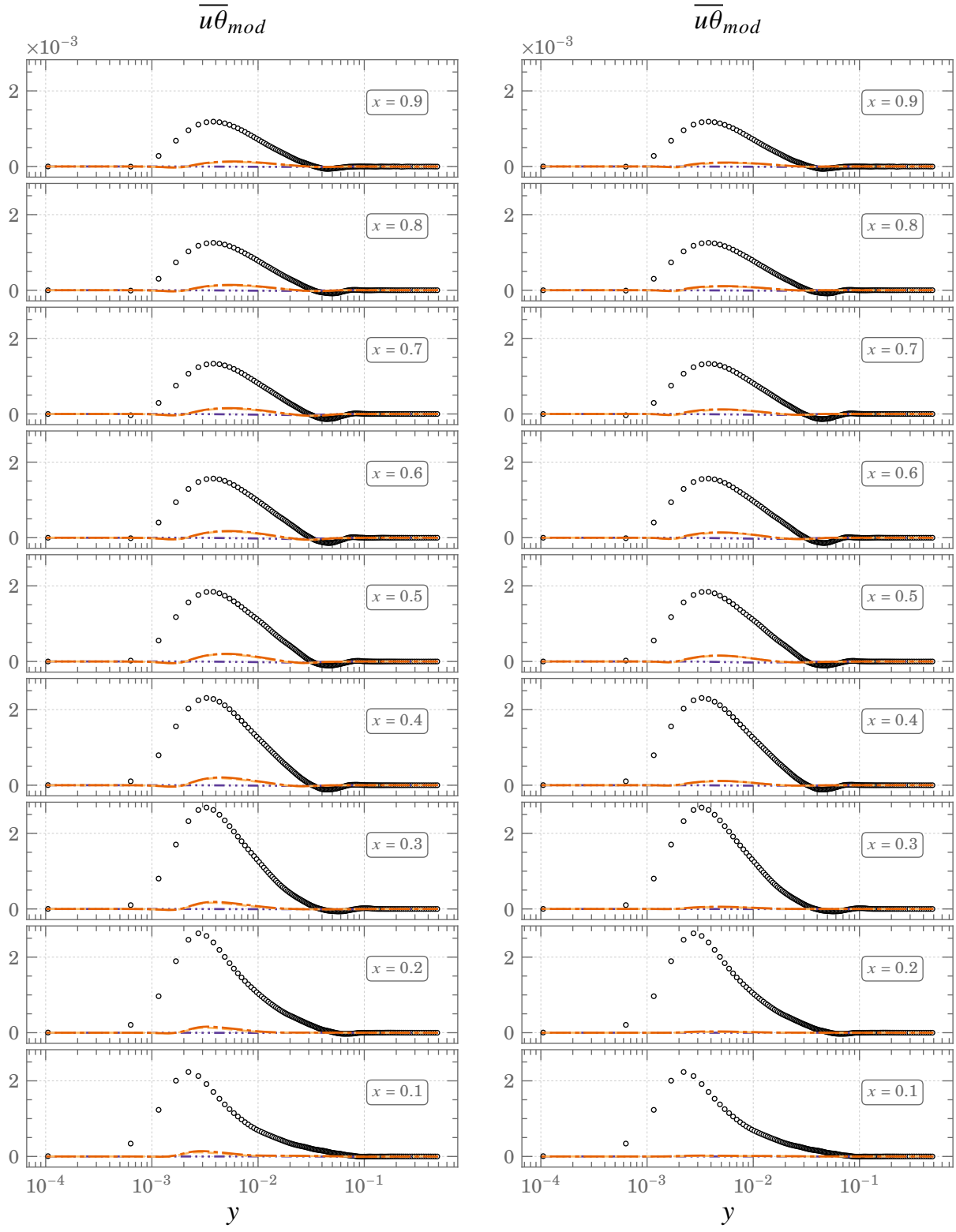

(a) Model: $k\omega$-SST

(b) Model: BL-v^2/k

Figure 4.27.: Mean profiles of modelled $\overline{u\theta}$ at $Ra \times 10^{11}$

$\circ\ \circ\ \circ$ *DNS* — *FBE* — *GGDH* — *SGDH*

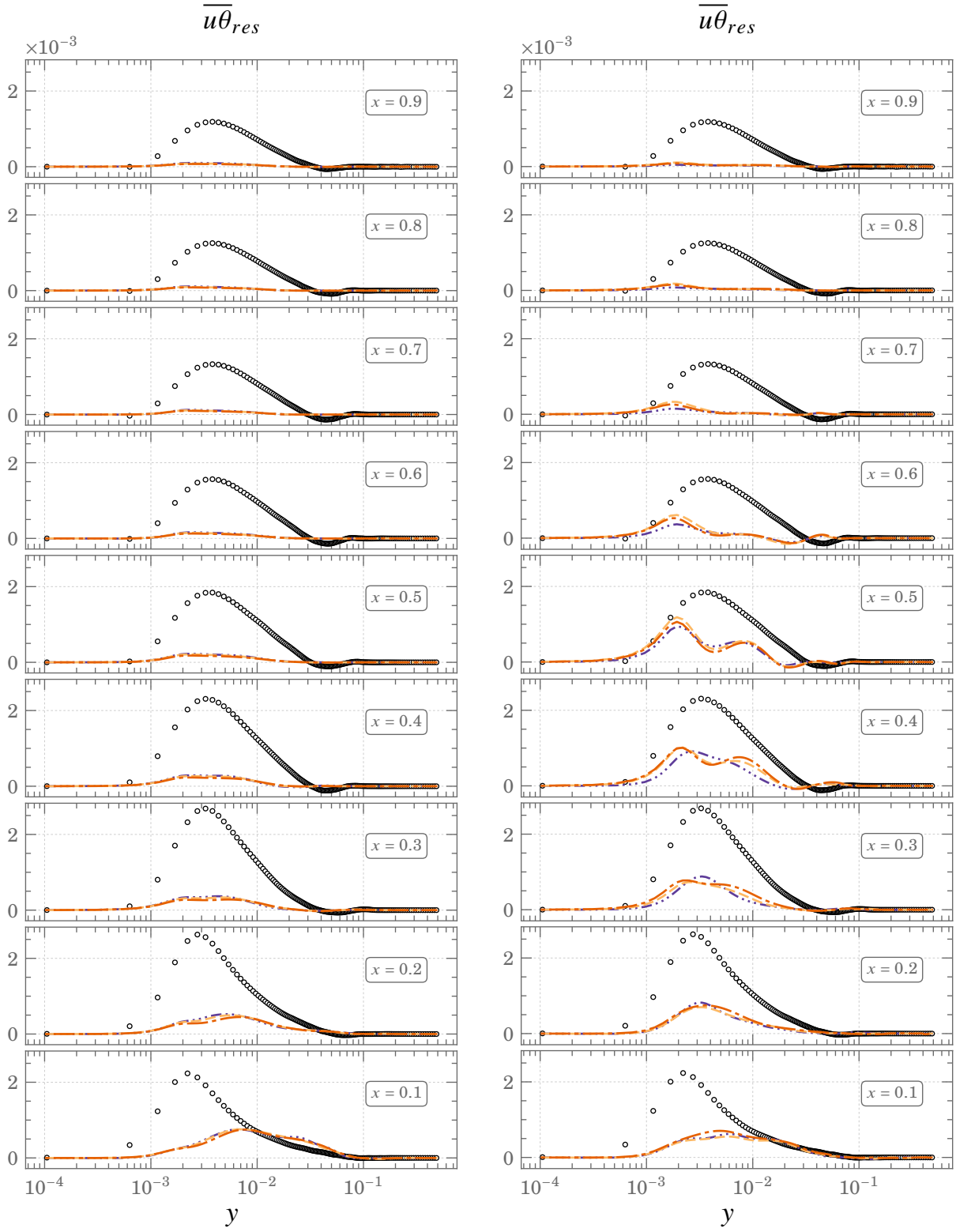

(a) Model: $k\omega$-SST

(b) Model: BL-v^2/k

Figure 4.28.: Mean profiles of resolved $\overline{u\theta}$ at $Ra \times 10^{11}$

○ ○ ○ *DNS* *FBE* *GGDH* *SGDH*

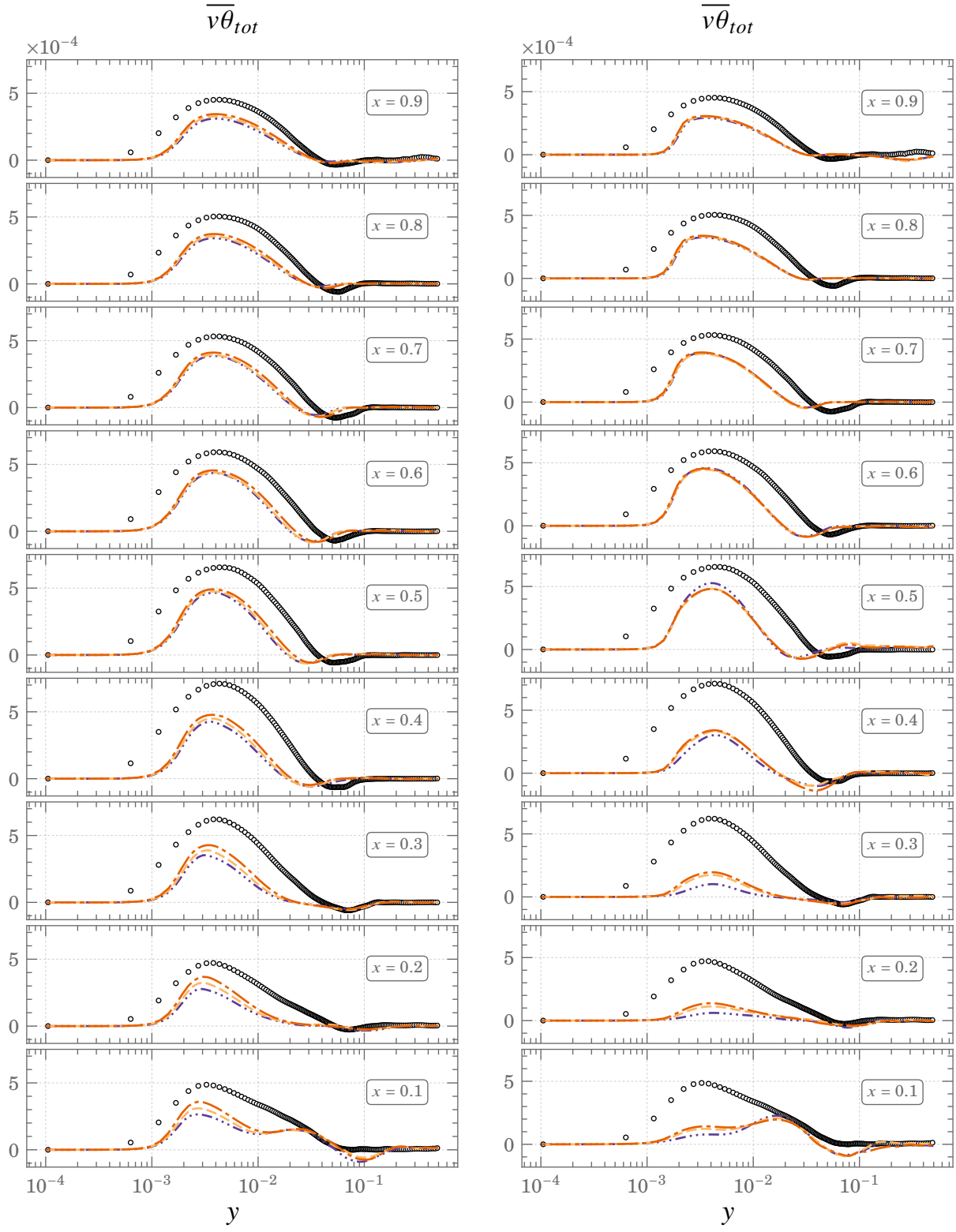

(a) Model: $k\omega$-SST

(b) Model: BL-v^2/k

Figure 4.29.: Mean profiles of $\overline{v\theta}$ at $Ra \times 10^{11}$

○ ○ ○ *DNS* —·— *FBE* – – – *GGDH* ···· *SGDH*

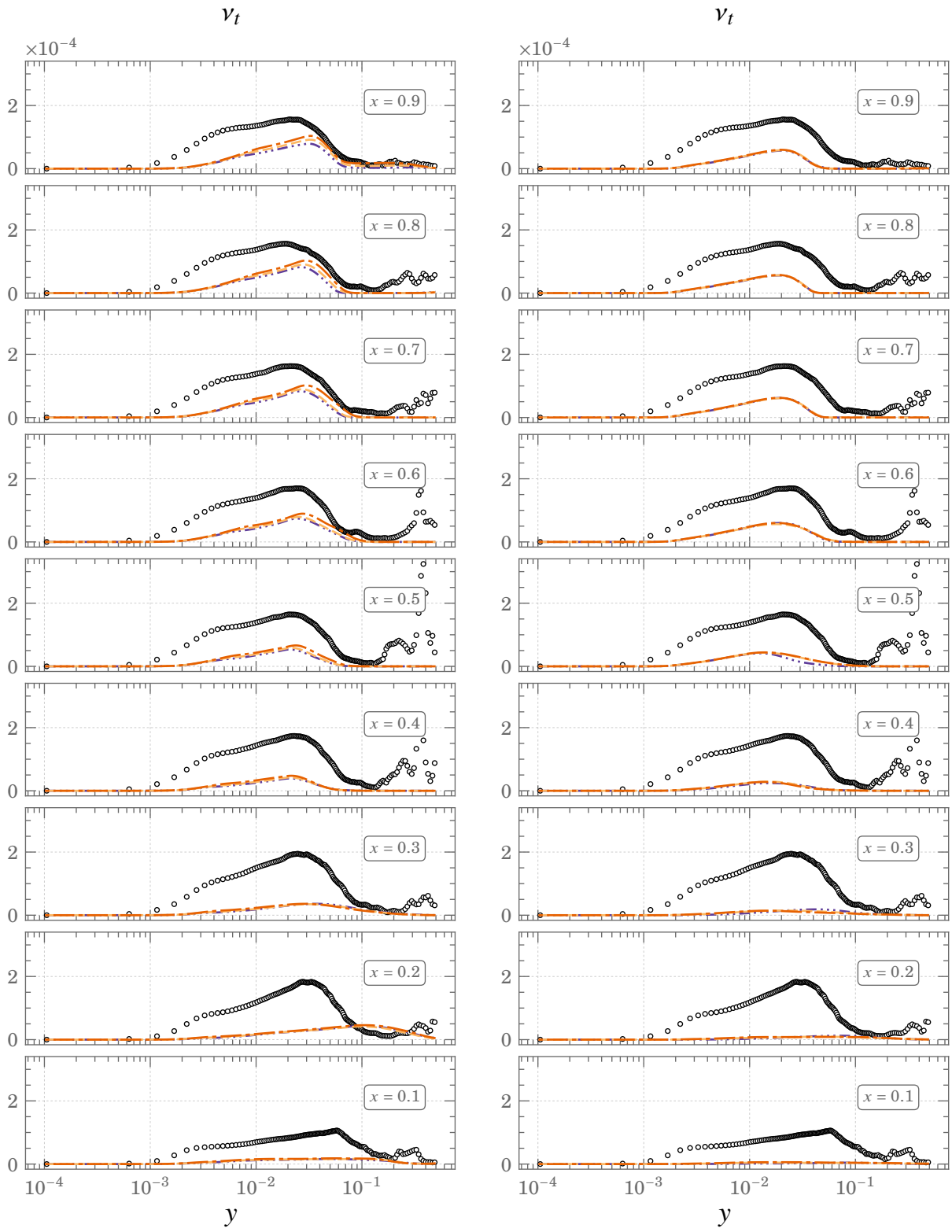

(a) Model: $k\omega$-SST

(b) Model: BL-v^2/k

Figure 4.30.: Mean profiles of ν_t at $Ra \times 10^{11}$

$\circ\ \circ\ \circ$ *DNS* —·— *FBE* – – – *GGDH* ···· *SGDH*

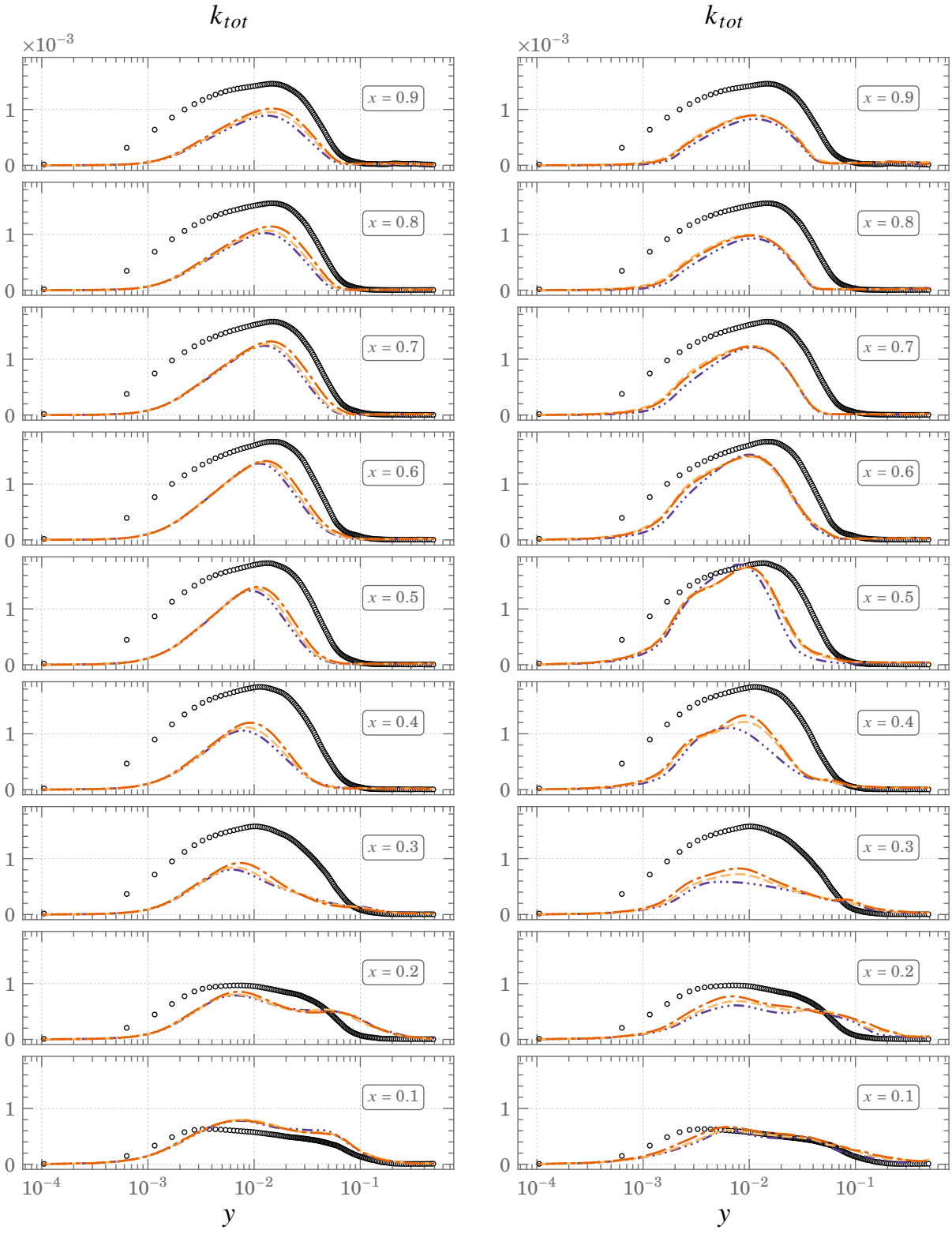

(a) Model: $k\omega$-SST

(b) Model: BL-v^2/k

Figure 4.31.: Mean profiles of total turbulent kinetic energy, k_{tot}, at $Ra \times 10^{11}$
○ ○ ○ *DNS* — · — *FBE* – – – *GGDH* ··· *SGDH*

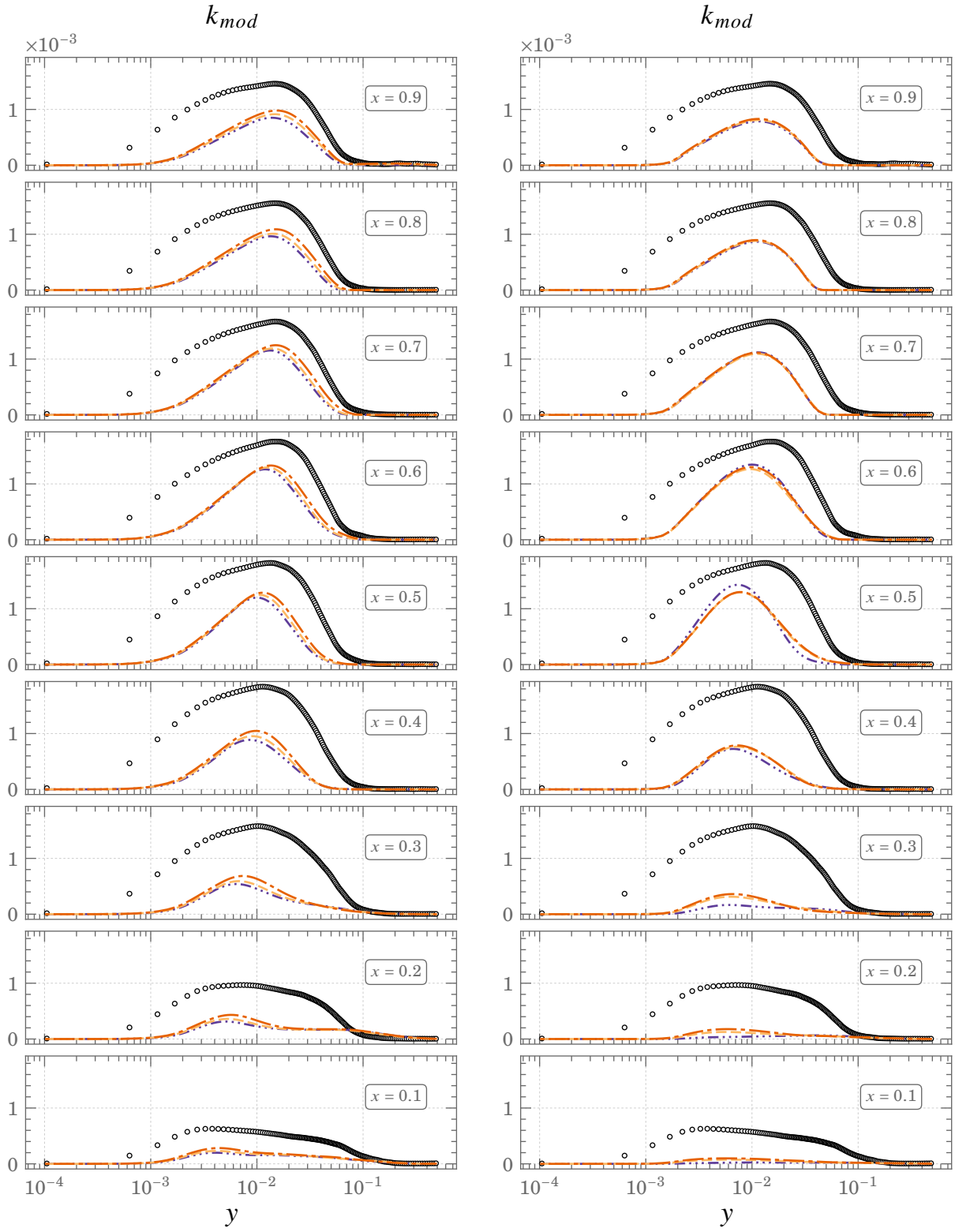

(a) Model: $k\omega$-SST

(b) Model: BL-v^2/k

Figure 4.32.: Mean profiles of modelled turbulent kinetic energy, k_{mod}, at $Ra \times 10^{11}$
○ ○ ○ *DNS* *FBE* *GGDH* *SGDH*

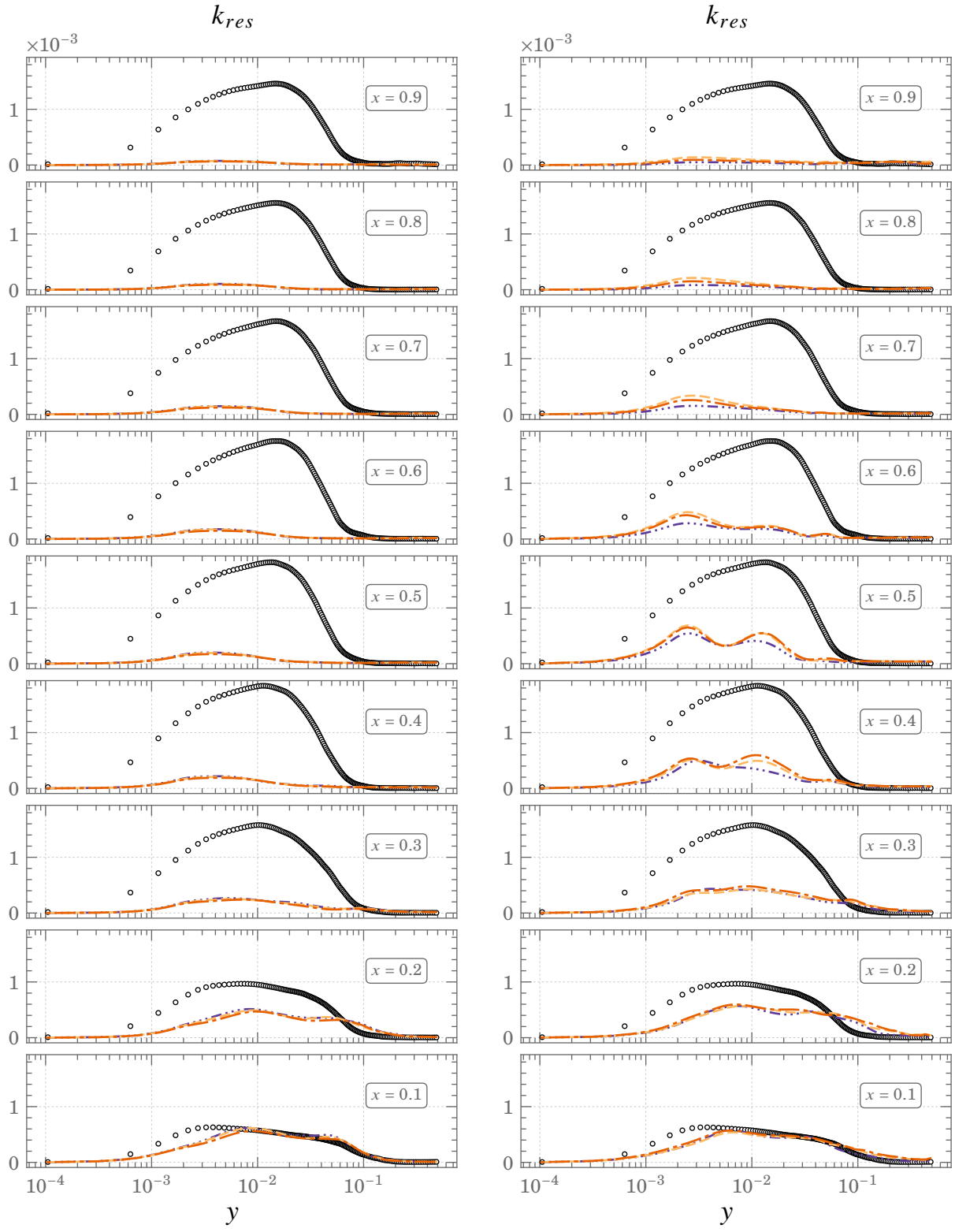

(a) Model: $k\omega$-SST

(b) Model: BL-v^2/k

Figure 4.33.: Mean profiles of resolved urbulent kinetic energy, k_{res}, at $Ra \times 10^{11}$
○ ○ ○ *DNS* *FBE* *GGDH* *SGDH*

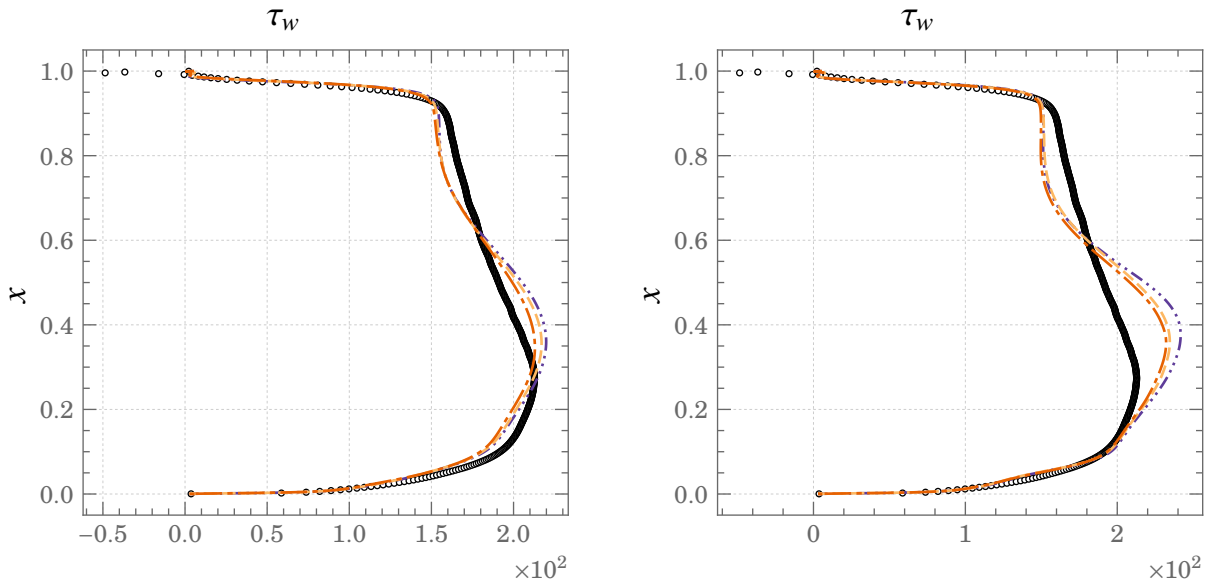

(a) Model: $k\omega$-SST (b) Model: BL-v^2/k

Figure 4.34.: Profiles of Wall shear stress, τ_w, at the hot wall for $Ra \times 10^{11}$
○ ○ ○ *DNS* *FBE* *GGDH* *SGDH*

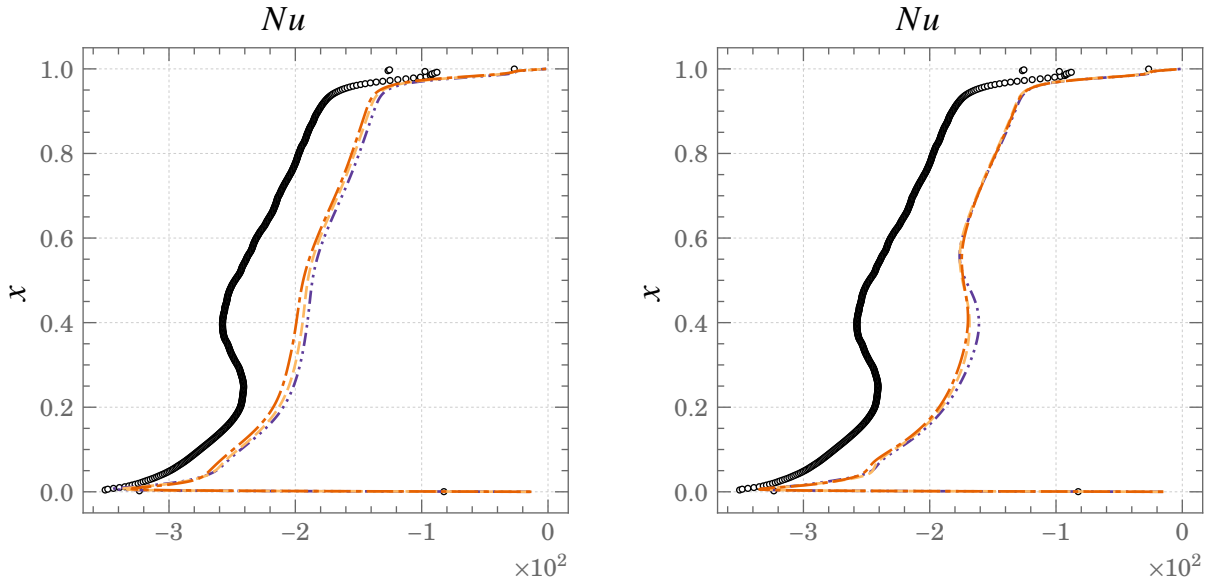

(a) Model: $k\omega$-SST (b) Model: BL-v^2/k

Figure 4.35.: Profiles of Nusselt number at the hot wall for $Ra \times 10^{11}$
○ ○ ○ *DNS* *FBE* *GGDH* *SGDH*

4.4. Note on the forms of buoyancy production terms in the turbulence scale determining equations

In considering two-equation turbulence closure models, the first equation solved is generally the transport equation for kinetic energy, k and a second transport equation dependant on the choice of the model. It is general consensus to include the production term for buoyancy in the transport equation for kinetic energy.

$$\mathcal{G} = -\beta g_i \overline{u_i \theta}$$

with an appropriate model for the heat fluxes. However, the form of the production term for buoyancy in the second transported quantity is not generally agreed upon or in some cases not accounted for outright. Consider for the case where the second transport equation is the dissipation rate, ε. The definition of the buoyancy production term in the dissipation rate equation can take the forms as described below,

1. **Analogous to the shear production,** $\mathcal{P}_\varepsilon$, the buoyancy production can be defined as,

$$\mathcal{G}_\varepsilon = C_{\varepsilon 3} \frac{1}{\tau} \mathcal{G} \tag{4.38}$$

   where $C_{\varepsilon 3}$ is a constant generally taken to be equal to $C_{\varepsilon 1} (= 1.44)$.

2. **Based on the flux Richardson number,** R_f The constant $C_{\varepsilon 3}$ is by nature an empirical correction term (Rodi, 1984) and has to be calibrated depending on the flow regime under study. One way to achieve this is through the introduction of a flux Richardson number, R_f, defined as the ratio of buoyancy production and shear production.

$$R_f = -\frac{\mathcal{G}}{\mathcal{P}}$$

The production terms in the dissipation rate equation are redefined as,

$$\mathcal{G}_\varepsilon = C_{\varepsilon 1}\frac{1}{\tau}(\mathcal{P}+\mathcal{G})(1+C_{\varepsilon 3}R_f)$$

Rodi (1984) noted that the above definition, along with the use of the SGDH model would mean that $C_{\varepsilon 3}$ would have to be close to 1.0 for horizontal shear layers (where the wall normal velocity is aligned with the gravity vector) and close to 0.0 for vertical shear layers (where the wall normal velocity is normal to the gravity vector). To account for these flow regimes, Rodi (1984) redefined the flux Richardson number as,

$$R_f = -\frac{\mathcal{G}_{\overline{vv}}}{\mathcal{P}+\mathcal{G}}$$

where, $\mathcal{G}_{\overline{vv}} = 2\mathcal{G}$ is the wall normal buoyancy production, thus allowing to use a single value for the constant $C_{\varepsilon 3} = 0.8$.

3. **Accounting for the effect of stratification** As suggested in Viollet (1987) and Viollet et al. (1983), the effect of stratification can be taken into account. In the presence of stable stratification, the buoyancy production term, $\mathcal{G}_k$, is negative and acts as a sink hence damping turbulence — $C_{\varepsilon 3} = 0$ in Equation (4.38). While in the presence of unstable stratification, the buoyancy production term is positive and acts as a source hence enhancing turbulence — $C_{\varepsilon 3} = 1.44$ in Equation (4.38). In effect, the buoyancy source term is considered only when it is positive (Fletcher et al., 1994; Sinai et al., 1995; Novozhilov, 2001) and can be written as follows,

$$\mathcal{G}_\varepsilon = C_{\varepsilon 3}\frac{1}{\tau}\max(\mathcal{G},0)$$

, with $C_{\varepsilon 3} = C_{\varepsilon 1} = 1.44$.

Owing to the test cases considered and keeping in line with the goals of the MONACO_2025 project, in this thesis the choice is made to use the form of the buoyancy source term ac-

counting for stratification in the second transport equation estimating the turbulence scales.

4.4.1. Formulation of the buoyancy production term in the transport equation for specific dissipation rate, ω

The specific dissipation rate transport equation in the $k\omega$-SST model writes,

$$\frac{D\omega}{Dt} = \frac{\gamma}{\nu_t}\mathcal{P} + \mathcal{G}_\omega^{SST} - \beta\omega^2 + \frac{\partial}{\partial x_j}\left[(\nu + \sigma_k \nu_t)\frac{\partial \omega}{\partial x_j}\right] + 2(1-F_1)\sigma_{\omega 2}\frac{1}{\omega}\frac{\partial k}{\partial x_i}\frac{\partial \omega}{\partial x_i} \tag{4.39}$$

The $k\omega$-SST model (as described in Section 2.6.4) is formulated as a blending between the $k-\omega$ (Wilcox, 1988) and $k-\epsilon$ (Jones et al., 1972) models.

$$\frac{D}{Dt}\omega^{\text{SST}} = F_1\frac{D}{Dt}\omega^{k\omega} + (1-F_1)\frac{D}{Dt}\omega^{k\varepsilon} \tag{4.40}$$

, where F_1 is the blending function, $\omega^{k\omega}$ is the contribution of the $k-\omega$ (Wilcox, 1988) model, and $\omega^{k\varepsilon}$ is the contribution of the $k-\epsilon$ (Jones et al., 1972) model. The $\omega^{k\varepsilon}$ term is obtained through a change of variable,

$$\omega = \frac{\varepsilon}{C_\mu k}$$

$$\frac{D\omega^{k\varepsilon}}{Dt} = \frac{1}{C_\mu k}\frac{D\varepsilon}{Dt} - \frac{\varepsilon}{C_\mu k^2}\frac{Dk}{Dt} \tag{4.41}$$

To illustrate using the shear production term $\mathcal{P}_\omega$ as an example, using Equation (4.41) in Equation (4.40) one can write,

$$\mathcal{P}_\omega^{\text{SST}} = F_1\mathcal{P}_\omega^{k\omega} + (1-F_1)\underbrace{\left[\frac{1}{C_\mu k}\mathcal{P}_\varepsilon - \frac{\varepsilon}{C_\mu k^2}\mathcal{P}\right]}_{\mathcal{P}_\omega^{k\varepsilon}}$$

Replacing $\mathcal{P}_\omega^{k\omega} = \frac{\gamma_1}{\nu_t}\mathcal{P}$ and $\mathcal{P}_\varepsilon = C_{\varepsilon 1}\frac{\varepsilon}{k}\mathcal{P}$ one can obtain the familiar representation of the

shear production term as seen in Equation (4.39).

$$\mathcal{P}_\omega^{\mathrm{SST}} = F_1 \frac{\gamma_1}{\nu_t}\mathcal{P} + (1-F_1)\left[\frac{1}{C_\mu k} C_{\varepsilon 1}\frac{\varepsilon}{k}\mathcal{P} - \frac{\varepsilon}{C_\mu k^2}\mathcal{P}\right]$$

with $\nu_t = C_\mu k^2/\varepsilon$:

$$\mathcal{P}_\omega^{\mathrm{SST}} = F_1 \frac{\gamma_1}{\nu_t}\mathcal{P} + (1-F_1)\left[\frac{C_{\varepsilon 1}}{\nu_t}\mathcal{P} - \frac{1}{\nu_t}\mathcal{P}\right]$$

$$\mathcal{P}_\omega^{\mathrm{SST}} = F_1 \frac{\gamma_1}{\nu_t}\mathcal{P} + (1-F_1)\frac{(C_{\varepsilon 1}-1)}{\nu_t}\mathcal{P}$$

with $C_{\varepsilon 1} - 1 = \gamma_2$,

$$\mathcal{P}_\omega^{\mathrm{SST}} = \frac{1}{\nu_t}\mathcal{P}\left[F_1\gamma_1 + (1-F_1)\gamma_2\right]$$

$$\mathcal{P}_\omega^{\mathrm{SST}} = \frac{\gamma}{\nu_t}\mathcal{P}$$

This blending of the models has to be revisited when considering the form buoyancy source term chosen.

$$\mathcal{G}_\omega^{\mathrm{SST}} = F_1\mathcal{G}_\omega^{k\omega} + (1-F_1)\underbrace{\left[\frac{1}{C_\mu k}\mathcal{G}_\varepsilon - \frac{\varepsilon}{C_\mu k^2}\mathcal{G}\right]}_{\mathcal{G}_\omega^{k\varepsilon}} \tag{4.42}$$

$$\mathcal{G}_\omega^{\mathrm{SST}} = F_1 \frac{\gamma_1}{\nu_t}\max(\mathcal{G},0) + (1-F_1)\left[\frac{1}{C_\mu k} C_{\varepsilon 1}\frac{\varepsilon}{k}\max(\mathcal{G},0) - \frac{\varepsilon}{C_\mu k^2}\mathcal{G}\right]$$

$$\begin{aligned}\mathcal{G}_\omega^{\mathrm{SST}} = {} & F_1 \frac{\gamma_1}{\nu_t}\max(\mathcal{G},0) \\ & + (1-F_1)\left[\frac{1}{C_\mu k} C_{\varepsilon 1}\frac{\varepsilon}{k}\max(\mathcal{G},0) - \frac{\varepsilon}{C_\mu k^2}\max(\mathcal{G},0) + \frac{\varepsilon}{C_\mu k^2}\max(\mathcal{G},0) - \frac{\varepsilon}{C_\mu k^2}\mathcal{G}\right]\end{aligned}$$

with $\nu_t = C_\mu k^2/\varepsilon$:

$$\mathcal{G}_\omega^{\mathrm{SST}} = F_1 \frac{\gamma_1}{\nu_t} \max(\mathcal{G}, 0) + (1 - F_1) \left[\frac{(C_{\varepsilon 1} - 1)}{\nu_t} \max(\mathcal{G}, 0) + \frac{1}{\nu_t} \max(\mathcal{G}, 0) - \frac{1}{\nu_t} \mathcal{G} \right]$$

with $C_{\varepsilon 1} - 1 = \gamma_2$,

$$\mathcal{G}_\omega^{\mathrm{SST}} = \frac{1}{\nu_t} \max(\mathcal{G}, 0) \left[F_1 \gamma_1 + (1 - F_1) \gamma_2 \right] + \frac{(1 - F_1)}{\nu_t} \left[\max(\mathcal{G}, 0) - \mathcal{G} \right]$$

$$\mathcal{G}_\omega^{\mathrm{SST}} = \frac{\gamma}{\nu_t} \max(\mathcal{G}, 0) + \frac{(1 - F_1)}{\nu_t} \left[\max(\mathcal{G}, 0) - \mathcal{G} \right]$$

- **Remark**:

  1. It is interesting to note that *by definition* the influence of buoyancy cannot be completely ignored exclusively in the transport equation for specific dissipation rate of the $k\omega$-SST model. Replacing, $\mathcal{G}_\omega^{k\omega} = 0$ and $\mathcal{G}_\varepsilon = 0$ in Equation (4.42) shows that the buoyancy term takes the form,

     $$\mathcal{G}_\omega^{\mathrm{SST}} = -\frac{(1 - F_1)}{\nu_t} \mathcal{G}$$

     This term is effective only when the model is in $k - \varepsilon$ mode. It can be viewed as sort of a correction term for buoyancy effects in $k - \varepsilon$ mode.

  2. This formulation of the source terms is available as an user option in Ansys FLUENT.

4.4.2. Comparison of the formulation of the source terms in the $k\omega$-SST model

This section aims to highlight the importance of the formulation of the buoyancy production term in the transport equation for specific dissipation rate of the $k\omega$-SST model. For the purposes of demonstrating the issues caused by the choice of the formulation, only the SGDH closure for the heat fluxes are illustrated in the following plots. The formulations of

the source terms compared are both based on the idea of accounting for the stratification which are as follows,

1. **Without** consideration for the blending in the $k\omega$-SST model:

$$\mathcal{G}_\omega = \frac{\gamma}{\nu_t} \max(\mathcal{G}, 0) \tag{4.43}$$

2. **With** consideration for the blending in the $k\omega$-SST model:

$$\mathcal{G}_\omega^{\text{SST}} = \frac{\gamma}{\nu_t} \max(\mathcal{G}, 0) + \frac{(1 - F_1)}{\nu_t} \left[\max(\mathcal{G}, 0) - \mathcal{G}\right] \tag{4.44}$$

Both formulations provide comparable results for the mean velocity and mean temperature as seen in Figure 4.36. However, larger differences arise when comparing the modelled kinetic energies as seen in Figure 4.37a. The $\mathcal{G}_\omega$ formulation predicts higher levels of modelled kinetic energy throughout the height of the cavity as compared to the $\mathcal{G}_\omega^{\text{SST}}$ formulation. In addition, although the prediction of the specific dissipation rate, ω, for the $\mathcal{G}_\omega$ formulation is inline with the reference DNS data, computed as $\omega = \varepsilon / C_\mu k$, it leads to the issue of high levels of turbulent viscosity towards the centre of the cavity. Since the core of the cavity is laminar, this level of turbulent viscosity is non-physical. The fixes this issue thanks to the proper consideration of the blending between $k - \omega$ and $k - \varepsilon$ models. It can also be noted from Figure 4.39a that the $\mathcal{G}_\omega^{\text{SST}}$ formulation allows the model to transition from $k - \omega$ to $k - \varepsilon$, where the blending function remains 0, and hence in $k - \varepsilon$ mode, at the centre of the cavity which is in stark contrast to the blending function predicted by the $\mathcal{G}_\omega$ formulation.

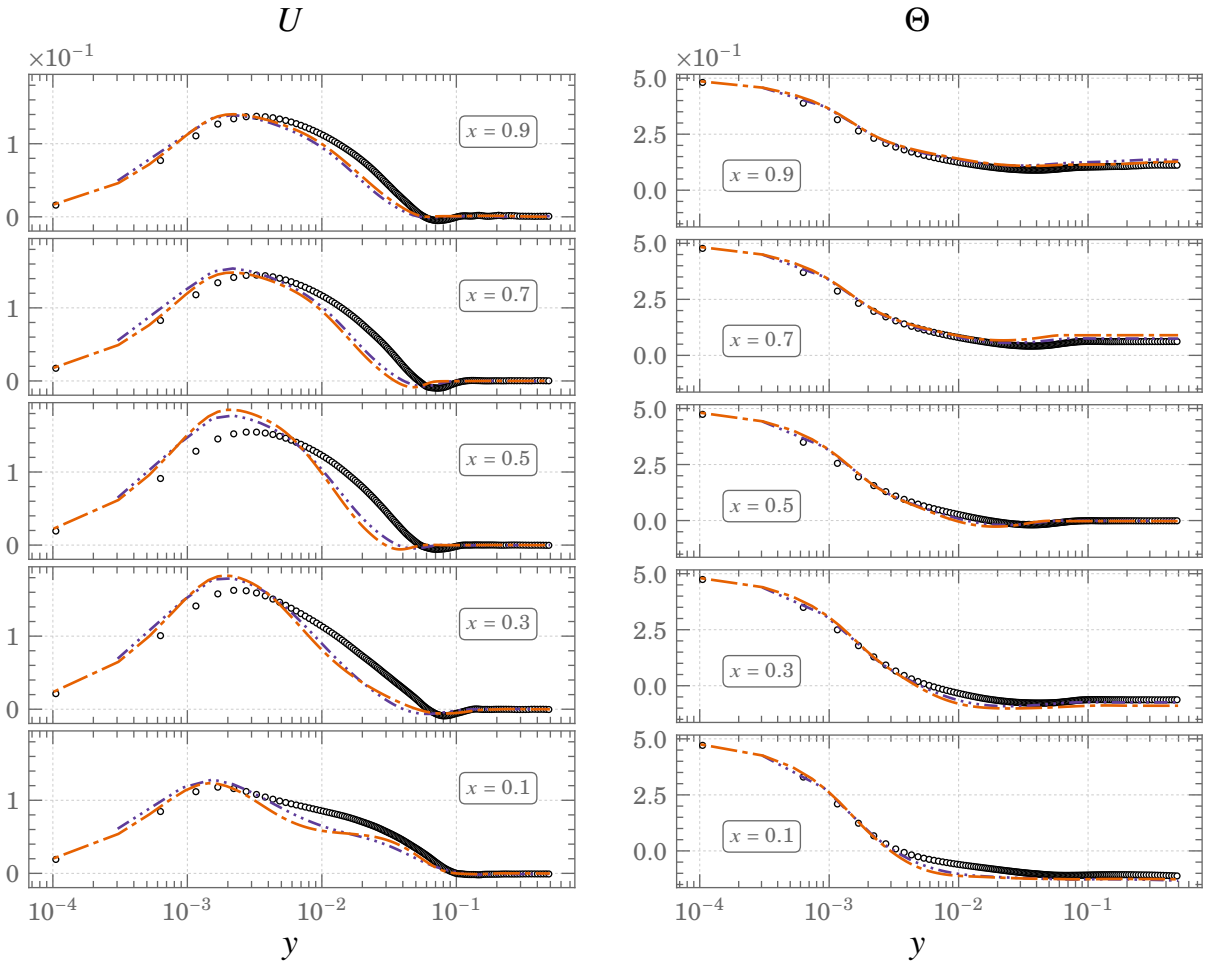

(a) Mean velocity, U

(b) Mean Temperature, Θ

Figure 4.36.: Mean profiles of Velocity and Temperature for SGDH heat flux closure at $Ra \times 10^{11}$ ∘ ∘ ∘ DNS G_ω^{SST} $G_\omega^{k\omega}$

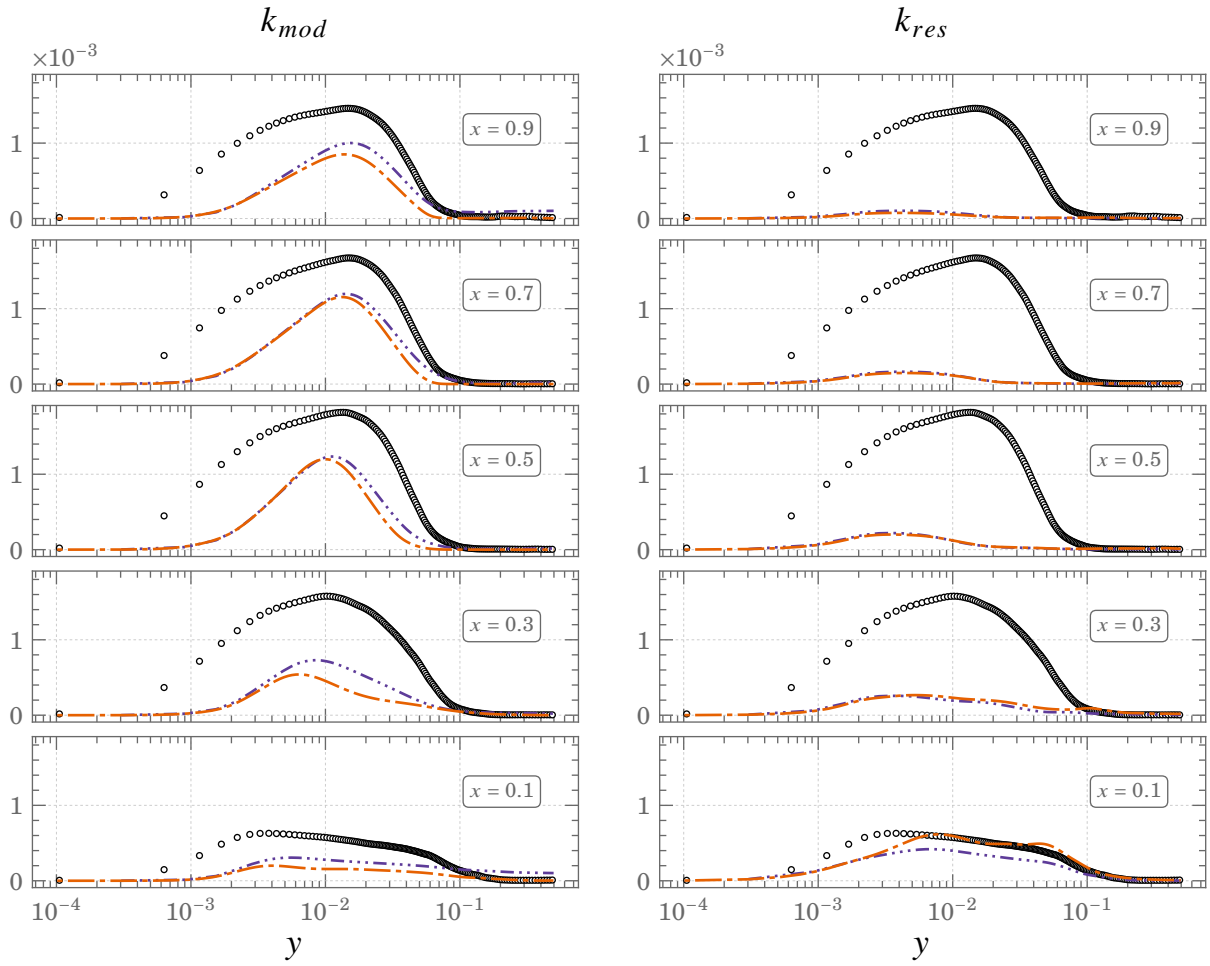

(a) Total kinetic energy, k_{tot}

(b) Turbulent viscosity, ν_t

Figure 4.37.: Profiles of the modelled and resolved total kinetic energy for SGDH heat flux closure at $Ra \times 10^{11}$ ∘ ∘ ∘ DNS G_ω^{SST} $G_\omega^{k\omega}$

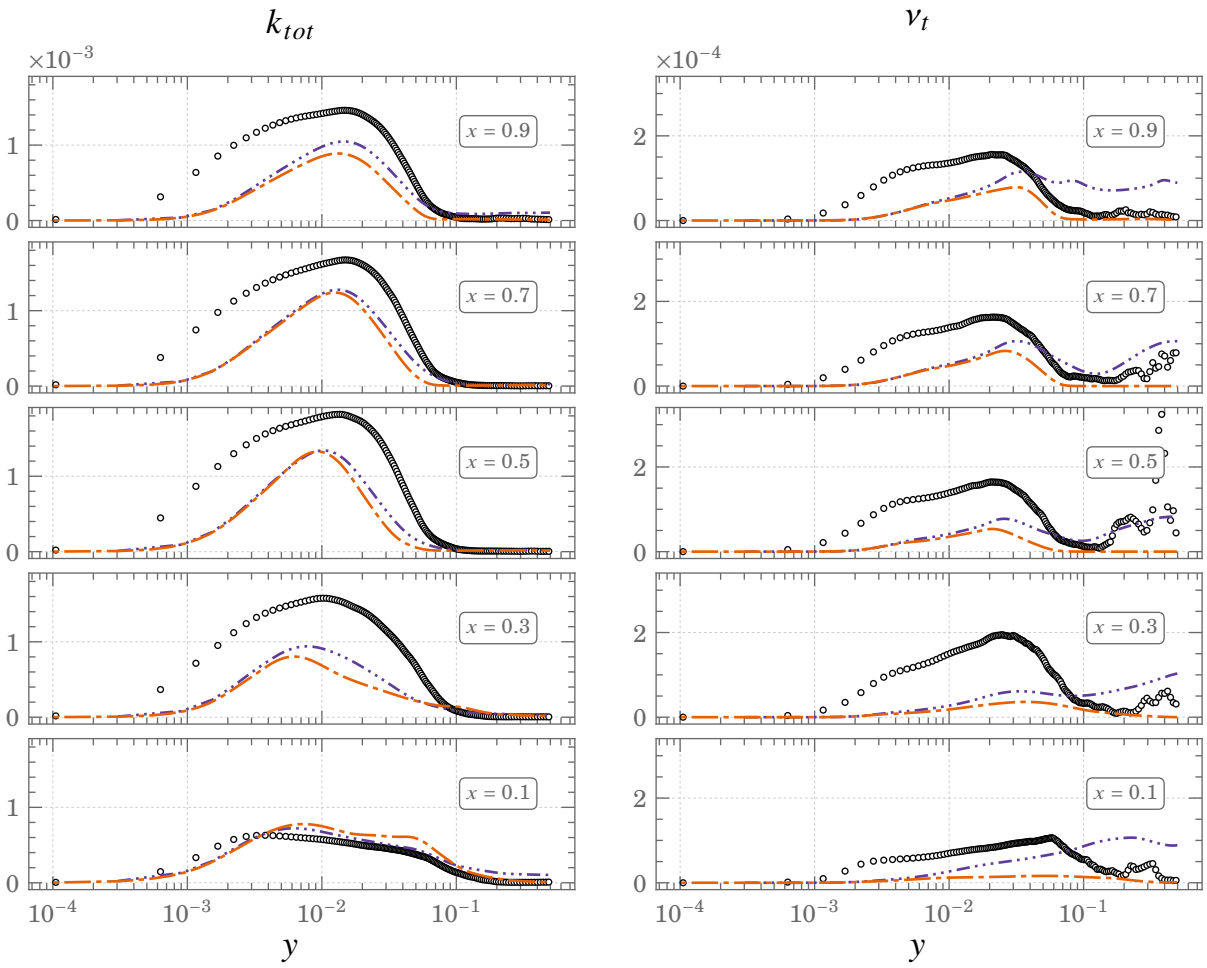

(a) Total kinetic energy, k_{tot}

(b) Turbulent viscosity, ν_t

Figure 4.38.: Profiles of the total kinetic energy and turbulent viscosity for SGDH heat flux closure at $Ra \times 10^{11}$ ∘ ∘ ∘ DNS G_ω^{SST} $G_\omega^{k\omega}$

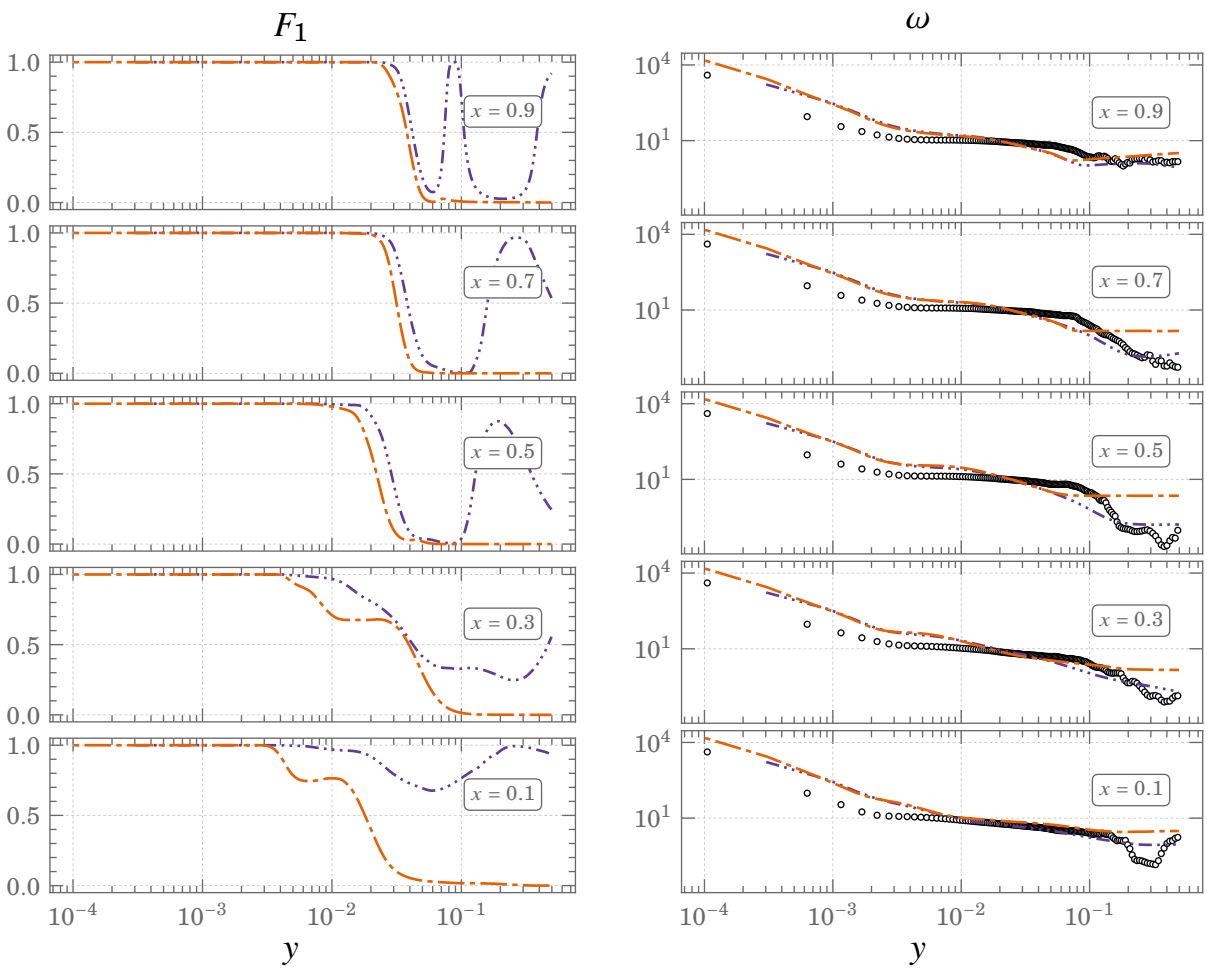

(a) Mean velocity, U

(b) Mean Temperature, Θ

Figure 4.39.: Profiles of the blending function, F_1 and Specific dissipation rate, ω for SGDH heat flux closure at $Ra \times 10^{11}$ ∘ ∘ ∘ DNS G_ω^{SST} $G_\omega^{k\omega}$

4.5. Chapter summary

The developments carried out during the course of the MONACO_2025 project in regards to the RANS modelling of natural convection flows were presented in this chapter. To demonstrate the need for better accountability of buoyancy effects in the commonly used RANS models, a baseline study is performed. It was demonstrated that the Full buoyancy extended model improves the balance between the terms in the transport equations of momentum and energy leading to better predictions of mean statistics. These tests were first performed on the differentially heated vertical channel (Kis et al., 2014) and then the model performance is assessed using the differentially heated square cavity (Sebilleau et al., 2018). Finally a detailed examination of the source terms in the transport equation of the specific dissipation rate equation sheds light on the importance of their derivation. The reformulated source terms help in avoiding non-physical predictions of the turbulent viscosity owing to the correction in ω.

Chapter 5.

Development of a hybrid RANS/LES model for natural convection

In the present chapter, the development of a hybrid RANS/LES model for natural convection flows is described. Keeping mind that the reader may not be familiar with the prior works leading to the development of the hybrid method used in this thesis, some foundational concepts established in the work of Friess et al. (2015) are briefly described. The hybrid model then formulated by Manceau (2018) and further developed/reformulated in the work of Duffal (2020) is presented. The formulation of the hybrid approach based on the $k\omega$-SST model from the work of Duffal (2020) is further developed for natural convection cases. The issues specifically encountered in natural convection flows are described and solutions are developed to tackle these issues. Following this a comparison of the HTLES models with different levels of buoyancy sensitisation of the underlying RANS model is presented. Finally, the performance of the HTLES model in the square DHC is assessed in comparison to LES and the previously developed RANS models.

5.1. The HTLES approach

5.1.1. Equivalence between hybrid methods: motivations and developments

Based on the strong theoretical foundations laid by Chaouat et al. (2005) and Schiestel et al. (2005) in developing the PITM model, Fadai-Ghotbi et al. (2010a) developed the *Temporal-PITM (TPITM)* model (see Section 2.7.4). The TPITM model is motivated by the advantages of the use of temporal filtering, wherein the consistency between in the formulations of RANS and LES can be extended to cases of statistically stationary flows while hybrid RANS/LES methods based on spatial filters are, in theory, restricted to homogeneous flows. The formulation of TPITM uses a hybridisation function, $C^*_{\varepsilon 2}$, which allows for a seamless transition from RANS to LES modes as a function of the energy ratio.

$$C^*_{\varepsilon 2} = C_{\varepsilon 1} + r\,(C_{\varepsilon 2} - C_{\varepsilon 1}) \quad ; \quad r = \frac{k_{\mathrm{m}}}{k} \tag{5.1}$$

The hybridisation function notably appears in the transport equation for the dissipation rate, ε_m, which leads to some issues since the hybridisation mechanism is only indirectly affecting the transport of modelled energy k_m. Due to macro-fluctuations in the velocity gradients and consequently in production of sub-filter energy (Carpy, 2006; Fadai-Ghotbi, 2007), the necessary levels of the energy ratio could not be maintained leading to the model reverting to RANS mode. Additionally, in flows not dominated by the Kelvin-Helmholtz instability, pseudo-laminarisation was observed due to difficulties in sustaining resolved fluctuations during computations.

Faced with similar issues, Schiestel et al. (2005) proposed an averaging procedure for the terms in the sub-filter viscosity. Following the same procedure Carpy (2006) and Fadai-Ghotbi (2007) performed averaging for the production terms. Although the method resulted in promising results, Fadai-Ghotbi et al. (2010a) noted that the energy ratio observed was lower than that of the target imposed *a-priori*. This issue was tackled in the work of Friess

(2010), who introduced a dynamic procedure whereby the hybridisation function is corrected through a comparison of the observed and targetted energy ratios.

In a further step toward eliminating these problems, Friess et al. (2015) shifted the hybridisation function to the transport equation of modelled kinetic energy. This is achieved through the definition of an equivalence criteria between two hybrid approaches, i.e., establishing a relationship between the hybridisation functions of the hybrid models considered. They postulated that,

> Postulate: Two hybrid approaches based on the same closure, but using a different method of control of the energy partition, yield similar low-order statistics of the resolved velocity fields provided that they yield the same level of sub-filter energy.

Admitting of the postulate above, a *Hybrid-equivalence* (*H-equivalence*) criterion is defined in view of the statistical quantities as follows,

> *H-equivalence*: Two hybrid approaches based on the same closure are said to be *H-equivalent* if they lead to the same partition of energy in a particular situation.

Another important property considered by Friess et al. (2015) is that of *Self-consistency of hybrid methods*, which says,

> *Self-consistency of hybrid methods*: Given that the cut-off wave-number or frequency of the filter is in the inertial range of the energy spectrum, the dissipation due to resolved motions remains negligible compared to the modelled dissipation and is thus not affected by the mechanisms involved in the partitioning of energy, such that
>
> $$\varepsilon = \varepsilon_m$$

Brief demonstration of H-equivalence between PITM and DES (Friess et al., 2015)

Friess et al. (2015) carried out an analysis based on the *perturbation method* in order to establish a relationship between the hybridisation functions of the models, PITM ($C^*_{\varepsilon 2}$) and DES(ψ), through their closure equations for k_m and ε_m.

- Closure equations for PITM

$$\frac{Dk_m}{Dt} = \mathcal{P}_m - \varepsilon_m + \mathcal{D}_m \tag{5.2}$$

$$\frac{D\varepsilon_m}{Dt} = C_{\varepsilon 1}\frac{\varepsilon_m}{k_m}\mathcal{P}_m - C^*_{\varepsilon 2}\frac{\varepsilon_m^2}{k_m} + \mathcal{D}_\varepsilon \tag{5.3}$$

$$C^*_{\varepsilon 2} = C_{\varepsilon_1} + r\left(C_{\varepsilon_2} - C_{\varepsilon_1}\right) \tag{5.4}$$

- Closure equations for DES

$$\frac{Dk_m}{Dt} = \mathcal{P}_m - \psi\varepsilon_m + \mathcal{D}_m \tag{5.5}$$

$$\frac{D\varepsilon_m}{Dt} = C_{\varepsilon 1}\frac{\varepsilon_m}{k_m}\mathcal{P}_m - C_{\varepsilon 2}\frac{\varepsilon_m^2}{k_m} + \mathcal{D}_\varepsilon \tag{5.6}$$

$$\psi = F_{DES} = \max\left(1; \frac{k_m^{3/2}/\varepsilon_m}{C_{DES}\Delta}\right) \tag{5.7}$$

In essence, the methodology involves introducing *infinitesimal perturbations of the hybridisation functions*, $\delta C^*_{\varepsilon 2}$ and $\delta\psi$, in the closure equations which induce *variations in the modelled energy*, δk_m. Invoking the postulate defined previously, a relationship between the hybridisation functions can be obtained since the same perturbation induced by the hybridisation functions lead to the same level of the modelled energy of the two hybrid methods and corresponds to the same level of perturbations of the lower order statistics of the resolved scales. Further integrating the relationship between the RANS limit ($C^*_{\varepsilon 2} = C_{\varepsilon 2}$ and $\psi = 1$) and some arbitrary value towards the shift to the LES limit, Friess et al. (2015) found the following relations based on various hypotheses to simplify the equations. Three different relations were reported,

- Case of Homogeneous turbulence

  By considering an equilibrium state, such as the asymptotic behaviour observed for production-to-dissipation ratio, $\mathcal{P}/\varepsilon = 1$, or the turbulence time scale ratio, $\tau = k_m/\varepsilon_m$, in homogeneous shear layers and the hypothesis of *self-consistency* ($\delta\varepsilon = 0$).

$$\psi = 1 + (C_{\varepsilon 2} - C_{\varepsilon 1})\,(1 - r) \tag{5.8}$$

- Inhomogeneous turbulence in straight ducts assuming *self-consistency* ($\delta\varepsilon = 0$)

  In such a case, the equations can be simplified since both k_m and ε_m are in equilibrium along the mean streamlines. Considering that the diffusion terms are modelled using a gradient diffusion hypothesis, the relation writes

$$\psi = 1 + \left(\frac{C_{\varepsilon 2}}{C_{\varepsilon 1}} - 1\right)(1 - r) \tag{5.9}$$

- Inhomogeneous turbulence in straight ducts without the assumption of *self-consistency*

  Assuming *self-consistency* may not be a valid approach when considering that the dissipation rate is empirically modelled. The empirical simplifications, designed for RANS models, do not represent the physical dissipation rate during the shift from RANS mode to LES mode and thus the variations in dissipation rate need to be considered. Additionally, due to the complex nature of the ensuing analysis, Friess et al. (2015) considered only the eddy-viscosity models leading to the relation,

$$\psi = 1 + \left(\frac{C_{\varepsilon 2}}{C_{\varepsilon 1}} - 1\right)(1 - r^{C_{\varepsilon 1}/C_{\varepsilon 2}}) \tag{5.10}$$

Role of the hybridisation function and energy ratio

The consequence of the *H-equivalence* criteria is that the hybridisation can now be dictated by the energy ratio imposed by the model. The DES model is hybridized by replacing the

RANS length scale (l_{RANS}) by a length scale (l_{DES}) that is dependent on the grid step (see Section 2.7.3). Friess et al. (2015) developed an equivalent-DES model by modifying the hybridisation function using the equivalence criterion. l_{DES} can be reformulated using the hybridisation function, $\psi(r)$, obtained using the equivalence criteria. In a standard DES model,

$$\psi = F_{DES} = \max\left(1; \frac{k_m^{3/2}/\varepsilon_m}{l_{DES}}\right), \quad \text{where } l_{DES} = C_{DES}\Delta. \tag{5.11}$$

In the equivalent-DES model of Friess et al. (2015) arising from the equivalence criteria, the length scale l_{DES} is revisited,

$$l_{eq-DES} = \frac{k_m^{3/2}}{\varepsilon_m \psi(r)} = \frac{r^{3/2}k^{3/2}}{\psi(r)\varepsilon}, \text{(with self-consistency: } \varepsilon_m = \varepsilon) \tag{5.12}$$

Assuming the cut-off wave-number is in the inertial range of the Kolmogorov spectrum ($\kappa_c = \pi/\Delta$), the energy ratio is estimated as in the PITM model (Equation (2.116)) or the TPITM model (Equation (2.122)) using the dispersion relation, $\omega = \kappa\sqrt{k}$.

$$r = \frac{k_m}{k} = \frac{3}{2}C_K\left(\omega_c\frac{k}{\varepsilon}\right)^{-2/3} = \frac{1}{\beta_0}\left(\omega_c\frac{k}{\varepsilon}\right)^{-2/3} = \frac{1}{\beta_0}\left(\kappa_c\frac{k^{3/2}}{\varepsilon}\right)^{-2/3} = \frac{1}{\beta_0}\left(\frac{\pi}{\Delta}\frac{k^{3/2}}{\varepsilon}\right)^{-2/3} \tag{5.13}$$

Introducing Equation (5.13) in Equation (5.12),

$$l_{eq-DES} = \left(\frac{1}{\beta_0^{3/2}\pi\psi(r)}\right)\Delta = C_{eq-DES}\Delta \tag{5.14}$$

where the co-efficient C_{eq-DES} is now a function of the energy partition imposed in the model and not a constant as in standard DES. Friess et al. (2015) calibrated β_0 and C_{DES} such that the length scales obtained by both models are in agreement as a function of the grid step, Δ, and demonstrated that standard DES is a linear approximation of the equivalence criteria obtained for ψ (Equations (5.8) to (5.10)). Finally, the equivalence criteria was validated by comparing the low-order statistics between TPITM and equivalent-DES using *Elliptic Blending-RSM* as the base RANS model. The hybridisation function for the equivalent-DES

was formulated as,

$$F_{eq-DES} = \max\left(1; \frac{k_{sfs}^{3/2}/\varepsilon_{sfs}}{l_{eq-DES}}\right) \tag{5.15}$$

where l_{eq-DES} is computed using Equation (5.14) and $\psi(r)$ is computed using the more general equivalence of Equation (5.10). The agreement in lower order statistics observed showed that the equivalence criteria can be used to dynamically hybridize any given system of turbulence scale determining equations and pilot the switch from RANS to LES and vice-versa through the energy ratio.

5.1.2. Formulation of the HTLES model

In using the methodology laid down in Friess et al. (2015), Manceau (2018) developed the original *Hybrid Temporal LES (HTLES)* model establishing an H-equivalence with TPITM. The hybridisation is performed in a manner similar to the equivalent-DES with the hybridisation function being transferred to the transport equation of the sub-filter kinetic energy. The main difference lies in the use of a time scale, T, in lieu of a length scale, l_{eq-DES}, in the dissipation term of the sub-filter energy equation.

$$\psi(r)\varepsilon_m = \frac{k_m}{T} \tag{5.16}$$

- The original formulation of the HTLES model writes:

$$\nu_{\text{sfs}} = C_\mu \frac{k_{\text{sfs}}^2}{\varepsilon_{\text{sfs}}} \tag{5.17}$$

$$\frac{Dk_{\text{sfs}}}{Dt} = \mathcal{P}_{\text{sfs}} + \mathcal{D}_{k\text{sfs}} - \frac{k_{\text{sfs}}}{T} \tag{5.18}$$

$$\frac{D\varepsilon_{\text{sfs}}}{Dt} = C_{\varepsilon 1}\frac{\varepsilon_{\text{sfs}}}{k_{\text{sfs}}}\mathcal{P}_{\text{sfs}} + \mathcal{D}_{\varepsilon\text{sfs}} - C_{\varepsilon 2}\frac{\varepsilon_{\text{sfs}}}{k_{\text{sfs}}} \tag{5.19}$$

$$T = \frac{k_m}{\psi(r)\varepsilon_m} = \frac{rk}{\psi(r)\varepsilon}, \quad \text{with} \quad \psi(r) = 1 + \left(\frac{C_{\varepsilon 2}}{C_{\varepsilon 1}} - 1\right)(1 - r^{C_{\varepsilon 1}/C_{\varepsilon 2}}) \tag{5.20}$$

Remark: the assumption of a *self-consistent* hybrid model is made such that, $\overline{\varepsilon_{\text{sfs}}} = \varepsilon_m = \varepsilon$.

- Switch between the RANS and LES modes:

  The switch is driven by the energy ratio through its influence on the hybridisation function, $\psi(r)$, and hence the time-scale, T, in the destruction term, k_{sfs}/T, of the transport equation of the sub-filter kinetic energy.

  - RANS mode:

$$\begin{aligned} r = 1 \implies \psi(r) = 1 \implies T = \frac{k_m}{\varepsilon_m} \\ \implies \frac{k_{\text{sfs}}}{T} = \frac{k_{\text{sfs}}}{k_m}\varepsilon_m = \varepsilon_m = \varepsilon \end{aligned} \tag{5.21}$$

  - LES mode:

$$\begin{aligned} r < 1 \implies \psi(r) > 1 \implies T = \frac{k_m}{\psi(r)\varepsilon_m} \\ \implies \frac{k_{\text{sfs}}}{T} = \frac{k_{\text{sfs}}}{k_m}\psi(r)\varepsilon_m \approx \psi(r)\varepsilon_m = \psi(r)\varepsilon \end{aligned} \tag{5.22}$$

In the work of Duffal (2020), the hypothesis leading to the assumption of *self-consistency* is revisited leading to a new formulation of the HTLES model. Friess et al. (2015) considered a self-consistent model such that the resolved dissipation, ε_r, is negligible due to the cut-off frequency being in the inertial range and so, all the dissipation is modelled through the transport equation for the dissipation rate i.e.,

$$\overline{\varepsilon_{\text{sfs}}} = \varepsilon_m = \varepsilon \tag{5.23}$$

However, Duffal (2020) noted that this hypothesis does not hold in certain cases such as that observed when the model switches to LES mode ($\psi(r) > 1$) in an equilibrium layer

of the logarithmic region of a boundary layer. In this case, the production and dissipation terms of the sub-filter kinetic energy transport are in equilibrium, which in HTLES implies that,

$$\mathcal{P}_m = \underbrace{\frac{k_m}{T} = \psi(r)\varepsilon_m}_{\substack{\text{equilibrium in} \\ \text{TKE equation}}} \neq \underbrace{\varepsilon = \varepsilon_m}_{\substack{\text{dissipation rate} \\ \text{assuming self-consistency}}} \tag{5.24}$$

To put the above equation in words, there exists a disparity between the dissipation rate computed through its sub-filter transport equation ε_m and its representation in the sub-filter transport equation of kinetic energy $\psi(r)\varepsilon_m$. Assuming self-consistency, the model should ideally reproduce the correct equilibrium in the logarithmic region, i.e., $\mathcal{P}_m = \varepsilon_m$, which is the case in TPITM for instance.

Duffal (2020) proposed a reformulation of the HTLES model by redefining the sub-filter dissipation rate such that,

$$\varepsilon_m = \psi(r)\varepsilon_m^* \tag{5.25}$$

with ε_m^* being the variable solved using the second sub-filter transport equation.

$$\frac{D\varepsilon_{\text{sfs}}^*}{Dt} = C_{\varepsilon 1}\frac{\varepsilon_{\text{sfs}}^*}{k_{\text{sfs}}}\mathcal{P}_{\text{sfs}} + \mathcal{D}_{\varepsilon\text{sfs}} - C_{\varepsilon 2}\frac{\varepsilon_{\text{sfs}}^*}{k_{\text{sfs}}} \tag{5.26}$$

The self-consistency assumption is revised as,

$$\varepsilon = \varepsilon_m = \psi(r)\overline{\varepsilon_{\text{sfs}}^*} = \psi(r)\varepsilon_m^*. \tag{5.27}$$

This revision of the sub-filter dissipation rate removes the disparity previously noted in the example of the equilibrium layer of the logarithmic region of a boundary layer such that,

$$\mathcal{P}_m = \underbrace{\frac{k_m}{T} = \psi(r)\varepsilon_m^*}_{\substack{\text{equilibrium in} \\ \text{TKE equation}}} = \underbrace{\varepsilon_m = \varepsilon}_{\substack{\text{dissipation rate} \\ \text{assuming self-consistency}}} \tag{5.28}$$

Duffal (2020) performed the same analysis as Friess et al. (2015) (see Section 5.1.1) to establish *H-equivalence* between the TPITM model and the new formulation of HTLES in order to determine the relationship between their hybridisation functions, $C^*_{\varepsilon 2}$ and $\psi(r)$, respectively.

- Closure equations for TPITM

$$\frac{Dk_m}{Dt} = \mathcal{P}_m - \varepsilon_m + \mathcal{D}_m \tag{5.29}$$

$$\frac{D\varepsilon_m}{Dt} = C_{\varepsilon 1}\frac{\varepsilon_m}{k_m}\mathcal{P}_m - C^*_{\varepsilon 2}\frac{\varepsilon_m^2}{k_m} + \mathcal{D}_\varepsilon \tag{5.30}$$

- Closure equations for the new formulation of HTLES

$$\frac{Dk_m}{Dt} = \mathcal{P}_m - \psi\varepsilon^*_m + \mathcal{D}_m \tag{5.31}$$

$$\frac{D\varepsilon^*_m}{Dt} = C_{\varepsilon 1}\frac{\varepsilon^*_m}{k_m}\mathcal{P}_m - C_{\varepsilon 2}\frac{\varepsilon^{*2}_m}{k_m} + \mathcal{D}^*_{\varepsilon m} \tag{5.32}$$

Carrying out the perturbation analysis in the same conditions as considered by Friess et al. (2015) (described in Section 5.1.1), Duffal (2020) arrived at a single expression relating $\psi(r)$ and $C^*_{\varepsilon 2}$ in all the cases: Homogeneous turbulence; Inhomogeneous turbulence in straight ducts assuming self-consistency; Inhomogeneous turbulence in straight ducts without the assumption of self-consistency for eddy-viscosity models.

$$\psi(r) = \frac{C_{\varepsilon 2}}{C^*_{\varepsilon 2}} = \frac{C_{\varepsilon 2}}{C_{\varepsilon 1} + r\left(C_{\varepsilon 2} - C_{\varepsilon 1}\right)}. \tag{5.33}$$

Evaluation of the turbulent viscosity

In order to close the $\mathcal{NS}$ system of equations, the turbulent viscosity needs to be reviewed w.r.t the new formulation of the sub-filter transport variables k_m and ε^*_m. Following suit as per the developments of PITM (Chaouat et al., 2005) and TPITM (Fadai-Ghotbi et al.,

2010b), ν_m is defined by invoking Heisenberg's hypothesis (Hinze et al., 1975), leading to,

$$\nu_m = C_\kappa \int_{\kappa_c}^{\infty} \kappa^{-3/2} E(\kappa)^{1/2} d\kappa \tag{5.34}$$

where C_κ is a co-efficient. In order to reformulate the expression in the temporal domain, the spatial energy spectrum $E(\kappa)$ is relayed to the Eulerian temporal spectrum, $E(\omega)$ by $dk = E(\kappa)d\kappa = E(\omega)d\omega$. Furthermore, the dispersion relation, proposed by Tennekes (1975), $\omega = U_s\kappa$ is employed such that the eddies in the inertial range of the spectrum are advected/swept by the large scale motion assuming U_s is their sweeping velocity. In the presence of a mean flow, the sweeping velocity is defined as $U_s = U + \gamma\sqrt{k}$, where U is the magnitude of mean velocity and $\gamma\sqrt{k}$ represents the characteristic velocity of the large energetic motions. The turbulent viscosity can be rewritten in the temporal framework by introducing these relations as follows,

$$\nu_m = C_\kappa \int_{\omega_c}^{\infty} U_s \omega^{-3/2} E(\omega)^{1/2} d\omega \tag{5.35}$$

Assuming that the cut-off frequency is in the inertial range of the equilibrium Eulerian spectrum and using the dispersion relation, $\omega = U_s\kappa$, the temporal energy spectrum is defined as $E(\omega) = \frac{3}{2} C_K \varepsilon^{2/3} U_s^{2/3} \omega_c^{-2/3}$. This expression can be used to simplify the relation for the turbulent viscosity, which leads to,

$$\nu_m = \frac{3}{4} C_\kappa C_K^{1/2} \varepsilon^{1/3} U_s^{4/3} \omega_c^{-4/3} = C_\mu \frac{k_m^2}{\varepsilon} \tag{5.36}$$

where $C_\mu = 1/3 C_\kappa C_K^{-3/2}$ and the modelled energy, k_m, is evaluated from the temporal Eulerian spectrum as,

$$k_m = \int_{\omega_c}^{\infty} E(\omega) d\omega = \frac{3}{2} C_K \varepsilon^{2/3} U_s^{2/3} \omega_c^{-2/3} \tag{5.37}$$

It is important to note that in the new formulation of the HTLES model, the self-consistency assumption (Equation (5.27)) implies that the dissipation rate in the turbulent viscosity contains the hybridisation function, such that,

$$\nu_m = C_\mu \frac{k_m^2}{\varepsilon} = C_\mu \frac{k_m^2}{\psi(r)\varepsilon_m^*} \tag{5.38}$$

Evaluation of the energy ratio, r

Manceau (2018) proposed the formulation to relate the energy ratio, r, to the cut-off frequency of the temporal filter, ω_c, explicitly. Assuming the cut-off frequency is in the inertial range of an equilibrium Eulerian spectrum, the sub-filter kinetic energy ($k_m = \overline{k_{\text{sfs}}}$) is given by Equation (5.37) and r_K (K for Kolmogorov) can be evaluated as,

$$r_K = \frac{k_m}{k} = \frac{1}{k}\int_{\omega_c}^{\infty} E(\omega)d\omega = \frac{1}{\beta_0}\left(\frac{U_s}{\sqrt{k}}\right)^{2/3}\left(\omega_c \frac{k}{\varepsilon}\right)^{-2/3} \tag{5.39}$$

where $\beta_0 = 2/(3C_K)$ and the dissipation rate is given by $\varepsilon = \varepsilon_m = \psi(r)\varepsilon_m^*$ due to the hybrid method being assumed self-consistent.

Furthermore, the role of the cut-off frequency needs clarification. The model can resolve structures of frequency no more than $\omega = \pi/dt$ in accordance with the Nyquist theorem, where dt is the time step. Moreover, given a small enough time step to be able to resolve small structures of a very high frequency, the grid then limits the resolution of the flow structures through a characteristic cut-off wave-number, $\kappa_c = \pi/\Delta$, where Δ is the spatial filter width. Manceau (2018), used the dispersion relation to relate the two such that the highest resolvable frequency is a function of both the time-step and the grid-step as follows,

$$\omega_c = \min\left[\frac{\pi}{dt}, \frac{U_s \pi}{\Delta}\right] \tag{5.40}$$

where $U_s = U + \gamma\sqrt{k}$ to account for the advection due to both the mean flow and the characteristic velocity of the large scale motions and the spatial filter width is evaluated as

the cube-root of the cell volume, $\Delta = \Omega^{1/3}$.

For a constant time-step π/dt is constant and is only effective for large sweeping velocities or when encountering regions of very refined grids. In practice, imposing a small enough time-step or if the sweeping CFL number, $U_s dt/\Delta$, is small enough, the cut-off frequency is defined by the grid-step throughout the domain and the energy ratio becomes,

$$r_K = \frac{1}{\beta_0}\left(\frac{\pi}{\Delta}\frac{k^{3/2}}{\varepsilon}\right)^{-2/3} \tag{5.41}$$

whereby recovering the energy ratio evaluated in the PITM model which is based on spatial filtering.

A practical issue to note with the formulation of r_K is that Equation (5.39) does not comply with the RANS limit, $\lim_{\omega_c \to 0} r = 1$, since the equilibrium Eulerian spectrum is valid for the inertial range and does not hold for the large scales and thus r_K can be > 1. This shortcoming is overcome (Fadai-Ghotbi et al., 2010a; Manceau, 2018; Tran et al., 2012) by declaring a constraint on the energy ratio, r, such that,

$$r = \min\left[1; r_K\right] \tag{5.42}$$

Switch between the RANS and LES modes

As done for the original HTLES model (Manceau, 2018), in the new formulation (Duffal, 2020) of the HTLES model the switch is driven by the energy ratio, r, through its influence on the hybridisation function, $\psi(r)$, and hence the time-scale, T, in the destruction term, k_{sfs}/T, of the transport equation of the sub-filter kinetic energy.

- RANS mode:

  When the cut-off frequency goes to zero, the HTLES model recovers the RANS equa-

tions since the hybridisation function $\psi(r) = 1$.

$$\begin{aligned} r = 1 \implies \psi(r) = 1 \implies T = \frac{k_m}{\varepsilon_m} = \frac{k_m}{\psi(r)\varepsilon_m^*} = \frac{k_m}{\varepsilon_m^*} \\ \implies \frac{k_{\text{sfs}}}{T} = \frac{k_{\text{sfs}}}{k_m}\varepsilon_m^* = \varepsilon_m^* = \varepsilon_m = \varepsilon \end{aligned} \tag{5.43}$$

- LES mode:

  In LES mode, the energy ratio is lower than 1 and $\psi(r)$ increases thus increasing the dissipation rate of the sub-filter kinetic energy and hence leading to a reduction in the modelled contribution.

$$\begin{aligned} r < 1 \implies \psi(r) > 1 \implies T = \frac{k_m}{\psi(r)\varepsilon_m^*} \\ \implies \frac{k_{\text{sfs}}}{T} = \frac{k_{\text{sfs}}}{k_m}\psi(r)\varepsilon_m^* \approx \psi(r)\varepsilon_m^* = \varepsilon_m = \varepsilon \end{aligned} \tag{5.44}$$

  Also, it is interesting to note that the dissipation rate observed in the new formulation is equivalent to the physical dissipation rate (similarly seen for the TPITM model). In contrast, for the original formulation of HTLES (as well as the equivalent-DES) $\varepsilon = \psi(r)\varepsilon_m$ (Equation (5.22)) with $\psi(r) > 1$ in LES mode, which leads to a further augmentation of the dissipation rate of the sub-filter kinetic energy as compared to the physical dissipation rate computed (ε_m) using the second transport equation.

5.1.3. HTLES model using the $k\omega$-SST model

The prior sections focused on the developments of the HTLES strategy applied to the $k - \varepsilon$ model in order to have a clear sight of the development process starting from the *H-equivalence* method to the derivation of the new formulation of HTLES. In the present section, the HTLES model based on the $k\omega$-SST model (Duffal et al., 2022) is described. As discussed in the previous chapters, the $k\omega$-SST model (Menter, 1994) is a low-Reynolds number model that is a blend between the $k - \omega$ and $k - \varepsilon$ models which is well suited for wall bounded flows. The model switches to the $k - \omega$ model in the near wall regions and to

$k-\varepsilon$ model in the far field. The closure equations of the $k\omega$-SST RANS model write,

$$\frac{\partial k}{\partial t}+U_j\frac{\partial k}{\partial x_j}=\mathcal{P}_k+\frac{\partial}{\partial x_j}\left[\left(\nu+\frac{\nu_t}{\sigma_k}\right)\frac{\partial k}{\partial x_j}\right]-C_\mu k\omega \tag{5.45}$$

$$\frac{\partial \omega}{\partial t}+U_j\frac{\partial \omega}{\partial x_j}=\frac{\gamma_\omega}{\nu_t}\mathcal{P}_k+\frac{\partial}{\partial x_j}\left[\left(\nu+\frac{\nu_t}{\sigma_\omega}\right)\frac{\partial \omega}{\partial x_j}\right]-\beta_\omega\omega^2+2(1-F_1)\frac{\nu_t}{\sigma_{\omega 2}}\frac{1}{k}\frac{\partial \omega}{\partial x_j}\frac{\partial k}{\partial x_j} \tag{5.46}$$

Owing to this blending, Duffal (2020) noted two ways of applying the HTLES methodology to the $k\omega$-SST model.

- Method-1: Introduce a change of variable in the $k-\varepsilon$ HTLES model

$$k-\varepsilon \text{ TPITM} \xrightarrow{\text{h-equivalenvce}} k-\varepsilon \text{ HTLES} \xrightarrow{\text{change of variable}} k\omega\text{-SST HTLES} \tag{5.47}$$

  This process is similar to the manner in which the $k\omega$-SST RANS model is derived and leads to the hybridisation function being preserved as in Equation (5.33). However, Duffal (2020) concludes that the derivation leads to the hybridisation function, $\psi(r)$, appearing in the co-efficient of the destruction term of the second transport equation (Equation (5.46)), $\beta_\omega = C_\mu(C_{\varepsilon 2}-\psi(r))$ which increases the complexity of the model formulation possibly leading to similar issues observed in TPITM which the H-equivalence strategy aimed to solve.

- Method-2: H-equivalence with $k\omega$-SST TPITM of Bentaleb et al. (2011)

$$k-\varepsilon \text{ TPITM} \xrightarrow{\text{change of variable}} k\omega\text{-SST TPITM} \xrightarrow{\text{h-equivalenvce}} k\omega\text{-SST HTLES} \tag{5.48}$$

  This method of derivation entails conducting a perturbation analysis to establish equivalence with the $k\omega$-SST TPITM model of Bentaleb et al. (2011), thus transferring the hybridisation function to the transport equation of sub-filter kinetic energy as previously seen for the derivation of $k-\varepsilon$ HTLES.

H-equivalence between $k\omega$-SST TPITM and $k\omega$-SST HTLES

Due to the shortcomings noted for the 1st method, Duffal (2020) derived the $k\omega$-SST HTLES model following method-2. The closure equations for the models between which the equivalence is established are as follows,

- $k\omega$-SST TPITM (Bentaleb et al., 2011)

$$\nu_m = \frac{k_m}{\omega_m} \tag{5.49}$$

$$\frac{Dk_m}{Dt} = \mathcal{P}_m + \mathcal{D}_m - \overbrace{C_\mu k_m \omega_m}^{\varepsilon_m} \tag{5.50}$$

$$\frac{D\omega_m}{Dt} = \gamma_\omega \frac{\omega_m}{k_m}\mathcal{P}_m + \mathcal{D}_{\omega m} - \beta^*_\omega \omega_m^2 + C\mathcal{D}_{\omega m} \tag{5.51}$$

- $k\omega$-SST HTLES

$$\nu_m = \frac{k_m}{\psi_\omega \omega^*_m} \tag{5.52}$$

$$\frac{Dk_m}{Dt} = \mathcal{P}_m + \mathcal{D}_m - \overbrace{C_\mu k_m \psi_\omega \omega^*_m}^{\psi\varepsilon^*_m} \tag{5.53}$$

$$\frac{D\omega^*_m}{Dt} = \gamma_\omega \frac{\omega^*_m}{k_m}\mathcal{P}_m + \mathcal{D}^*_{\omega m} - \beta_\omega \omega^{*2}_m + C\mathcal{D}^*_{\omega m} \tag{5.54}$$

In establishing a *H-equivalence* between the two models, Duffal (2020) performed the perturbation analysis and obtained the same expression relating the hybridisation functions, β^*_ω and ψ_ω, for all the cases: Homogeneous turbulence; Inhomogeneous turbulence in straight ducts assuming self-consistency; Inhomogeneous turbulence in straight ducts without the assumption of self-consistency for eddy-viscosity models.

$$\psi_\omega(r) = \frac{\beta_\omega}{\beta^*_\omega} = \frac{\beta_\omega}{C_\mu \gamma_\omega + r(\beta_\omega - C_\mu \gamma_\omega)} \tag{5.55}$$

Assuming self-consistency of the hybrid method and noting that the dissipation rate is

computed as $\varepsilon_m = C_\mu k_m \omega_m$, the physical dissipation rate of the model can be written as,

$$\varepsilon = \underbrace{\psi \varepsilon_m^*}_{\varepsilon_m} = C_\mu k_m \underbrace{\psi \omega_m^*}_{\omega_m} \tag{5.56}$$

In a similar manner to that of the $k-\varepsilon$ HTLES, the hybridisation function is introduced in the definition of the turbulent viscosity, ν_m (Equation (5.52)). Furthermore, the turbulent viscosity is modified in the $k\omega$-SST RANS model using Bradshaw's assumption (Menter, 1994) and as such in HTLES model the sub-filter turbulent viscosity, ν_{sfs}, writes,

$$\nu_{\text{sfs}} = \frac{a_1 k_{\text{sfs}}}{\max(a_1 \psi_\omega \omega_{\text{sfs}}^*; \mathcal{S}F_2)} \tag{5.57}$$

As noted in Section 2.6.4, Menter et al. (2003b) proposed a production limiter to limit the overestimation of the turbulent kinetic energy production in stagnation regions (Equation (2.98)) which, in the HTLES formulation, takes the form

$$\mathcal{P}_{\text{sfs}} = min\left(\nu_{\text{sfs}} \mathcal{S}^2, 10 C_\mu k_{\text{sfs}} \psi_\omega \omega_{\text{sfs}}^*\right) \tag{5.58}$$

with the inclusion of the modified specific dissipation rate, ω_{sfs}^*. Additionally, as in the RANS formulation of $k\omega$-SST, the production term in the specific dissipation rate is written as

$$\mathcal{P}_{\omega\text{sfs}} = \gamma_\omega \frac{1}{\nu_{\text{sfs}} \psi_\omega} \mathcal{P}_{\text{sfs}}, \tag{5.59}$$

so as to guarantee the correct dimensional co-efficient $\omega_{\text{sfs}}^*/k_{\text{sfs}} = \nu_{\text{sfs}} \psi_\omega$ thus accounting for the modification of ν_{sfs} (Equation (5.57)).

The blending functions, F_1 and F_2, have been left unchanged in the HTLES formulation (Duffal, 2020) keeping in line with the other hybrid models employing the $k\omega$-SST closure (Bentaleb et al., 2011; Strelets, 2001; Travin et al., 2002). The express reason being that these function activate in regions similar to the switch between RANS and LES, which results in the $k-\omega$ model being active in the near-wall regions (as intended by the SST

model) and $k-\varepsilon$ being the sub-filter scale model far from the wall where the hybrid model is in LES mode.

Switch between the RANS and LES modes

As seen before for the $k-\varepsilon$ HTLES, the $k\omega$-SST HTLES model is sensitised to the filter width through a time scale in the destruction term of the sub-filter kinetic energy. Again, the energy ratio plays a crucial role and is computed using the relation,

$$r = \min\left(1; \underbrace{\frac{1}{\beta_0}\left(\frac{U_s}{\sqrt{k}}\right)^{2/3}\left(\omega_c \frac{k}{C_\mu k_m \psi_\omega \omega_m^*}\right)^{-2/3}}_{r_K}\right) \quad \text{with} \quad \omega_c = min\left[\frac{\pi}{dt}, \frac{U_s \pi}{\Delta}\right] \text{ and } \Delta = \Omega^{1/3} \tag{5.60}$$

The time scale, T, can be deduced from the destruction term $C_\mu k_m \psi_\omega \omega_m^* = k_m/T$:

$$T = \frac{1}{C_\mu \psi_\omega \omega_m^*} = \frac{r}{\psi_\omega(r)} \frac{k}{C_\mu k_m \omega_m^*} \tag{5.61}$$

The switch occurs in a manner similar to that of $k-\varepsilon$ HTLES,

- RANS mode:

  When the cut-off frequency goes to zero, the HTLES model recovers the RANS equations since the hybridisation function $\psi(r) = 1$.

$$\begin{aligned} r = 1 \implies \psi_\omega(r) = 1 \implies T = \frac{k_m}{\varepsilon_m} = \frac{k_m}{C_\mu k_m \psi_\omega \omega_m^*} = \frac{1}{C_\mu \omega_m} \\ \implies \frac{k_{\text{sfs}}}{T} = k_{\text{sfs}} C_\mu \cancel{\psi_\omega^{1}} \omega_m^* = \varepsilon_m^* = \varepsilon_m = \varepsilon \end{aligned} \tag{5.62}$$

- LES mode:

  In LES mode, the energy ratio is lower than 1 and $\psi(r)$ increases thus increasing the dissipation rate of the sub-filter kinetic energy and hence leading to a reduction in

the modelled contribution.

$$\begin{aligned} r < 1 \implies \psi(r) > 1 \implies T = \frac{1}{C_\mu \psi_\omega \omega_m^*} \\ \implies \frac{k_{\text{sfs}}}{T} = k_{\text{sfs}} C_\mu \psi_\omega \omega_m^* \approx \psi(r) \varepsilon_m^* = \varepsilon_m = \varepsilon \end{aligned} \tag{5.63}$$

Calibration of the model:

The assumption of self-consistency ($\varepsilon = \varepsilon_m$) means that in LES mode the sub-filter dissipation needs to be correctly predicted in order to have the correct level of resolved energy. To ensure this, correct evaluation of the energy ratio is paramount since it controls the amount of sub-filter and resolved contributions in the model. In order to verify that the HTLES model provides the correct level of sub-filter dissipation in LES mode, Duffal (2020) assessed the energy cascade (resolved energy spectra) using HTLES model in decaying isotropic turbulence (DIT) in comparison with the reference database of Kang et al. (2003) at $Re_\lambda = 720$. The co-efficient, β_0, in Equation (5.60) has a theoretical value of $\beta_0 = 2/(3C_K) = 0.44$. In their assessment, Duffal (2020) found that the correct levels of sub-filter dissipation was found at $\beta_0 = 0.44$ for $k - \varepsilon$ HTLES whereas, the β_0 was adjusted to 0.48 in the case of $k\omega$-SST HTLES to ensure the same level of resolved energy. This minor discrepancy is attributed to the fact that the change of variable between the ω-equation and ε-equation is not exact. Thus for the $k\omega$-SST HTLES $\beta_0 = 0.48$ is used subsequently.

Improvements of the HTLES model for wall-bounded flows

The main objective shared by all the hybrid methods, irrespective of their formulations or theoretical foundations, is to be able to predict wall-bounded flows well. Following the development of the new formulation of the HTLES model, Duffal (2020) focussed attention on studying the model behaviour in the near-wall regions. The improvements carried out in this regard are briefly described in this section.

Internal consistency constraint (ICC) As with any hybrid method, in simulations of wall-bounded flows using the HTLES model the near-wall region is in RANS mode and the large scale structures far from the wall are resolved using LES. However, there are no set mechanisms to stop the resolved motions from penetrating into the RANS regions. Duffal (2020) observed the partition of energy in the simulations of channel flows and noted the presence of resolved energy in the RANS regions. While this is a positive aspect of the model in and of itself, since it can provide information about the pressure and temperature fluctuations at the wall, the issue comes from the fact that the HTLES model is built on the assumption that the resolved energy is 0 in the RANS region. In particular the time scale, T, evaluated according to Equation (5.61) contains the total energy ($k = k_m + k_r$) in its formulation. Consequently, when the model is in RANS mode, the additional resolved energy penetrating the RANS region increases the time scale thereby reducing the dissipation term of the sub-filter kinetic energy (k_{sfs}/T) to levels lower than that expected from the RANS formulation. This leads to an underestimation of the HTLES velocity profile in the RANS regions as well as in the region of transition from RANS to LES.

To address the issue, Duffal (2020) devised a constraint, called *internal consistency constraint (ICC)* to exclude the contribution of the resolved energy in the time scale when the model is in RANS mode. This is achieved by adding a co-efficient to the definition of the time scale, such that the time scale with ICC writes,

$$T = \frac{r}{\psi_\omega(r)} \frac{k_m + c_r k_r}{C_\mu k_m \omega_m^*}, \quad \text{where} \quad c_r = \begin{cases} 0 \text{ if } r = 1 \\ 1 \text{ if } r < 1 \end{cases} \tag{5.64}$$

The constraint successfully erased the underestimation of velocity in the RANS region thus ensuring that the HTLES profile tends to the RANS solution consistently.

Shielding function (f_s) The definition of the ICC did not, however, solve the mismatch of the velocity profile in the transition and LES regions. In order to take full advantage of

the hybrid strategy, it is important to have a switch from RANS to LES with an objective of minimizing the number of grid cells in the near wall region as compared to LES. With the energy ratio, r, evaluated using $r = \min[1; r_K]$ where r_K is given by Equation (5.39), Duffal (2020) observed that the transition happens too close to the wall. Using the equality $C_\mu^{3/4} k^{3/2}/\varepsilon = C_K d_w$ in the log-layer, where d_w is the wall-distance and a cut-off frequency based on the grid step ($\omega_c = U_s \pi/\Delta$), r_K reduces to

$$r_K = \frac{C_\mu^{1/2}}{\beta_0 \pi^{2/3} C_K^{2/3}} \left(\frac{\Delta}{d_w}\right)^{2/3}. \tag{5.65}$$

Through the above analysis of r_K in the log-layer, Duffal et al. (2022) noted that the transition happens closer to the wall when the grid is refined. This issue is encountered in numerous hybrid approaches and leads to the phenomena of modelled stress depletion (MSD) and grid induced separation (GIS) (Spalart et al., 2006). In order to force the hybrid model to remain in RANS mode in the near-wall region, Spalart et al. (2006) proposed a new version of the DES model, with the addition of a *shielding function*, called Delayed-DES (DDES) method. Other techniques such as the use of the elliptic blending equation to form a shielding function has been proposed by Fadai-Ghotbi et al. (2010b) for the TPITM model. Duffal (2020) used the formulation of the energy ratio of Fadai-Ghotbi et al. (2010b) to incorporate the shielding function such that,

$$r = (1 - f_s) \times 1 + f_s \times \min[1; r_K] \tag{5.66}$$

- ***Grid independent shielding function***:
  Duffal (2020) developed the first of the shielding functions based on a set of criteria, given below,
  - RANS mode should extend up to the log-layer
  - the shielding function should have a sharp transition to counter the decrease in r_K as the wall distance increases

- f_s should be grid-independent
- f_s should be independent of the closure

With the above constraints in mind, Duffal (2020) defined a length scale ratio to be used as the kernel of a hyperbolic tangent function to obtain a relation for the shielding function f_s. The length scale ratio, ξ_K, is a comparison of the distance to the wall and a turbulent length scale. Given that the HTLES model is developed with the assumption of self-consistency (resolved dissipation is negligible), the total dissipation, ε, is given by the modelled dissipation rate ε_m and is independent of the grid. Thus the turbulent length scale in ξ_K is chosen to be the *kolmogorov length scale* ($(\nu/\varepsilon)^{1/4}$), which allows to write the shielding function, f_s, as

$$f_s(\xi_K) = 1 - tanh[\xi_K^{p_1}], \quad \text{where} \quad \xi_K = C_1 \frac{(\nu/\varepsilon)^{1/4}}{d_w} \tag{5.67}$$

where $C_1 = 45$ and $p_1 = 8$ are coefficients calibrated such that the model is in RANS mode up to $y^+ = 100$ and a sharp switch from RANS to LES is imposed between $y^+ = 100$ and 200.

- ***Grid-dependent shielding function***:

  With the shielding function defined previously, Duffal (2020) observed a log-layer mismatch where the HTLES velocity profile is overestimated in the LES region, especially at higher Re numbers. This issue has plagued many a hybrid methods and varied strategies to solve this issue have been proposed (Keating et al., 2006; Shur et al., 2008). This phenomenon of log-layer mismatch is essentially due to the lack of grid resolution to resolve turbulent fluctuations while the hybrid model has switched to LES mode. Duffal (2020) proposed a second shielding function such that the model does not switch to LES when the grid is considered too coarse in any of the co-ordinate directions (i.e., when the anisotropy of the grid is high). In a manner similar to the first shielding function a hyperbolic tangent function is used with the kernel being a

length scale ratio which is now based on the comparison of the maximum grid size, $\Delta_{\max} = \left[\Delta_x, \Delta_y, \Delta_z\right]$, and the distance to the wall.

$$f_s(\xi_D) = 1 - tanh[\xi_D^{p_2}], \quad \text{where} \quad \xi_D = C_2 \frac{\Delta_{\max}}{d_w} \tag{5.68}$$

In order to have a similar rate of transition as before, the coefficients are calibrated as $C_2 = 1.2$ and $p_2 = 6$.

The two shielding functions are combined to form a two-fold shielding function such that,

$$f_s = 1 - tanh\left[\max\left[\xi_K^{p_1}; \xi_D^{p_2}\right]\right] \tag{5.69}$$

The definition ensures that the HTLES model is in RANS mode until $y^+ = 100$, irrespective of the grid resolution and/or Re numbers, thanks to the grid-independent shielding function, $f_s(\xi_K)$. Furthermore, in cases where the grid is too coarse, for the given Re number, the grid-dependent shielding function, $f_s(\xi_D)$, ensures that the LES mode is not activated too early, thus avoiding the issue of log-layer mismatch. In essence the two-fold shielding function works to assure the HTLES model consistent with both the RANS and LES limits. However necessary the shielding function may be, it would be remiss to not mention the fact that the mere inclusion of the shielding function has induced empiricism in to the model.

5.2. $k\omega$-SST HTLES model for natural convection flows

In this thesis, further developments are carried out to the $k\omega$-SST HTLES model employed for the computations of natural convection flows. Furthermore, the developments presented subsequently are carried out considering the benchmark DNS of Sebilleau et al. (2018) due to the high Ra number obtained at $Ra = 10^{11}$. The developments of Duffal (2020) were made with forced channel flows in mind, as is standard practice for primary developments

of hybrid methods. As discussed in Chapter 3, natural convections flows require additional considerations in the $\mathcal{NS}$ and the turbulence transport equations to account for the physics and the turbulence scales. This section provides a breakdown of the aforementioned considerations in order to modify the HTLES model to simulate natural convection flows.

5.2.1. Sub-filter transport equations

As seen in Section 3.6.2, the transport equation for the turbulent kinetic energy gains an additional buoyancy term thanks to the turbulent heat fluxes, such that,

$$\frac{Dk_{\text{sfs}}}{Dt} = \mathcal{P}_{\text{sfs}} + \mathcal{G}_{\text{sfs}} + \mathcal{D}_{k\text{sfs}} - \frac{k_{\text{sfs}}}{T} \tag{5.70}$$

where $\mathcal{G} = \overline{\mathcal{G}_{\text{sfs}}} = -\beta g_i \overline{u_i \theta}$.

In regards to the buoyancy source term in the transport equation for the specific dissipation rate, the particularities of the $k\omega$-SST model have been assessed in Section 4.4.1 and are henceforth considered here as presented previously for the $k\omega$-SST RANS model. Notably, the form of the source term, $\mathcal{G}_{\omega}^{SST}$, arises due to the blending between the $k-\omega$ and $k-\varepsilon$ models. In the HTLES formulation, the blending functions have been left unchanged and since the new formulation of the source term is based on the blending function F_1, it is therefore kept the same leading to the sub-filter scale transport equation for the specific dissipation rate as follows,

$$\frac{\partial \omega_{\text{sfs}}}{\partial t} + U_j \frac{\partial \omega_{\text{sfs}}}{\partial x_j} = \frac{\gamma_\omega}{\nu_{\text{sfs}}} \mathcal{P}_{k\text{sfs}} + \mathcal{G}_{\omega\text{sfs}}^{SST} + \frac{\partial}{\partial x_j}\left[\left(\nu + \frac{\nu_{\text{sfs}}}{\sigma_\omega}\right)\frac{\partial \omega_{\text{sfs}}}{\partial x_j}\right] - \beta_\omega \omega_{\text{sfs}}^2 + 2(1-F_1)\frac{\nu_{\text{sfs}}}{\sigma_{\omega 2}}\frac{1}{k}\frac{\partial \omega_{\text{sfs}}}{\partial x_j}\frac{\partial k_{\text{sfs}}}{\partial x_j} \tag{5.71}$$

with

$$\mathcal{G}_{\omega}^{\text{SST}} = \frac{\gamma}{\nu_m}\max(\mathcal{G},0) + \frac{(1-F_1)}{\nu_m}\left[\max(\mathcal{G},0) - \mathcal{G}\right]. \tag{5.72}$$

5.2.2. Shielding function (f_s)

To state the obvious, natural convection flows present very different driving mechanisms compared to forced channel flows, i.e., flow driven due to the temperature boundary condition imposed at the vertical walls. A direct consequence of the driving mechanism is that the vertically heated differential cavity considered in this thesis (see Section 3.7) presents very thin boundary layers. The two characteristics that are important to note are:

- As noted by Sebilleau et al. (2018), the boundary layers get thinner with increasing Ra numbers.
- The boundary layers at the hot and cold walls in cavity flows are separated by a stratified core which again is enlarged with increasing Ra numbers.

These characteristics require that the grid used to simulate natural convection in a cavity needs to be quite fine close to the wall in comparison to the grid distribution in forced channel flows. Additionally, the switch from RANS to LES should not be too far from the wall since a switch to LES in the quiescent laminar core would not be conducive for the development of resolved structures. With these considerations, the shielding function imposed due to the anisotropy of the mesh ($f_s(\xi_D)$) is not considered in the computations thus giving the shielding function as,

$$f_s = f_s(\xi_K) = 1 - tanh[\xi_K^{p_1}], \quad \text{where} \quad \xi_K = C_1 \frac{(\nu/\varepsilon)^{1/4}}{d_w} \tag{5.73}$$

with $C_1 = 45$ and $p_1 = 8$. As will be seen further (Figure 5.12), the grid-dependent shielding function which is computed to validate the above hypothesis is essentially ineffective for the test case considered.

5.2.3. Formulation of the model

With the above considerations in mind, the preliminary formulation of the $k\omega$-SST HTLES model used for simulating natural convection flows is as follows,

$$\nu_{\text{sfs}} = \frac{a_1 k_{\text{sfs}}}{\max(a_1 \psi_\omega \omega^*_{\text{sfs}}; \mathcal{S}F_2)} \tag{5.74}$$

$$\frac{Dk_{\text{sfs}}}{Dt} = \mathcal{P}_{\text{sfs}} + \mathcal{G}_{\text{sfs}} + \mathcal{D}_{k\text{sfs}} - \frac{k_{\text{sfs}}}{T} \tag{5.75}$$

$$\frac{\partial \omega^*_{\text{sfs}}}{\partial t} + U_j \frac{\partial \omega^*_{\text{sfs}}}{\partial x_j} = \frac{\gamma_\omega}{\nu_{\text{sfs}}} \mathcal{P}_{k\text{sfs}} + \mathcal{G}^{SST}_{\omega\text{sfs}} + \frac{\partial}{\partial x_j}\left[\left(\nu + \frac{\nu_{\text{sfs}}}{\sigma_\omega}\right)\frac{\partial \omega^*_{\text{sfs}}}{\partial x_j}\right] - \beta_\omega \omega^{*2}_{\text{sfs}} + 2(1-F_1)\frac{\nu_{\text{sfs}}}{\sigma_{\omega 2}}\frac{1}{k}\frac{\partial \omega^*_{\text{sfs}}}{\partial x_j}\frac{\partial k_{\text{sfs}}}{\partial x_j} \tag{5.76}$$

$$\mathcal{P}_{\text{sfs}} = min\left(\nu_{\text{sfs}} \mathcal{S}^2, 10 C_\mu k_{\text{sfs}} \psi_\omega \omega^*_{\text{sfs}}\right) \tag{5.77}$$

$$T = \frac{r}{\psi_\omega(r)} \frac{k_m + c_r k_r}{C_\mu k_m \omega^*_m}, \quad \text{where} \quad c_r = \begin{cases} 0 \text{ if } r = 1 \\ 1 \text{ if } r < 1 \end{cases} \tag{5.78}$$

$$\psi_\omega(r) = \frac{\beta_\omega}{\beta^*_\omega} = \frac{\beta_\omega}{C_\mu \gamma_\omega + r(\beta_\omega - C_\mu \gamma_\omega)} \tag{5.79}$$

$$r = (1 - f_s) \times 1 + f_s \times \min[1; r_K] \tag{5.80}$$

$$r_K = \frac{1}{\beta_0}\left(\frac{U_s}{\sqrt{k}}\right)^{2/3}\left(\omega_c \frac{k}{C_\mu k_m \psi_\omega \omega^*_m}\right)^{-2/3} \quad \text{with} \quad \omega_c = min\left[\frac{\pi}{dt}, \frac{U_s \pi}{\Delta}\right],\ U_s = U + \gamma\sqrt{k},\ \text{and } \Delta = \Omega^{1/3} \tag{5.81}$$

where Ω is the volume of the cell, $\gamma = 2/3$ and $\beta_0 = 0.48$.

$$f_s = f_s(\xi_K) = 1 - tanh[\xi_K^{p_1}], \quad \text{where} \quad \xi_K = C_1 \frac{(\nu/\varepsilon)^{1/4}}{d_w} \tag{5.82}$$

with $C_1 = 45$ and $p_1 = 8$.

The estimation of statistically averaged quantities, $\overline{\phi}$, during the course of the simulation are provided by defining an exponentially-weighted average (Pruett et al., 2003), with a time filter width (Δ_T) corresponding to several flow-through times, such that

$$\frac{\partial \overline{\phi}(t, \Delta_T)}{\partial t} = \frac{\widetilde{\phi}(t) - \overline{\phi}(t, \Delta_T)}{\Delta_T} \tag{5.83}$$

5.2.4. Numerical setup

The calculations are performed using the open-source CFD software distributed under the GNU General Public License and developed by EDF, named *Code_Saturne*. The code is based on a finite-volume method using fully co-located arrangement for the variables. SIMPLEC algorithm is used for solving the velocity-pressure system. The time-marching scheme is based on a second-order accurate Crank-Nicholson scheme.

A hybrid convection scheme is defined for the filtered velocity equation similar to that proposed by Travin et al. (2002). Duffal (2020) used the coefficient, c_r (from Equation (5.64)), to blend a centred scheme (to be used in LES mode) and a second-order linear upwind (SOLU) scheme (to be used in RANS mode), such that

$$\phi_{\mathrm{HYB}} = (1 - c_r)\phi_{\mathrm{SOLU}} + c_r \phi_{\mathrm{CDS}} \tag{5.84}$$

The hybrid scheme allows to satisfy the requirement of a centred scheme for LES while avoiding the numerical instabilities of such schemes in RANS by switching to an upwind scheme. The convection terms in the transport equations of the turbulent variables are solved using a first order upwind scheme to prioritize numerical stability.

5.2.5. Grid sensitivity study

In the use of the HTLES model, it is important to assess the sensitivity of the model to refinement in the grid. In particular, the impact of higher resolution of the unsteady motions thanks to grid refinement needs to be studied. To that end, the simulations of the square

DHC test case (see Figure 3.2a) using the $k\omega$-SST HTLES model (with SGDH for the heat fluxes) is studied with the following parameters:

- refinement in wall-normal directions, x and y, with the grids listed in Table 5.1
- refinement in the periodic direction, z, with the grids listed in Table 5.2

All the grids are structured and the number of cells in the wall-normal directions is kept equal. The length of the domain in the periodic direction ($L_z = 0.15$) is kept the same as that of the DNS database (Sebilleau et al., 2018), which was chosen such that the two-point correlations in space of velocity and temperature decay to 0 at a separation of $L_z/2$ ensuring an uncorrelated turbulent field. The grids, A and B, represent the coarser set of grids with grid A being coarsened compared to B while keeping the same number of points in z. The grids, C and D, represent the finer set of grids with grid C being coarsened compared to D while keeping the same number of points in z.

Observations for simulations with grids A, B, C, and D:

- velocity profiles show little sensitivity to grid refinement as seen in (Figure 5.1a)
- the same is true for the temperature profiles (not shown here)
- at cavity heights $x \leq 0.5$, the total kinetic energy predictions are similar for all the meshes (Figure 5.1b)
- at cavity heights $x > 0.5$, the predictions of total kinetic energy improves with grid refinement (A $\rightarrow$ D) far from the wall
- Figure 5.2b shows that these improvements are mainly due to the improvements in the resolved kinetic energy
- the variations due to the modelled contribution are not significant in comparison (Figure 5.2a)

In view of these observations, further analysis is conducted using grid B in order to study the effects of refinement in the periodic direction. As listed in Table 5.2, grid B is coarsened and refined in the periodic direction to obtain the grids BC and BF respectively. Similar to the observations made previously, the only noticeable differences are due to the improvements in the resolved kinetic energy at cavity heights $x > 0.5$ (Figure 5.4). However, only negligible differences are noted between the grid B and its finer counterpart, BF.

In conclusion, noting the compartmentalisation of the modelled and resolved energy for the grids presented in Table 5.1 and Table 5.2, grid B is chosen for further simulations presented in this chapter.

- Caveat:

  It is important to note here that due to the overlap between the work carried out in this thesis and the development of the new formulation of HTLES by Duffal (2020), the grid sensitivity study has been carried out using the original formulation of the HTLES model (Section 5.1.2) with the inclusion of ICC (Section 5.1.3) and the shielding function (Section 5.1.3), $f_s(\xi_K)$. The exercise was not repeated with the new formulation of the HTLES model as the above analysis was deemed satisfactory due to the marginal differences noted between the grids considered.

Table 5.1.: Grids refined in x and y

Ra	Grid	Δ_x^+	Δ_y^+	Δ_z^+	N_x	N_y	N_z
	A	< 1	< 1	23	249	249	60
10^{11}	B	< 1	< 1	23	332	332	60
	C	< 1	< 1	17	415	415	80
	D	< 1	< 1	17	498	498	80

Table 5.2.: Grids refined in z

Ra	Grid	Δ_x^+	Δ_y^+	Δ_z^+	N_x	N_y	N_z
	BC	< 1	< 1	35	332	332	40
10^{11}	B	< 1	< 1	23	332	332	60
	BF	< 1	< 1	17	332	332	80

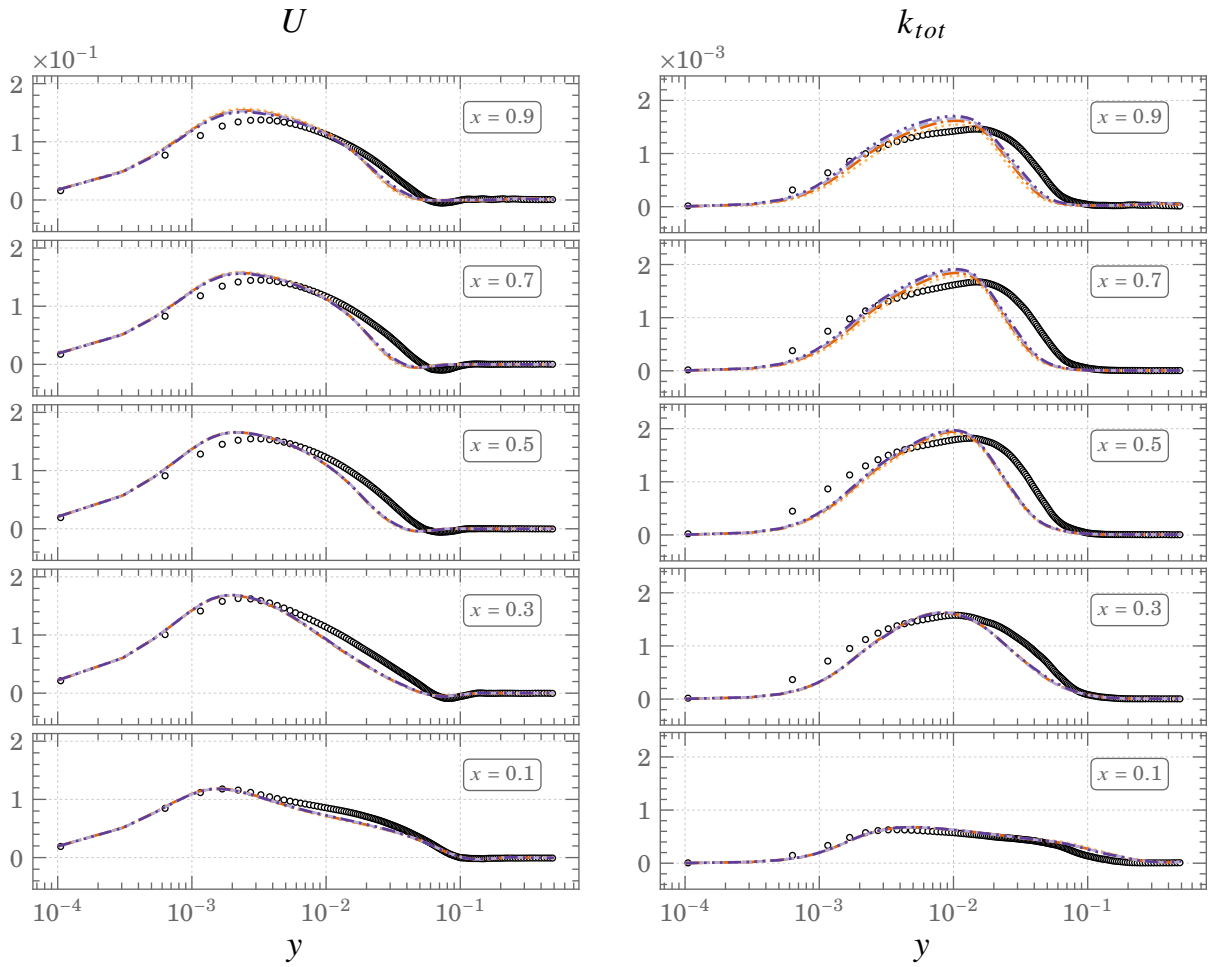

(a) Mean velocity, U

(b) Total kinetic energy, k_{tot}

Figure 5.1.: Mean profiles of Velocity and total kinetic energy for various meshes at $Ra \times 10^{11}$ ∘ ∘ ∘ DNS 249^2 332^2 415^2 498^2

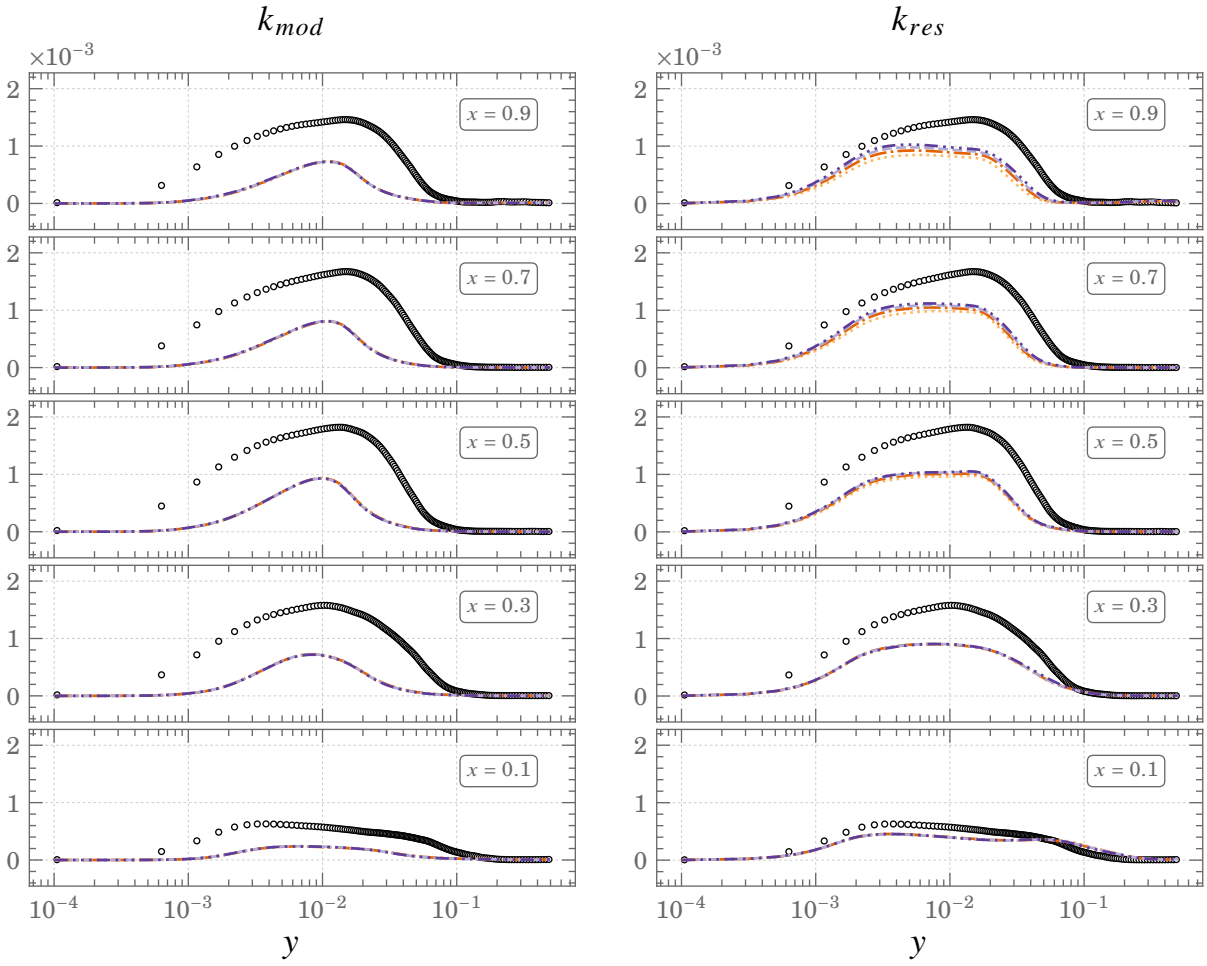

(a) Modelled kinetic energy, k_{mod}

(b) Resolved kinetic energy, k_{res}

Figure 5.2.: Mean profiles of modelled and resolved turbulent kinetic energy for various meshes at $Ra \times 10^{11}$

DNS 249^2 332^2 415^2 498^2

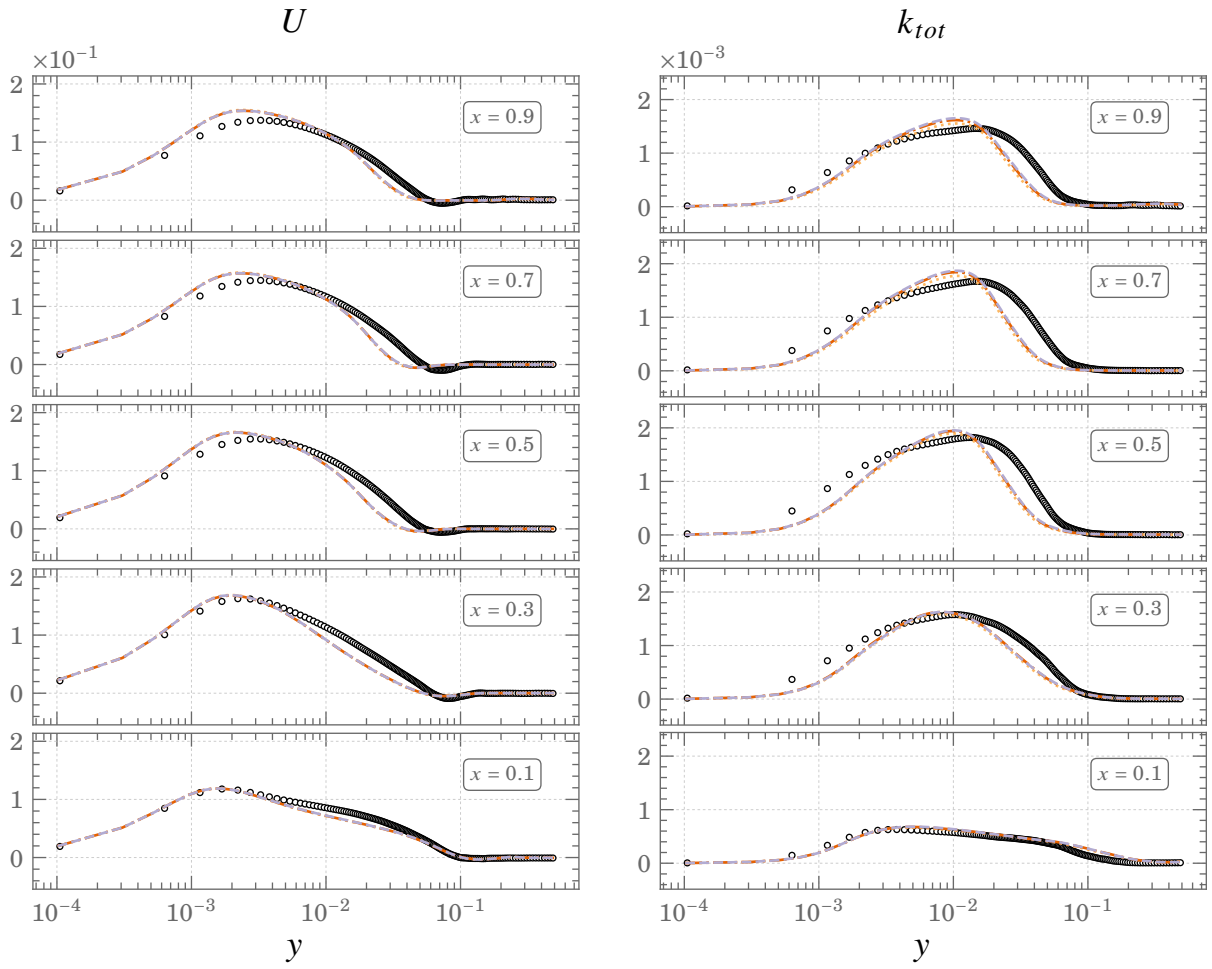

(a) Mean velocity, U

(b) Total kinetic energy, k_{tot}

Figure 5.3.: Mean profiles of Velocity and total kinetic energy for various meshes at $Ra \times 10^{11}$ ∘ ∘ ∘ DNS ····· $332^2 \times 40$ –·–· $332^2 \times 60$ – – – $332^2 \times 80$

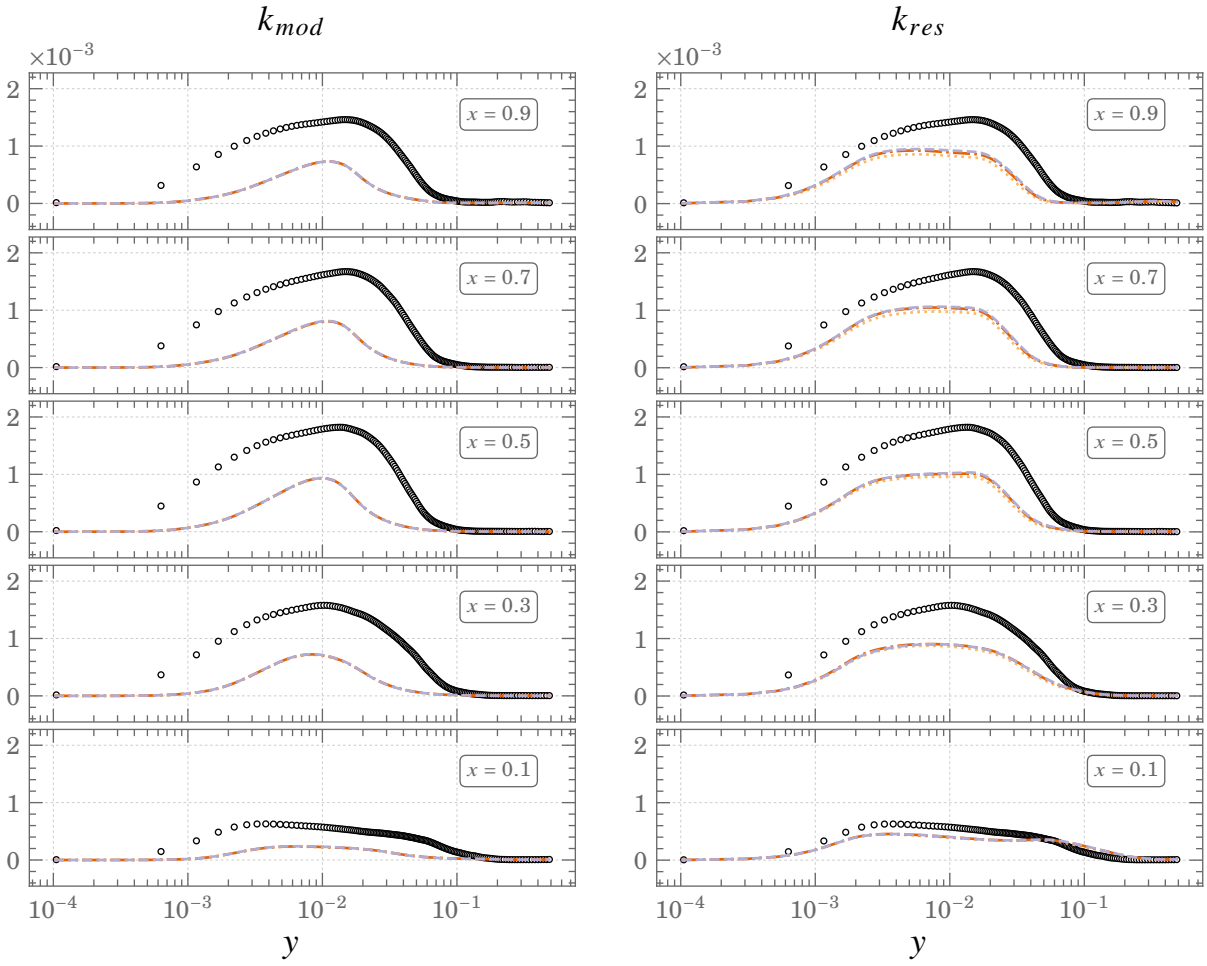

(a) Modelled kinetic energy, k_{mod}

(b) Resolved kinetic energy, k_{res}

Figure 5.4.: Mean profiles of modelled and resolved turbulent kinetic energy for various meshes at $Ra \times 10^{11}$

DNS $332^2 \times 40$ $332^2 \times 60$ $332^2 \times 80$

5.2.6. Identification of the failure of the shielding function

As mentioned previously, the HTLES model is built on solid theoretical bases with empiricism being introduced due to the declaration of a shielding function which guards the model from transitioning to LES too close to the wall. The definition and calibration of the shielding function was carried out in the forced channel flow and further tested successfully in the *periodic hill flow* test case in the work of Duffal (2020). In this section, the behaviour of the shielding function is studied in the context of natural convection flows using the *Square Differentially heated cavity* of Sebilleau et al. (2018) at $Ra = 10^{11}$.

***A priori* tests using the DNS database**

The shielding function we are concerned with, $f_s(\xi_K)$, is defined with a kernel based on the ratio of the Kolmogorov length scale and the wall distance.

$$\xi_K = C_1 \frac{(\nu/\varepsilon)^{1/4}}{d_w} \tag{5.85}$$

These quantities can be easily verified *a priori* using the time averaged statistics from the DNS database. The exact wall distance is easily calculated for the *Square DHC* thanks to its simple geometry (Figure 3.2a) for a point $p(x, y)$ as,

$$d_w = \min(|p(x) - 0|; |p(x) - 1|; |p(y) - 0|; |p(y) - 1|) \tag{5.86}$$

giving the wall distance as shown in Figure 5.5.

Figure 5.6 shows the plots of the dissipation rate, ε, the kernel, ξ_K, and the shielding function, $f_s(\xi_K)$, plotted at various heights of the cavity. It can be observed that in the stratified core region ($y > 0.1$), there are oscillations in the dissipation rate due to the flow exhibiting very low levels of turbulence. These oscillations carry over to the kernel function, ξ_K, which is further exaggerated due to the coefficient, $p_1 = 8$ in the definition of f_s.

$$f_s(\xi_K) = 1 - \tanh[\xi_K^{p_1}] \tag{5.87}$$

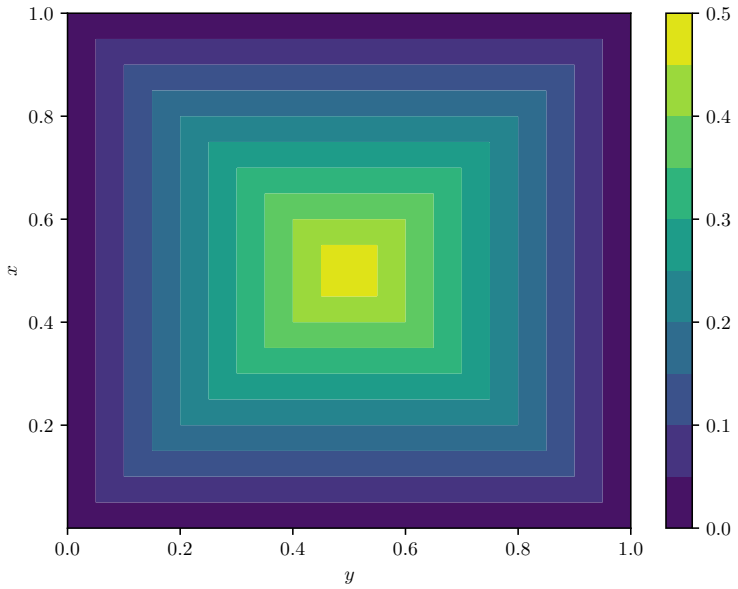

Figure 5.5.: exact wall distance in the Square DHC

The effect of these oscillations is seen clearly at cavity height $x = 0.1$ in the plot of the shielding function in Figure 5.6c where the shielding function dips back to zero. The express purpose of the shielding function is to delay the switch from RANS to LES in the near wall region after which the energy ratio should only be a function of the Kolmogorov energy ratio, r_K. However the observed behaviour of the shielding function will lead to an unintended modification of the energy ratio, r, far from the wall since,

$$r = (1 - f_s) \times 1 + f_s \times \min[1; r_K]. \tag{5.88}$$

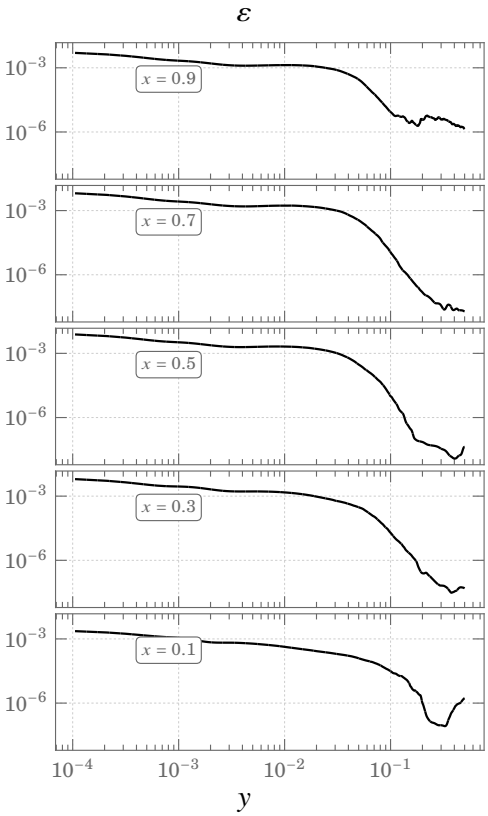

(a) Dissipation rate, ε

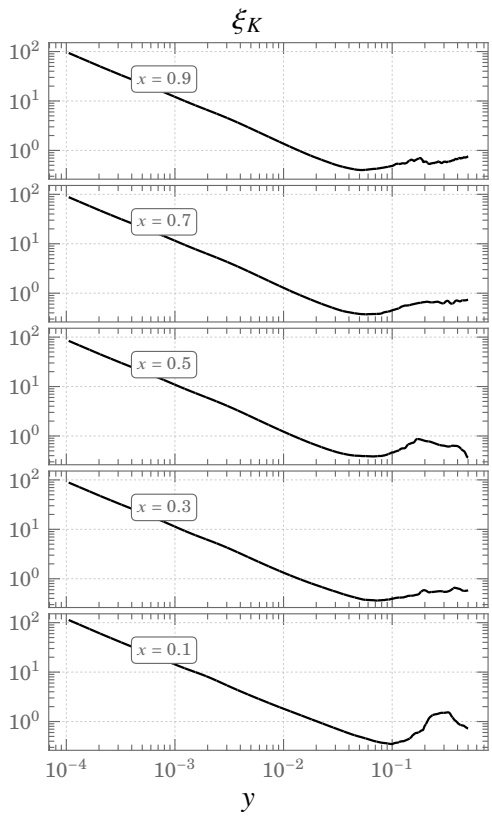

(b) Kernel of the shielding function, ξ_K

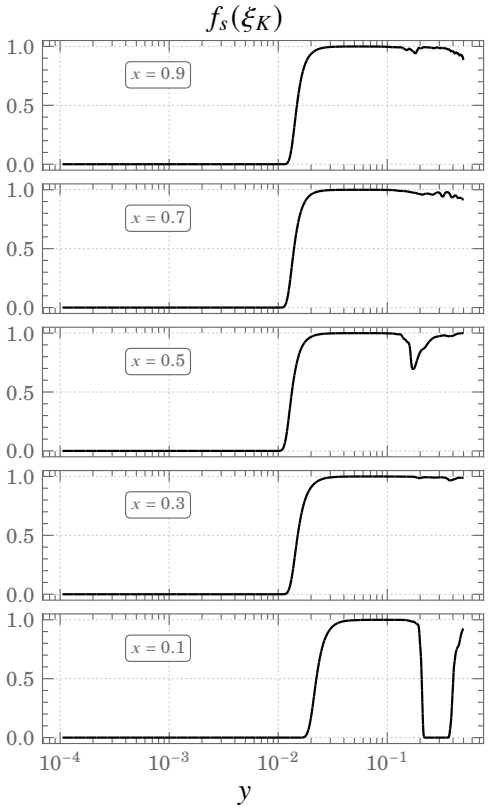

(c) shielding function, $f_s(\xi_K)$

Figure 5.6.: Behaviour of the shielding function, $f_s(\xi_K)$ — *a priori* tests

HTLES simulations performed using the formulation of the model as in Section 5.2.3 shows that the unintended behaviour of the shielding function is greatly magnified as compared to the *a priori* tests. Figure 5.7a shows that the shielding function goes to zero in multiple instances along the height of the cavity. As a consequence the energy ratio is modified such that the model goes back and forth between RANS and LES modes far from the walls as seen in Figure 5.7b. This behaviour can be better noted by observing the Q-criterion (Figure 5.8) where the energy ratio is seen to be 1 and hence the model is in RANS mode in large areas of the cavity far from the walls.

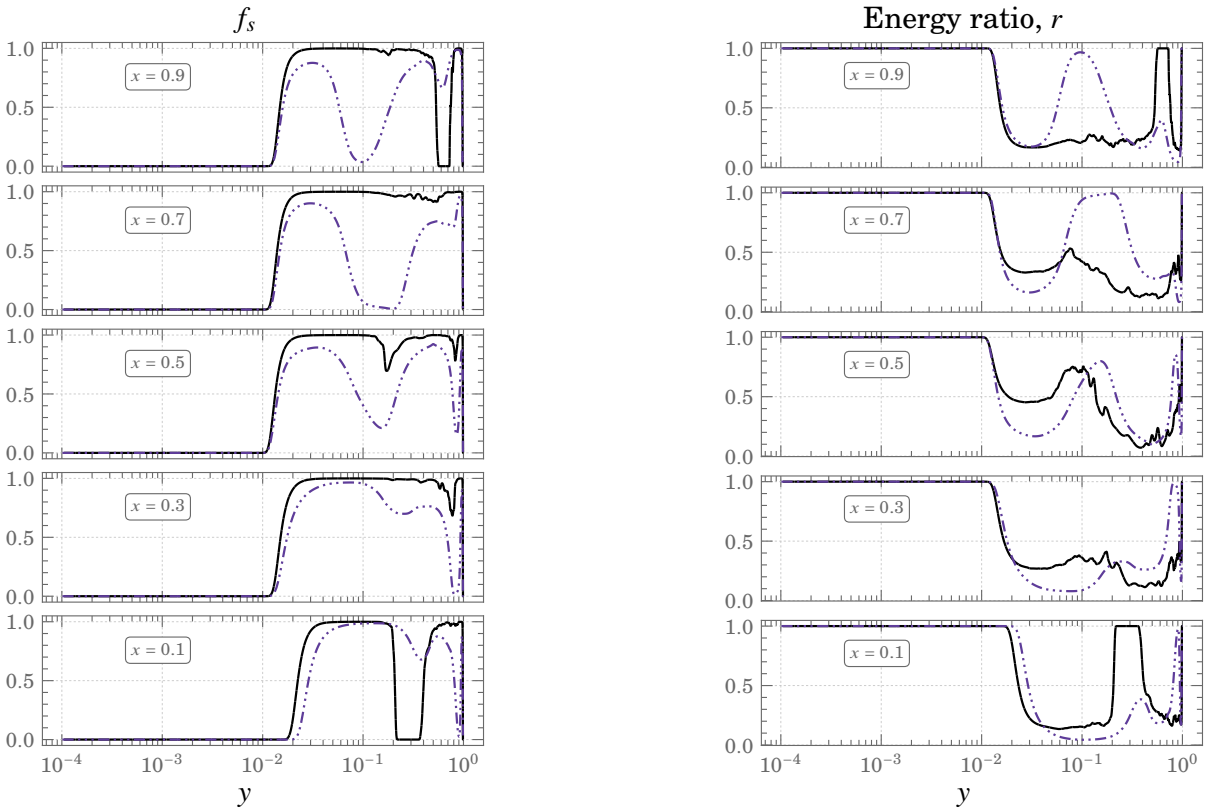

(a) Shielding function, $f_s(\xi_K)$

(b) Energy ratio, r

Figure 5.7.: Behaviour of the shielding function and its impact on the energy ratio in HTLES

$f_s(\xi_K)$ —— DNS

Due to the issues presented by the shielding function and the ensuing modification of the energy ratio presented above, in the present thesis, a new shielding function is developed

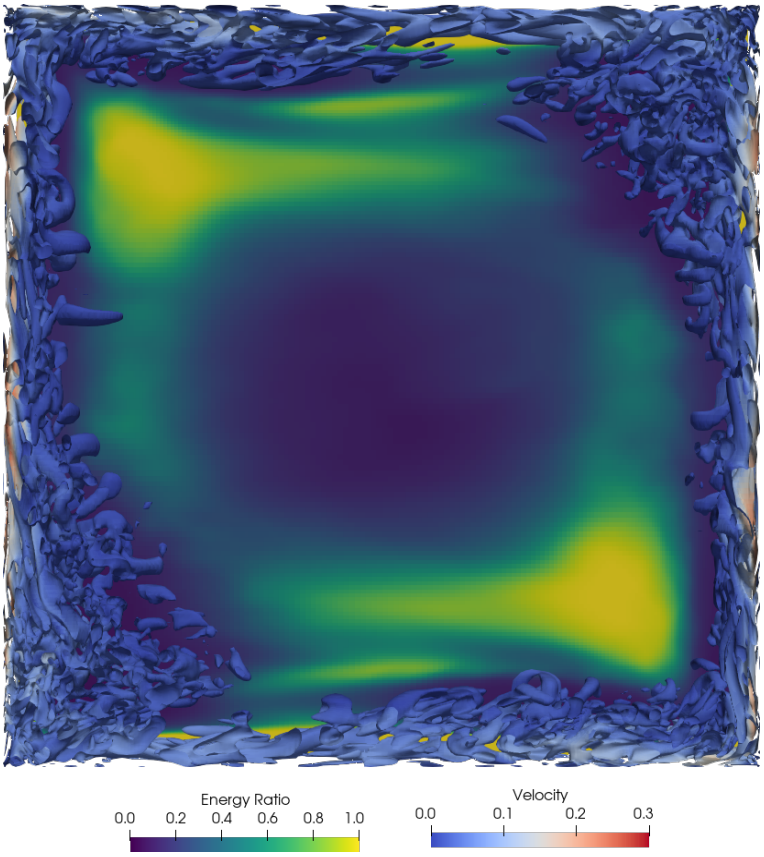

Figure 5.8.: Q-criterion of iso-contours at Q=0.1 with countour of the energy ratio in the background

with the aim of alleviating these problems such that the energy ratio is only guided by the Kolmogorov energy ratio, r_K, far from the wall.

5.3. Development of a new shielding function

In this section the steps involved in the development of a new shielding function are presented. As a first step, the developments are made using the channel flow in forced convection regime test case (see Figure 5.9) of Moser et al. (1999) at $Re_\tau = 590$. In the process of developing the new formulation of the HTLES model, Duffal (2020) explored several formulations of the shielding functions such as,

- the shielding function of the DDES model, f_d (Spalart et al., 2006)

$$f_d = 1 - \tanh[(C_d r_d^p)] = \begin{cases} 1, \text{ if } r_d << 1 \\ 0, \text{ elsewhere} \end{cases}, \text{ where } r_d = \frac{\nu + \nu_{\text{sfs}}}{\sqrt{1/2(\widetilde{S}^2 + \widetilde{\Omega}^2)C_\kappa^2 d_w^2}} \tag{5.89}$$

- the various shielding functions seen in IDDES (Shur et al., 2008)

- the blending functions defined in the $k\omega$-SST model

- using the integral length scale in the kernel of the shielding function

$$\xi_L = C_1 \frac{k^{3/2}/\varepsilon}{d_w} \tag{5.90}$$

- the use of elliptic blending equation of the EB-family of models (Manceau et al., 2002)

$$f_s = \alpha^p, \text{ where } \alpha - L^2 \nabla^2 \alpha = 1 \tag{5.91}$$

with the length scale, $L = C_L \max\left(k^{3/2}/\varepsilon\ ;\ \ C_\eta(\nu^3/\varepsilon)^{1/4}\right)$

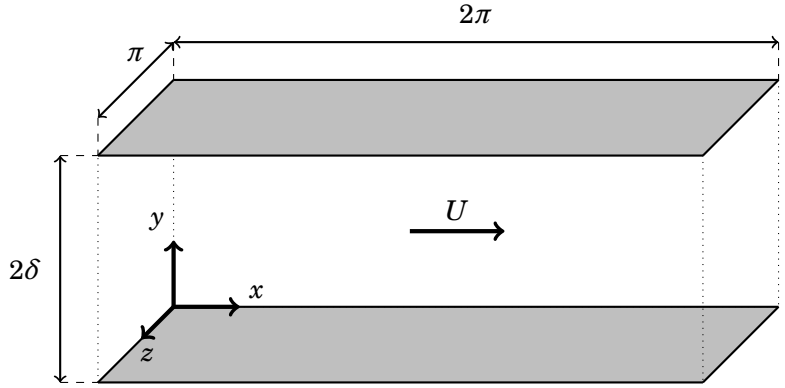

Figure 5.9.: Illustration of a forced channel flow

These functions were forgone for one or both of the following reasons:

- due to their dependence on the mesh

- due to the additional complexity introduced with their incorporation

However, in the present thesis the elliptic shielding, $f_s(\alpha)$, path is further explored. To note, a shielding function based on the elliptic blending equation has already been implemented in the context of TPITM by Fadai-Ghotbi et al. (2010a) with $p = 2$ in Equation (5.91). Furthermore, the same was implemented in the $k\omega$-SST HTLES by Afailal et al. (2019) by adding an additional elliptic blending equation to the model.

The motivation to use the elliptic shielding in the present thesis boils down to the need for a robust shielding function that does not influence the model in the regions far from the boundaries. The advantage of the elliptic blending equation in this regard is that the variable α, being the solution to the elliptic equation, is forced to 1 far from the wall since whatever the length scale L, the solution of the elliptic equation (see Equation (5.91)) goes to 1 when the distance to the wall is large compared to L. In other words, the wall distance is implicit in the elliptic equation and such equations are used for the computation of wall distances in complex geometries in many industrial codes, for instance in the open source CFD software *Code_Saturne* (Archambeau et al., 2004). This can be further noted by the analytical solution for α given for a semi-definite domain bounded by a wall located at $y = 0$ and for a constant L, which writes,

$$\alpha = 1 - \exp\left(-\frac{y}{L}\right) \tag{5.92}$$

The choice of the length scale, L, is an important factor for the elliptic shielding function. In the EB-RSM formulations, the length scale is a comparison between the Kolmogorov and the integral length scales in order to have the correct near wall behaviour for the model. It is important to note that our purposes for the use of the elliptic equation are solely for its use as a shielding function and not to model the physics directly. As such, the elliptic equation is reformulated with the following considerations,

- the presence of the integral length scale, $k^{3/2}/\varepsilon$, poses issues since it is dependent on the grid due to the dependence of resolved kinetic energy on the grid and hence the

total kinetic energy, $k = k_m + k_r$.

- akin to the choice made for the grid-independent shielding function by Duffal (2020), the Kolmogorov length scale is chosen for the implementation of the elliptic shielding in this thesis.

Thus the shielding function can be formulated as,

$$f_s = \alpha^p, \text{ where } \alpha - L_s^2 \nabla^2 \alpha = 1 \tag{5.93}$$

with the length scale, $L_s = C_s(\nu^3/\varepsilon)^{1/4}$. The constants C_s and p need to be calibrated. In order to match the rest of the criteria set forth by Duffal et al. (2022) for the definition of a grid-independent shielding function in Section 5.1.3, the focus of the calibration of the constants was such that the new elliptic shielding should match the original shielding function, $f_s(\xi_K)$, in both the rate of transition and the point at which the transition occurs in a channel flow in forced convection regime.

Using the channel flow database of Moser et al. (1999) *a priori* tests were conducted whereby the elliptic equation was solved using the open-source finite volume code *FiPy* (Guyer et al., 2009) based on the python programming language (van Rossum, 1995). The forced channel flow is reduced to a 1-D problem thanks to the periodicities in the stream-wise and span-wise directions, and the elliptic equation is solved on a 1-D grid in the implicit form as shown below,

$$\nabla^2 \alpha = \frac{\alpha - 1}{L_s^2} \tag{5.94}$$

These tests being extensive in nature are not shown here for the sake of brevity; results for the case of $C_s = 16$ and $p = 40$ are plotted in Figures 5.10 and 5.11. The conclusions for the calibration of C_s and p in the formulation as in Equation (5.93) are as follows:

- the point of switch from RANS to LES can be controlled by varying C_s to match $f_s(\xi_K)$
- the rate of transition is controlled by the parameter p

- the rate of transition of the shielding function is too slow compared to $f_s(\xi_K)$
- p needs to be assigned very high values > 100 to be able to match the rate of transition obtained by the hyperbolic tangent function used in $f_s(\xi_K)$

In lieu of assigning such high values for p, further tests were conducted leading to the formulation of the elliptic shielding of the form,

$$f_s = f_s(\xi_\alpha) = 1 - \tanh(\xi_\alpha), \text{ where } \xi_\alpha = \frac{1 - \alpha^{p1}}{\alpha^{p2}} \tag{5.95}$$

with the length scale, $L_s = C_s(\nu^3/\varepsilon)^{1/4}$. The idea behind this formulation is to use the solution of the elliptic equation, α, to replicate the kernel, ξ_K, of the shielding function in Equation (5.67). In doing so, the rate of transition can be better aligned with that achieved by Duffal (2020), while still taking advantage of the properties of the elliptic equation. To that end the coefficients were calibrated to be $C_s = 13$ and $p1 = p2 = 40$.

In comparing the results from the elliptic shielding functions $f_s(\alpha^p)$ and $f_s(\xi_\alpha)$, with that obtained from $f_s(\xi_K)$, it can be seen from Figure 5.10 that the mean velocity profiles are well predicted using both the new shielding functions. However, the rate of transition obtained with $f_s(\alpha^p)$ is too slow, thus extending the transition region. Additionally the switch from RANS to LES starts much closer to the wall in comparison. Furthermore, Table 5.3 provides some quantitative data in support of the observations made from the plots. f_s-start shows the point at which the shielding function deviates from 0, defined as y^+ at $f_s > 0.01$. f_s-end shows the point at which the shielding function is almost equal to 1, defined as y^+ at $f_s > 0.95$. $f_s = 0.5$ shows the point at which the shielding function is equal to 0.5, defined as y^+ at $f_s = 0.5$. f_s-rate gives the slope of the shielding function at $f_s = 0.5$, which highlights the rate of transition set by the shielding function. The data shows that the shielding function $f_s(\alpha^p)$ behaves vastly different to that of the original shielding function $f_s(\xi_K)$ with a slower rate of transition in addition to the start of the transition being quite close to the wall. The results obtained using $f_s(\xi_\alpha)$ are in much better

agreement to the original shielding function which is further confirmed by the Figure 5.11 comparing the kinetic energy partitions.

In conclusion, keeping in line with the criteria set for the shielding function set by Duffal (2020) (see Section 5.1.3) the computations for the natural convection flows are done using the shielding function $f_s(\xi_\alpha)$ defined by Equation (5.95). The issue observed previously in natural convection flows where the model switched between RANS and LES abruptly (Figures 5.7 and 5.8) due to the misbehaviour of the shielding function is now fixed as can be seen in Figure 5.12, obtained using the HTLES model with the new shielding function. Additionally, it can be seen also from Figure 5.12 that the grid-dependent shielding function $f_s(\xi_D)$, remains inactive in the simulations of the square DHC. Note that, $f_s(\xi_D)$ seen in Figure 5.12 is computed for the purpose of demonstration and will not be a part of the formulation of the HTLES model for natural convection flows used henceforth. Finally, a global view of the simulation domain seen in Figure 5.13, emphasises the fact that the model now behaves as intended with the shielding function only being active in the near wall regions.

Table 5.3.: Comparison of the $k\omega$-SST HTLES simulations with different shielding functions

CASE	f_s-start	f_s-end	$f_s = 0.5$	f_s-rate
$f_s(\xi_K)$	114.63^+	152^+	7.83	277^+
$f_s(\xi_\alpha)$	103.88^+	152^+	5.57	256^+
$f_s(\alpha^p)$	76.49^+	166^+	3.69	348^+

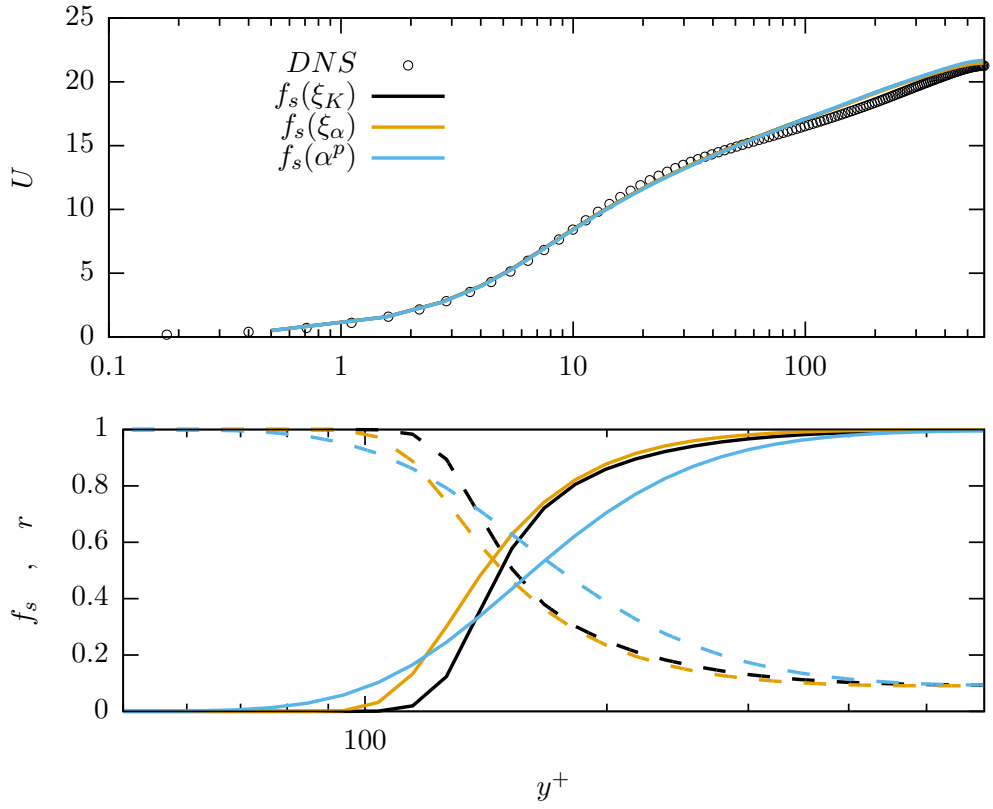

Figure 5.10.: TOP: Profiles of mean velocity
BOTTOM: profiles of the shielding function and energy ratio (dashed lines)

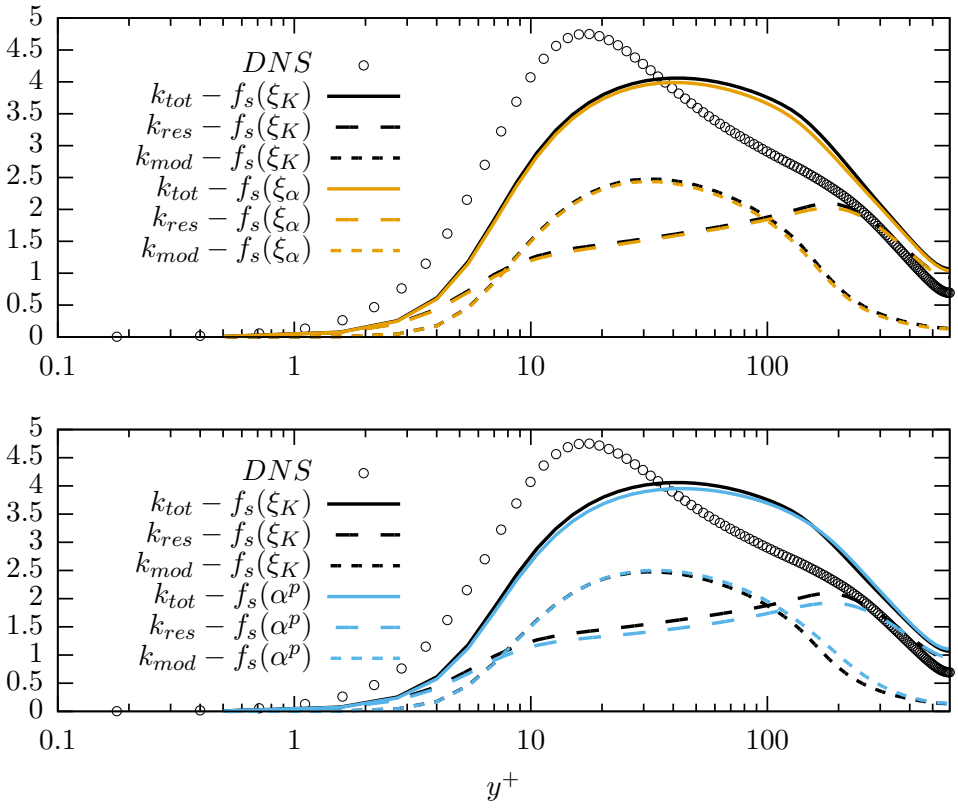

Figure 5.11.: TOP: Comparison of the kinetic energy partition b/w $f_s(\xi_K)$ and $f_s(\xi_\alpha)$
BOTTOM:Comparison of the kinetic energy partition b/w $f_s(\xi_K)$ and $f_s(\alpha^p)$

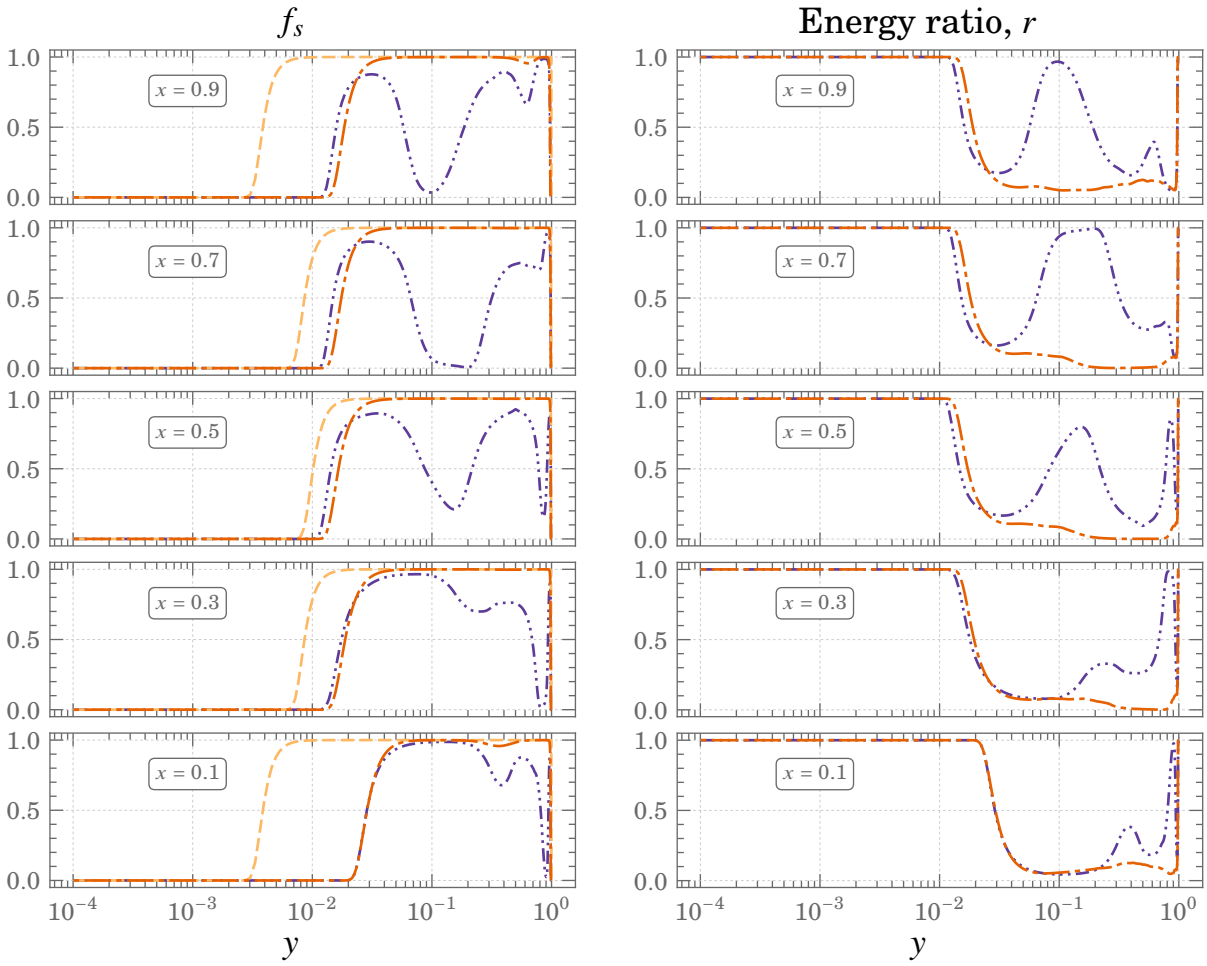

(a) Shielding function, f_s

(b) Energy ratio, r

Figure 5.12.: Behaviour of the shielding functions and the resulting energy ratio imposed by the model in a Square DHC at $Ra = 10^{11}$

$f_s(\xi_D)$ $f_s(\xi_K)$ $f_s(\xi_\alpha)$

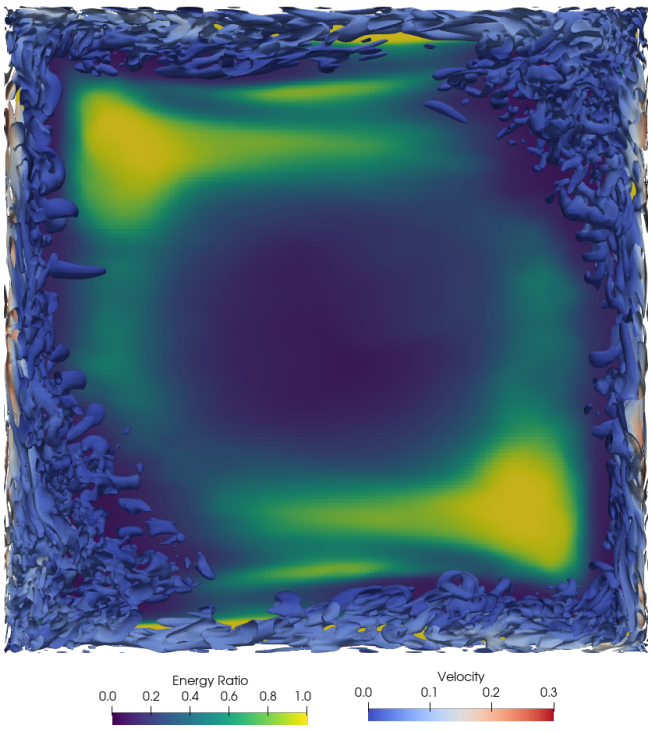

(a) simulation with $f_s(\xi_K)$

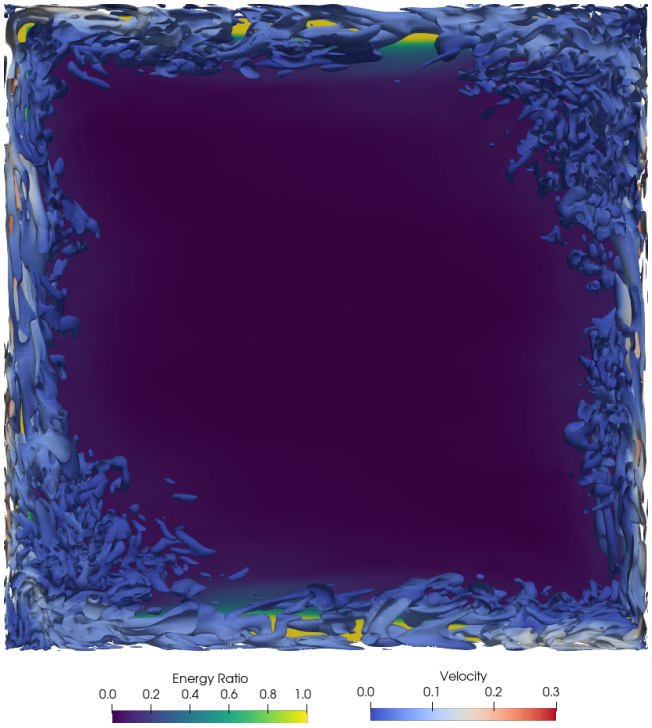

(b) simulation with $f_s(\xi_\alpha)$

Figure 5.13.: Q-criterion of iso-contours at Q=0.1 with countour of the energy ratio in the background

5.4. Validation of the new HTLES approach in square DHC

With the new shielding function described in the previous section, which led to a reduced influence of empiricism in the HTLES model thanks to the alleviation of the influence of the shielding function far from the wall, the current section is dedicated to the presentation of the results obtained using the $k\omega$-SST HTLES model in the square DHC. A particular focus is made on the influence of the buoyancy sensitisation of the underlying RANS model as described in Chapter 4.

5.4.1. Performance of the buoyancy sensitised HTLES model

The square differentially heated cavity is chosen as the test case to analyse the performance of the HTLES model due to the very high Rayleigh number achieved in the DNS benchmark and thus a high level of turbulence observed. To recall, the core idea behind the use of hybrid RANS/LES models is to improve upon the mean flow as compared to RANS while still have the ability to resolve unsteady motion which can provide valuable information in the design and development process. It was seen that RANS simulations for the square cavity already present some level of unsteady motions, which is observed even on refined grids. The test case is thus ideal for the development of hybrid strategies for natural convection flows in order to asses their advantages and disadvantages, particularly in regards to the influence of the higher resolution of unsteady motion on flow statistics. The RANS models discussed previously form the basis for the HTLES model, with different levels of accounting for the effects of buoyancy namely: SGDH, GGDH, and Full buoyancy extended model (FBE). This section compares the predictions of the $k\omega$-SST HTLES models derived from these different RANS closures in order to identify the importance of accounting for buoyancy effects in the modelled motion. Profiles are plotted at 9 locations along the height of the cavity ranging from $0.1 \leq x \leq 0.9$ up to half the wall-normal direction from the hot wall since the test case presents centrosymmetry.

Global hybrid methods rely on various functions to control the compartmentalisation of

energy between modelled (RANS) and resolved (LES) motions. In the HTLES model, the energy ratio is first estimated using the Kolmogorov hypothesis of the equilibrium Eulerian spectrum. However, using this as a control parameter causes the model to switch from RANS to LES mode too close to the wall, additionally, r_K is highly dependent on the grid refinement. It can be seen from Figure 5.14b that the switch would happen very close to the wall. Close to the wall the Kolmogorov energy ratio is greater than 1, which is not physical, and thus this ratio is limited in the implementation of HTLES such that $r_k = \min(1, r_K)$. In order to avoid a switch very close to the boundaries, a shielding function is defined such that the switch from RANS to LES is made around $y^+ = 100$. This switch is calibrated for an isothermal forced flow in a channel in the preceding sections. As seen in Figure 5.14a, the shielding function delays the switch to LES around $y = 10^{-2}$ for all the profiles, which is approximately $y^+ = 100$. It is interesting to note that the switching point is quite similar to that of a forced channel flow and can be attributed to the fact that the test case presents a high level of turbulence which results in a similar estimate for the Kolmogorov length scale upon on which the kernel of the shielding function is based.

The ratio of energy imposed by the HTLES model is a function of the shielding function and the Kolmogorov energy ratio, such that,

$$r = 1 - f_s + f_s \min(1, r_K) \tag{5.96}$$

As seen in Figure 5.15a, the energy ratio follows the shielding function and the model starts to switch from RANS mode to LES mode. When the shielding function is 1, the imposed energy ratio is equal to $\min(1, r_K)$ which corresponds to the profiles in Figure 5.14b. Figure 5.15b shows the effective ratio of energy of modelled to total kinetic energy observed during the simulations. Although this quantity has no impact on the simulation itself since the switch from RANS to LES is dictated by Equation (5.96), its analysis provides some interesting insights. It can be noted that the modelled energy composes of just under 50% of the total energy at its peak and starts to reduce once the switch to LES mode has begun.

Unlike the imposed energy ratio (Equation (5.96) and fig. 5.15a), r_{eff} does not go to 1 at the wall since both k_{mod} and k_{res} go to zero and the ratio $r_{eff} = k_{mod}/(k_{mod} + k_{res})$ can possibly have any value. However, since k_{mod} goes to 0 at the wall faster than k_{res} (Figure 5.19) r_{eff} does not present any mathematically undefined behaviour. Furthermore, it can be noted that far from the wall modelled energy does not go completely to zero and has some contribution nearly up to $y = 0.2$ for most of the cavity heights. The effective energy ratio corresponds well with that of the imposed energy ratio, after the switch, with qualitatively very similar trends noticeable in both plots. Moreover, the buoyancy model used in the RANS equations have an effect on the turbulence scales which is evident in the effective energy ratio, r_{eff}, at cavity heights $x < 0.5$. This is further noticeable in Figure 5.19 where the modelled energy contribution of FBE > GGDH > SGDH, whereas the contrary is true for the resolved energy (SGDH > GGDH > FBE).

The mean velocity profiles are plotted in Figure 5.16a. The profiles for velocity are well predicted by HTLES model with negligible differences between the different buoyancy models implemented. The velocity is over predicted very close to the wall where the model is in RANS mode, the same behaviour was observed with the RANS models analysed previously. The velocity profiles are under predicted in the region of the switch from RANS to LES, however, this misprediction reduces consistently towards the top of the cavity.

The temperature profiles plotted in Figure 5.16b show excellent agreement with the DNS reference in the regions where the HTLES is model is in LES mode ($y > 10^{-2}$). In the near wall region where the model is fully in RANS mode the temperature profiles are slightly over predicted, just as in the case of the velocity profiles. Further it can be seen from Figure 5.17, which shows the temperature stratification, that the predictions of the HTLES model is in excellent agreement with the DNS data. Again, as is the case for the velocity profiles, there is negligible influence of the buoyancy model used.

The contributions of the modelled and resolved parts of the various turbulent quantities can be studied to better understand the behaviour of the model. The total kinetic energy profiles plotted in Figure 5.18a show excellent agreement with DNS at cavity height $x \leq 0.2$.

At cavity heights $x > 0.2$, the model exhibits an under prediction very close to the wall but the energy increases rapidly until $y = 10^{-2}$. This is due to the presence of resolved structures that seep in to the boundary layer as can be seen in the plot for the resolved kinetic energy in Figure 5.19a. This is possible since the HTLES model does not restrict the development of resolved structures in the RANS regions, however their influence is restricted in the hybridisation function through the Internal Consistency Constraint (ICC). The modelled kinetic energy diminishes quickly once the switch to LES mode begins as seen in Figure 5.19b and as previously noted from the plots of the effective energy ratio in Figure 5.15b. Furthermore, due to the under-prediction of turbulent viscosity (Figure 5.24b) the development of unsteady motions are not subdued by the model in the RANS regions.

The profiles of total $\overline{uu}$ shown in Figure 5.18b are over estimated considerably towards the top of the cavity while they agree well with DNS near the bottom of the cavity $x < 0.4$. The overestimation is due to the high amount of resolved $\overline{uu}$ observed, shown in Figure 5.20a. The influence of the buoyancy models can be noted in the resolved profiles of $\overline{uu}$ while no such influence can be seen in the modelled profiles. In contrast to the composition of $\overline{uu}$ where the modelled contribution is far less than that of the resolved contribution, the profiles of $\overline{vv}$ (Figure 5.22) and $\overline{ww}$ (Figure 5.23) show a greater contribution of the modelled parts. Due to a lack in the resolved fluctuations, both $\overline{vv}$ and $\overline{ww}$ are underestimated. The turbulent shear stress (Figure 5.24a) predictions improve gradually towards the top of the cavity with nearly equal contributions of modelled and resolved parts (Figure 5.25) with little influence from the buoyancy models used.

The stream-wise heat flux $\overline{u\theta}$ (Figure 5.26), is predicted well in the top half of the cavity while it is under-predicted in the bottom half with the majority of its contribution coming from the resolved field (Figure 5.27). In particular with SGDH, $\overline{u\theta}$ is zero without stratification and remains weak with stratification as can be seen in Figure 5.27b. The wall normal heat flux $\overline{v\theta}$ (Figure 5.26), is under-predicted for all the profiles with the contribution from the resolved motions (Figure 5.28) being minimal.

Finally, the profiles of wall shear stress (Figure 5.29a) is well predicted for all the buoyancy

models in the fully turbulent regions $x > 0.3$. In the weakly turbulent regions (\(x < 0.3)), however, the wall shear stress is under-predicted. The Nusselt number (Figure 5.29b) is severely under-predicted but marginal improvements are seen for the full buoyancy extended model (FBE) as compared to GGDH and SGDH.

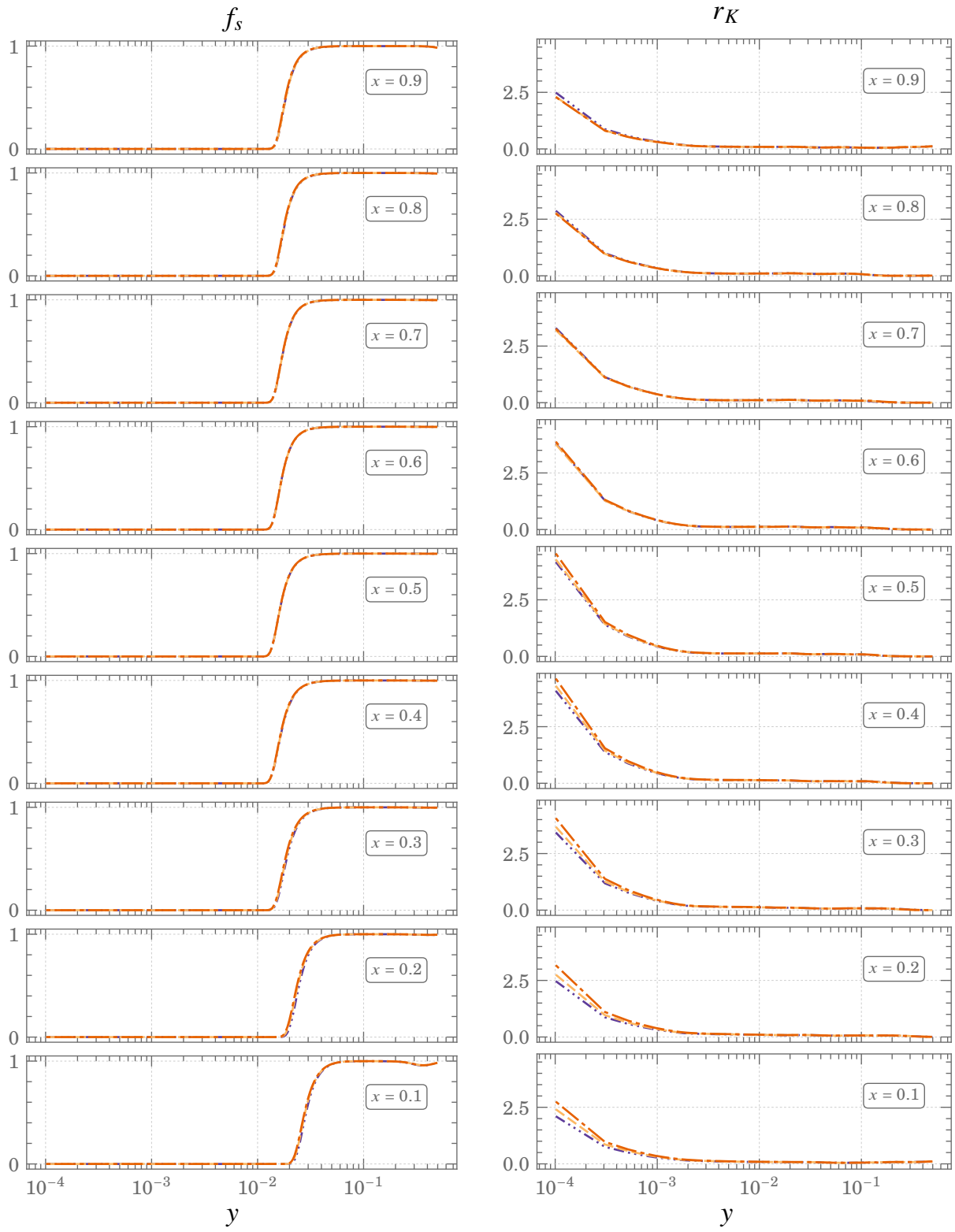

(a) Shielding function, f_s

(b) bounded Kolmogorov energy ratio, r_k

Figure 5.14.: Quantities influencing the energy ratio imposed in the HTLES model for Square DHC at $Ra = 10^{11}$

FBE *GGDH* *SGDH*

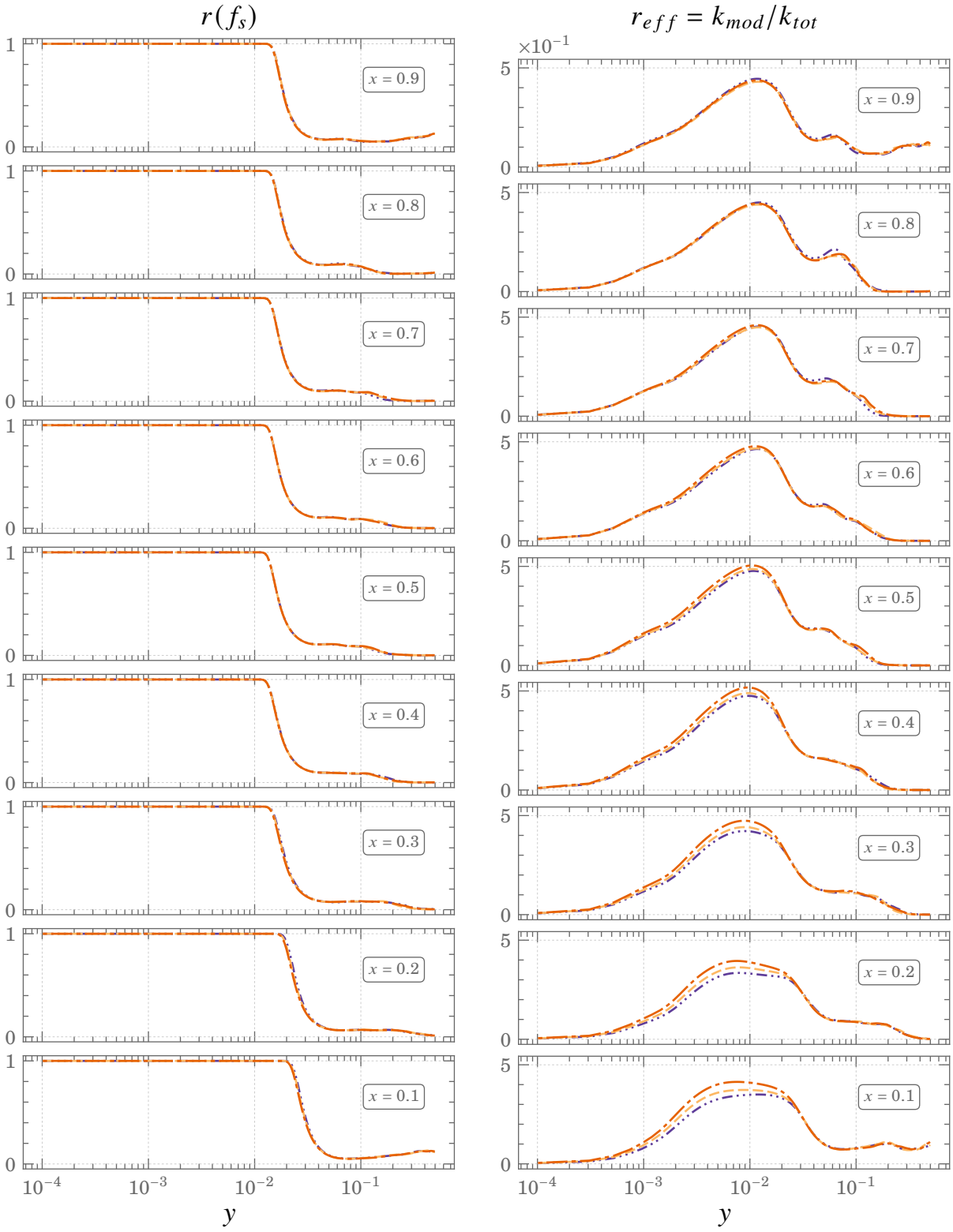

(a) Imposed energy ratio, $r(f_s)$

(b) Effective energy ratio, r_{eff}

Figure 5.15.: Compartmentalisation of the energy ratio, imposed and observed, in the HTLES model for Square DHC at $Ra = 10^{11}$

FBE *GGDH* *SGDH*

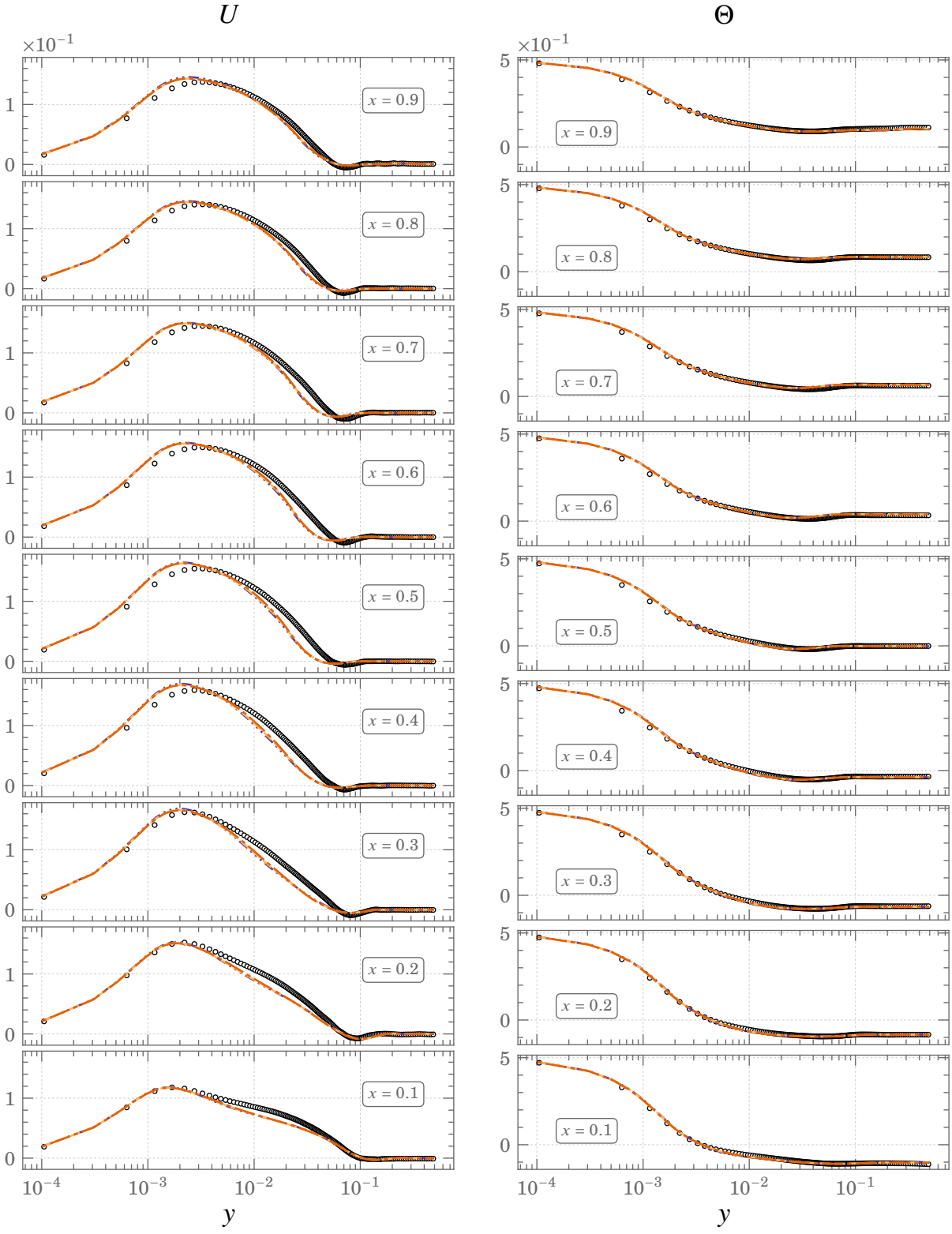

(a) Mean velocity, U

(b) Mean temperature, Θ

Figure 5.16.: Mean velocity and temperature profiles using the HTLES model for Square DHC at $Ra = 10^{11}$

○ ○ ○ *DNS* — *FBE* — *GGDH* — *SGDH*

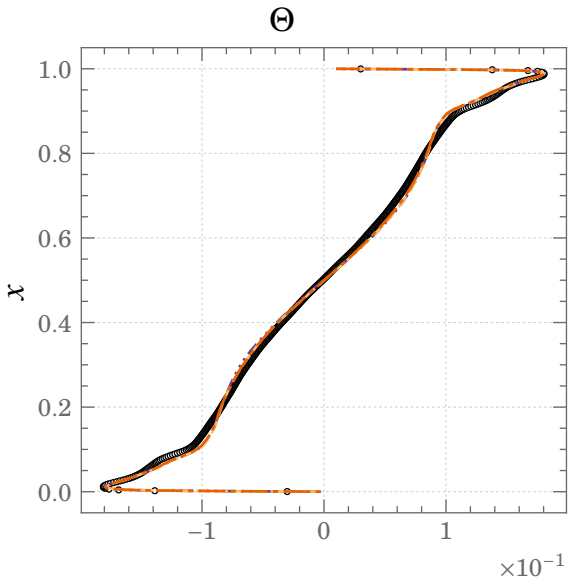

Figure 5.17.: Stratification observed using the HTLES model for Square DHC at $Ra \times 10^{11}$
∘ ∘ ∘ *DNS* *FBE* *GGDH* *SGDH*

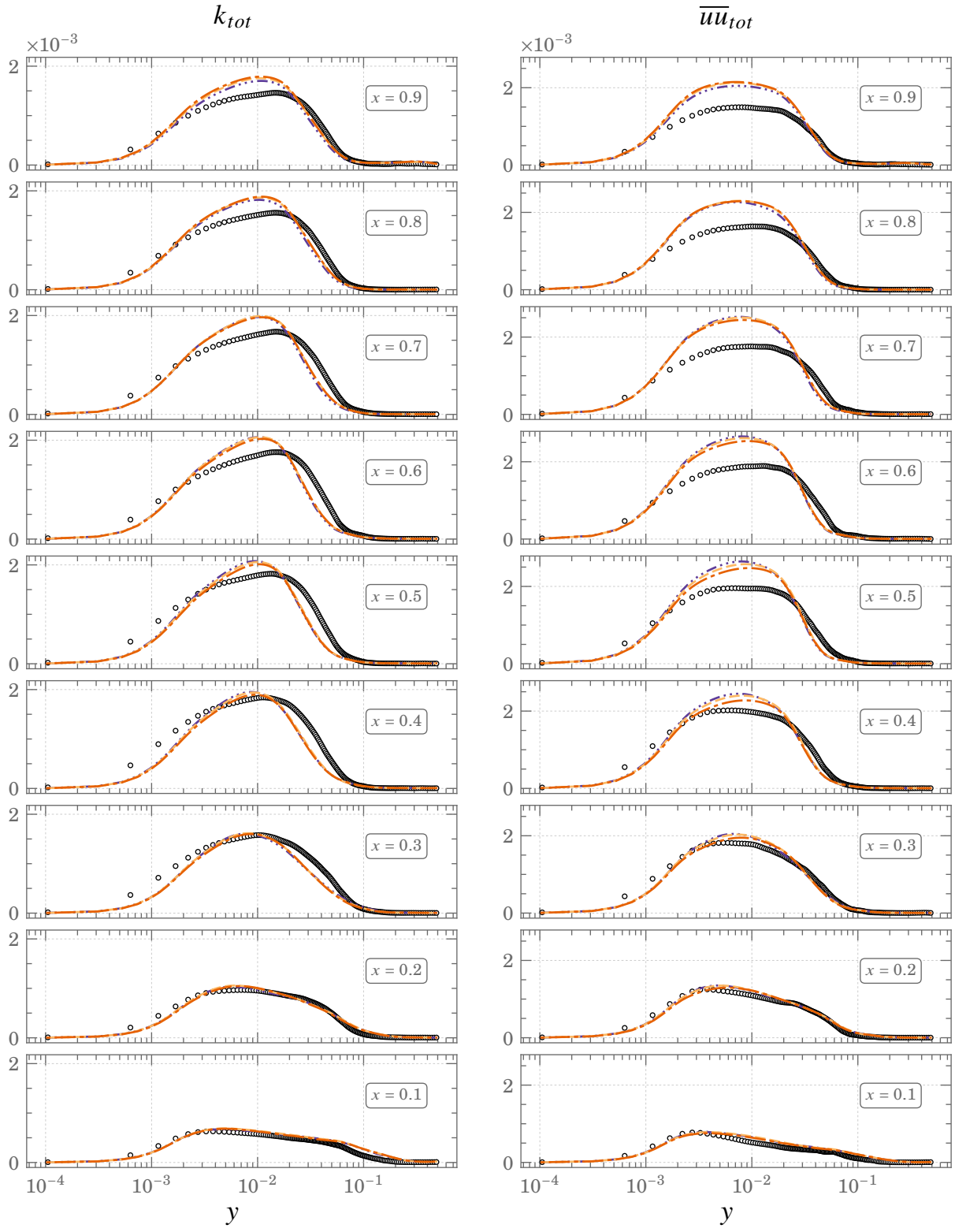

(a) Total kinetic energy

(b) Total $\overline{uu}$

Figure 5.18.: Predictions of tital kinetic energy and total $\overline{uu}$ using the HTLES model for Square DHC at $Ra = 10^{11}$

○ ○ ○ *DNS* — · — *FBE* — — *GGDH* — ·· — *SGDH*

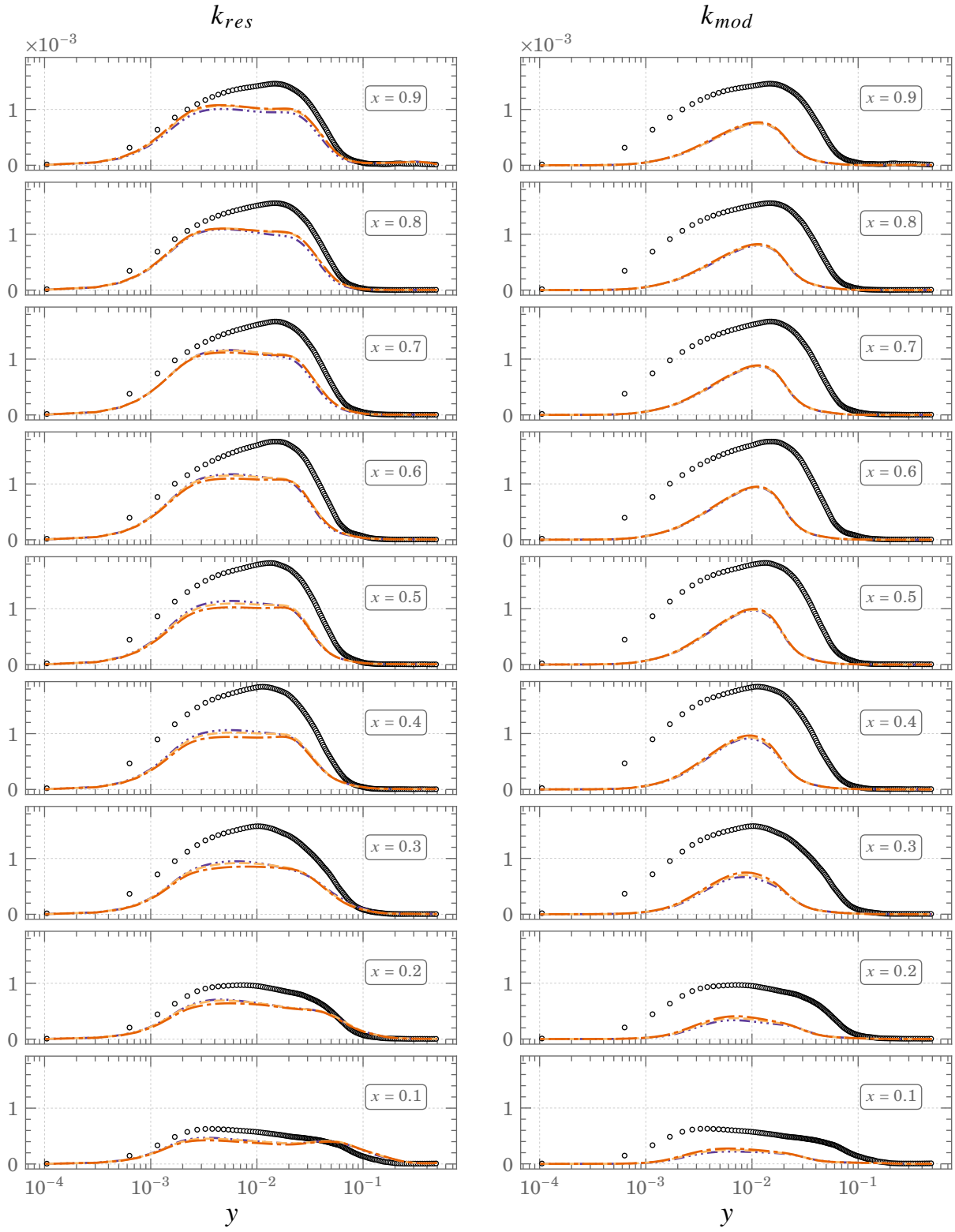

(a) Resolved kinetic energy

(b) Modelled kinetic energy

Figure 5.19.: Resolved and modelled contributions of total kinetic energy using the HTLES model for Square DHC at $Ra = 10^{11}$

$\circ\ \circ\ \circ$ *DNS* — *FBE* — *GGDH* — *SGDH*

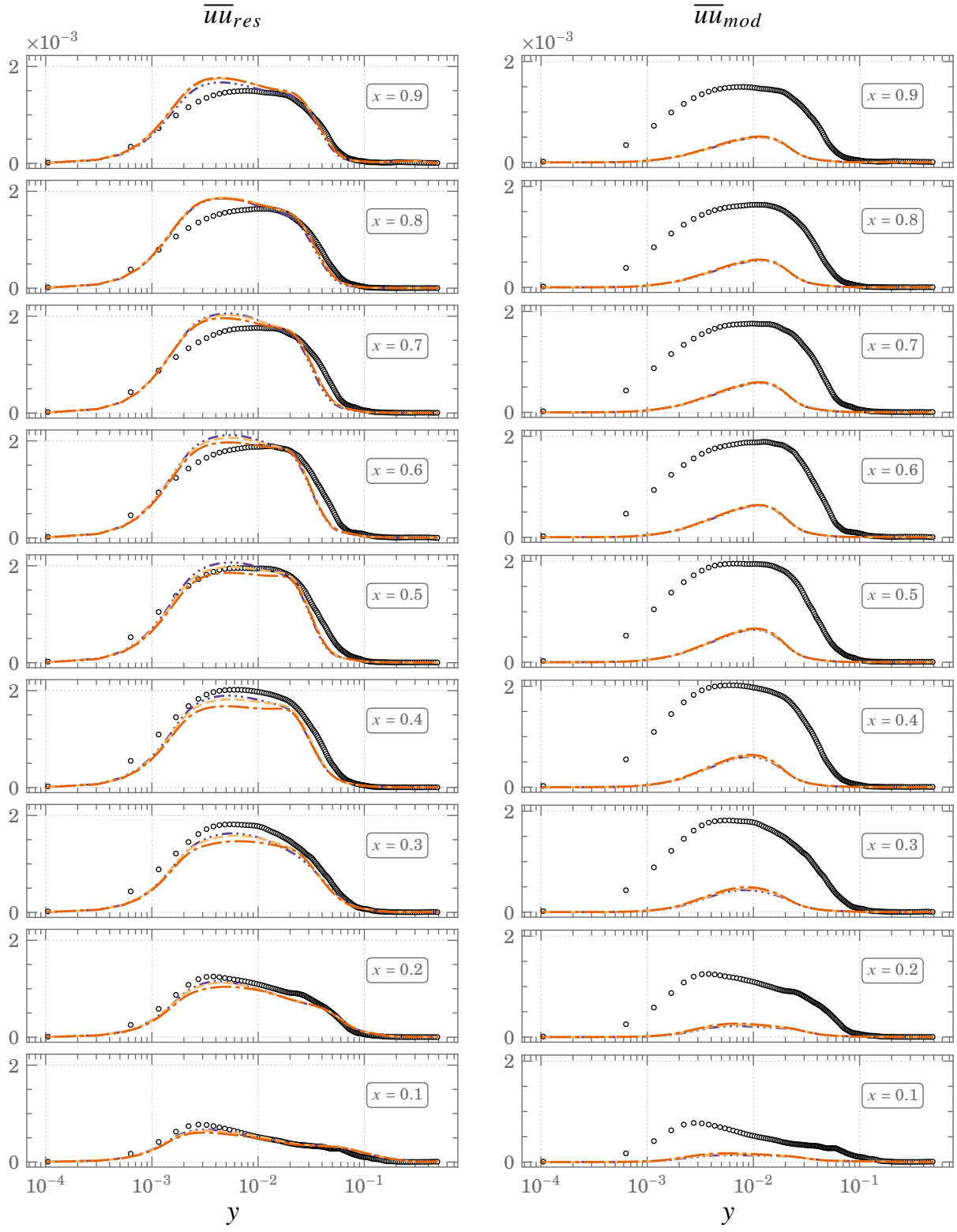

(a) Resolved $\overline{uu}$ (b) Modelled $\overline{uu}$

Figure 5.20.: Resolved and modelled contributions of $\overline{uu}$ using the HTLES model for Square DHC at $Ra = 10^{11}$

○ ○ ○ *DNS* *FBE* *GGDH* *SGDH*

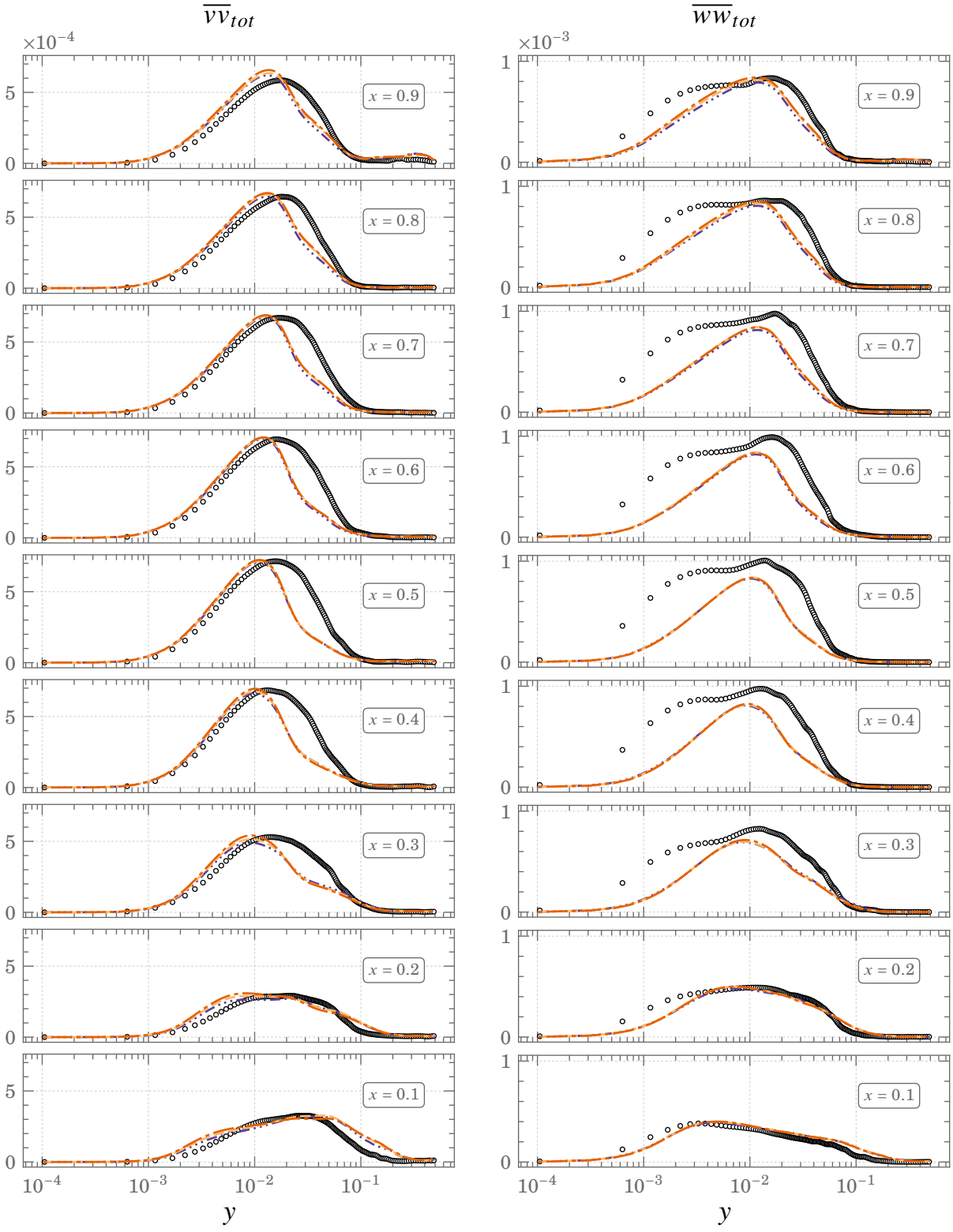

(a) Total $\overline{vv}$ (b) Total $\overline{ww}$

Figure 5.21.: Predictions of total $\overline{vv}$ and total $\overline{ww}$ using the HTLES model for Square DHC at $Ra = 10^{11}$

○ ○ ○ *DNS* *FBE* *GGDH* *SGDH*

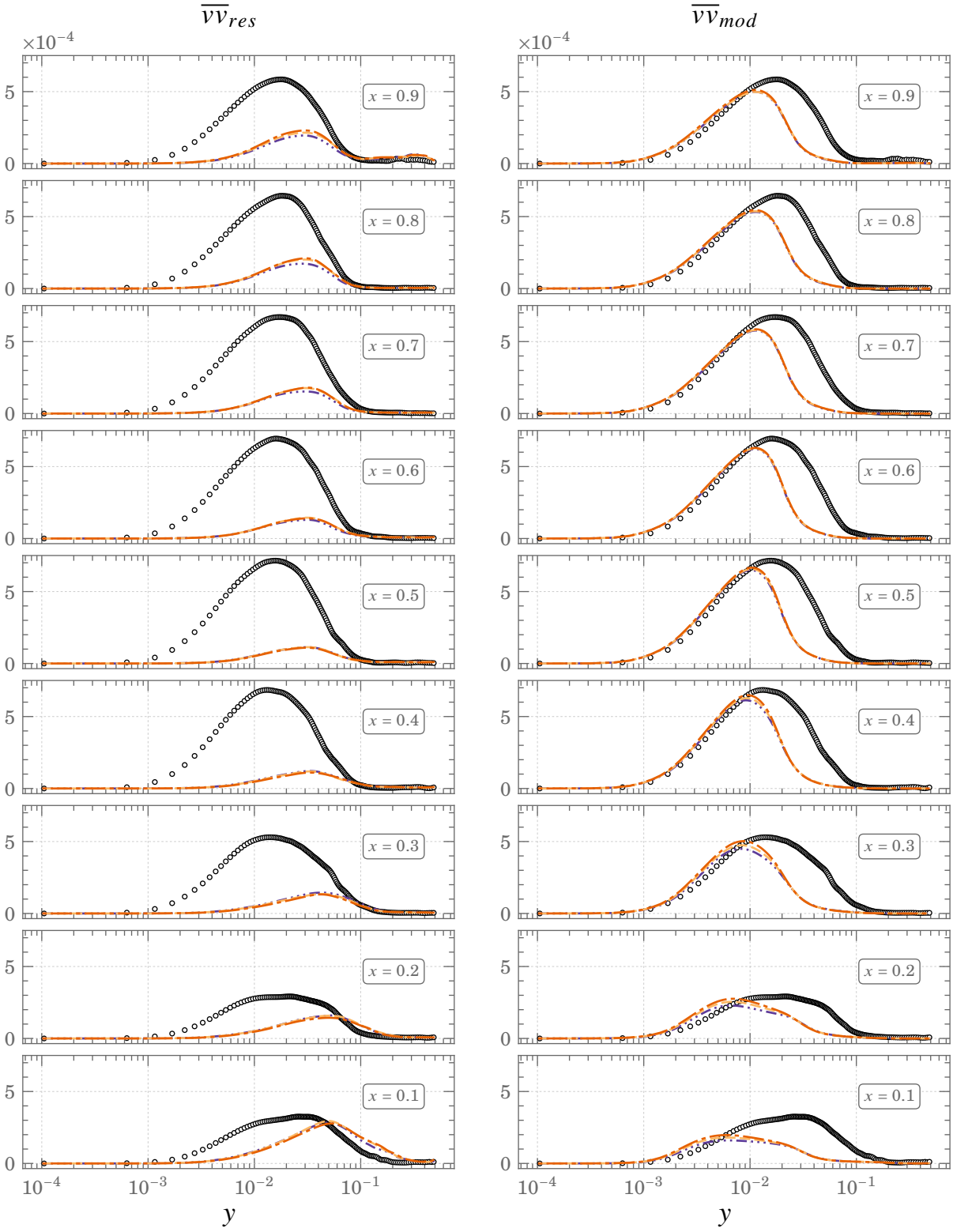

(a) Resolved $\overline{vv}$ (b) Modelled $\overline{vv}$

Figure 5.22.: Resolved and modelled contributions of $\overline{vv}$ using the HTLES model for Square DHC at $Ra = 10^{11}$

○ ○ ○ *DNS* — · — *FBE* – – – *GGDH* — ·· — *SGDH*

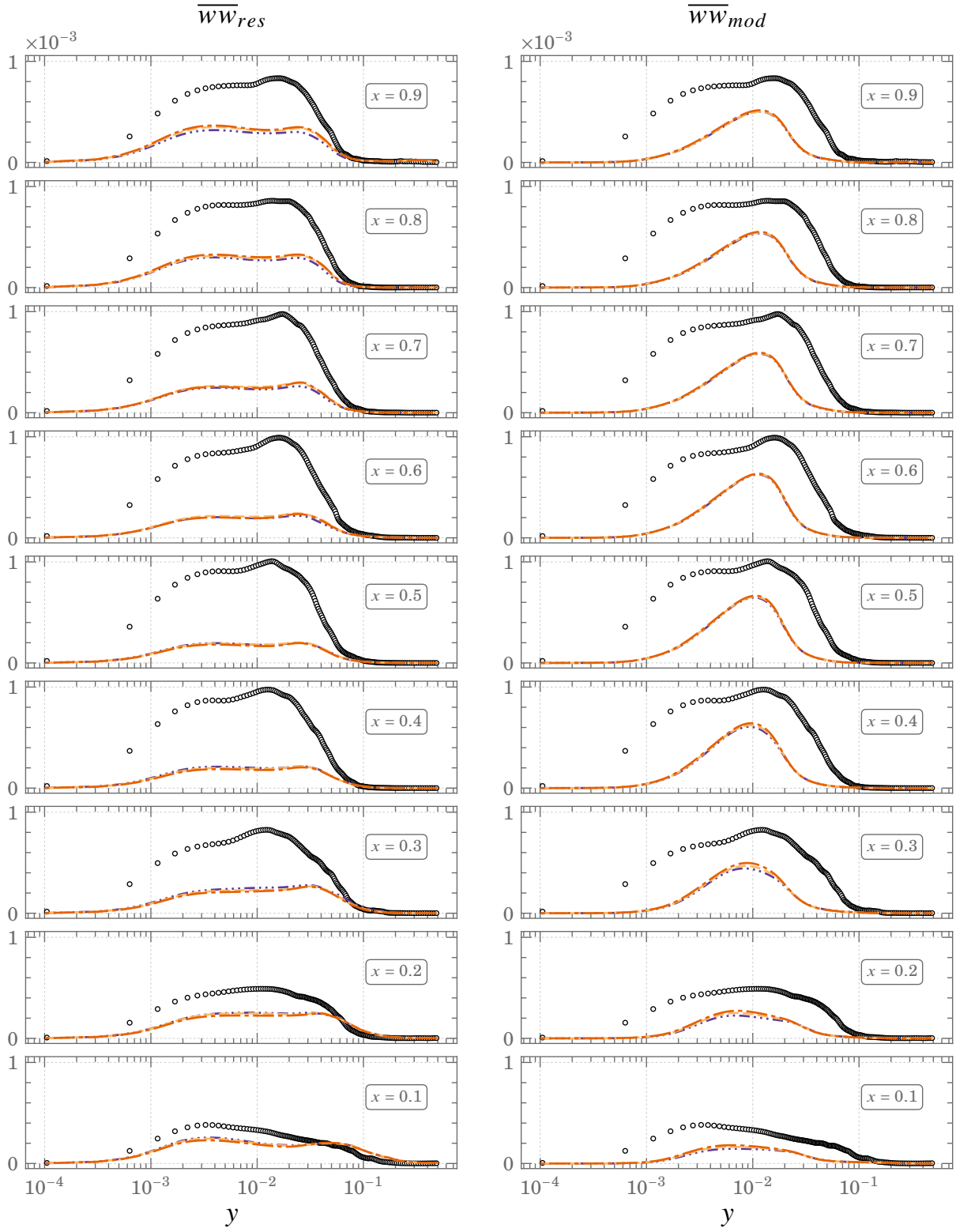

(a) Resolved $\overline{ww}$ (b) Modelled $\overline{ww}$

Figure 5.23.: Resolved and modelled contributions of $\overline{ww}$ using the HTLES model for Square DHC at $Ra = 10^{11}$

DNS FBE $GGDH$ $SGDH$

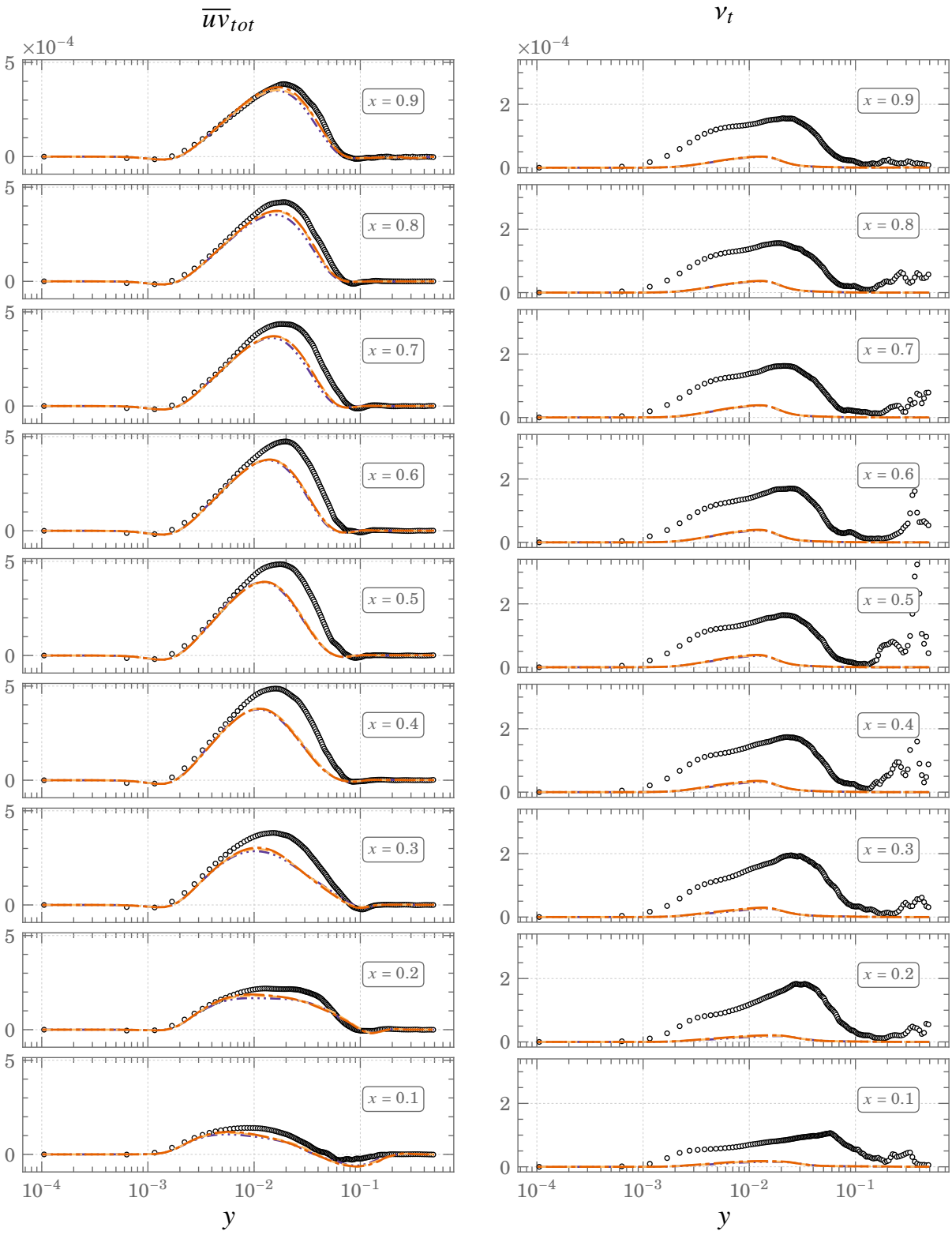

(a) Total $\overline{uv}$

(b) Turbulent viscosity ν_t

Figure 5.24.: Predictions of total shear stress, $\overline{uv}$ and turbulent viscosity, ν_t using the HTLES model for Square DHC at $Ra = 10^{11}$

○ ○ ○ *DNS* — · — *FBE* – – – *GGDH* ··· *SGDH*

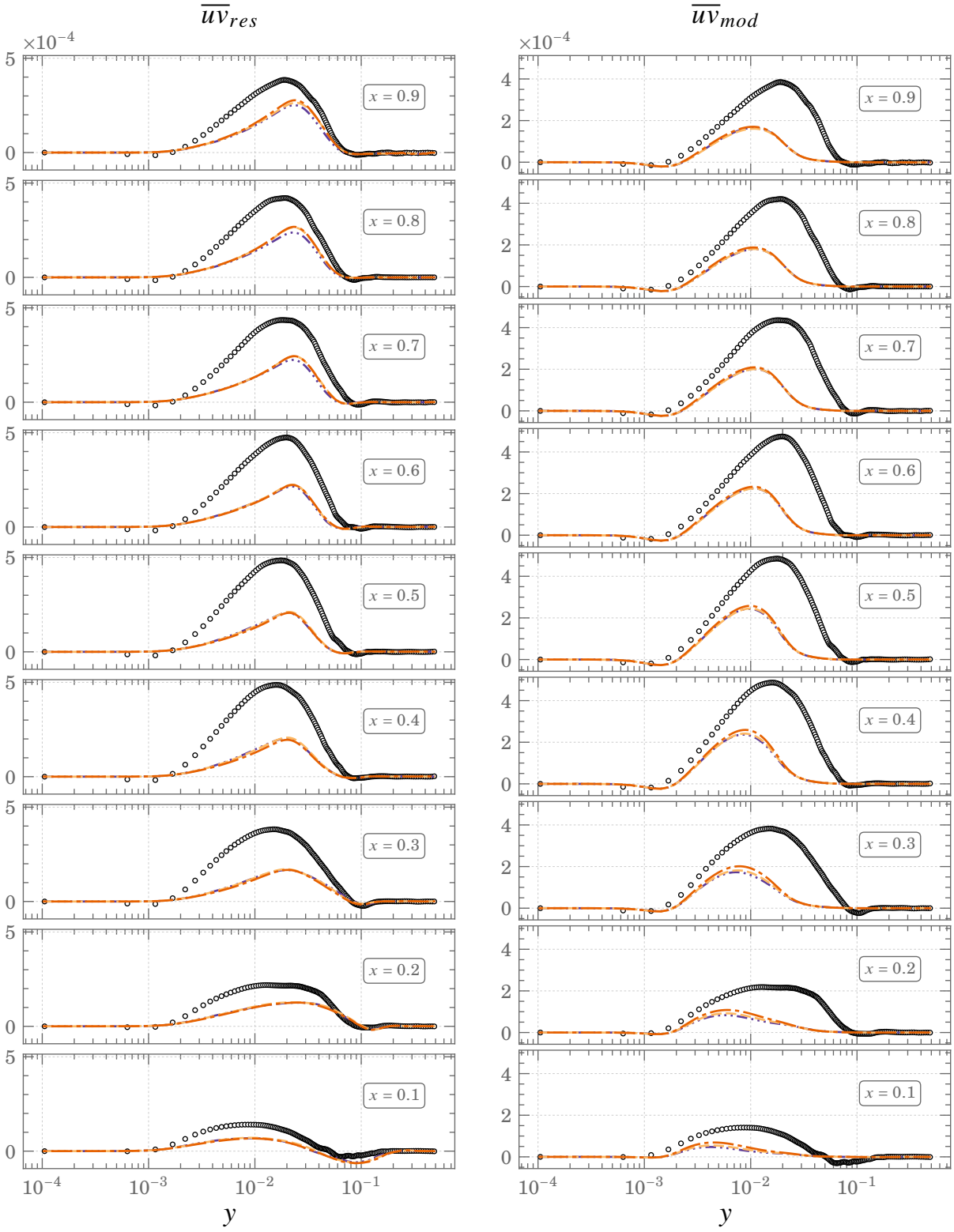

(a) Resolved $\overline{uv}$

(b) Modelled $\overline{uv}$

Figure 5.25.: Resolved and modelled contributions of $\overline{uv}$ using the HTLES model for Square DHC at $Ra = 10^{11}$

$\circ\ \circ\ \circ$ *DNS* — *FBE* — *GGDH* — *SGDH*

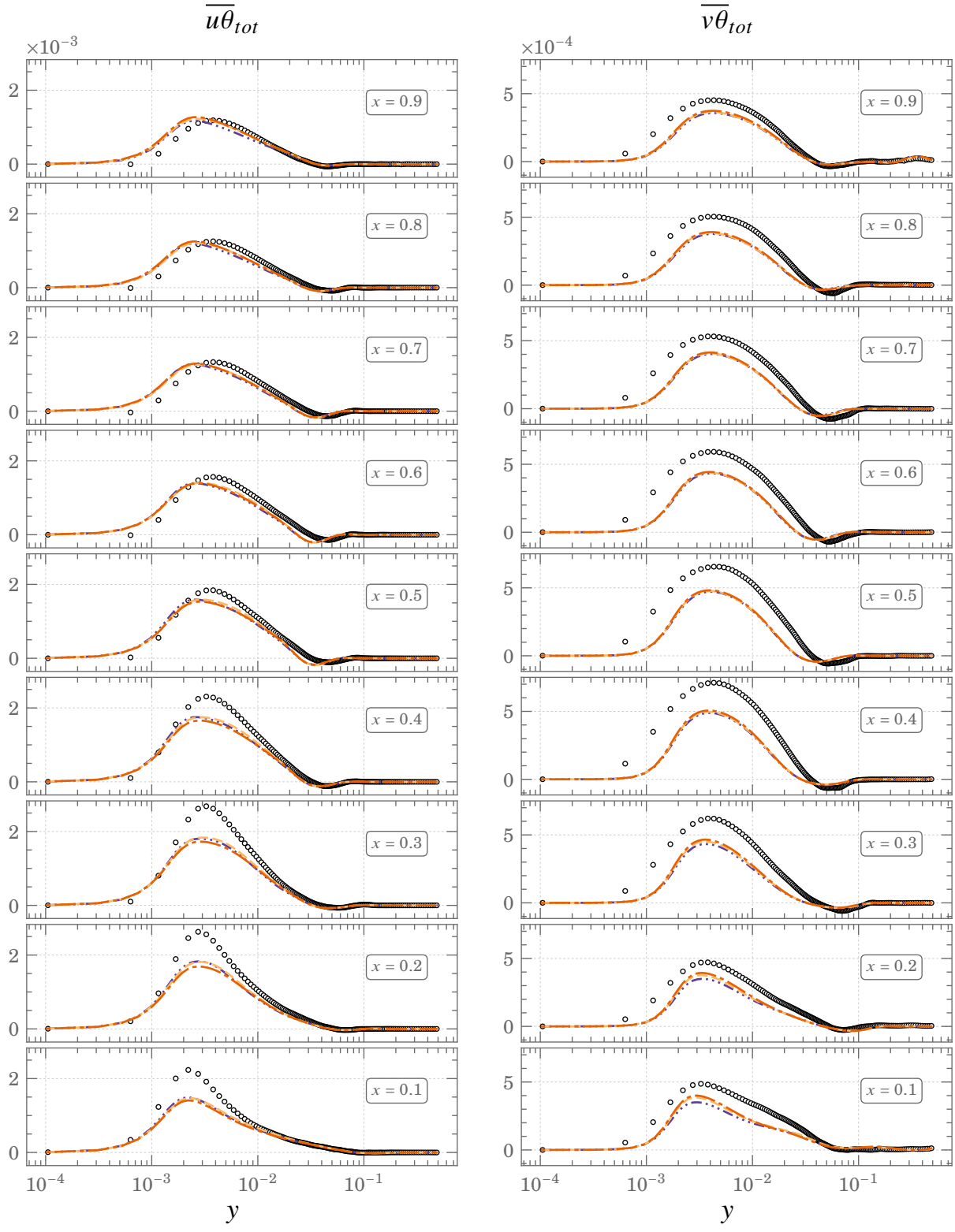

(a) Total $\overline{u\theta}$

(b) Total $\overline{v\theta}$

Figure 5.26.: Predictions of total $\overline{u\theta}$ and total $\overline{v\theta}$ using the HTLES model for Square DHC at $Ra = 10^{11}$

$\circ\ \circ\ \circ$ *DNS* — *FBE* - - *GGDH* ··· *SGDH*

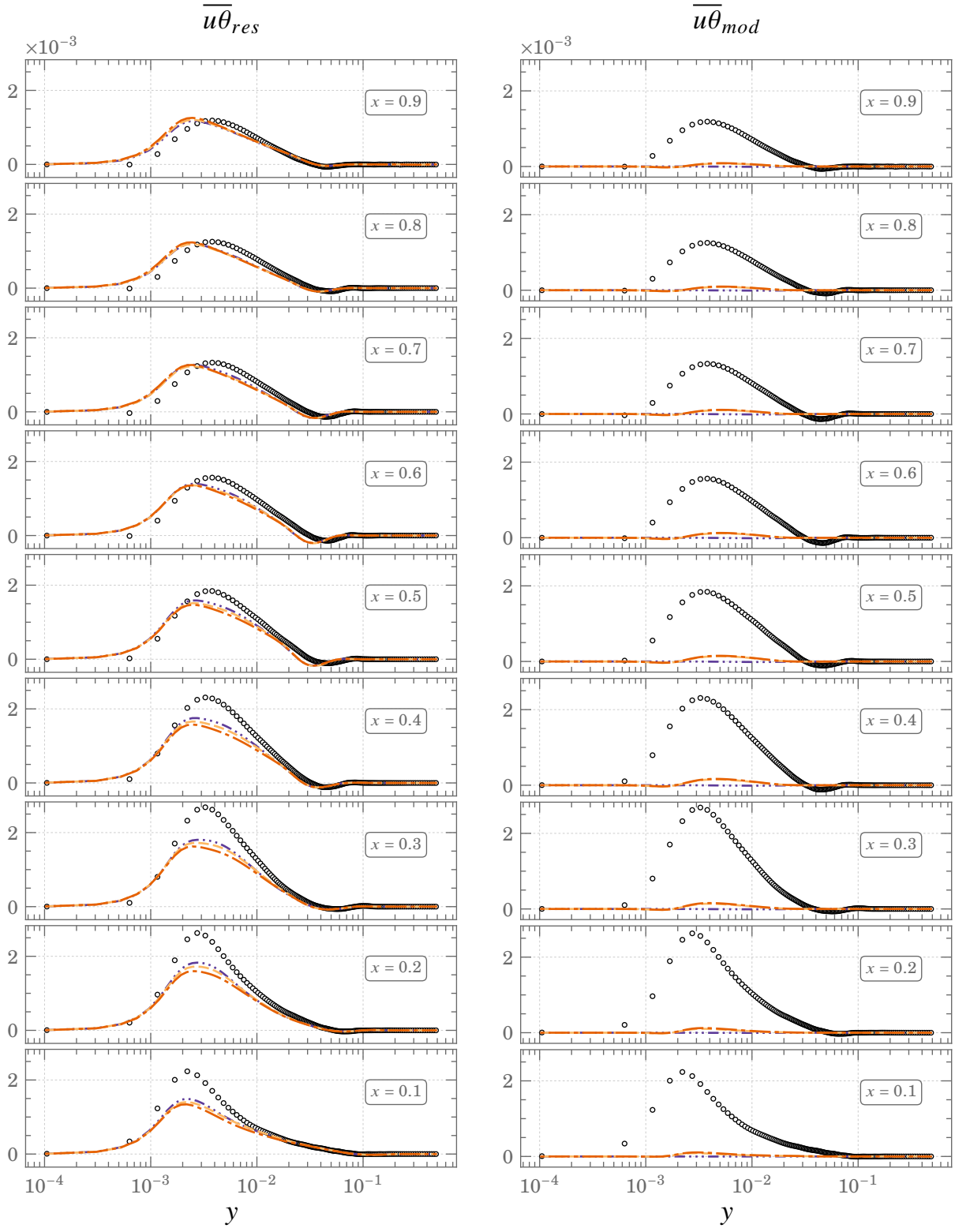

(a) Resolved $\overline{u\theta}$

(b) Modelled $\overline{u\theta}$

Figure 5.27.: Resolved and modelled contributions of $\overline{ut}$ using the HTLES model for Square DHC at $Ra = 10^{11}$

○ ○ ○ *DNS* —·— *FBE* – – – *GGDH* ··· *SGDH*

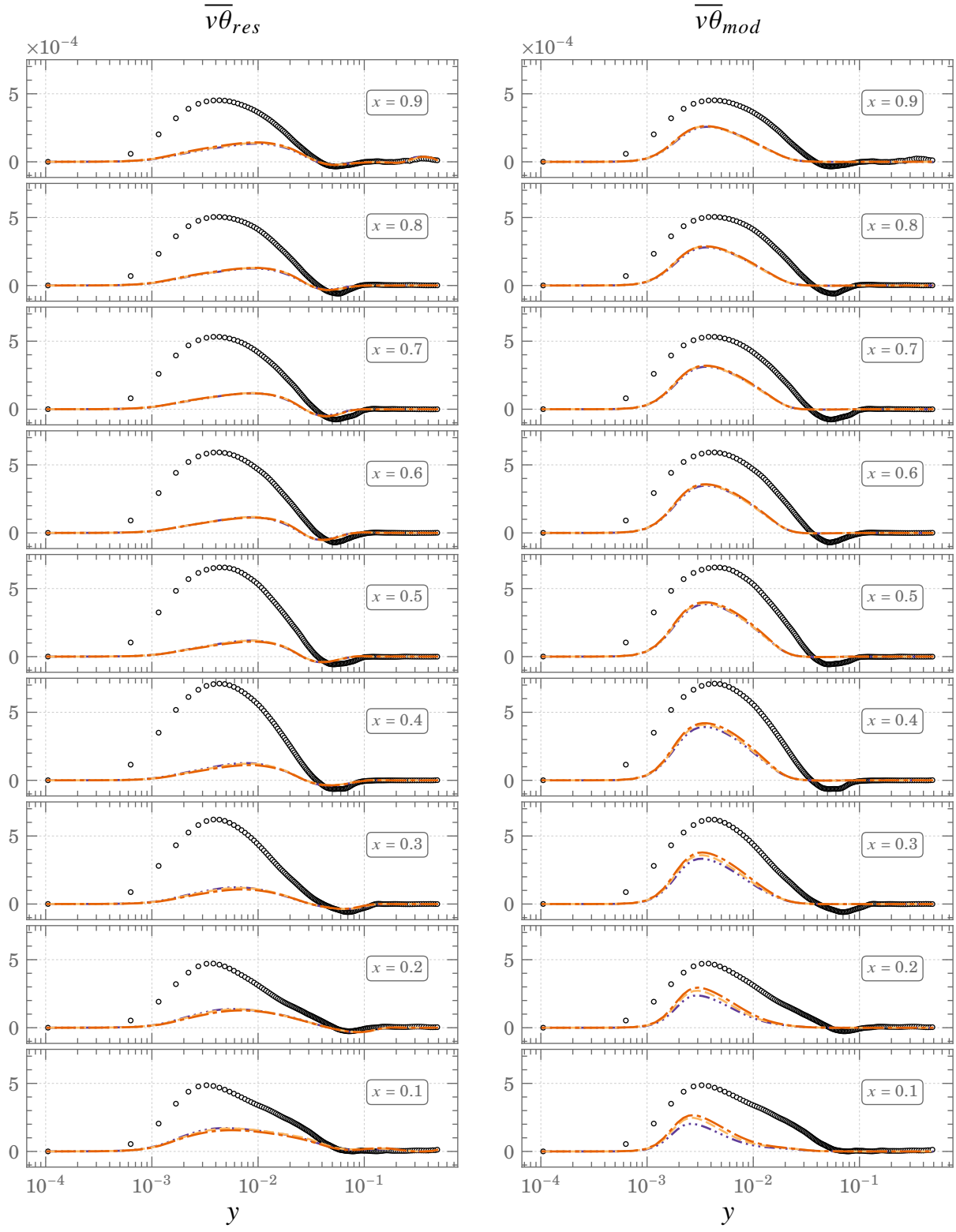

(a) Resolved $\overline{v\theta}$

(b) Modelled $\overline{v\theta}$

Figure 5.28.: Resolved and modelled contributions of $\overline{v\theta}$ using the HTLES model for Square DHC at $Ra = 10^{11}$

○ ○ ○ *DNS* — *FBE* — *GGDH* — *SGDH*

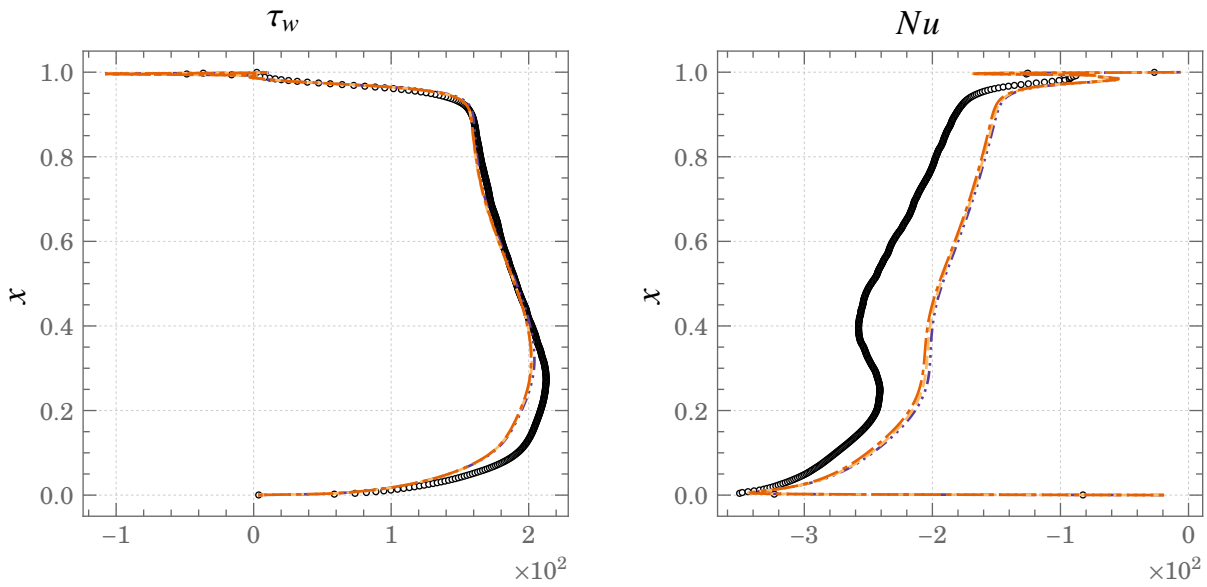

(a) Shear stress, τ_w

(b) Nusselt number, Nu

Figure 5.29.: Profiles of Wall shear stress and Nusselt number at the hot wall using the HTLES model for Square DHC at $Ra \times 10^{11}$

DNS FBE $GGDH$ $SGDH$

5.4.2. Comparison of RANS, HTLES, and LES

In this section the $k\omega$-SST HTLES model sensitised to buoyancy effects using FBE is compared to its RANS counterparts ($k\omega$-SST and BL-v^2/k with FBE shown in Section 4.3) and more importantly to an LES employing the Dynamic Smagorinsky model (Section 2.5.4). We have seen that RANS models are not sufficient for the prediction of natural convection flows and as demonstrated before (Chapter 4), sensitising eddy-viscosity models to buoyancy effects has shown only marginal improvements for the square DHC case. Although more sophisticated models are available (Section 3.6), issues arise concerning numerical stability and the added computational costs of solving additional transport equations. On the other end of the spectrum, LES models are limited in their range of application since complex geometries at large Reynolds/Rayleigh numbers would demand very high computational power. The HTLES model is developed with the aim of achieving a middle ground between these two extremes and as such the following exercise allows to assess if the HTLES model can deliver on these goals. The grids used for the computations compared henceforth are listed in Table 5.4. The LES simulations are performed using the standard defaults of *code_saturne*. The grid presented in Table 5.4 represents the coarsest of the LES computed (see appendix for comparison of the LES grids and models)

Table 5.4.: Grid parameters

Model	Δ_x^+	Δ_y^+	Δ_z^+	N_x	N_y	N_z
RANS $k\omega$-SST FBE	< 1	< 1	-	249	249	1
RANS BL-v^2/k FBE	< 1	< 1	-	332	332	1
HTLES $k\omega$-SST FBE	< 1	< 1	23	332	332	60
LES Dyn. Smag.	< 1	< 1	17	498	498	80

Figures 5.30 to 5.35 show the first and second order quantities along the height of the cavity. Figures 5.36 and 5.37 show the shear stress and Nusselt number profiles along the hot wall and the top wall respectively. Figures 5.38 to 5.41 show the profiles at the mid width of the cavity at $y = 0.5$.

The mean velocity profiles (Figure 5.30) predicted by HTLES are improved considerably

throughout the height of the cavity in comparison to RANS. On the other hand, in comparison to LES the profiles are comparable in the near wall region and far from the wall, $y > 10^{-2}$ where the model switches from RANS to LES (see Figure 5.15a), there is a clear under-prediction of the velocity profiles although this discrepancy diminishes towards the top of the cavity. Interestingly, the mean temperature profiles of HTLES are improved in comparison to both RANS and LES models especially in the stratified core region, which is further evidenced by the mid cavity profile of temperature (Figure 5.38) showing stratification in the cavity.

The kinetic energy profiles are improved compared to RANS but degraded compared to LES since the HTLES model over-predicts the profiles at cavity heights $x > 0.5$ due to $\overline{uu}$ (Figure 5.31b) being largely over-predicted. In regards to the other contributors to the total kinetic energy, as noted in the previous section the contribution to $\overline{vv}$ (Figure 5.22) is mainly due to the modelled part, thus the profiles (Figure 5.32a) suffer particularly in the region of the switch as compared to LES and RANS, whereas, improvements are noted only in the near wall regions compared to RANS. Furthermore, $\overline{ww}$ (Figure 5.32b) shows improvements compared to RANS but insufficiently as compared to LES where the profiles are very well predicted. Due to these factors, it can seen in Figure 5.31a that the total kinetic energy profiles are particularly lacking in the region where the switch from RANS to LES occurs.

The common theme of the HTLES model predictions is that the profiles are improved overall as compared to RANS and the predictions start to be in line with that of LES towards the top of the cavity; this theme is particularly noticeable in the profiles of $\overline{uv}$ (Figure 5.33a). Also, it is interesting to note that the production terms (Figures 5.33b and 5.34b) are better predicted compared to RANS while being quite comparable to the profiles obtained by LES except for the near wall regions.

In regards to the heat fluxes, the profiles of $\overline{u\theta}$ (Figure 5.35a) are drastically improved compared to RANS and well predicted compared to LES at cavity heights ($x > 0.5$). As noted in the previous section (Figure 5.27), these improvements can be attributed to the

unsteady motions penetrating the RANS zones. However, similar to that observed for $\overline{vv}$, the contribution to $\overline{v\theta}$ comes mainly from the modelled part thus the HTLES profiles (Figure 5.35b) are comparable to RANS while being under-predicted compared to LES.

The profiles of shear stress at the hot wall (Figure 5.36a) show considerable improvements compared to both RANS and LES especially at cavity heights $x < 0.6$. The shear stress profiles at the top wall (Figure 5.37a) are in good agreement with LES results, with improvements perceived compared to RANS at $y > 0.3$. Nusselt number profiles (Figure 5.36b) at the hot wall do not present improvements compared to RANS since the contribution to $\overline{v\theta}$ is mainly due to the modelled part in the HTLES model, while the LES performs slightly better but good agreement with DNS is seen only close the top and bottom of the cavity. Furthermore, the Nusselt number profiles at the top wall (Figure 5.37b) are greatly improved compared to RANS close to the hot wall $y < 0.5$ thanks to the good prediction of $\overline{u\theta}$, however, the prediction at $y > 0.5$ suffers due to the under-prediction of $\overline{u\theta}$ in those regions, as can be seen at the profile $x = 0.1$ in Figure 5.35 (centrosymmetry). In the same vein, the better prediction of $\overline{u\theta}$ by LES leads to the better prediction of Nusselt number at the top wall compared to HTLES and RANS.

The HTLES model performs extremely well at predicting the profiles at mid-cavity ($y = 0.5$, Figures 5.38 to 5.41) with the predictions clearly better than RANS. Additionally, the plots show that the HTLES predictions are directly comparable to LES if not better. Of particular note is that the HTLES model predicts stratification exceptionally well as compared to both LES and RANS as seen in Figure 5.38b

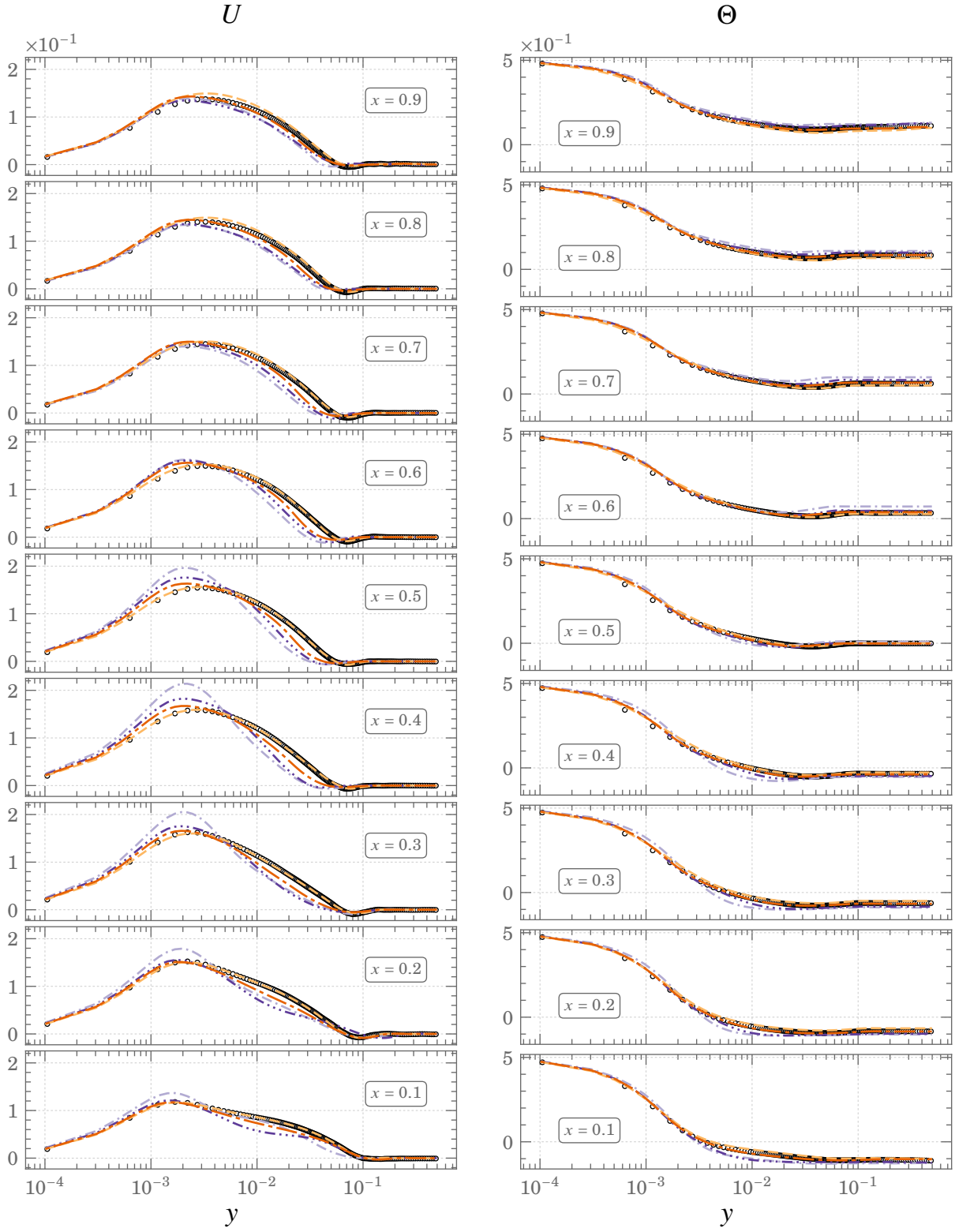

(a) Mean velocity, U

(b) Mean temperature, Θ

Figure 5.30.: Comparisons of mean velocity and temperature profiles for Square DHC at $Ra = 10^{11}$

○ ○ ○ *DNS* *HTLES* *LES* *RANS – BL* *RANS – KW*

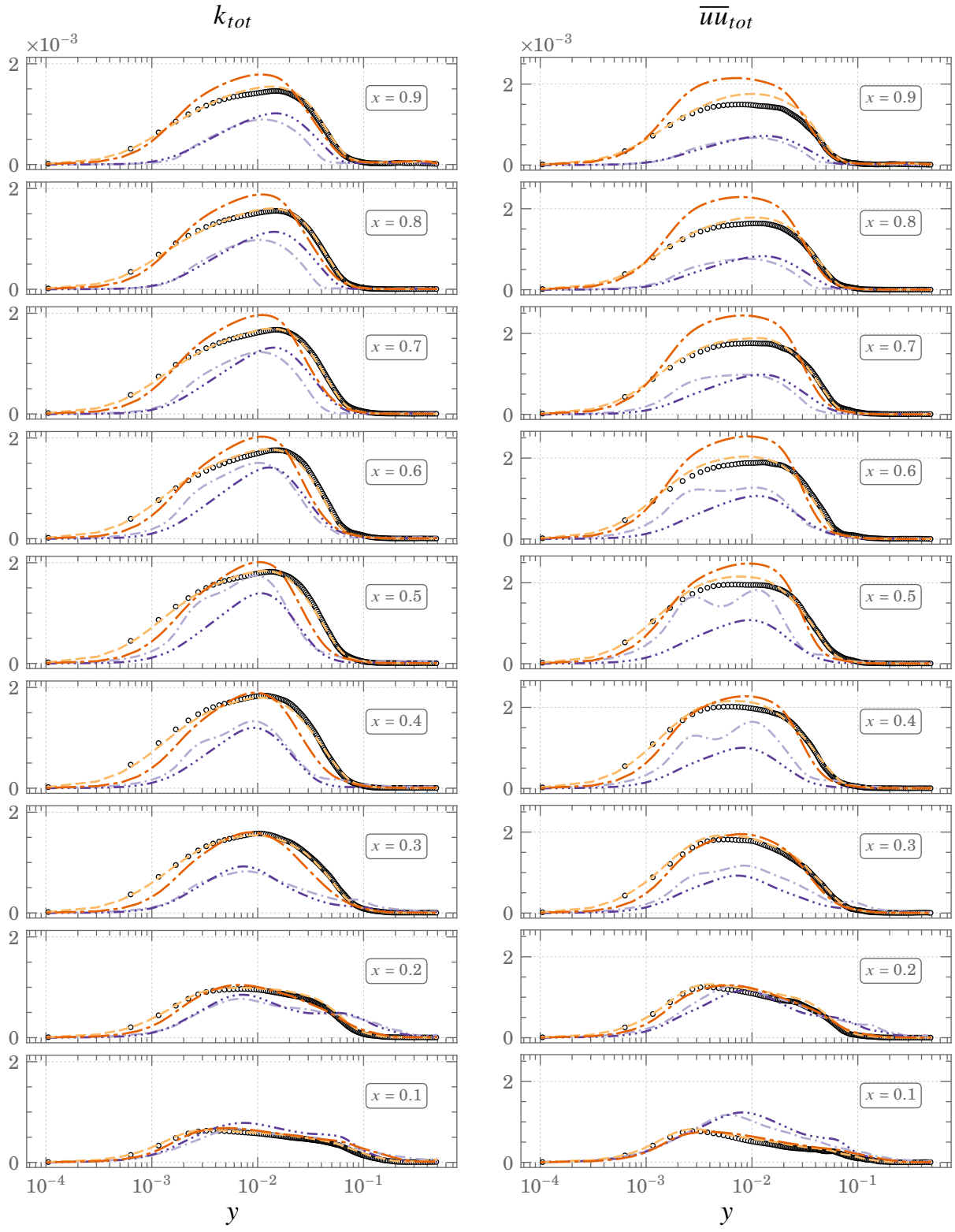

(a) total kinetic energy, k_{tot}

(b) $\overline{uu}_{tot}$

Figure 5.31.: Comparisons of k_{tot} and $\overline{uu}_{tot}$ profiles for Square DHC at $Ra = 10^{11}$

$\circ\ \circ\ \circ$ *DNS* — *HTLES* — *LES* — *RANS – BL* — *RANS – KW*

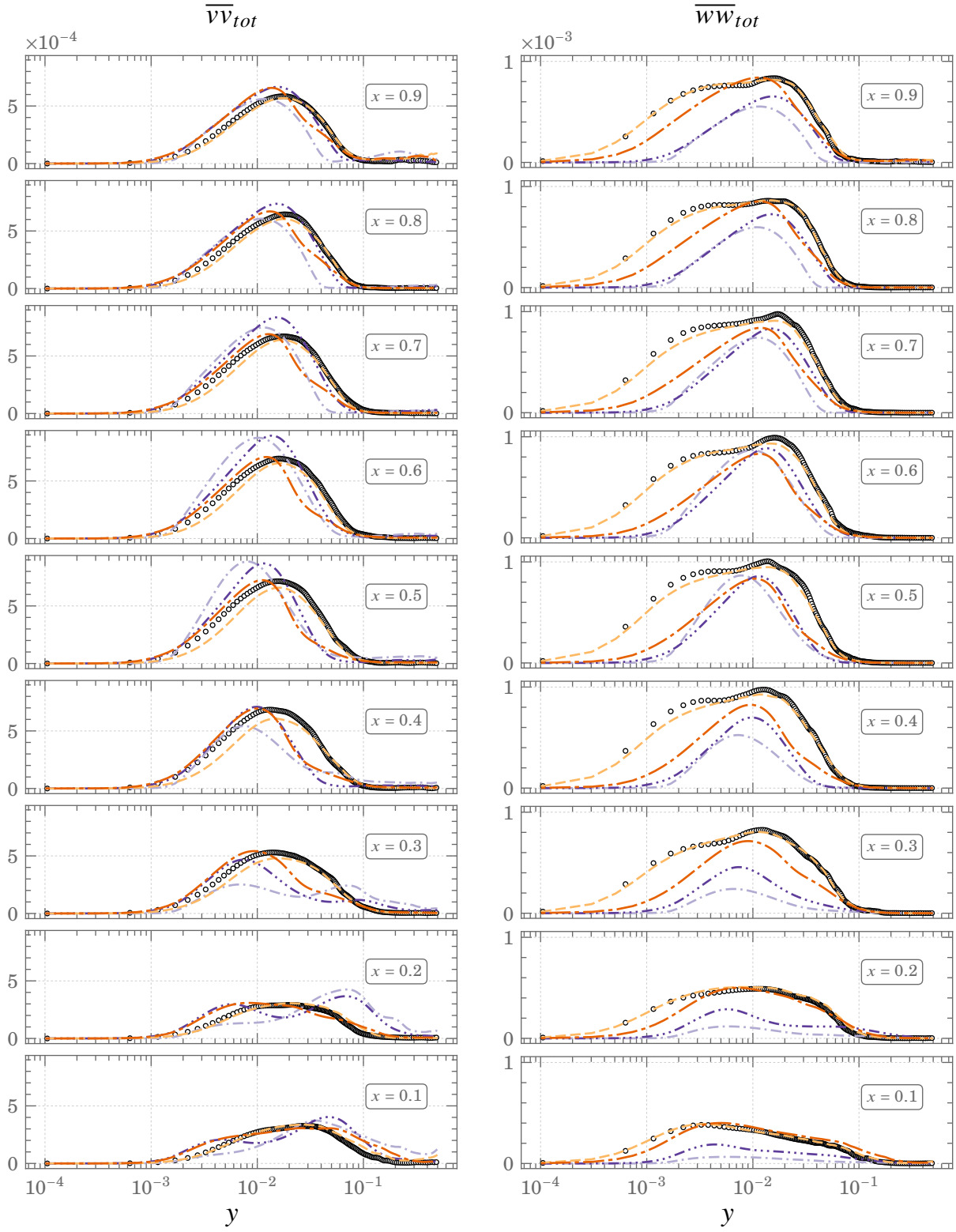

(a) $\overline{vv}_{tot}$ (b) $\overline{ww}_{tot}$

Figure 5.32.: Comparisons of $\overline{vv}_{tot}$ and $\overline{ww}_{tot}$ profiles for Square DHC at $Ra = 10^{11}$
○ ○ ○ *DNS* *HTLES* *LES* *RANS − BL* *RANS − KW*

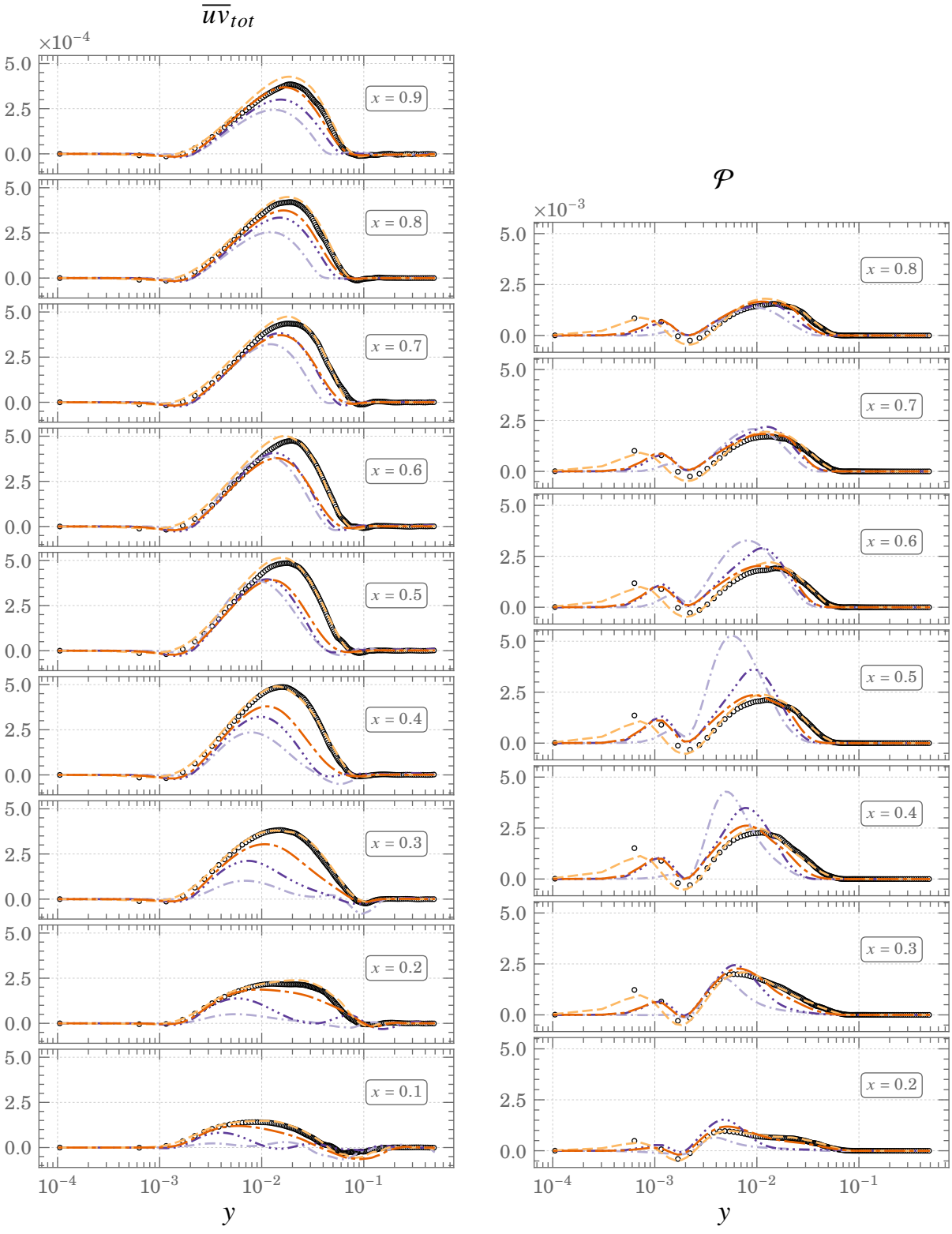

(a) $\overline{uv}_{tot}$ (b) shear production, $\mathcal{P}$

Figure 5.33.: Comparisons of $\overline{uv}_{tot}$ and shear production, $\mathcal{P}$, profiles for Square DHC at $Ra = 10^{11}$

$\circ\ \circ\ \circ\ DNS$ $-\cdot-$ $HTLES$ $--$ LES $-\cdot\cdot-$ $RANS-BL$ $-\cdot\cdot\cdot-$ $RANS-KW$

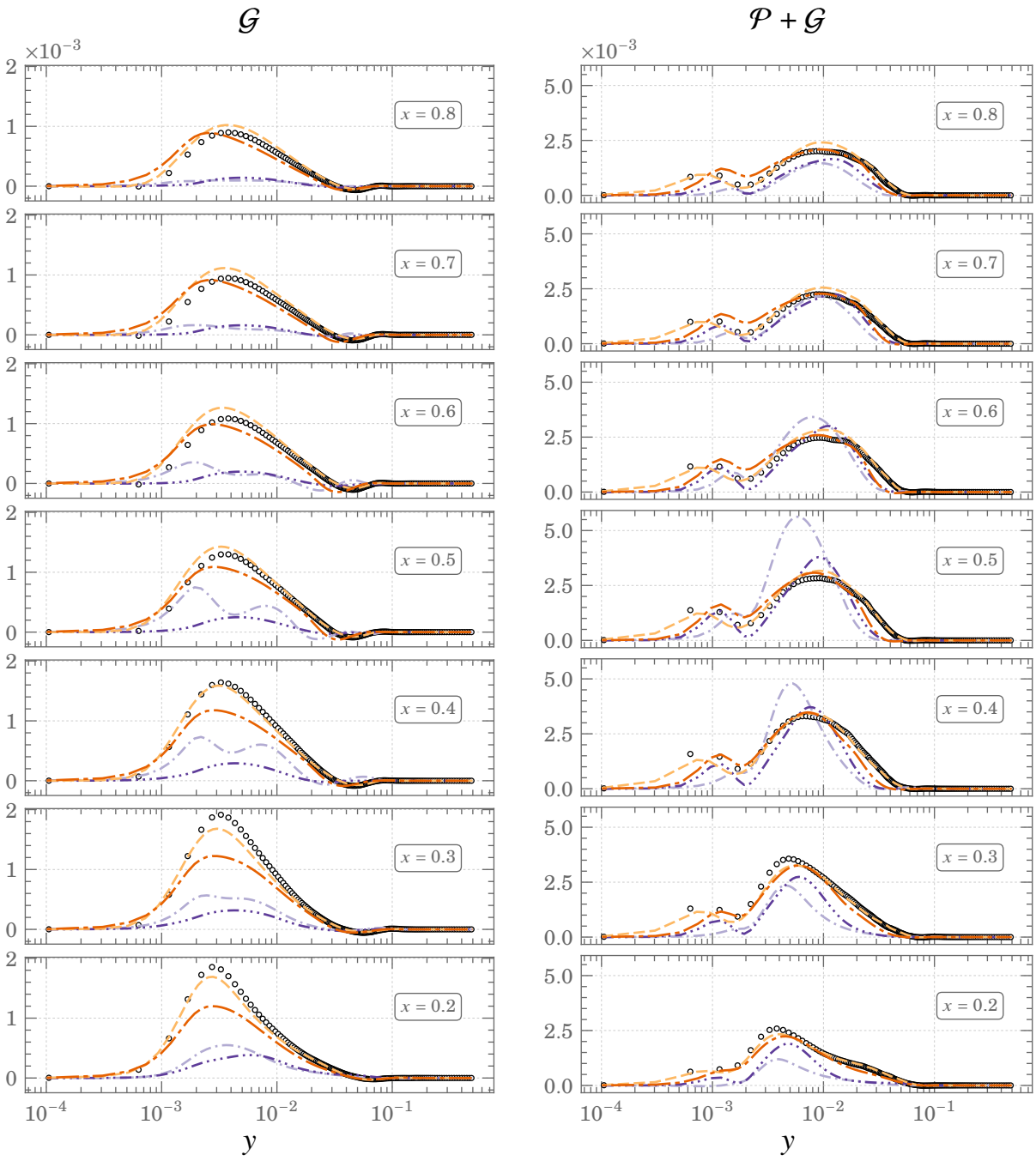

(a) buoyancy production, $\mathcal{G}$

(b) Total production, $\mathcal{P}+\mathcal{G}$

Figure 5.34.: Comparisons of buoyancy production, $\mathcal{G}$, and total production, $\mathcal{P}+\mathcal{G}$, profiles for Square DHC at $Ra = 10^{11}$

○ ○ ○ *DNS* —·— *HTLES* – – – *LES* —··— *RANS − BL* —···— *RANS − KW*

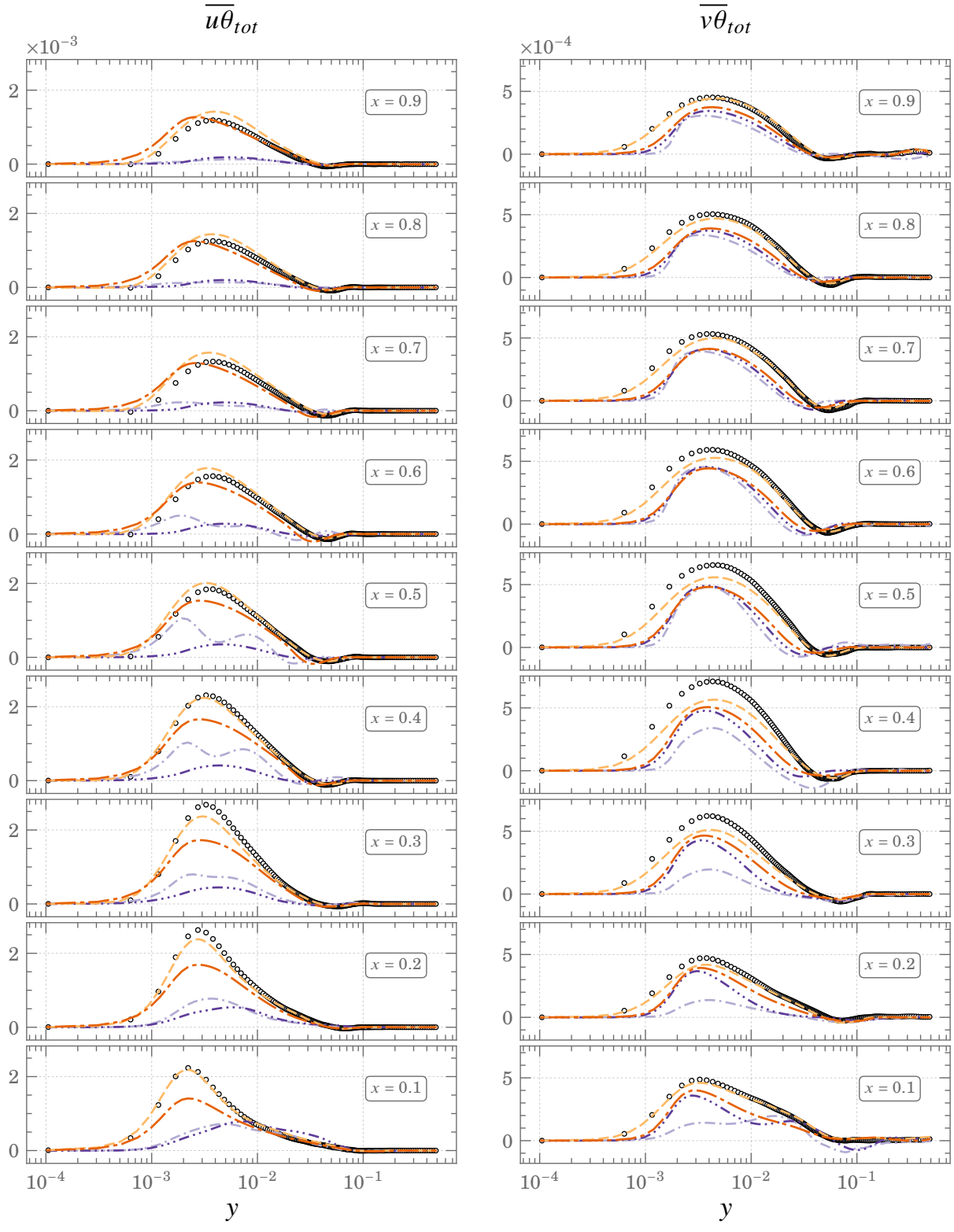

(a) $\overline{u\theta}_{tot}$ (b) $\overline{v\theta}_{tot}$

Figure 5.35.: Comparisons of $\overline{u\theta}_{tot}$ and $\overline{v\theta}_{tot}$ profiles for Square DHC at $Ra = 10^{11}$
○ ○ ○ *DNS* *HTLES* *LES* *RANS – BL* *RANS – KW*

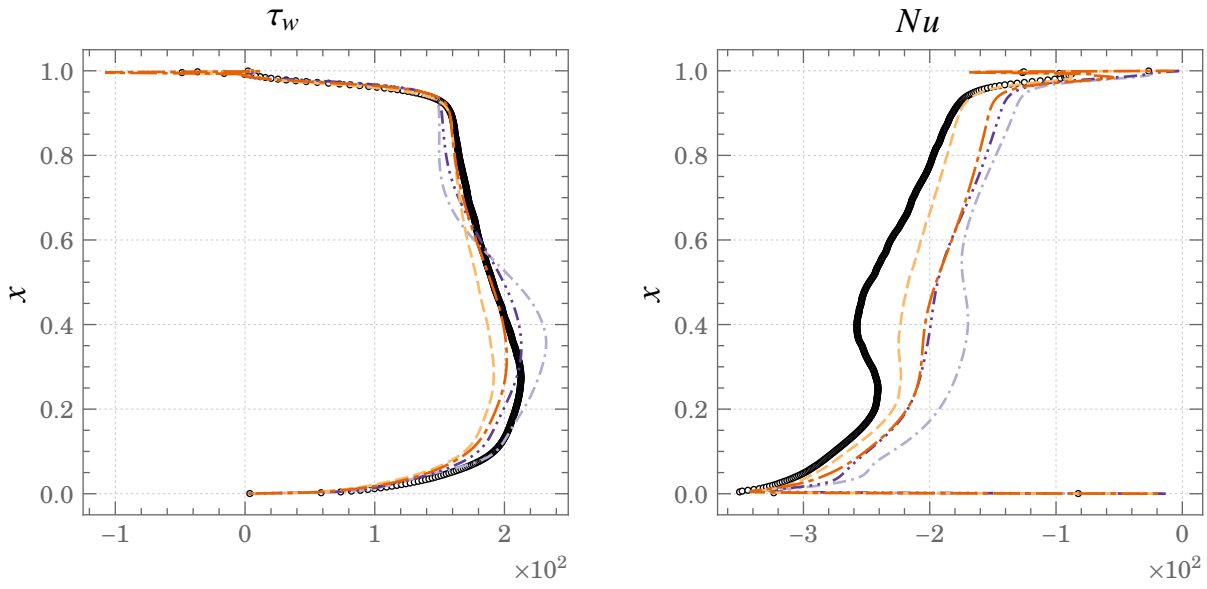

(a) shear stress, τ_w (b) Nusselt number, Nu

Figure 5.36.: Comparisons of shear stress and Nusselt number profiles at the hot wall for Square DHC at $Ra = 10^{11}$

$\circ\ \circ\ \circ\ DNS$ $HTLES$ LES $RANS-BL$ $RANS-KW$

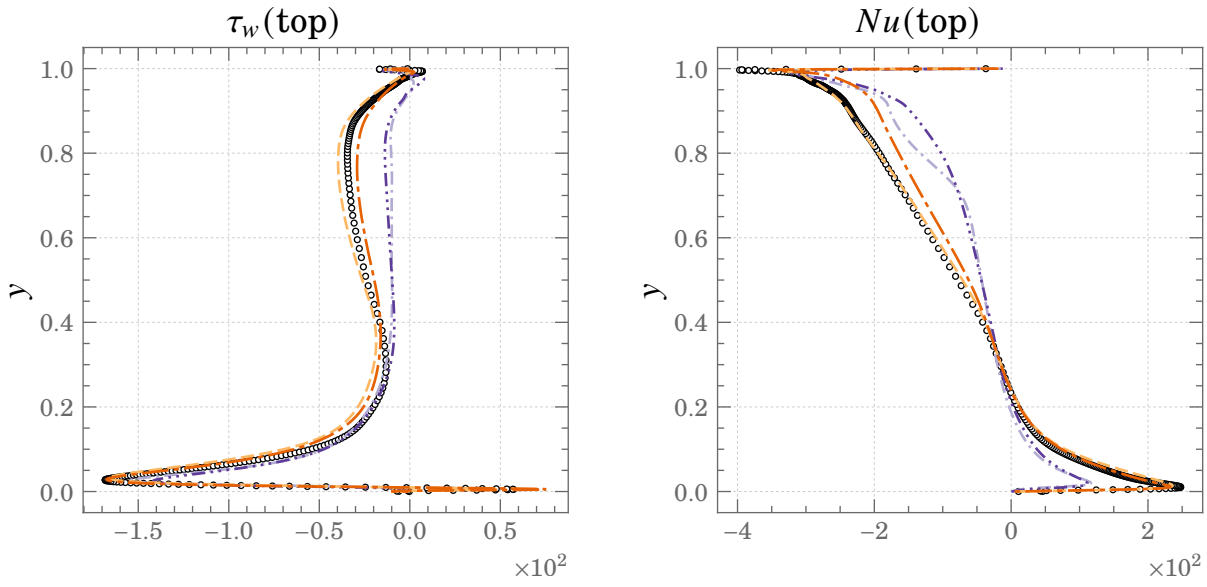

(a) top wall: shear stress, τ_w (b) top wall: Nusselt number, Nu

Figure 5.37.: Comparisons of shear stress and Nusselt number profiles at the top wall for Square DHC at $Ra = 10^{11}$

$\circ\ \circ\ \circ\ DNS$ $HTLES$ LES $RANS-BL$ $RANS-KW$

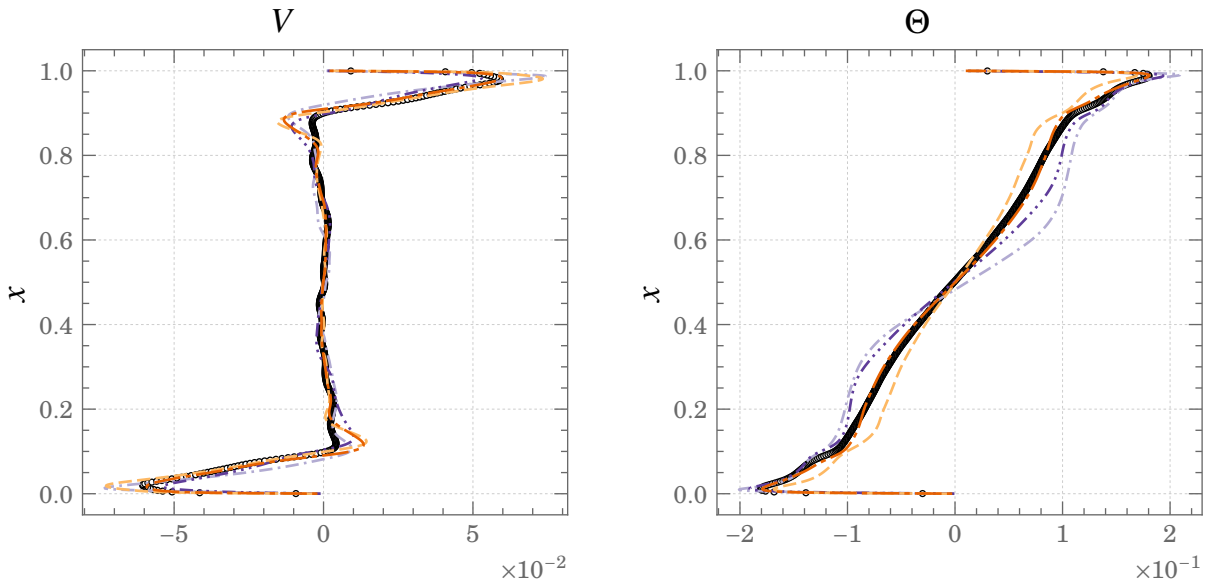

(a) Mean horizontal velocity, V

(b) Mean temperature stratification

Figure 5.38.: Comparisons of mean horizontal velocity and temperature strtification profiles at the mid cavity ($y = 0.5$) for Square DHC at $Ra = 10^{11}$

$\circ\ \circ\ \circ\ DNS$ $-\cdot-$ $HTLES$ $--$ LES $-\cdot\cdot-$ $RANS-BL$ $-\cdot\cdot\cdot-$ $RANS-KW$

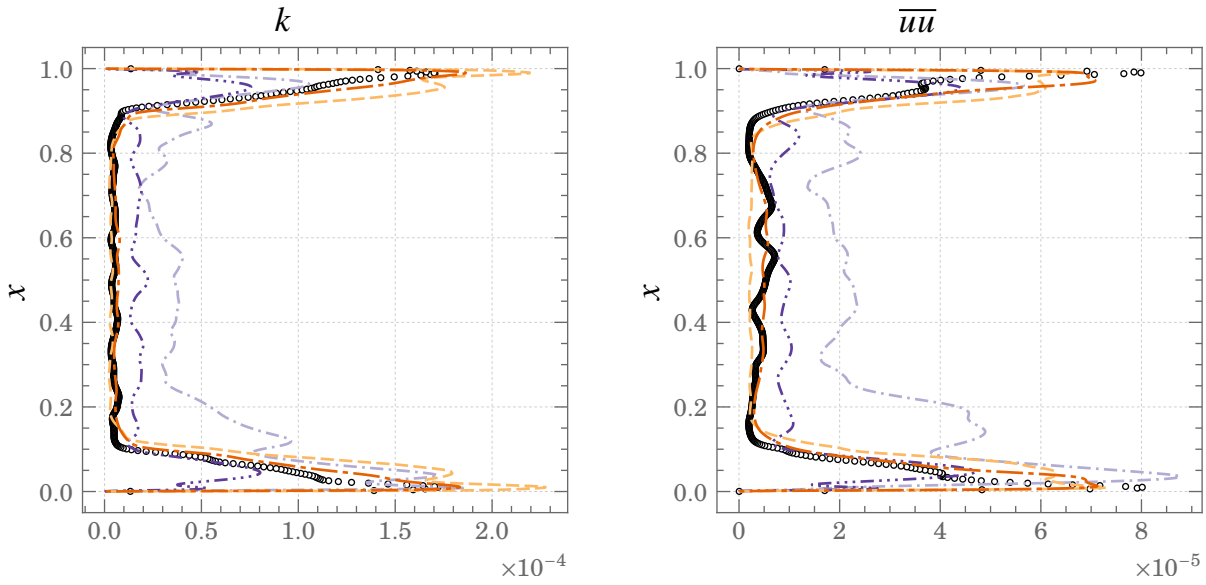

(a) total kinetic energy, k_{tot}

(b) $\overline{uu}_{tot}$

Figure 5.39.: Comparisons of total kinetic energy and $\overline{uu}_{tot}$ profiles at the mid cavity ($y = 0.5$) for Square DHC at $Ra = 10^{11}$

$\circ\ \circ\ \circ\ DNS$ $-\cdot-$ $HTLES$ $--$ LES $-\cdot\cdot-$ $RANS-BL$ $-\cdot\cdot\cdot-$ $RANS-KW$

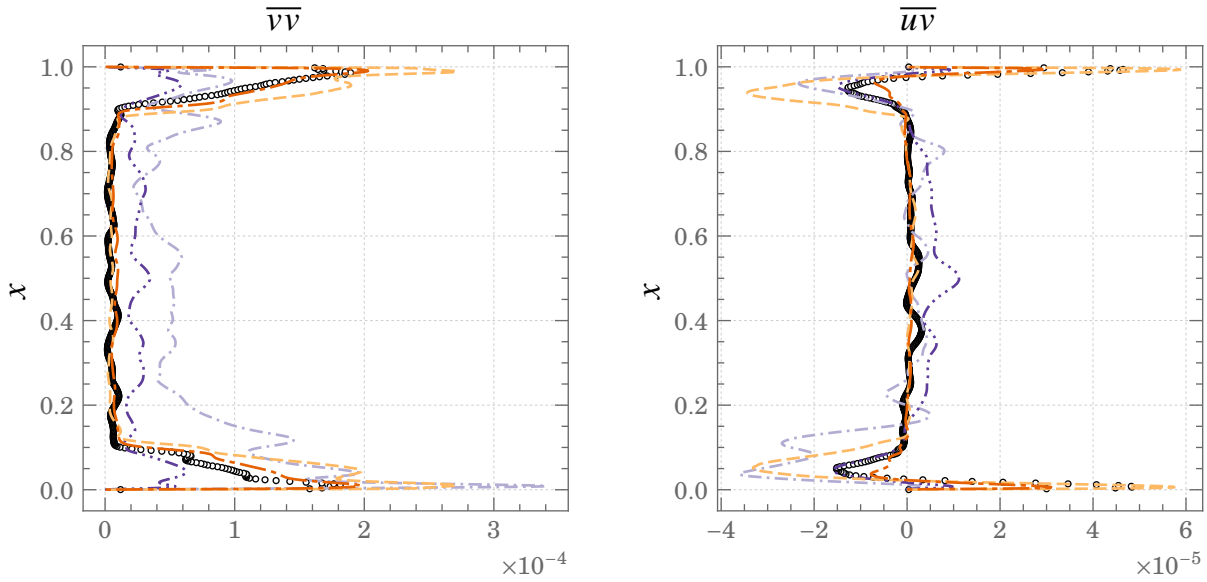

(a) $\overline{vv}_{tot}$ (b) $\overline{uv}_{tot}$

Figure 5.40.: Comparisons of $\overline{vv}_{tot}$ and $\overline{uv}_{tot}$ profiles at the mid cavity ($y = 0.5$) for Square DHC at $Ra = 10^{11}$

DNS $HTLES$ LES $RANS - BL$ $RANS - KW$

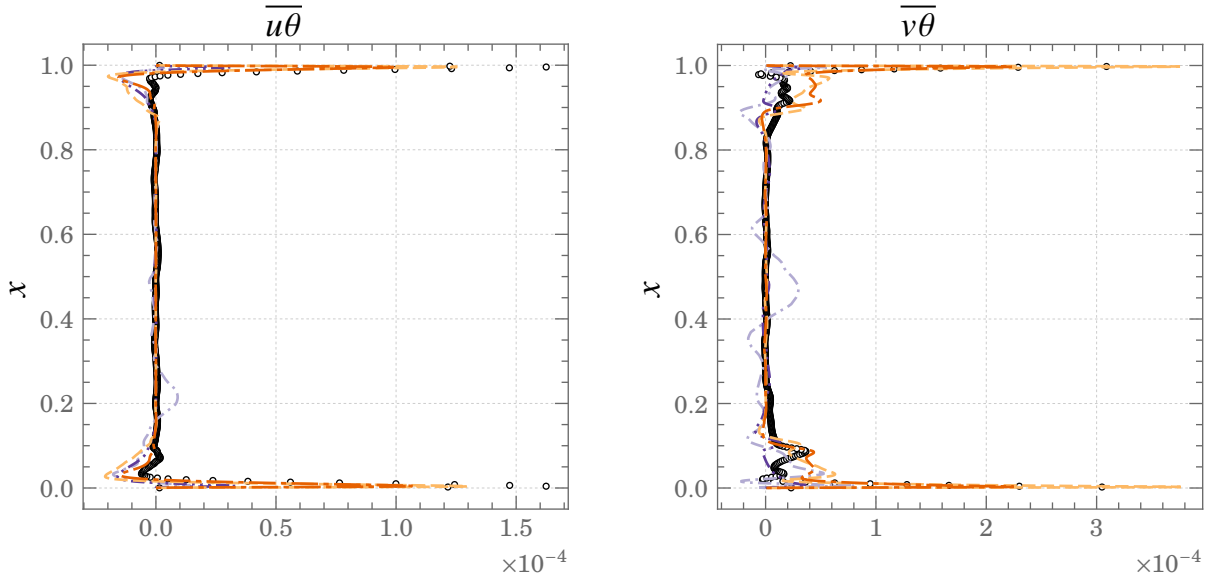

(a) $\overline{u\theta}_{tot}$ (b) $\overline{v\theta}_{tot}$

Figure 5.41.: Comparisons of $\overline{u\theta}_{tot}$ and $\overline{v\theta}_{tot}$ profiles at the mid cavity ($y = 0.5$) for Square DHC at $Ra = 10^{11}$

DNS $HTLES$ LES $RANS - BL$ $RANS - KW$

5.5. Chapter summary

Firstly, this chapter served to establish the foundational concepts and the formulation of the HTLES model. Following which the developments of the HTLES model in regards to natural convection flows are presented. Due to the complex physical phenomena encountered in the square DHC test case, the shielding function exhibits a behaviour whereby the energy ratio was unintentionally modified in the regions far from the boundaries. In order to solve this issue, a new shielding function is developed which is calibrated so as to produce near identical results in a channel flow in forced convection regime as compared to the formulation of Duffal (2020). In the ensuing sections, the new form of the shielding function is used and comparisons between the different levels of accounting for buoyancy in the underlying RANS model of the HTLES approach are provided. Interestingly, the accounting for the buoyancy effects through the buoyancy extended model (FBE) in HTLES retained the marginal improvements that were noticed in the RANS simulation (Chapter 4). Finally, the HTLES model is evaluated in comparing with the RANS models and LES using the dynamic Smagorinsky model. It is clearly evident from these comparisons that the HTLES model performs better than both the $k\omega$-SST and BL-v^2/k RANS models in the prediction of all the quantities. Thanks to the resolved unsteady motion penetrating the RANS region of the HTLES model, the predictions are corrected in the near wall regions as compared to the RANS models. Moreover, the results demonstrate that the predictions from the HTLES model are very much comparable to that of LES with the better prediction of stratification by HTLES being a highlight.

Chapter 6.

Conclusions and recommendations for future work

6.1. Conclusions

In the present thesis, turbulence models have been developed in order to tackle buoyancy driven flows. As the cornerstone of the MONACO_2025 project, the main objective of the thesis is to lift the technical barrier of computing unsteady natural convection flows while aiming to strike a good balance between accuracy and computational cost in industry relevant flow configurations through the development of hybrid RANS/LES strategies. Additionally, keeping in mind the current standard practices of the industrial sector, RANS models of the eddy-viscosity genre are sensitised to buoyancy effects so as to facilitate rapid dissemination to industrial simulation codes. Also, the work on the RANS models allows to improve the regions solved in RANS mode in the hybrid RANS/LES context. An important factor in the choice of the eddy-viscosity models is that they should be integrable down to the wall since wall functions are not well developed for natural convection flows and are an ongoing topic of research. As such, the developments in the thesis are carried out using the popular $k\omega$-SST and BL-v^2/k models.

The conclusion for the work carried out in this thesis is classified into 2 parts,

- Model developments for RANS: This section concludes the work carried out in developing/improving the RANS models previously developed by Jameel (2020)
- Model developments for hybrid RANS/LES: This section concludes the work carried out in developing the HTLES model previously developed by Duffal (2020)

6.1.1. Model developments for RANS

In the industrial sectors, RANS models are predominantly employed for forced convection flows. The industry relies heavily on expensive full-scale experiments in the design process involving natural convection flows. Moreover, simple gradient diffusion hypothesis (SGDH) is used to approximate the heat fluxes due to its simplicity in implementation and numerical robustness. However, the use of SGDH is insufficient for complex buoyancy driven flows because the formulation assumes that the heat flux vector and the temperature gradient are aligned and thus fails to predict the buoyancy effects correctly when the flow does not present stratification or is only weakly stratified. In order to rectify this issue, all the while retaining model simplicity and respecting the industry requirements of robustness, the present thesis follows up on the work of Jameel (2020) by further developing the buoyancy extended model through validation in industry relevant configuration such as the square differentially heated cavity. Additionally, special attention is paid to the formulation of the source terms in the transport equation for the specific dissipation rate ω, of the $k\omega$-SST model and the source terms are derived with proper consideration to the blending of $k-\varepsilon$ and $k-\omega$ models. Interestingly, it is revealed through the process of deriving the source terms that the influence of buoyancy cannot be completely ignored exclusively in the transport equation for specific dissipation rate of the $k\omega$-SST model as a result of the blending of $k-\varepsilon$ and $k-\omega$ models.

The validation of the RANS models are carried out using DNS databases of two test cases:

1. the purely academic case of differentially heated vertical channel flow

2. an industry relevant case of square differentially heated cavity

In regards to the eddy-viscosity based RANS models sensitised to buoyancy, the need to accounting for buoyancy effects is clearly seen in the results obtained for the vertical channel flow. The analysis of the baseline models, using SGDH and GGDH, revealed that the turbulent shear stress $\overline{uv}$ and turbulent heat flux $\overline{v\theta}$ are incorrectly predicted. The use of the full buoyancy extended model (FBE) leads to a better balance in the momentum and transport equations and hence a better prediction of the mean quantities. Significant improvements are obtained for the $k\omega$-SST model with FBE while the improvements for BL-v^2/k with FBE have been modest given that the baseline performance of the model is rather good. The results observed for the square DHC show marginal but consistent improvements with increasing degrees of accounting for buoyancy effects for both the $k\omega$-SST and BL-v^2/k models. Furthermore, the reformulation of the buoyancy source term in the transport equation for specific dissipation rate ω of the $k\omega$-SST leads to a correction of the non-physical turbulent viscosity observed in the stratified core region of the square DHC owing to the correction of the profiles for ω. The reformulation also corrects the behaviour of the blending function F_1 such that the $k\omega$-SST model does not fluctuate between the $k-\omega$ and $k-\varepsilon$ modes in the stratified core region.

6.1.2. Model developments for hybrid RANS/LES

In the pursuit of developing a cost effective and accurate turbulence model for the simulation of unsteady natural convection flows, the HTLES model (Duffal, 2020) is developed in the context of buoyancy affected flows. Hybrid RANS/LES methods are only occasionally applied to buoyant flows, in this regard the works of Abramov et al. (2003), Andreani et al. (2016), Ashrafi et al. (2017), Hadziabdic et al. (2022), and Kocutar et al. (2015) can be mentioned. In particular, models focused on accounting for buoyancy effects on the unresolved scales are exceptionally rare (Kenjeres et al., 2006). The HTLES model is the result of over a decade of continuous progress made in the temporal filtering approach for RANS/LES

methods (TPITM (Fadai-Ghotbi et al., 2010a) → H-equivalence (Friess et al., 2015) → Equivalent-DES (Friess et al., 2015) → HTLES (Duffal, 2020; Manceau, 2018)). In the present thesis, the RANS models sensitised to buoyancy effects form the underlying closure for the HTLES approach. It was found that the shielding function used to ensure that the HTLES model stays in RANS mode in the near wall region misbehaves leading to an unintended modification of the energy ratio in the regions far from the wall. The consequences were that the HTLES model abruptly switched between RANS and LES modes far from the boundaries. In order to correct this behaviour, a new shielding function based on an elliptic equation is implemented. The new shielding function is first calibrated in channel flows in forced convection regime such that the model behaviour remains near identical to the formulation of Duffal (2020) in such flow configurations.

The validation of the $k\omega$-SST HTLES model was carried out in the square DHC owing to the high level of turbulence presented by the test case. The HTLES simulations using the new shielding function validated that the shielding function behaves as intended and the model no longer switches abruptly between RANS and LES modes. Furthermore, validation of the shielding function in such a test case which presents complicated physics serves as a metric for the increased robustness of the HTLES model which is of particular interest in regards to industry readiness. The comparisons of the HTLES model with different levels of accounting for buoyancy effects in the underlying RANS models show that the marginal improvements noted previously in the pure RANS simulations are retained in the HTLES approach while gaining the ability to resolve unsteady motion. It is particularly important to emphasise that improvements can be found using hybrid methods for buoyant flows by better accounting for buoyancy effects even while using simplified methods such as extensions to eddy-viscosity models. Furthermore, assessment of the HTLES model with its RANS counterparts and the high fidelity simulation of LES using dynamic Smagorinsky model shows that the HTLES model is able to predict mean quantities comparable to that of LES and provide significant improvements over RANS. This fact is especially notable for the profiles at the center of the cavity, with excellent predictions for the temperature

stratification obtained for the HTLES model.

6.2. Recommendations for future work

6.2.1. In the short term

The work carried out in the present thesis has been exploratory in nature being the first attempt at employing the HTLES method for buoyancy flows. As such, in addition to the $k\omega$-SST HTLES formulation, a HTLES formulation based on the BL-v^2/k model was explored. However, the model was found to exhibit divergence issues in cavity flows when coupled with the HTLES method. Such divergence issues are not present when the BL-v^2/k HTLES model is used for the case of the vertical differentially heated channel, however, due to the low Rayleigh number and the lack of strong large-scale forcing the test case is not ideal for testing hybrid models. The BL-v^2/k model showed comparable results to the $k\omega$-SST model for the square DHC and it can be seen in Appendix B for the rectangular DHC that the BL-v^2/k model predicts transition to turbulence better as compared to $k\omega$-SST in addition to better prediction of the mean profiles. With the use of hybrid strategies for buoyant flows being in their infancy, it is of great interest to get to the root of such issues and build up the repertoire of models available so as to be better equipped to tackle industrial cases.

6.2.2. More complex heat flux models for RANS

As we have seen in Chapter 4, in the case of the square DHC the results obtained using the buoyancy extended model only provided marginal improvements compared to the baseline models. It would be of interest to use *Differential flux models (DFM)*, *Algebraic flux model (AFM)*, or their elliptic blending counterparts EB-DFM and EB-AFM (Dehoux et al., 2017) to better account for buoyancy effects. In his thesis, Sebilleau (2016) noted that the AFM and EB-AFM model presented divergence issues and that the use of DFM is recommended such that the trade-off between the additional computational cost versus better accounting

for the physics is in favour of the DFMs. Furthermore, the possibility of using explicit AFMs (Vanpouille et al., 2015) in order to evade the divergence issues can be explored.

6.2.3. HTLES approach with Reynolds-stress models

In view of the interest of using more complex models for buoyancy flows, it is prudent to probe into the issue of hybridising Reynolds-stress models so as to take full advantage of the hybrid approach. In this regards, Duffal (2020) has noted that the use of a second order model for the HTLES approach resulted in an increase in the energy spectra at the dissipative scales in their tests of decaying isotropic turbulence. The industry sector, however, is yet to adopt Reynolds stress models and as such the hybridisation of RSMs may remain an academic exercise for the foreseeable future.

6.2.4. Forcing techniques

The current research focus for the HTLES model revolves around the implementation of forcing techniques in order to develop active hybrid RANS/LES approaches aimed at mitigating the grey area problem (the zone of the switch from RANS to LES in hybrid methods). In this regard, Anisotropic linear forcing (ALF, de Laage de Meux et al. (2015)) is employed whereby the commutation errors arising due to the use of a variable filter width are accounted for so as to aid the development of resolved motions during the switch from RANS to LES. For natural convection flows, the use of such methods can be envisaged at least in the purely academic case of vertical differentially heated channel.

6.2.5. Transition flows

One of the challenges posed by natural convection test cases is that they present a laminar-to-turbulence transition regime. It can be seen in Appendix B that improving the predictions using HTLES for the rectangular cavity was unsuccessful. In regards to hybrid methods, the question of tackling such flows is wide open. One of the more important concerns to be

highlighted is that of the choice of technique (RANS models or LES) to use to handle the transition zones.

6.2.6. HTLES approach coupled with wall-functions

The previous recommendations revolved around academic interests where simpler geometries are used so as to assess and develop new models. In the industry however, encountering complex geometries is commonplace and in many such cases it is not possible to have a mesh fine enough close to the solid boundaries so as to meet the requirement of $y^+ < 1$. Wall-functions are interesting for such cases and are an active field of research in the context of buoyancy driven flows. Developments towards coupling hybrid methods with wall functions would prove interesting to bridge the gap between academia and industry.

Appendix A.

LES of square differentially heated cavity

In this chapter, a global overview of the LES results are presented which include the grid sensitivity study using the dynamic Smagorinsky model and comparisons of the results obtained using dynamic Smagorinsky, classic Smagorinsky, and the WALE models. The grid sensitivity study shows that the results do not improve drastically with grid refinement. Improvements are mainly noted in the prediction of Nusselt number along the hot wall (Figure A.7b), where the profiles improve with grid refinement. In regards to the comparison of the different models, the profiles show that the results are not sensitive to the choice of the model with only marginal differences noticeable particularly in the plots of shear stress (Figure A.19a) and Nusselt number (Figure A.19b).

A.1. Grid sensitivity study

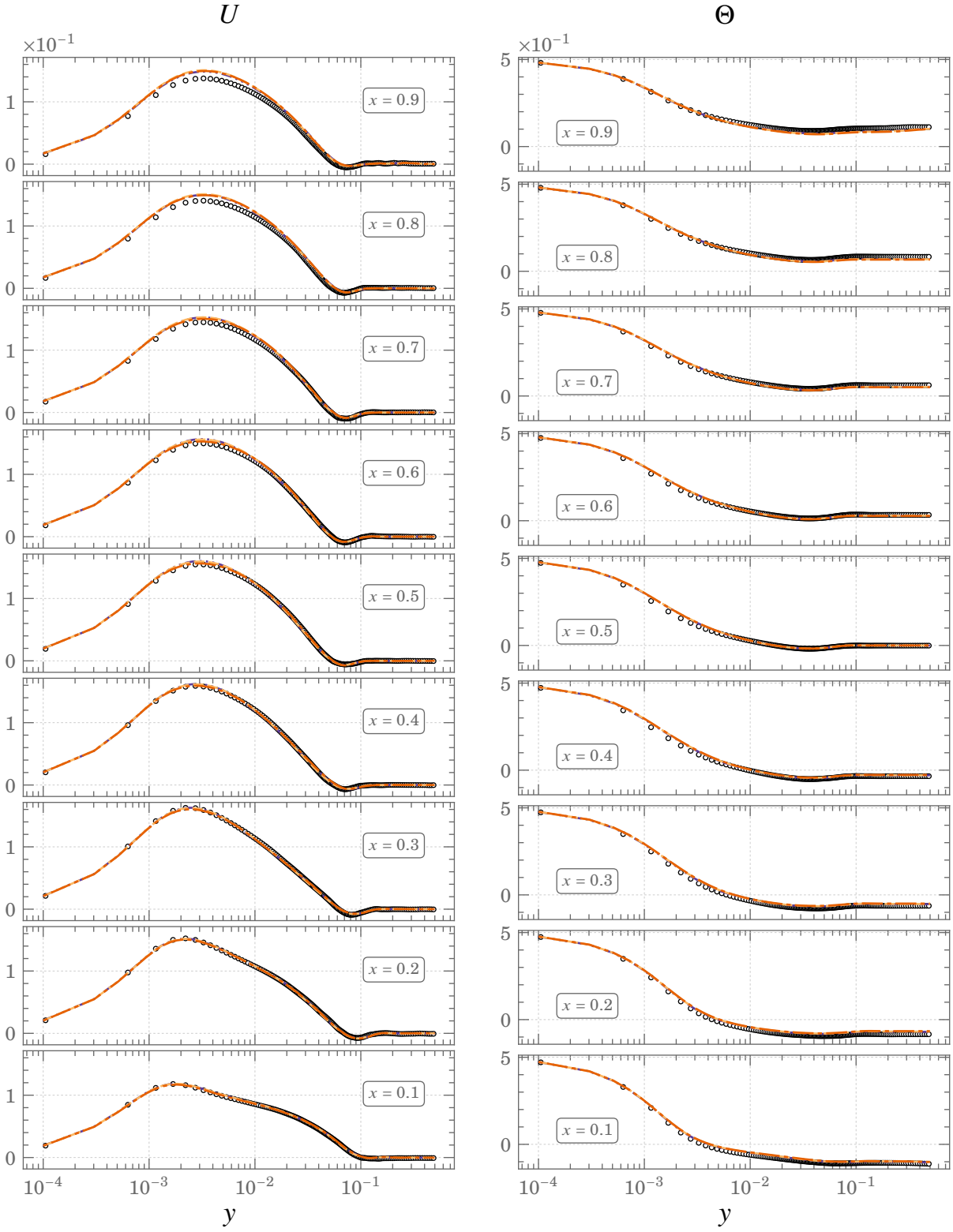

(a) Mean velocity, U

(b) Mean temperature, Θ

Figure A.1.: Comparisons of mean velocity and temperature profiles for Square DHC at $Ra = 10^{11}$

$\circ\ \circ\ \circ\ DNS$ — 498×80 — 664×80 — 996×100

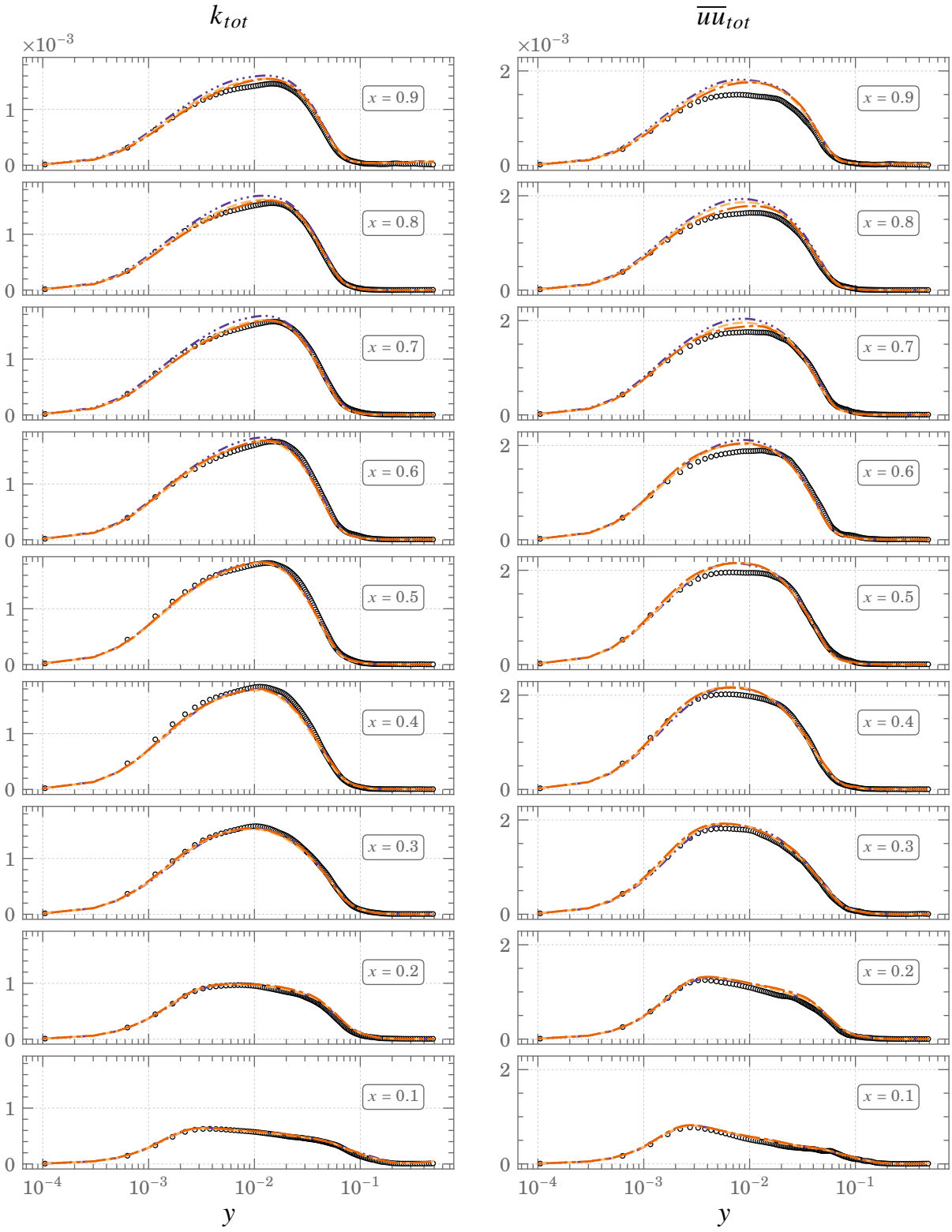

(a) total kinetic energy, k_{tot}

(b) $\overline{uu}_{tot}$

Figure A.2.: Comparisons of k_{tot} and $\overline{uu}_{tot}$ profiles for Square DHC at $Ra = 10^{11}$
○ ○ ○ DNS 498×80 664×80 996×100

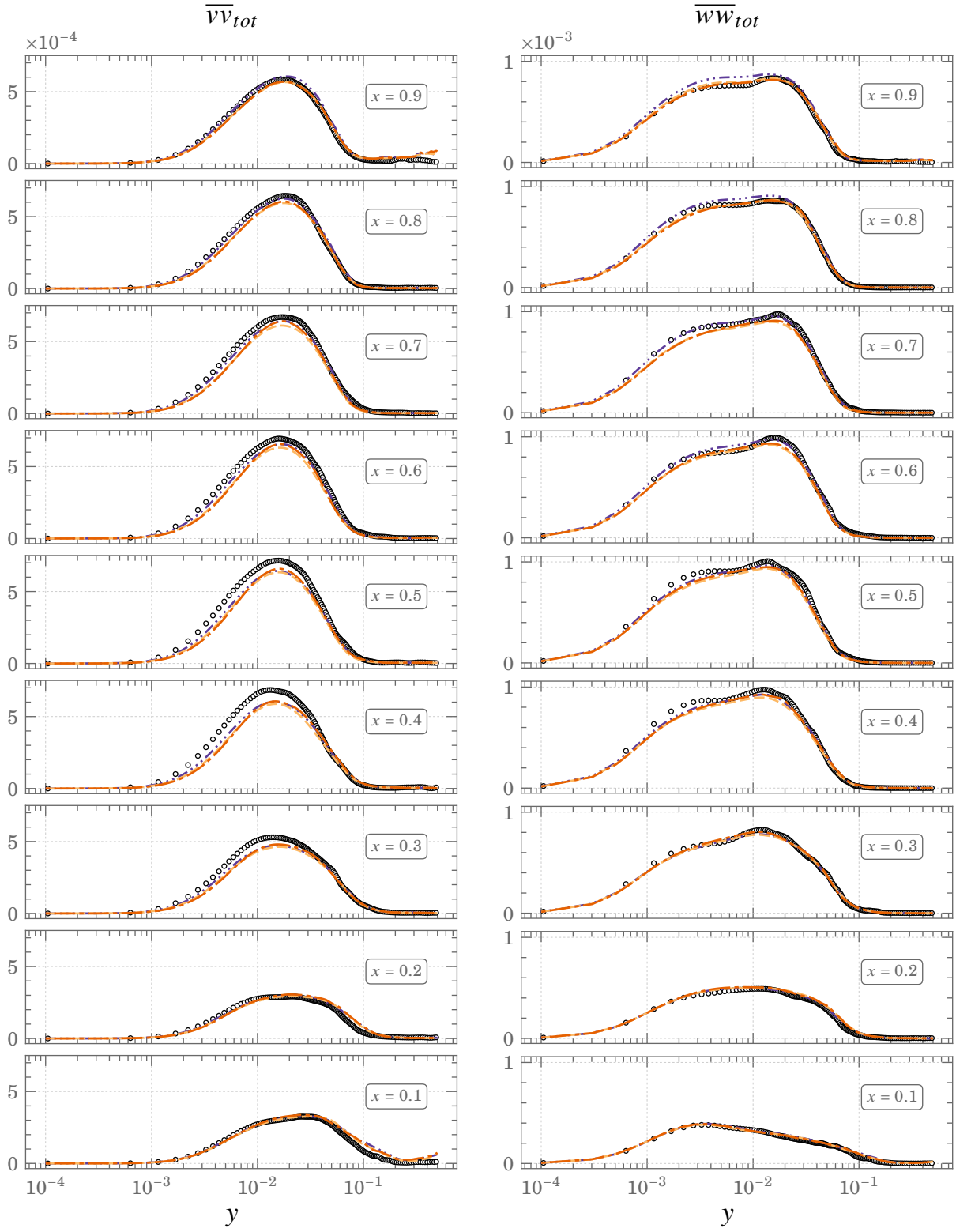

(a) $\overline{vv}_{tot}$ (b) $\overline{ww}_{tot}$

Figure A.3.: Comparisons of $\overline{vv}_{tot}$ and $\overline{ww}_{tot}$ profiles for Square DHC at $Ra = 10^{11}$
○ ○ ○ *DNS* 498 × 80 664 × 80 996 × 100

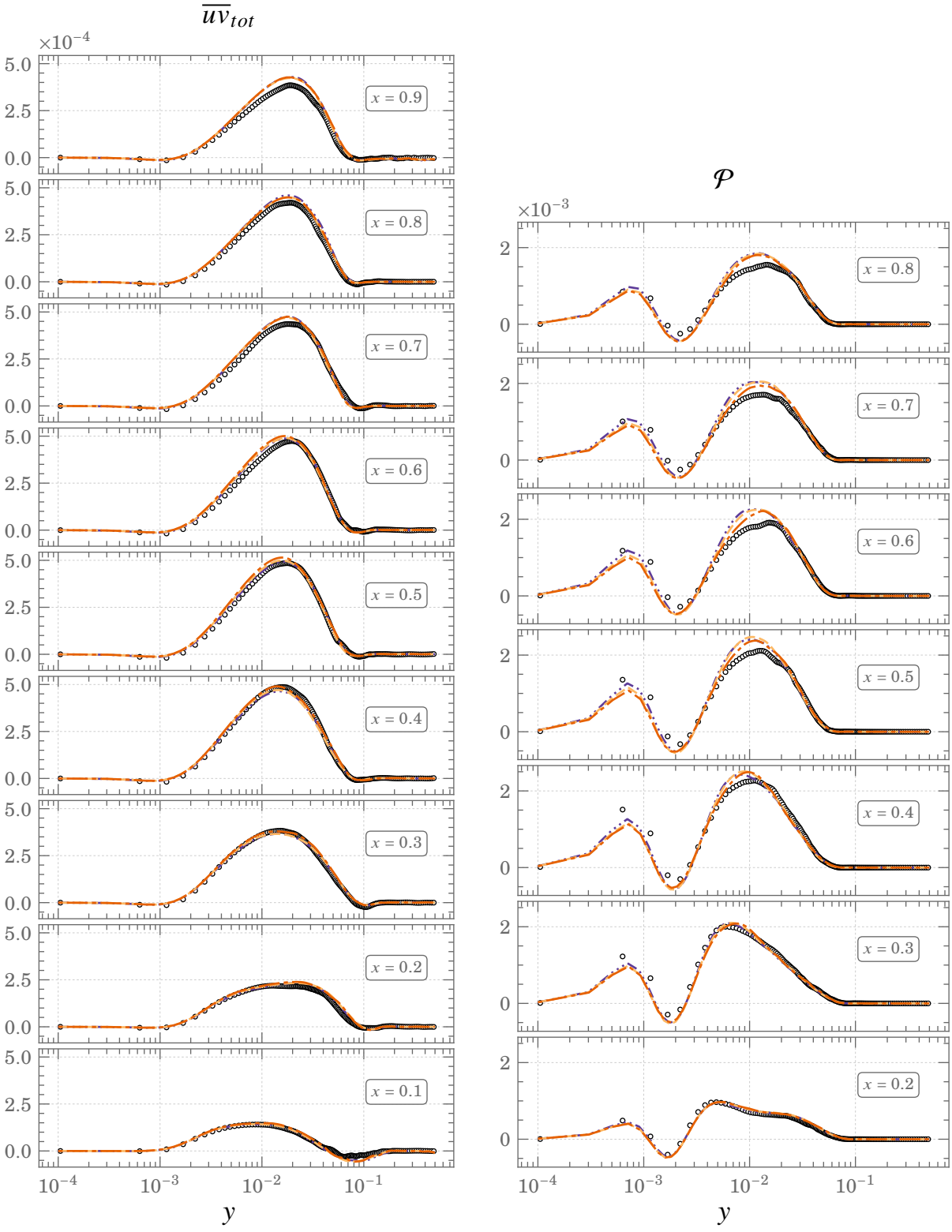

(a) $\overline{uv}_{tot}$ (b) shear production, $\mathcal{P}$

Figure A.4.: Comparisons of $\overline{uv}_{tot}$ and shear production, $\mathcal{P}$, profiles for Square DHC at $Ra = 10^{11}$

$\circ\ \circ\ \circ\ DNS$ $-\cdot-$ 498×80 $- - -$ 664×80 $\cdots$ 996×100

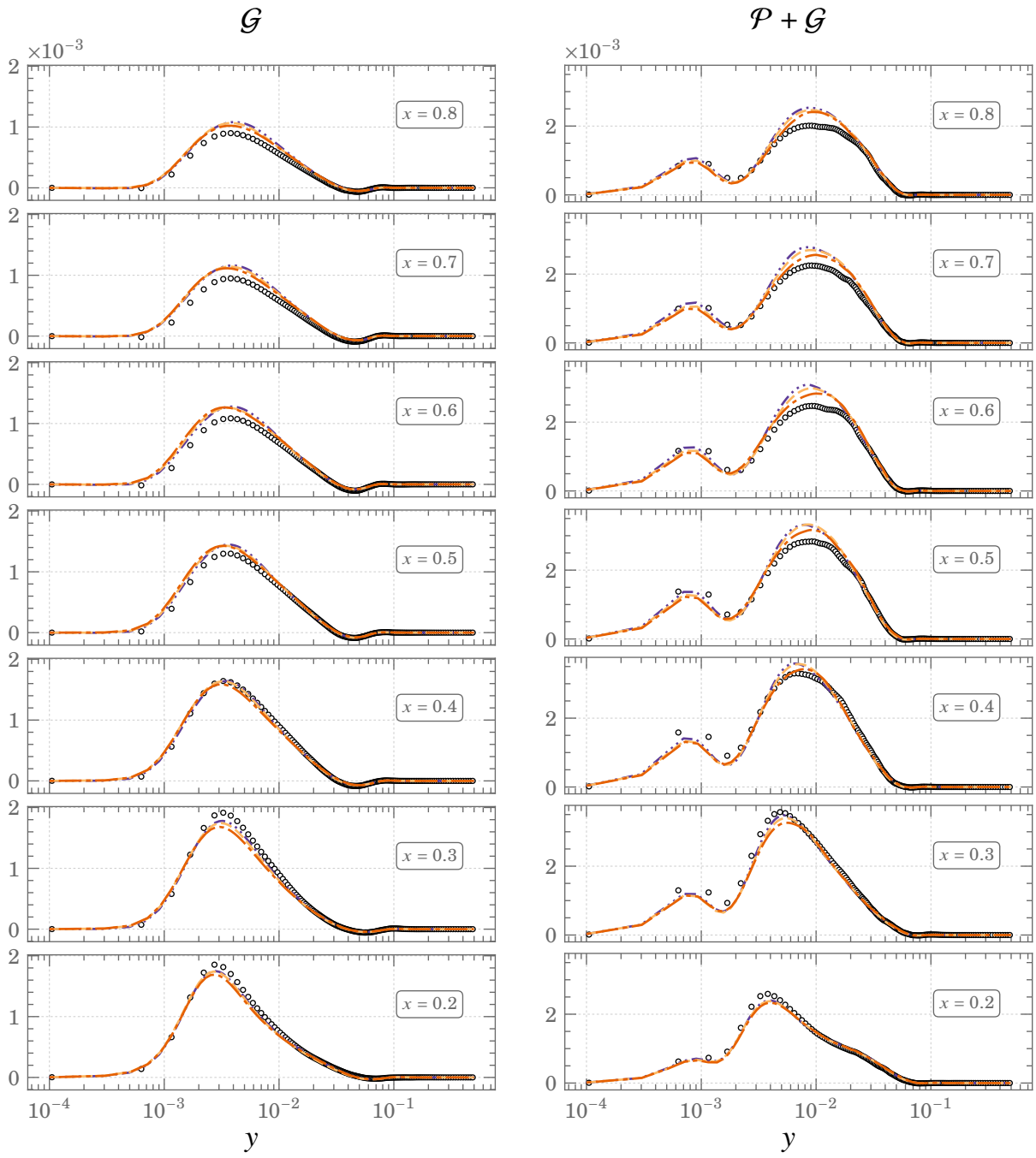

(a) buoyancy production, $\mathcal{G}$

(b) Total production, $\mathcal{P}+\mathcal{G}$

Figure A.5.: Comparisons of buoyancy production, $\mathcal{G}$, and total production, $\mathcal{P}+\mathcal{G}$, profiles for Square DHC at $Ra = 10^{11}$

$\circ\ \circ\ \circ$ *DNS* — 498×80 — 664×80 — 996×100

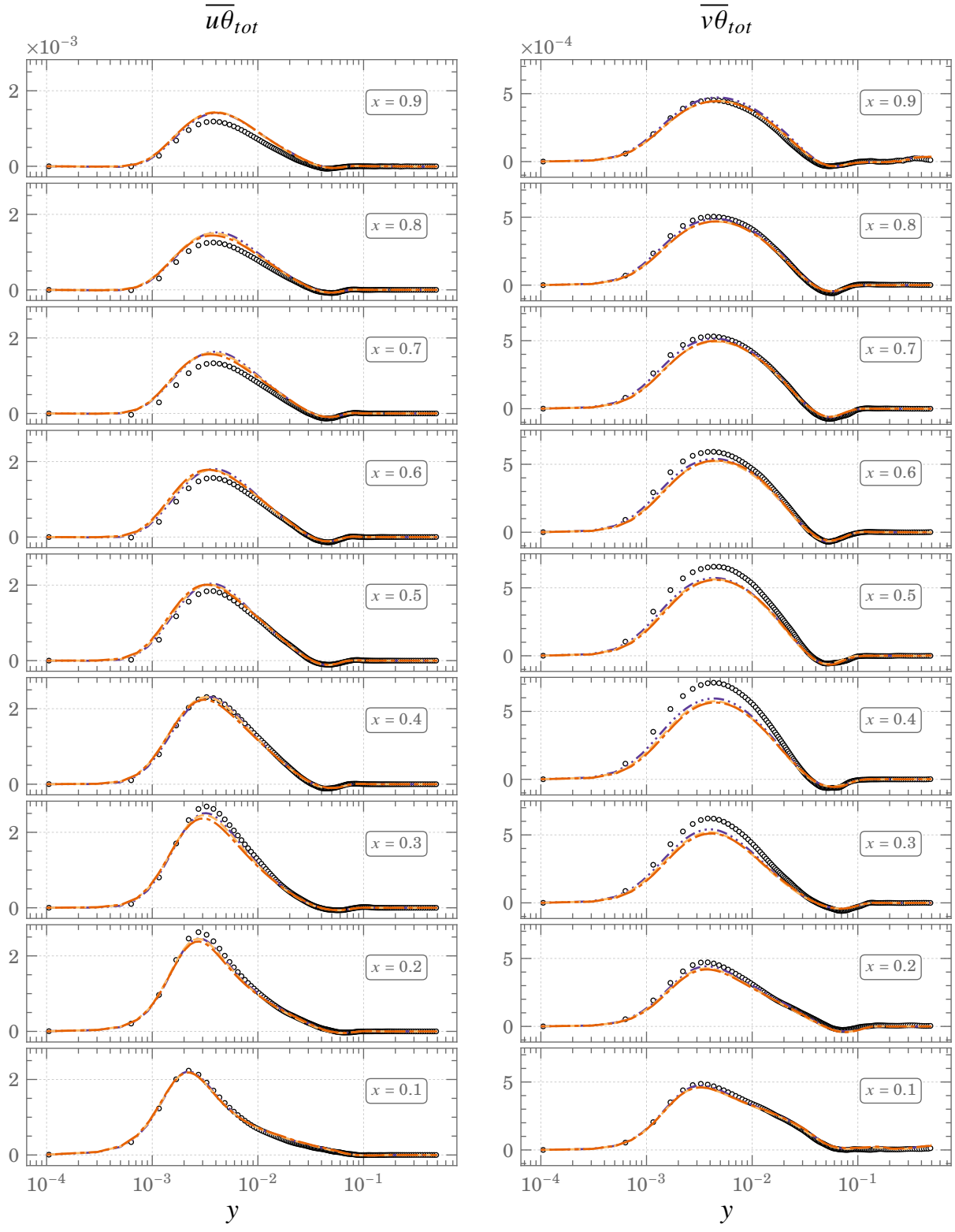

(a) $\overline{u\theta}_{tot}$ (b) $\overline{v\theta}_{tot}$

Figure A.6.: Comparisons of $\overline{u\theta}_{tot}$ and $\overline{v\theta}_{tot}$ profiles for Square DHC at $Ra = 10^{11}$
○ ○ ○ DNS 498×80 664×80 996×100

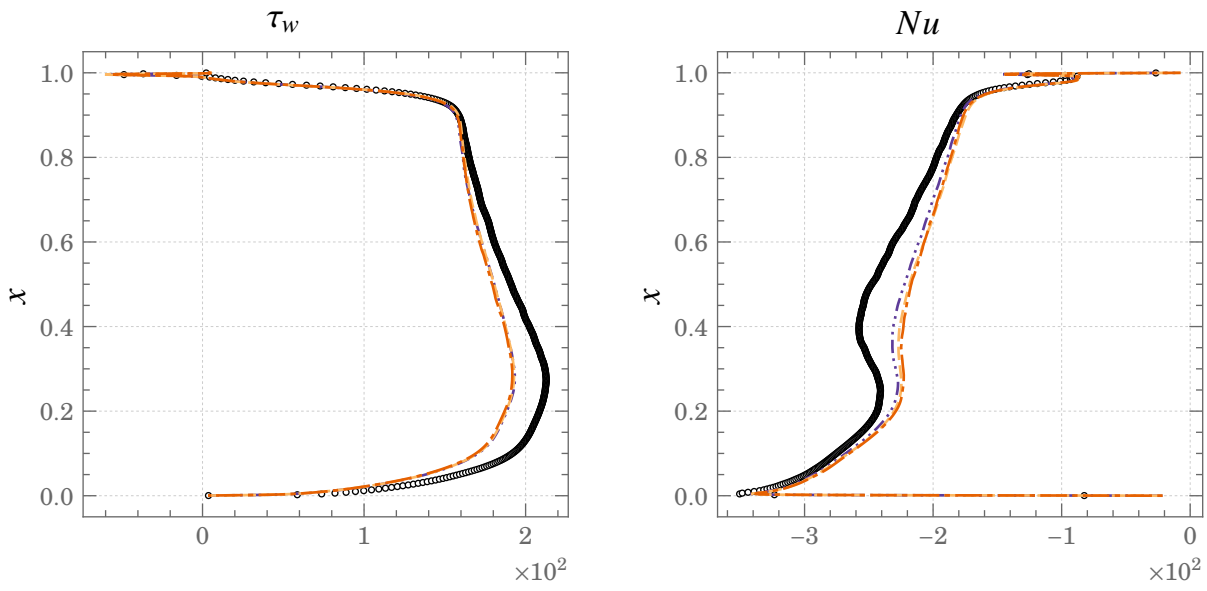

(a) shear stress, τ_w (b) Nusselt number, Nu

Figure A.7.: Comparisons of shear stress and Nusselt number profiles at the hot wall for Square DHC at $Ra = 10^{11}$

○ ○ ○ *DNS* 498 × 80 664 × 80 996 × 100

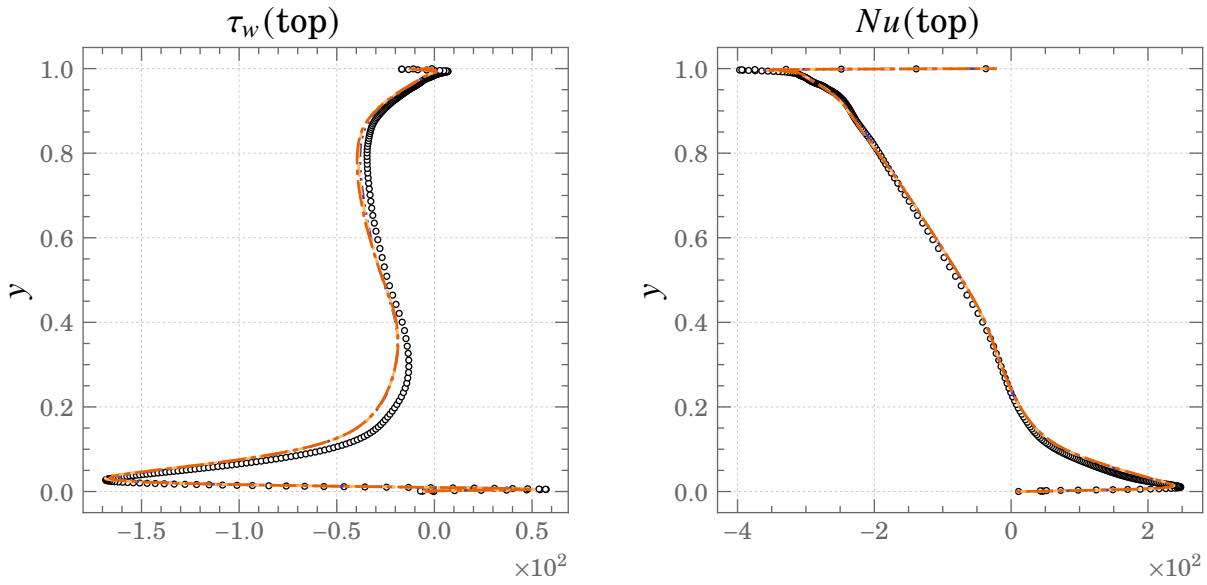

(a) top wall: shear stress, τ_w (b) top wall: Nusselt number, Nu

Figure A.8.: Comparisons of shear stress and Nusselt number profiles at the top wall for Square DHC at $Ra = 10^{11}$

○ ○ ○ *DNS* 498 × 80 664 × 80 996 × 100

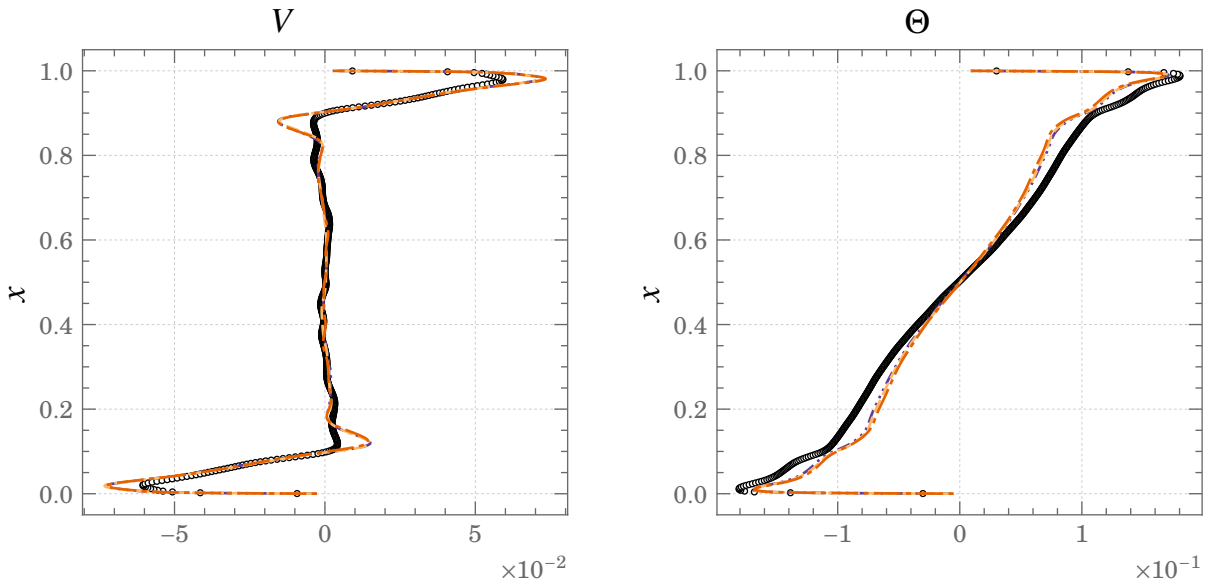

(a) Mean horizontal velocity, V (b) Mean temperature stratification

Figure A.9.: Comparisons of mean horizontal velocity and temperature strtification profiles at the mid cavity ($y = 0.5$) for Square DHC at $Ra = 10^{11}$

○ ○ ○ DNS 498×80 664×80 996×100

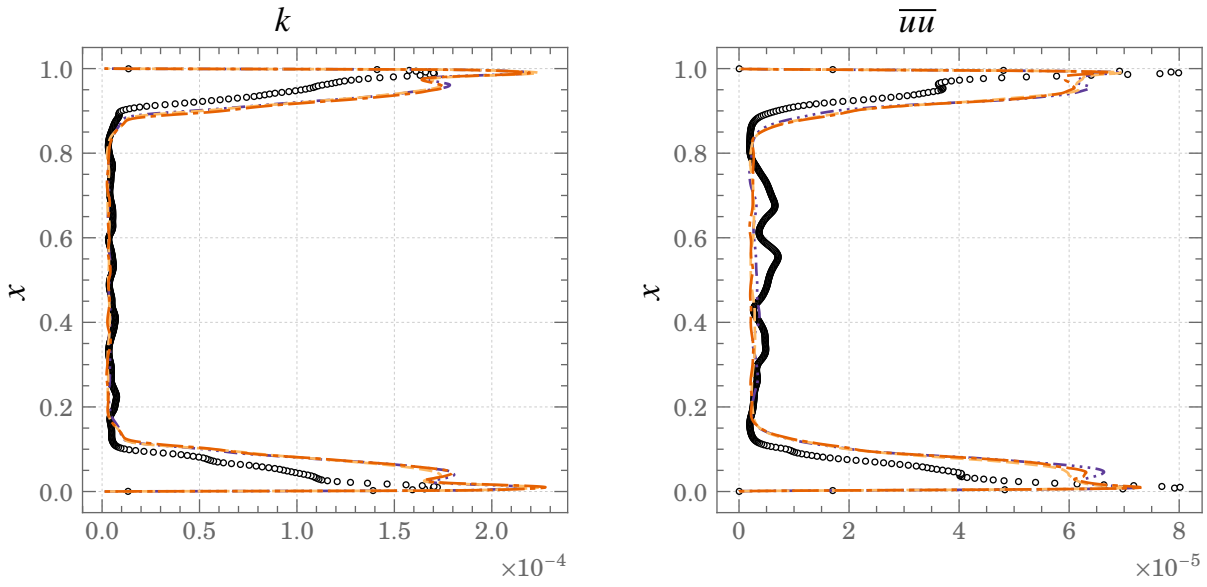

(a) total kinetic energy, k_{tot} (b) $\overline{uu}_{tot}$

Figure A.10.: Comparisons of total kinetic energy and $\overline{uu}_{tot}$ profiles at the mid cavity ($y = 0.5$) for Square DHC at $Ra = 10^{11}$

○ ○ ○ DNS 498×80 664×80 996×100

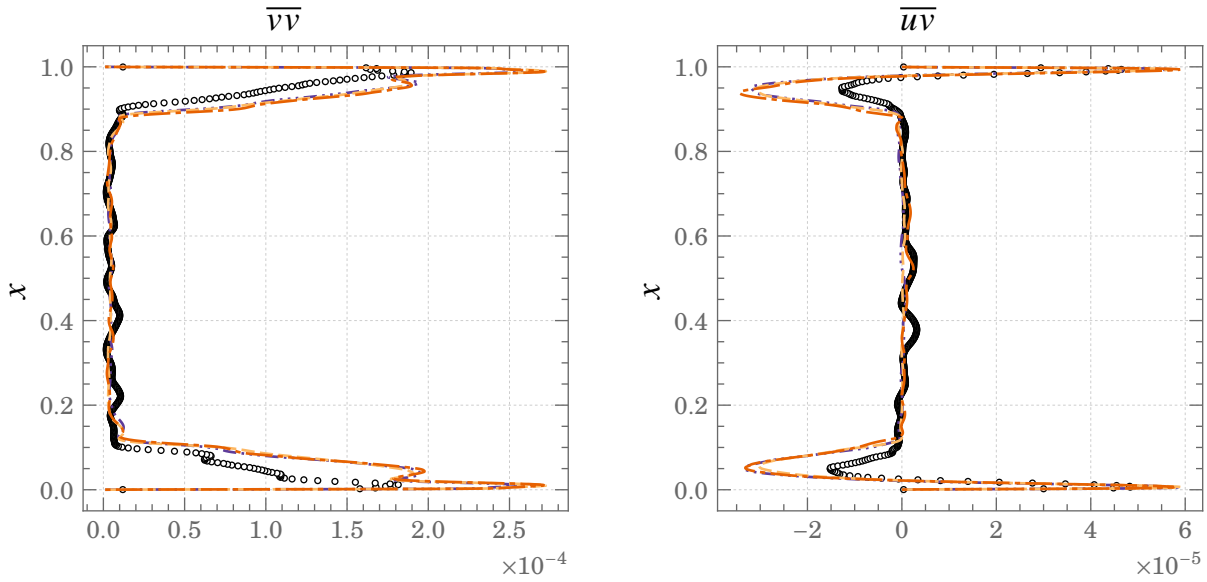

(a) $\overline{vv}_{tot}$ (b) $\overline{uv}_{tot}$

Figure A.11.: Comparisons of $\overline{vv}_{tot}$ and $\overline{uv}_{tot}$ profiles at the mid cavity ($y = 0.5$) for Square DHC at $Ra = 10^{11}$

○ ○ ○ DNS 498×80 664×80 996×100

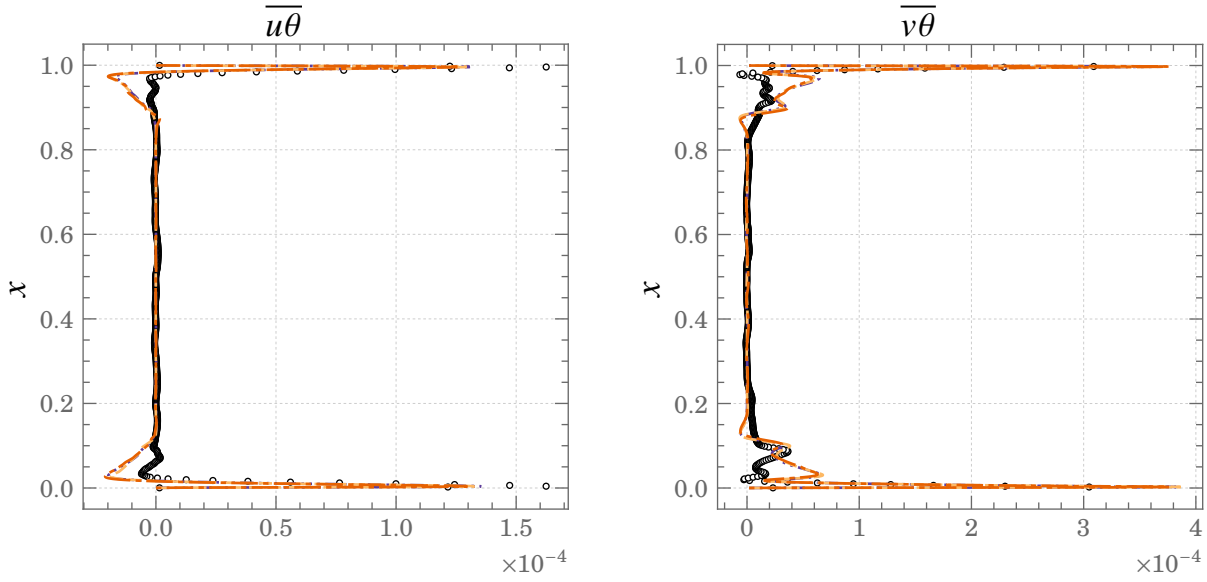

(a) $\overline{u\theta}_{tot}$ (b) $\overline{v\theta}_{tot}$

Figure A.12.: Comparisons of $\overline{u\theta}_{tot}$ and $\overline{v\theta}_{tot}$ profiles at the mid cavity ($y = 0.5$) for Square DHC at $Ra = 10^{11}$

○ ○ ○ DNS 498×80 664×80 996×100

A.2. Comparison of dynamic Smagorinsky, classic Smagorinsky, and WALE models

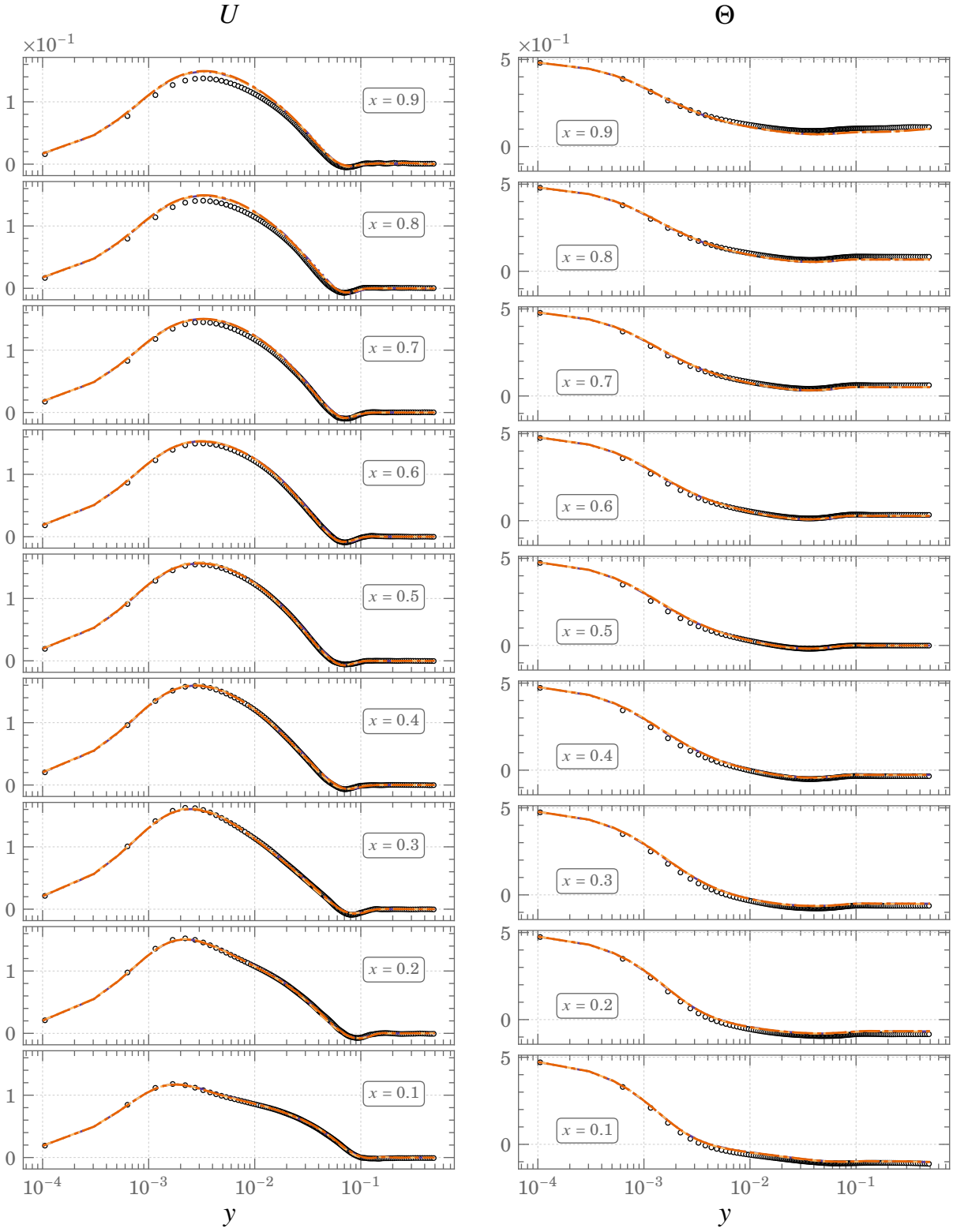

(a) Mean velocity, U

(b) Mean temperature, Θ

Figure A.13.: Comparisons of mean velocity and temperature profiles for Square DHC at $Ra = 10^{11}$

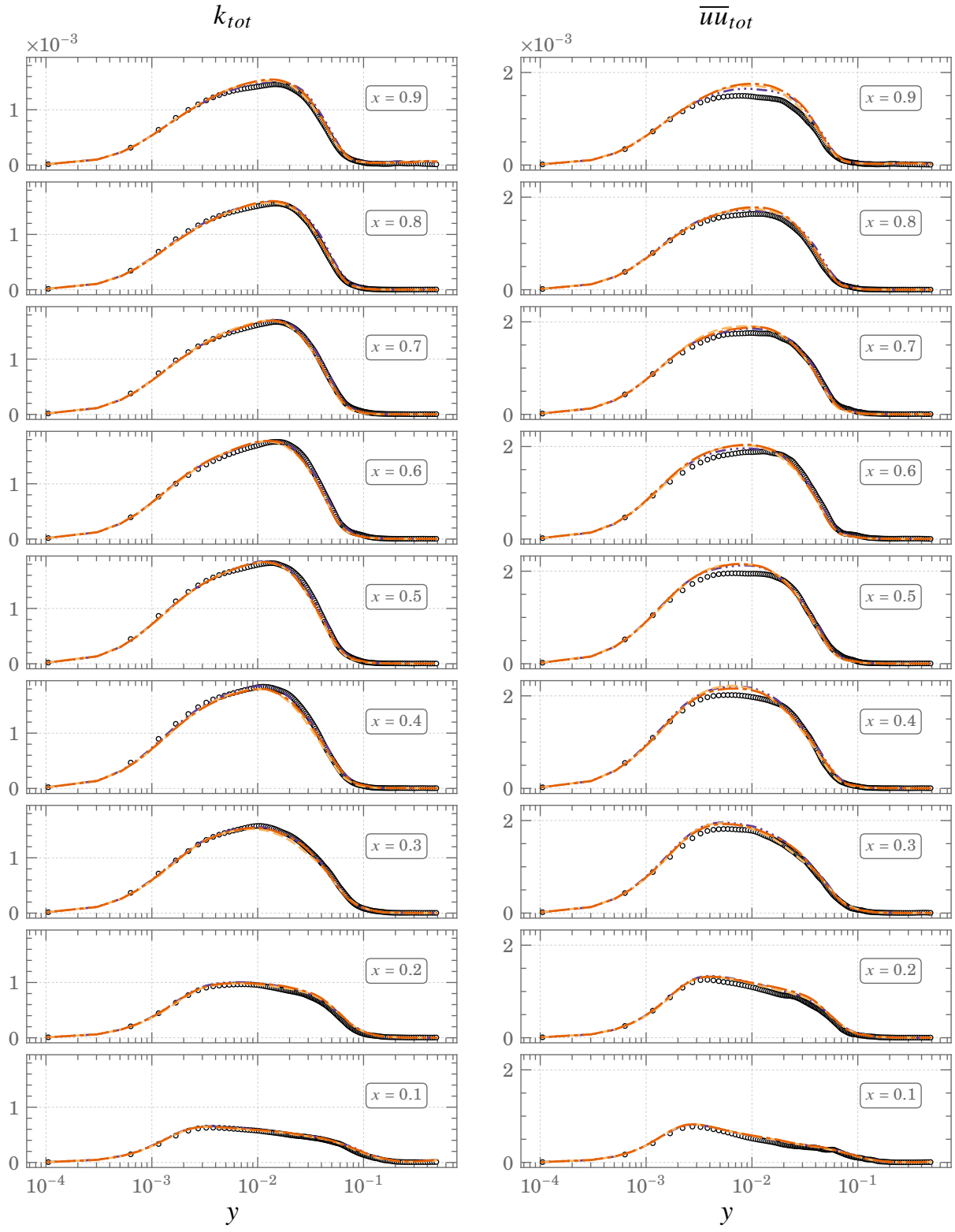

(a) total kinetic energy, k_{tot}

(b) $\overline{uu}_{tot}$

Figure A.14.: Comparisons of k_{tot} and $\overline{uu}_{tot}$ profiles for Square DHC at $Ra = 10^{11}$
○ ○ ○ DNS $Dyn - SMAG$ $SMAG$ $WALE$

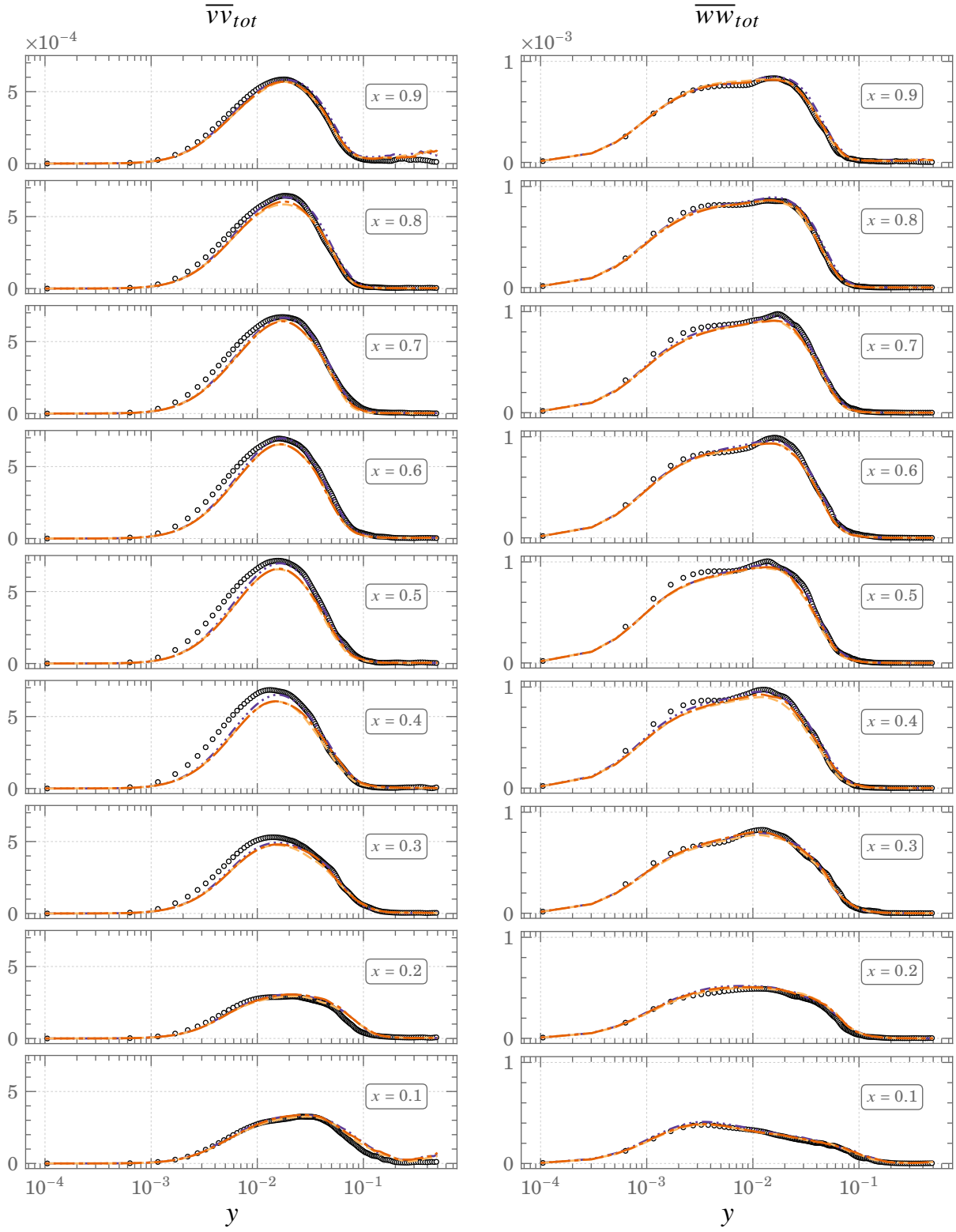

(a) $\overline{vv}_{tot}$ (b) $\overline{ww}_{tot}$

Figure A.15.: Comparisons of $\overline{vv}_{tot}$ and $\overline{ww}_{tot}$ profiles for Square DHC at $Ra = 10^{11}$
$\circ\ \circ\ \circ\ DNS$ $Dyn - SMAG$ $SMAG$ $WALE$

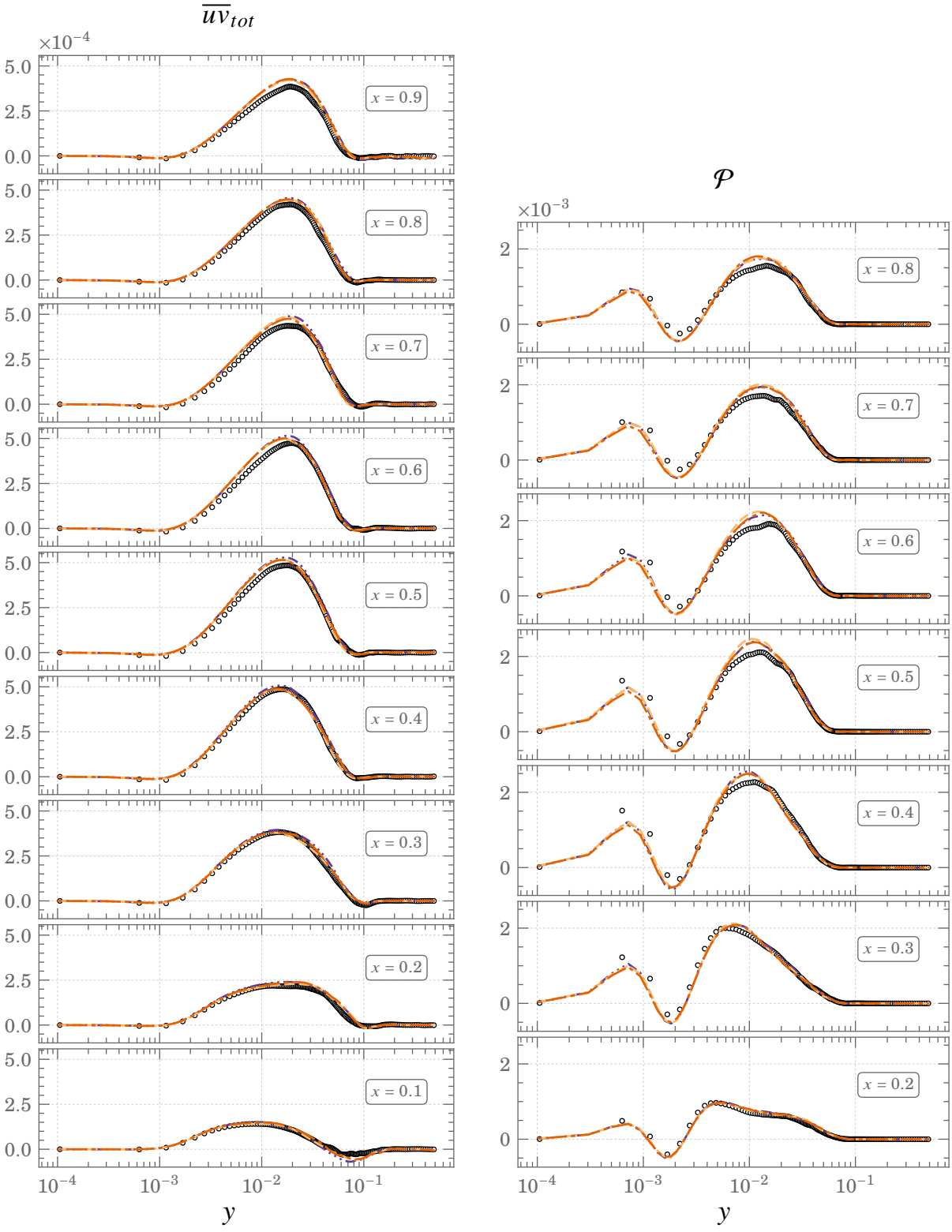

(a) $\overline{uv}_{tot}$ (b) shear production, $\mathcal{P}$

Figure A.16.: Comparisons of $\overline{uv}_{tot}$ and shear production, $\mathcal{P}$, profiles for Square DHC at $Ra = 10^{11}$

$\circ\ \circ\ \circ$ *DNS* — *Dyn – SMAG* — *SMAG* — *WALE*

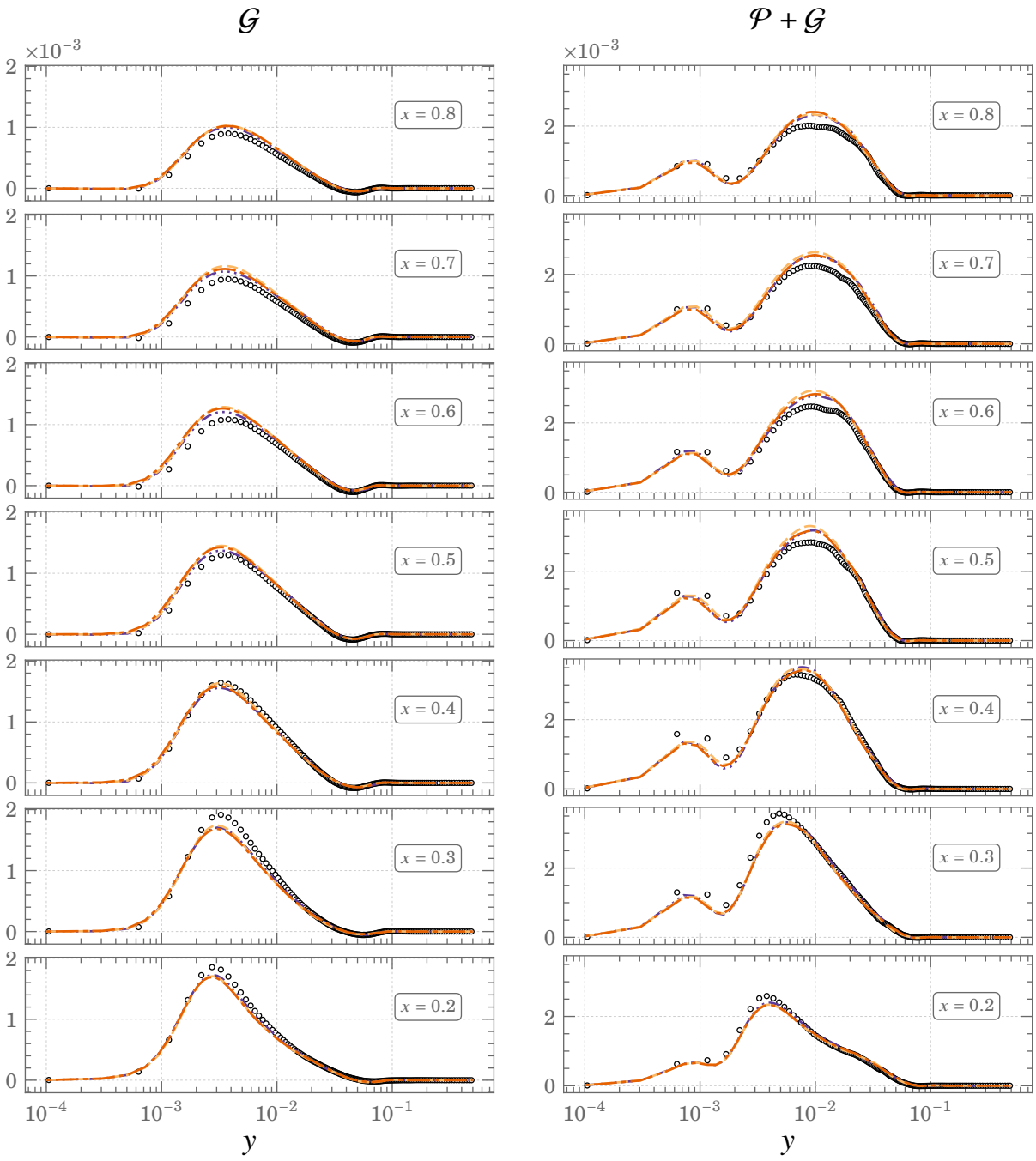

(a) buoyancy production, $\mathcal{G}$

(b) Total production, $\mathcal{P}+\mathcal{G}$

Figure A.17.: Comparisons of buoyancy production, $\mathcal{G}$, and total production, $\mathcal{P}+\mathcal{G}$, profiles for Square DHC at $Ra = 10^{11}$

$\circ\ \circ\ \circ\ DNS$ $-\cdot-$ $Dyn-SMAG$ $- - -$ $SMAG$ $-\cdot\cdot-$ $WALE$

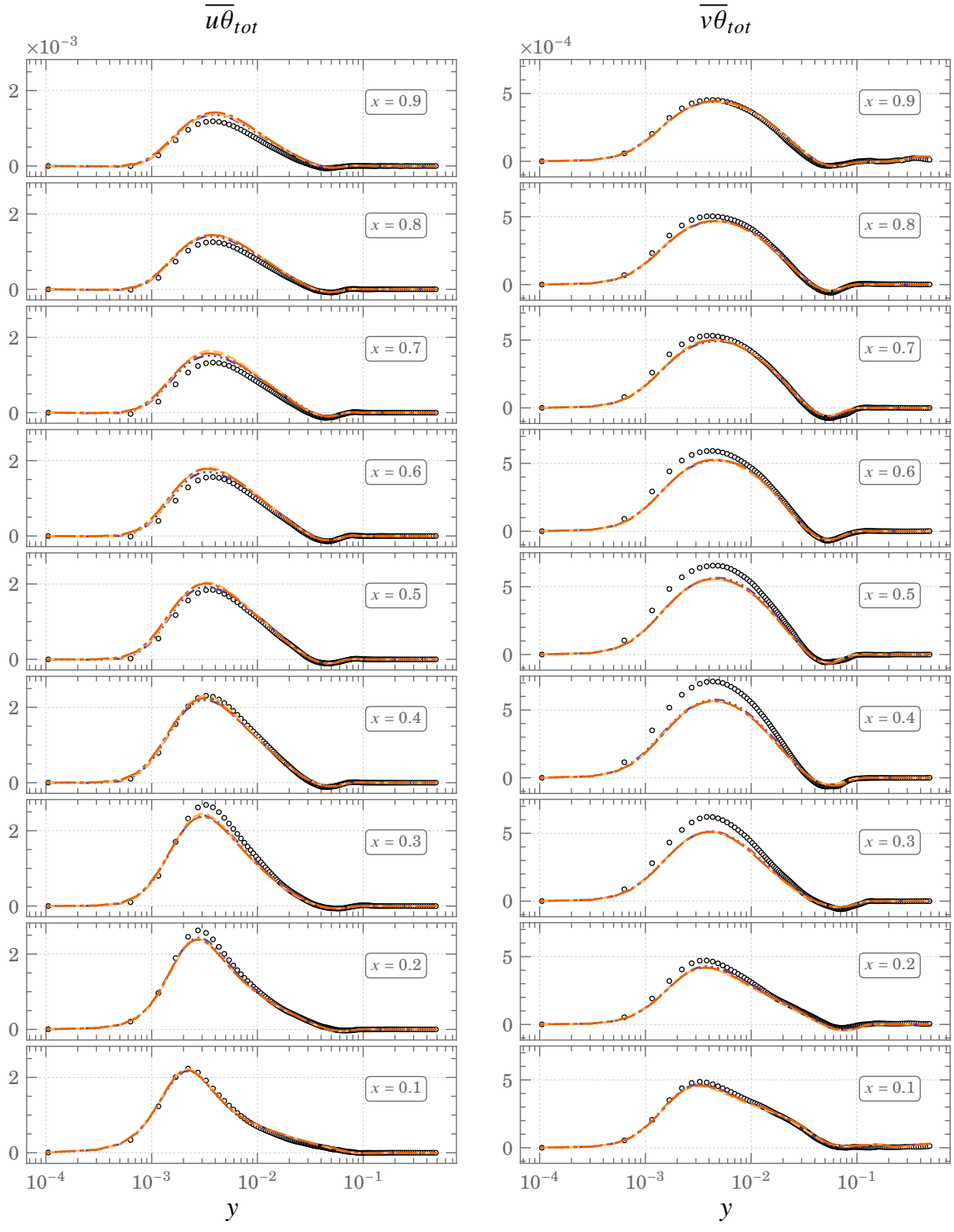

(a) $\overline{u\theta}_{tot}$ (b) $\overline{v\theta}_{tot}$

Figure A.18.: Comparisons of $\overline{u\theta}_{tot}$ and $\overline{v\theta}_{tot}$ profiles for Square DHC at $Ra = 10^{11}$
○ ○ ○ *DNS* *Dyn – SMAG* *SMAG* *WALE*

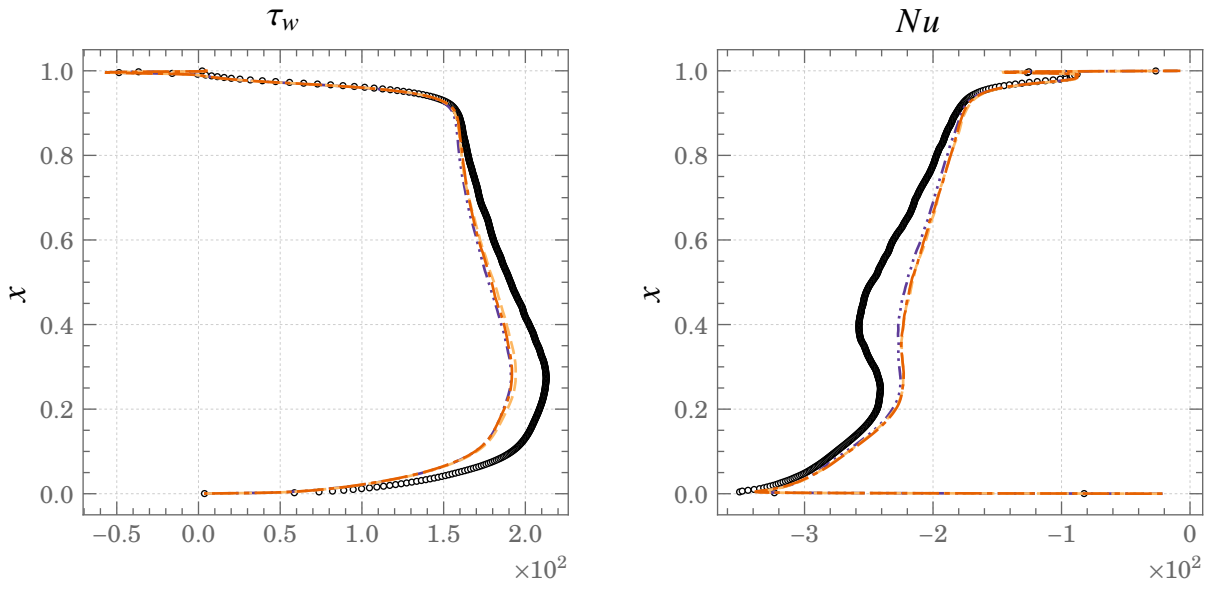

(a) shear stress, τ_w (b) Nusselt number, Nu

Figure A.19.: Comparisons of shear stress and Nusselt number profiles at the hot wall for Square DHC at $Ra = 10^{11}$

$\circ\ \circ\ \circ\ DNS$ $Dyn - SMAG$ $SMAG$ $WALE$

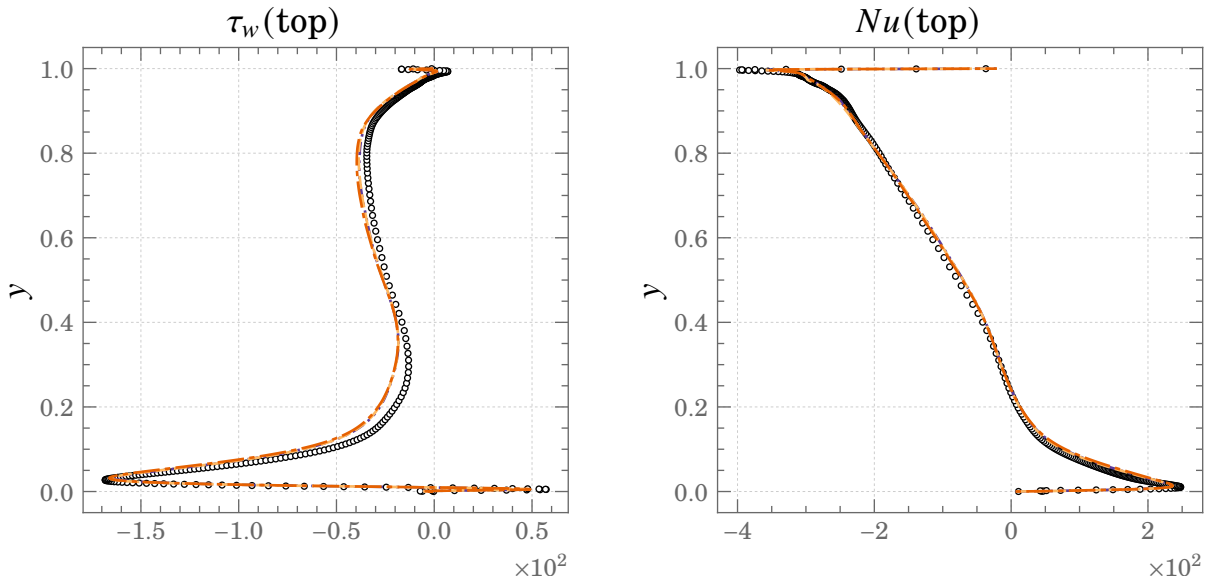

(a) top wall: shear stress, τ_w (b) top wall: Nusselt number, Nu

Figure A.20.: Comparisons of shear stress and Nusselt number profiles at the top wall for Square DHC at $Ra = 10^{11}$

$\circ\ \circ\ \circ\ DNS$ $Dyn - SMAG$ $SMAG$ $WALE$

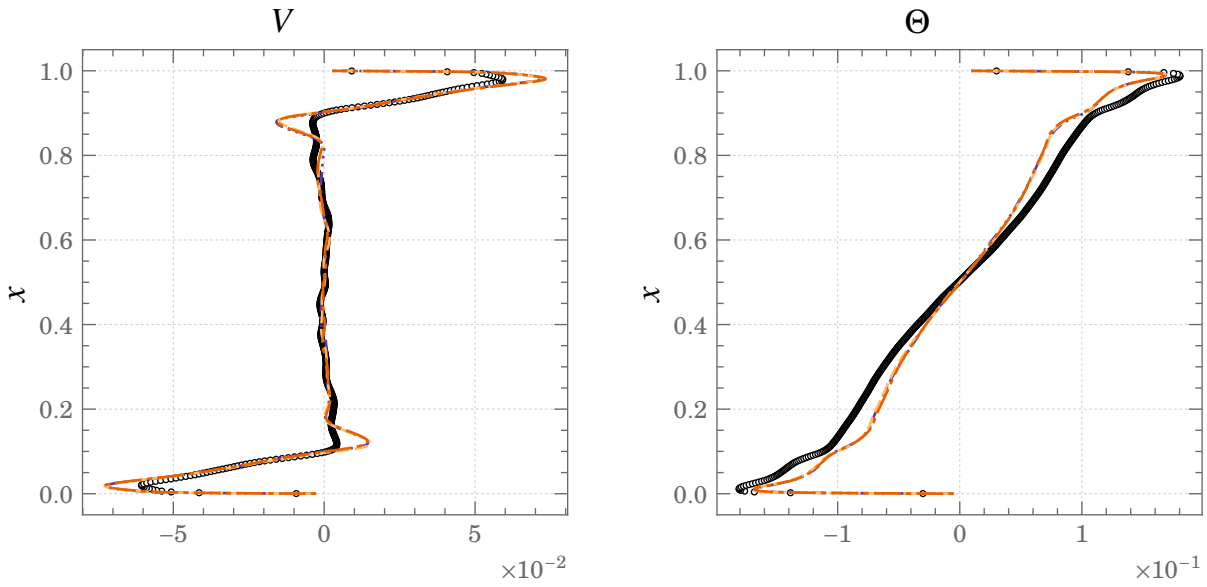

(a) Mean horizontal velocity, V (b) Mean temperature stratification

Figure A.21.: Comparisons of mean horizontal velocity and temperature strtification profiles at the mid cavity ($y = 0.5$) for Square DHC at $Ra = 10^{11}$
○ ○ ○ *DNS* *Dyn − SMAG* *SMAG* *WALE*

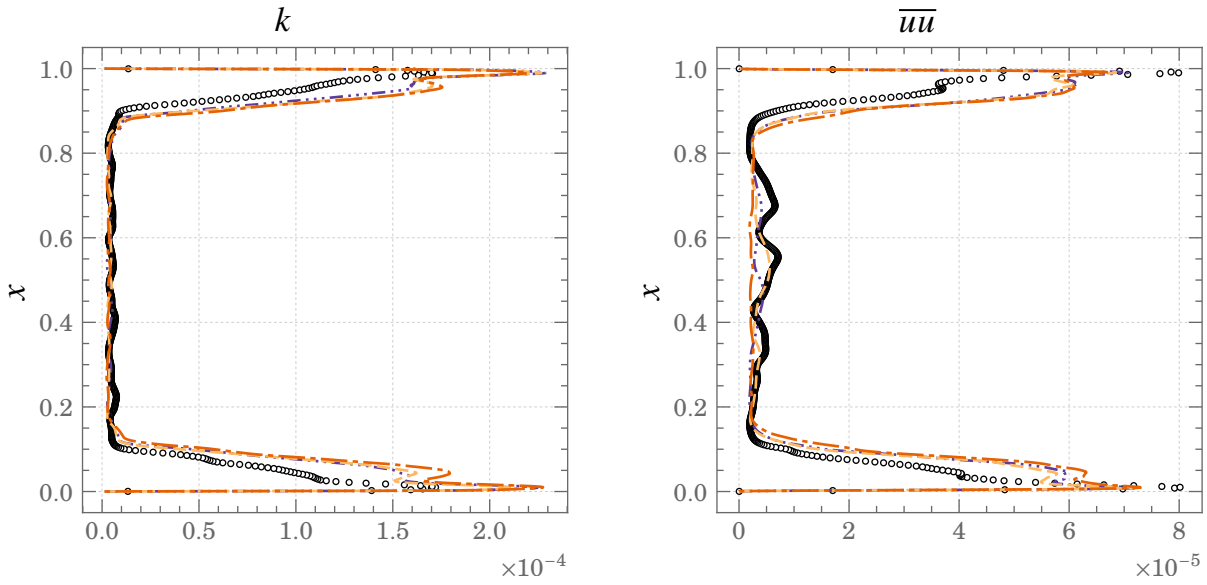

(a) total kinetic energy, k_{tot} (b) $\overline{uu}_{tot}$

Figure A.22.: Comparisons of total kinetic energy and $\overline{uu}_{tot}$ profiles at the mid cavity ($y = 0.5$) for Square DHC at $Ra = 10^{11}$
○ ○ ○ *DNS* *Dyn − SMAG* *SMAG* *WALE*

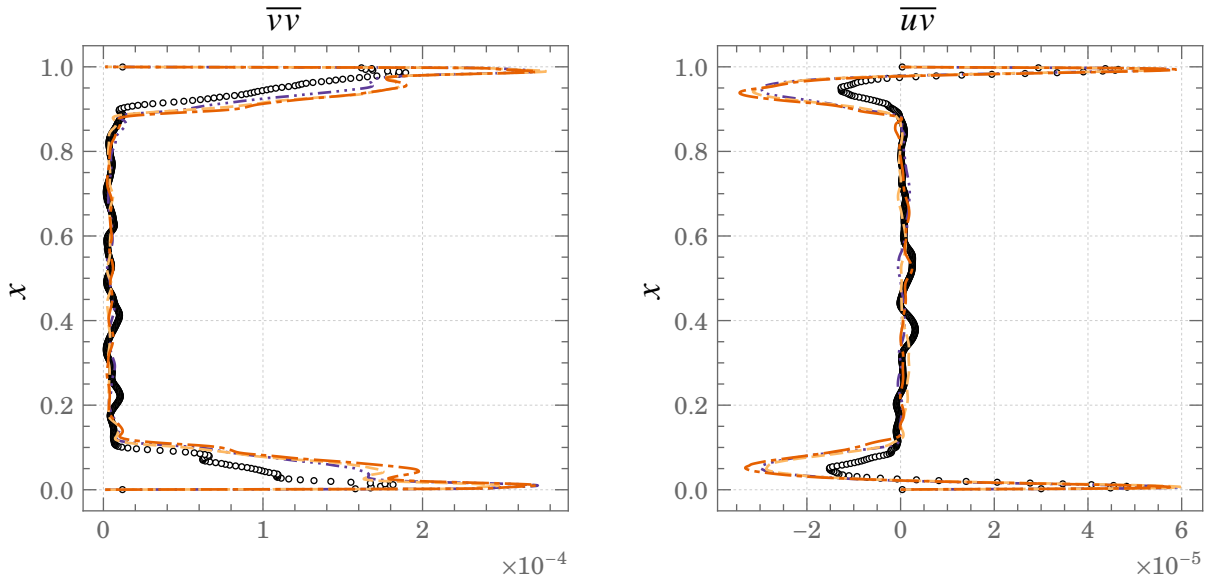

(a) $\overline{vv}_{tot}$ (b) $\overline{uv}_{tot}$

Figure A.23.: Comparisons of $\overline{vv}_{tot}$ and $\overline{uv}_{tot}$ profiles at the mid cavity ($y = 0.5$) for Square DHC at $Ra = 10^{11}$

$\circ\ \circ\ \circ\ DNS$ $Dyn - SMAG$ $SMAG$ $WALE$

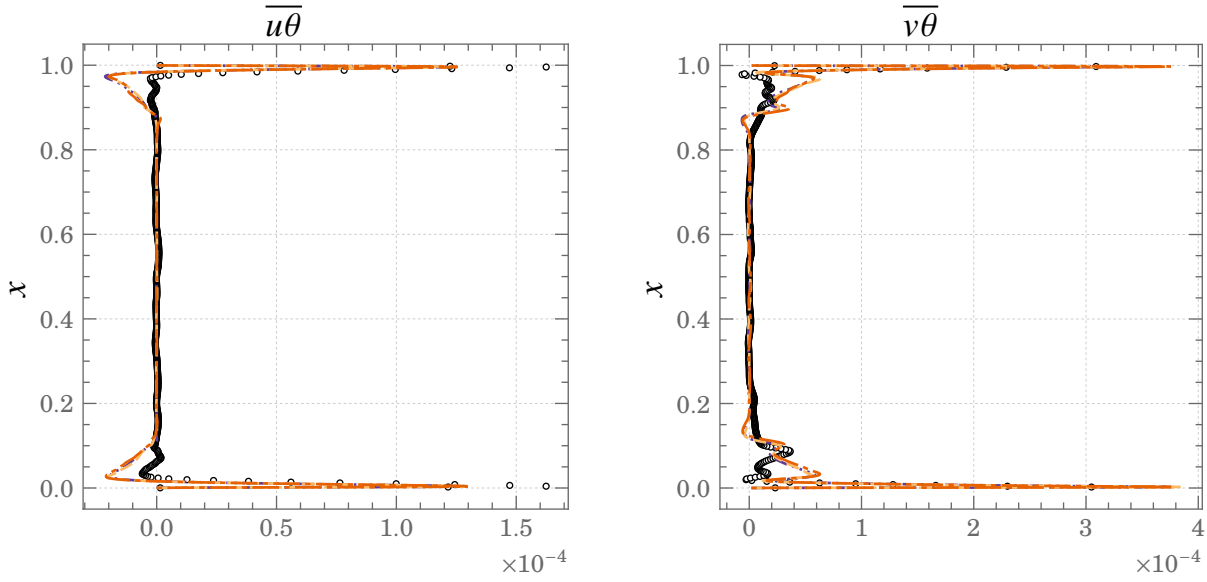

(a) $\overline{u\theta}_{tot}$ (b) $\overline{v\theta}_{tot}$

Figure A.24.: Comparisons of $\overline{u\theta}_{tot}$ and $\overline{v\theta}_{tot}$ profiles at the mid cavity ($y = 0.5$) for Square DHC at $Ra = 10^{11}$

$\circ\ \circ\ \circ\ DNS$ $Dyn - SMAG$ $SMAG$ $WALE$

Appendix B.

Rectangular differentially heated cavity

In this chapter, a brief overview of the results obtained for the rectangular differentially heated cavity of F. Trias et al. (2010a,b) are presented. The full range of models were tested for this case, however, only the comparisons between the full buoyancy extended model formulations of $k\omega$-SST, BL-v^2/k, and $k\omega$-SST HTLES are shown for the sake of brevity. In regards to the pure RANS simulations with accounting for buoyancy effects (not shown here), the different strategies employed to account for buoyancy do not improve the results for this case, irrespective of the models ($k\omega$-SST or BL-v^2/k). *A priori*,the results have to be analysed considering the fact that such models are not designed to handle test cases presenting laminar to turbulent transition very well. It can be noted from the shear stress (Figure B.1a) and Nusselt number (Figure B.1b) profiles that the models predict the start of the fully turbulent regime very differently, where $k\omega$-SST model predicts too early at $x = 0.2$ while the BL-v^2/k) model predicts a fully turbulent regime later at $x = 0.8$ than that observed in the DNS at $x = 0.6$. Observing the mean velocity profiles (Figure B.2a) it can be noted that the prediction of BL-v^2/k) model in the laminar ($x < 0.4$) and transition regions ($0.4 < x < 0.6$) regions is very good as compared to the $k\omega$-SST model. The temperature profiles are better predicted by the BL-v^2/k model (Figure B.2b) along with better prediction of stratification in comparison.

In regards to the HTLES model, the key observation to be made is the lack of resolved

energy (Figure B.3b) while the total energy (Figure B.3a) is fully composed of the modelled contribution (not shown here). Figure B.4 shows the shielding function, imposed energy ratio, and Kolmogorov energy ratio obtained for the test case along the full width of the cavity. It can be noted from the profiles of the shielding function that the model switches to LES only after cavity height $x > 0.4$ and does not transition completely near the top of the cavity. It is interesting to note that in this test case the model switches back to RANS mode due to the Kolmogorov energy ratio $\min(1, r_K)$ (see profile at $x = 0.5$ in Figures B.4b and B.4c) and that the shielding function behave as intended far from the wall. Although the HTLES model fails to improve on the RANS predictions for this rather challenging test case, it is however a positive aspect to note that the results have not degraded as compared to the RANS model.

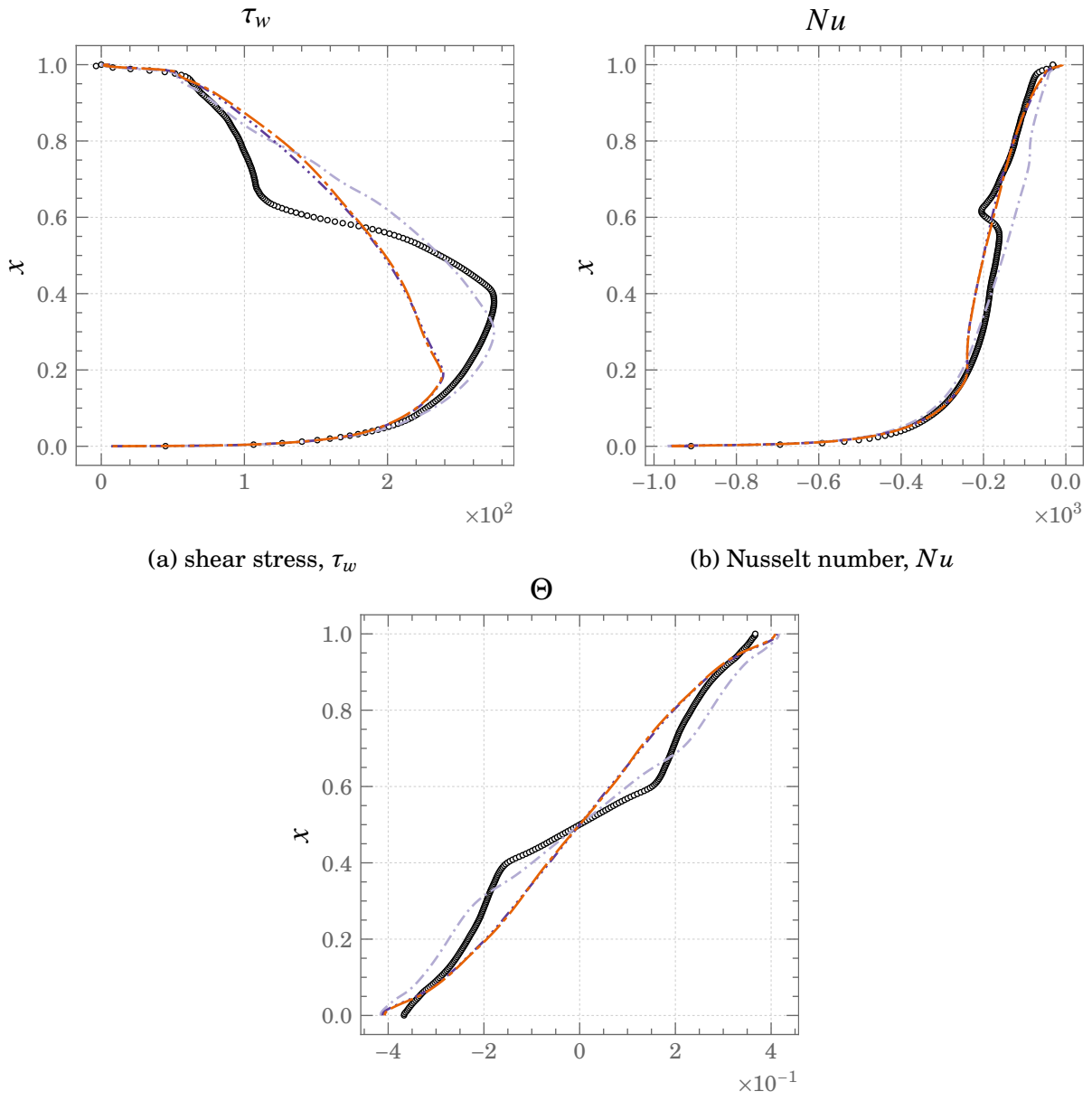

(a) shear stress, τ_w

(b) Nusselt number, Nu

(c) Mean temperature stratification

Figure B.1.: Comparisons of shear stress, Nusselt number, and temperature stratification profiles for Rectangular DHC at $Ra = 10^{11}$

$\circ\ \circ\ \circ\ DNS$ $-\cdot-$ $HTLES$ $-\cdot-$ $RANS-BL$ $-\cdot\cdot-$ $RANS-KW$

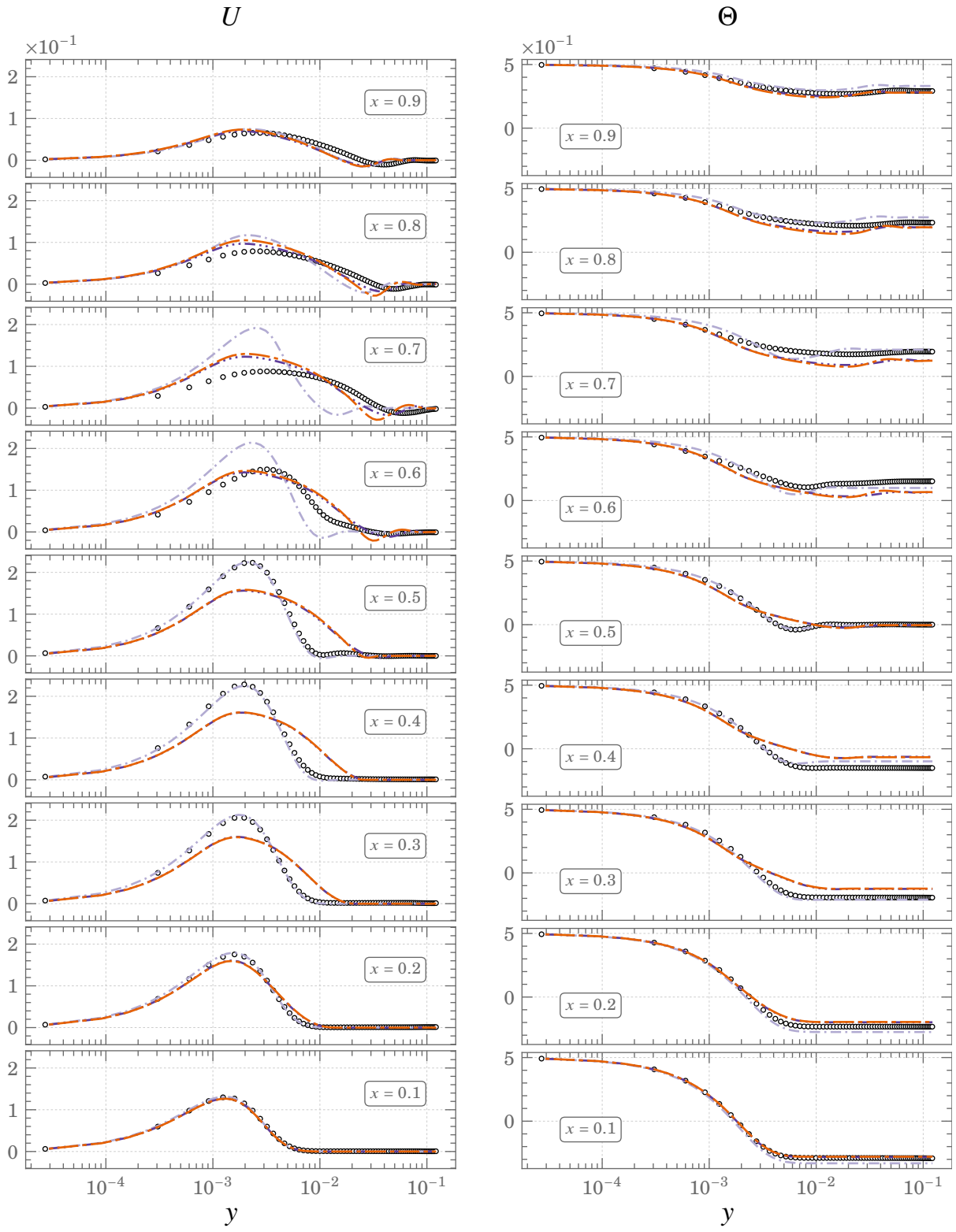

(a) Mean velocity, U

(b) Mean temperature, Θ

Figure B.2.: Comparisons of mean velocity and temperature profiles for Rectangular DHC at $Ra = 10^{11}$

○ ○ ○ *DNS* — *HTLES* — *RANS – BL* — *RANS – KW*

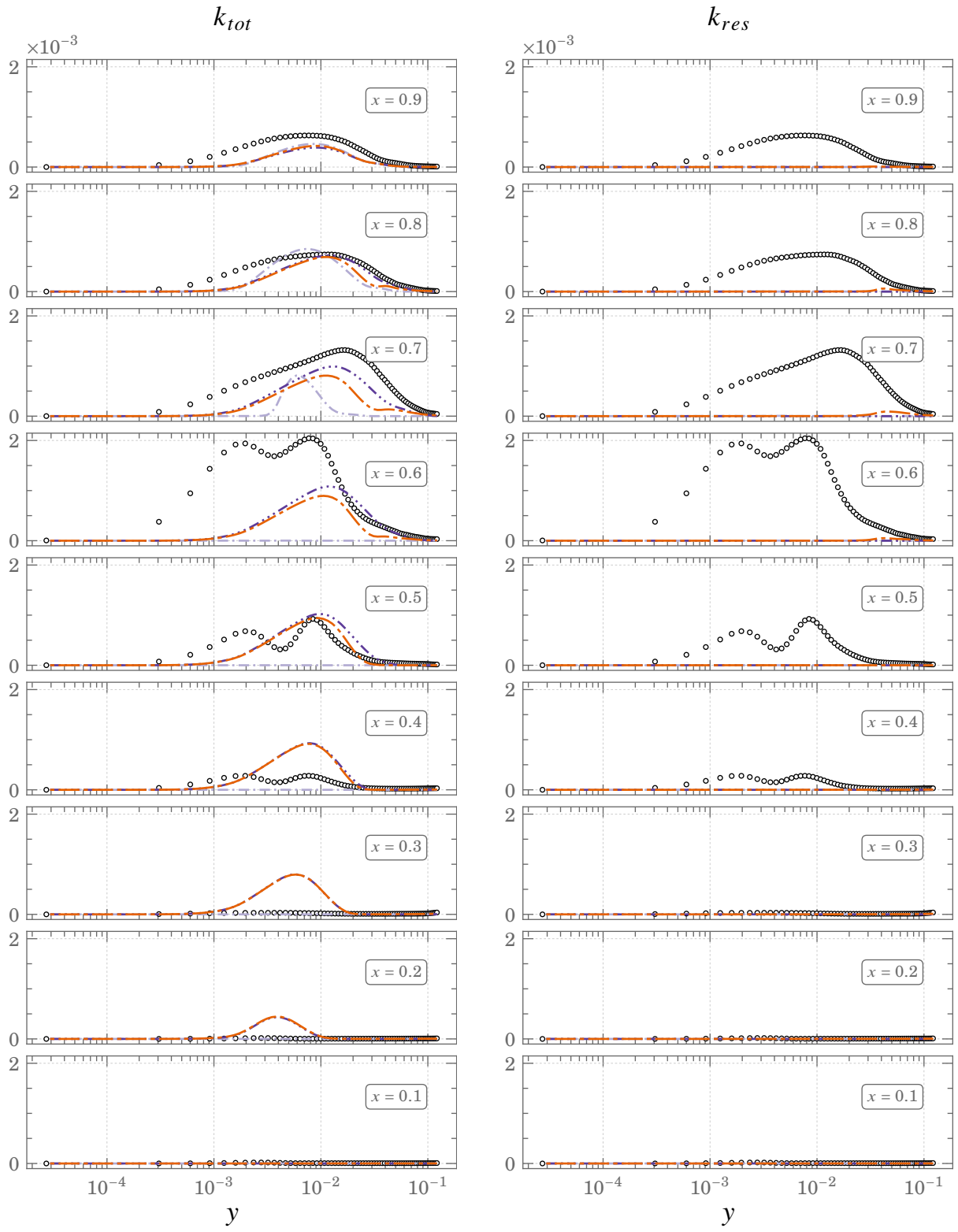

(a) total kinetic energy, k_{tot}

(b) $\overline{uu}_{tot}$

Figure B.3.: Comparisons of k_{tot} and k_{res} profiles for Rectangular DHC at $Ra = 10^{11}$

$\circ\ \circ\ \circ\ DNS$ $-\cdot-$ $HTLES$ $-\cdot-$ $RANS-BL$ $-\cdot\cdot-$ $RANS-KW$

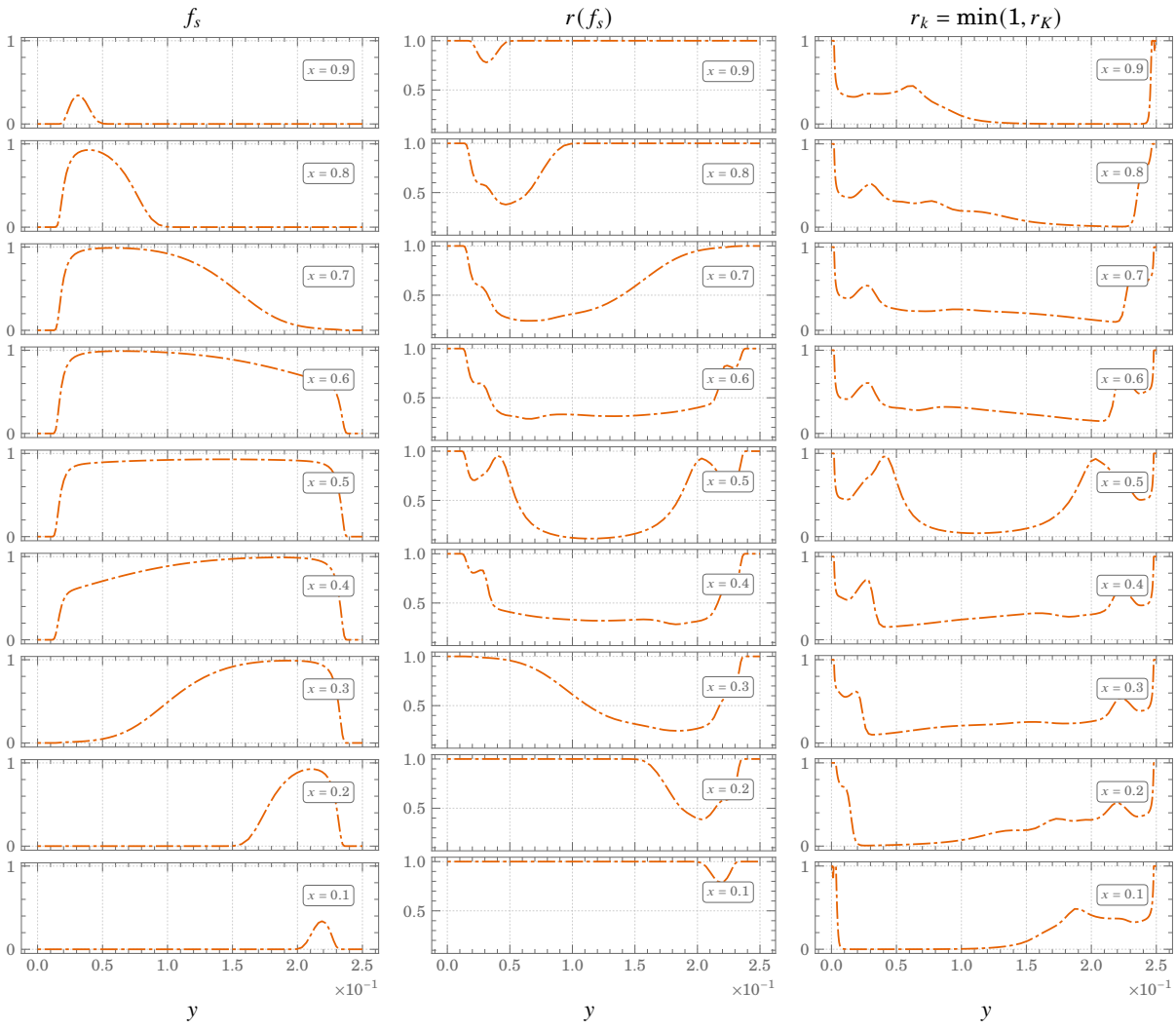

(a) shielding function, f_s (b) Imposed energy ratio, $r(f_s)$ (c) Kolmogorov energy ratio, $\min(1, r_K)$

Figure B.4.: profiles of f_s, $r(f_s)$, and $\min(1, r_K)$ for Rectangular DHC at $Ra = 10^{11}$
HTLES

Bibliography

Abramov, A G, N G Ivanov, and E M Smirnov (2003). “Numerical Study of High-Ra Rayleigh-Bénard Mercury and Water Convection in Confined Enclosures Using a Hybrid RANS/LES Technique”. *Proc. Eurotherm Seminar*.

Afailal, Al Hassan et al. (2019). “Development and Validation of a Hybrid Temporal LES Model in the Perspective of Applications to Internal Combustion Engines”.

Ampofo, F. and T.G. Karayiannis (2003). “Experimental Benchmark Data for Turbulent Natural Convection in an Air Filled Square Cavity”. *International Journal of Heat and Mass Transfer*.

Andreani, Michele, Arnoldo Badillo, and Ralf Kapulla (2016). “Synthesis of the OECD/NEA-PSI CFD Benchmark Exercise”. *Nuclear Engineering and Design*.

Archambeau, Frédéric, Namane Méchitoua, and Marc Sakiz (2004). “Code Saturne: A Finite Volume Code for the Computation of Turbulent Incompressible Flows - Industrial Applications”. *International Journal on Finite Volumes*.

Ashrafi, Khosro, Ali Ahmadi Orkomi, and Majid Shafipour Motlagh (2017). “Direct Effect of Atmospheric Turbulence on Plume Rise in a Neutral Atmosphere”. *Atmospheric Pollution Research*.

Bardina, J., J. Ferziger, and W. Reynolds (1980). “Improved Subgrid-Scale Models for Large-Eddy Simulation”. *13th Fluid and PlasmaDynamics Conference*. 13th Fluid and PlasmaDynamics Conference. American Institute of Aeronautics and Astronautics.

Bentaleb, Yacine and Remi Manceau (2011). “A Hybrid Temporal LES/RANS Formulation Based on a Two-Equation Subfilter Model”. *Seventh International Symposium on Turbulence and Shear Flow Phenomena*.

Billard, F. and D. Laurence (2012). “A Robust K-ε−/k Elliptic Blending Turbulence Model Applied to near-Wall, Separated and Buoyant Flows”. *International Journal of Heat and Fluid Flow*.

Bosshard, Christoph et al. (2013). “Large Eddy Simulation of the Differentially Heated Cubic Cavity Flow by the Spectral Element Method”. *Computers & Fluids*.

Boudjemadi, R. et al. (1997). “Budgets of Turbulent Stresses and Fluxes in a Vertical Slot Natural Convection Flow at Rayleigh Ra = 105and 5.4 105”. *International Journal of Heat and Fluid Flow*.

Carpy, S. (2006). *Contribution à La Modélisation Instationnaire de La Turbulence. Modélisations URANS et Hybride RANS/LES*.

Chaouat, Bruno and Roland Schiestel (2005). “A New Partially Integrated Transport Model for Subgrid-Scale Stresses and Dissipation Rate for Turbulent Developing Flows”. *Physics of Fluids*.

Chaouat, Bruno and Roland Schiestel (2009). “Progress in Subgrid-Scale Transport Modelling for Continuous Hybrid Non-Zonal RANS/LES Simulations”. *International Journal of Heat and Fluid Flow*.

Clifford, Corey E. and Mark L. Kimber (2020). “Assessment of RANS and LES Turbulence Models for Natural Convection in a Differentially Heated Square Cavity”. *Numerical Heat Transfer, Part A: Applications*.

Daly, Bart J. and Francis H. Harlow (1970). “Transport Equations in Turbulence”. *Physics of Fluids*.

Davidson, Lars (1990). “Second-Order Corrections of the k-ε Model to Account for Non-Isotropic Effects Due to Buoyancy”. *International Journal of Heat and Mass Transfer*.

Dehbi, A., F. Han, and Jarmo Kalilainen (2014). “Large Eddy Simulations of Flow inside a Cubical Differentially Heated Cavity under Realistic Boundary Conditions: International

Congress on Advances in Nuclear Power Plants, ICAPP 2014". *International Congress on Advances in Nuclear Power Plants, ICAPP 2014*.

Dehoux, F., S. Benhamadouche, and R. Manceau (2017). "An Elliptic Blending Differential Flux Model for Natural, Mixed and Forced Convection". *International Journal of Heat and Fluid Flow*.

Dehoux, Frédéric (2012). "Modélisation Statistique Des Écoulements Turbulents En Convection Forcée, Mixte et Naturelle". These de doctorat. Poitiers.

De Laage de Meux, B. et al. (2015). "Anisotropic Linear Forcing for Synthetic Turbulence Generation in Large Eddy Simulation and Hybrid RANS/LES Modeling". *Physics of Fluids*.

Dol, H.S., K. Hanjalic, and S. Kenjeres (1997). "A Comparative Assessment of the Second-Moment Differential and Algebraic Models in Turbulent Natural Convection". *International Journal of Heat and Fluid Flow*.

Duffal, Vladimir (2020). "Développement d'un modèle hybride RANS-LES pour l'étude des efforts instationnaires en paroi". PhD thesis. Université de Pau et des Pays de l'Adour.

Duffal, Vladimir, Benoît de Laage de Meux, and Rémi Manceau (2022). "Development and Validation of a New Formulation of Hybrid Temporal Large Eddy Simulation". *Flow, Turbulence and Combustion*.

Durbin, P. A. (1991). "Near-Wall Turbulence Closure Modeling without "Damping Functions"". *Theoretical and Computational Fluid Dynamics*.

Eidson, Thomas M. (1985). "Numerical Simulation of the Turbulent Rayleigh–Bénard Problem Using Subgrid Modelling". *Journal of Fluid Mechanics*.

Elder, J. W. (1965a). "Laminar Free Convection in a Vertical Slot". *Journal of Fluid Mechanics*.

Elder, J. W. (1965b). "Turbulent Free Convection in a Vertical Slot". *Journal of Fluid Mechanics*.

Fadai-Ghotbi, Atabak (2007). “Modélisation de la turbulence par approches URANS et hybride RANS-LES. prise en compte des effets de paroi par pondération elliptique.” PhD thesis. Université de Poitiers.

Fadai-Ghotbi, Atabak et al. (2010a). “A Seamless Hybrid RANS-LES Model Based on Transport Equations for the Subgrid Stresses and Elliptic Blending”. *Physics of Fluids*.

Fadai-Ghotbi, Atabak et al. (2010b). “Temporal Filtering: A Consistent Formalism for Seamless Hybrid RANS–LES Modeling in Inhomogeneous Turbulence”. *International Journal of Heat and Fluid Flow*.

Fletcher, D. F. et al. (1994). “Numerical Simulations of Smoke Movement from a Pool Fire in a Ventilated Tunnel”. *Fire Safety Journal*.

Friess, Christophe (2010). “Modélisation hybride RANS / LES temporelle des écoulements turbulents”. PhD thesis. Université de Poitiers.

Friess, Christophe, R. Manceau, and T.B. Gatski (2015). “Toward an Equivalence Criterion for Hybrid RANS/LES Methods”. *Computers & Fluids*.

Germano, M. (1992). “Turbulence: The Filtering Approach”. *Journal of Fluid Mechanics*.

Germano, Massimo et al. (1991). “A Dynamic Subgrid-scale Eddy Viscosity Model”. *Physics of Fluids A: Fluid Dynamics*.

Gibson, M. M. and B. E. Launder (1976). “On the Calculation of Horizontal, Turbulent, Free Shear Flows under Gravitational Influence”. *Journal of Heat Transfer*.

Guyer, Jonathan E., Daniel Wheeler, and James A. Warren (2009). “FiPy: Partial Differential Equations with Python”. *Computing in Science & Engineering*.

Hadziabdic, Muhamed et al. (2022). “A Rational Hybrid RANS-LES Model for CFD Predictions of Microclimate and Environmental Quality in Real Urban Structures”. *Building and Environment*.

Hanjalic, K. (2002). “One-Point Closure Models for Buoyancy-Driven Turbulent Flows”. *Annual Review of Fluid Mechanics*.

Hanjalic, Kemal and B. E. Launder (2011). *Modelling Turbulence in Engineering and the Environment: Second-Moment Routes to Closure*. Cambridge University Press.

Henkes, R. a. W. M. and P. Le Quéré (1996). "Three-Dimensional Transition of Natural-Convection Flows". *Journal of Fluid Mechanics*.

Hinze, J. O. and JO HINZE (1975). *Turbulence*. McGraw-Hill. Google Books: DfRQAAAAMAAJ.

Ince, N.Z. and B. E. Launder (1989). "On the Computation of Buoyancy-Driven Turbulent Flows in Rectangular Enclosures". *International Journal of Heat and Fluid Flow*.

Jakirlic, S. and K. Hanjalic (2002). "A New Approach to Modelling Near-Wall Turbulence Energy and Stress Dissipation". *Journal of Fluid Mechanics*.

Jameel, Syed Mohd Saad (2020). "Turbulence Modelling of Mixed and Natural Convection Regimes in the Context of the Underhood-Space of Automobiles." PhD thesis. Université de Pau et des Pays de l'Adour.

Jones, W.P and B. E. Launder (1972). "The Prediction of Laminarization with a Two-Equation Model of Turbulence". *International Journal of Heat and Mass Transfer*.

Kampé de Feriet, J. (1952). *Generalized Harmonic Analysis and Some Boundary Value Problems*. University of Maryland, Institute for Fluid Dynamics and Applied Mathematics. Google Books: byGNzQEACAAJ.

Kang, Hyung Suk, Stuart Chester, and Charles Meneveau (2003). "Decaying Turbulence in an Active-Grid-Generated Flow and Comparisons with Large-Eddy Simulation". *Journal of Fluid Mechanics*.

Keating, Anthony and Ugo Piomelli (2006). "A Dynamic Stochastic Forcing Method as a Wall-Layer Model for Large-Eddy Simulation". *Journal of Turbulence*.

Kenjeres, S. and K. Hanjalic (2006). "LES, T-RANS and Hybrid Simulations of Thermal Convection at High Ra Numbers". *International Journal of Heat and Fluid Flow*.

Kis, P. and H. Herwig (2014). "Natural Convection in a Vertical Plane Channel: DNS Results for High Grashof Numbers". *Heat and Mass Transfer*.

Kizildag, D. et al. (2014). "Large Eddy and Direct Numerical Simulations of a Turbulent Water-Filled Differentially Heated Cavity of Aspect Ratio 5". *International Journal of Heat and Mass Transfer*.

Kocutar, P., L. kerget, and J. Ravnik (2015). “Hybrid LES/URANS Simulation of Turbulent Natural Convection by BEM”. *Engineering Analysis with Boundary Elements*.

Kolmogorov, A. (1941). “The Local Structure of Turbulence in Incompressible Viscous Fluid for Very Large Reynolds Numbers”. *Proceedings of the Royal Society of London. Series A: Mathematical and Physical Sciences*.

Kolmogorov, Andrej Nikolaevich (1942). “Equations of Turbulent Motion in an Incompressible Fluid”. *Doklady Akademii Nauk SSSR*.

Kumar, Rajesh and Anupam Dewan (2016). “A Study of LES–SGS Closure Models Applied to a Square Buoyant Cavity”. *International Journal of Heat and Mass Transfer*.

Launder, B. E. (1975). “On the Effects of a Gravitational Field on the Turbulent Transport of Heat and Momentum”. *Journal of Fluid Mechanics*.

Launder, B. E. and B.I. Sharma (1974). “Application of the Energy-Dissipation Model of Turbulence to the Calculation of Flow near a Spinning Disc”. *Letters in Heat and Mass Transfer*.

Laurence, D. R., J. C. Uribe, and S. V. Utyuzhnikov (2005). “A Robust Formulation of the V2-f Model”. *Flow, Turbulence and Combustion*.

Le Quéré, Patrick and Masud Behnia (1998). “From Onset of Unsteadiness to Chaos in a Differentially Heated Square Cavity”. *Journal of Fluid Mechanics*.

Lee, Myoungkyu and Robert D. Moser (2015). “Direct Numerical Simulation of Turbulent Channel Flow up to Reτ = 5200”. *Journal of Fluid Mechanics*.

Leonard, A. (1975). “Energy Cascade in Large-Eddy Simulations of Turbulent Fluid Flows”. *Advances in Geophysics*. Elsevier.

Lilly, D. K. (1967). “The Representation of Small-Scale Turbulence in Numerical Simulation Experiments”. *Proc. IBM Scientific Computing Symposium on Environmental Sciences*.

Lilly, D. K. (1992). “A Proposed Modification of the Germano Subgrid-scale Closure Method”. *Physics of Fluids A: Fluid Dynamics*.

Lorenz, Edward N. (1963). “Deterministic Nonperiodic Flow”. *Journal of the Atmospheric Sciences*.

Manceau, Rémi (2018). “Progress in Hybrid Temporal LES”. *Progress in Hybrid RANS-LES Modelling*. Ed. by Yannick Hoarau et al. Springer International Publishing.

Manceau, Rémi and Kemal Hanjalic (2002). “Elliptic Blending Model: A New near-Wall Reynolds-Stress Turbulence Closure”. *Physics of Fluids*.

Menter, F. R. (1994). “Two-Equation Eddy-Viscosity Turbulence Models for Engineering Applications”. *AIAA Journal*.

Menter, F. R., M Kuntz, and R Langtry (2003a). “Ten Years of Industrial Experience with the SST Turbulence Model”. *TURBULENCE HEAT AND MASS TRANSFER, Turbulence, Heat and Mass Transfer, 4th:; Internal Symposium, Turbulence, Heat and Mass Transfer*. 4th International Symposium, Turbulence, Heat and Mass Transfer. Begell House.

Menter, F. R., Martin Kuntz, and Roland Bender (2003b). “A Scale-Adaptive Simulation Model for Turbulent Flow Predictions”. *41st Aerospace Sciences Meeting and Exhibit*. 41st Aerospace Sciences Meeting and Exhibit. American Institute of Aeronautics and Astronautics.

Monin, A. s et al. (1971). *STATISTICAL FLUID MECHANICS : Mechanics of Turbulence. Volume 1*. The MIT Press.

Moser, Robert D., John Kim, and Nagi N. Mansour (1999). “Direct Numerical Simulation of Turbulent Channel Flow up to Reτ=590”. *Physics of Fluids*.

Murakami, S. et al. (1996). “New Low-Reynolds-Number k-ε Model Including Damping Effect Due to Buoyancy in a Stratified Flow Field”. *International Journal of Heat and Mass Transfer*.

Naot, D (1970). “Interactions between Components of the Turbulent Velocity Correlation Tensor”. *Isr. J. Technol.*

Nicoud, F. and F. Ducros (1999). “Subgrid-Scale Stress Modelling Based on the Square of the Velocity Gradient Tensor”. *Flow, Turbulence and Combustion*.

Novozhilov, V. (2001). “Computational Fluid Dynamics Modeling of Compartment Fires”. *Progress in Energy and Combustion Science*.

Paolucci, Samuel and Donald R. Chenoweth (1989). “Transition to Chaos in a Differentially Heated Vertical Cavity”. *Journal of Fluid Mechanics* (-1).

Parneix, S., D. Laurence, and P. Durbin (1996). “Second Moment Closure Analysis of the Backstep Flow Database”.

Peng, S.-H. and L. Davidson (2000). “Numerical Investigation of Turbulent Buoyant Cavity Flow Using Large Eddy Simulation”. 3rd International Symposium on Turbulence, Heat and Mass Transfer.

Peng, Shia-Hui and Lars Davidson (2001). “Large Eddy Simulation for Turbulent Buoyant Flow in a Confined Cavity”. *International Journal of Heat and Fluid Flow*. Turbulent Heat and Mass Transfer - 3.

Peng, Shia-Hui and Lars Davidson (2002). “On a Subgrid-Scale Heat Flux Model for Large Eddy Simulation of Turbulent Thermal Flow”. *International Journal of Heat and Mass Transfer*.

Phillips, J.R. (1996). “Direct Simulations of Turbulent Unstratified Natural Convection in a Vertical Slot for Pr = 0.71”. *International Journal of Heat and Mass Transfer*.

Piomelli, Ugo et al. (2003). “The Inner–Outer Layer Interface in Large-Eddy Simulations with Wall-Layer Models”. *International Journal of Heat and Fluid Flow*. Selected Papers from the Fifth International Conference on Engineering Turbulence Modelling and Measurements.

Pope, Stephen B (2000). *Turbulent Flows*. Cambridge University Press.

Prandtl, L. (1925). “Bericht Über Untersuchungen Zur Ausgebildeten Turbulenz”. *ZAMM - Journal of Applied Mathematics and Mechanics / Zeitschrift für Angewandte Mathematik und Mechanik*.

Pruett, C. D. (2000). “Eulerian Time-Domain Filtering for Spatial Large-Eddy Simulation”. *AIAA Journal*.

Pruett, C. D. et al. (2003). “The Temporally Filtered Navier–Stokes Equations: Properties of the Residual Stress”. *Physics of Fluids*.

Pruett, C. D. et al. (2006). “A Temporal Approximate Deconvolution Model for Large-Eddy Simulation”. *Physics of Fluids*.

Richardson, Lewis Fry (1922). “Weather Prediction by Numerical Process”. *Quarterly Journal of the Royal Meteorological Society*.

Rodi, W. (1976). “A new algebraic relation for calculating the reynolds stresses”. *ZAMM - Journal of Applied Mathematics and Mechanics / Zeitschrift für Angewandte Mathematik und Mechanik*.

Rodi, Wolfgang (1984). *Turbulence Models and Their Application in Hydraulics: A State-of-the-Art Review*. Ed. by Wolfgang Rodi. 3rd ed. Routledge.

Rotta, J. (1951). “Statistische theorie nichthomogener turbulenz”. *Zeitschrift für Physik*.

Sagaut, Pierre (2006). *Large Eddy Simulation for Incompressible Flows: An Introduction*. 3rd ed. Scientific Computation. Springer.

Sagaut, Pierre, Sebastien Deck, and Marc Terracol (2006). *Multiscale and Multiresolution Approaches in Turbulence*. Imperial College Press ; Distributed by World Scientific.

Saury, Didier et al. (2011). “Natural Convection in an Air-Filled Cavity: Experimental Results at Large Rayleigh Numbers”. *International Communications in Heat and Mass Transfer*.

Schiestel, Roland (1987). “Multiple-Time-Scale Modeling of Turbulent Flows in One-Point Closures”. *The Physics of Fluids*.

Schiestel, Roland and Anne Dejoan (2005). “Towards a New Partially Integrated Transport Model for Coarse Grid and Unsteady Turbulent Flow Simulations”. *Theoretical and Computational Fluid Dynamics*.

Sebilleau, Frederic Claude Michel (2016). “Computational Analysis of Buoyancy Driven Flows across Scales”. Imperial College.

Sebilleau, Frederic Claude Michel et al. (2018). “Direct Numerical Simulation of an Air-Filled Differentially Heated Square Cavity with Rayleigh Numbers up to 10 11”. *International Journal of Heat and Mass Transfer*.

Sergent, A., P. Joubert, and P. Le Quéré (2003). "Development of a Local Subgrid Diffusivity Model for Large-Eddy Simulation of Buoyancy-Driven Flows: Application to a Square Differentially Heated Cavity". *Numerical Heat Transfer, Part A: Applications*.

Sergent, Anne et al. (2013). "Resolving the Stratification Discrepancy of Turbulent Natural Convection in Differentially Heated Air-Filled Cavities Part II: End Walls Effects Using Large Eddy Simulation". *International Journal of Heat and Fluid Flow*.

Shur, Mikhail L. et al. (2008). "A Hybrid RANS-LES Approach with Delayed-DES and Wall-Modelled LES Capabilities". *International Journal of Heat and Fluid Flow*.

Sinai, Y. L. and M. P. Owens (1995). "Validation of CFD Modelling of Unconfined Pool Fires with Cross-Wind: Flame Geometry". *Fire Safety Journal*.

Smagorinsky, J. (1963). "General Circulation Experiments with the Primitive Equations". *Monthly Weather Review*.

Soria, M. et al. (2004). "Direct Numerical Simulation of a Three-Dimensional Natural-Convection Flow in a Differentially Heated Cavity of Aspect Ratio 4". *Numerical Heat Transfer, Part A: Applications*.

Spalart, P. R. and S. Allmaras (1992). "A One-Equation Turbulence Model for Aerodynamic Flows". *30th Aerospace Sciences Meeting and Exhibit*. 30th Aerospace Sciences Meeting and Exhibit. American Institute of Aeronautics and Astronautics.

Spalart, P. R. et al. (1997). "Comments on the Feasibility of LES for Wings, and on a Hybrid RANS/LES Approach, International Conference; 1st, Advances in DNS/LES: Direct Numerical Simulation and Large Eddy Simulation". *Advances in DNS/LES: Direct Numerical Simulation and Large Eddy Simulation, International Conference; 1st, Advances in DNS/LES: Direct Numerical Simulation and Large Eddy Simulation*. Greyden Press; / United States; Air Force; Office of Scientific Research.

Spalart, P. R. et al. (2006). "A New Version of Detached-Eddy Simulation, Resistant to Ambiguous Grid Densities". *Theoretical and Computational Fluid Dynamics*.

Speziale, C. G. (1987). "On the Decomposition of Turbulent Flow Fields for the Analysis of Coherent Structures". *Acta Mechanica*.

Speziale, C. G., Sutanu Sarkar, and Thomas B. Gatski (1991). "Modelling the Pressure–Strain Correlation of Turbulence: An Invariant Dynamical Systems Approach". *Journal of Fluid Mechanics*.

Stolz, S. and N. A. Adams (1999). "An Approximate Deconvolution Procedure for Large-Eddy Simulation". *Physics of Fluids*.

Strelets, M. (2001). "Detached Eddy Simulation of Massively Separated Flows". *39th Aerospace Sciences Meeting and Exhibit*. 39th Aerospace Sciences Meeting and Exhibit. American Institute of Aeronautics and Astronautics.

Tennekes, Hendrik (1975). "Eulerian and Lagrangian Time Microscales in Isotropic Turbulence". *Journal of Fluid Mechanics*.

Tennekes, Hendrik and John Leask Lumley (1972). *A First Course in Turbulence*. MIT Press.

Tian, Y.S. and T.G. Karayiannis (2000a). "Low Turbulence Natural Convection in an Air Filled Square Cavity". *International Journal of Heat and Mass Transfer*.

Tian, Y.S. and T.G. Karayiannis (2000b). "Low Turbulence Natural Convection in an Air Filled Square Cavity". *International Journal of Heat and Mass Transfer*.

Tran, T T et al. (2012). "A Hybrid Temporal Les Approach Application to Flows around Rectangular Cylinders". 9th ERCOFTAC Int. Symp. on Eng. Turb. Modelling and Measurements.

Travin, A. et al. (2000). "Detached-Eddy Simulations Past a Circular Cylinder". *Flow, Turbulence and Combustion*.

Travin, A. et al. (2002). "Physical and Numerical Upgrades in the Detached-Eddy Simulation of Complex Turbulent Flows". *Advances in LES of Complex Flows*. Ed. by R. Friedrich and W. Rodi. Red. by R. Moreau. Springer Netherlands.

Trias, F. X. et al. (2007). "Direct Numerical Simulations of Two- and Three-Dimensional Turbulent Natural Convection Flows in a Differentially Heated Cavity of Aspect Ratio 4". *Journal of Fluid Mechanics*.

Trias, F.X. et al. (2010a). “Direct Numerical Simulation of a Differentially Heated Cavity of Aspect Ratio 4 with Rayleigh Numbers up to – Part II: Heat Transfer and Flow Dynamics”. *International Journal of Heat and Mass Transfer*.

Trias, F.X. et al. (2010b). “Direct Numerical Simulation of a Differentially Heated Cavity of Aspect Ratio 4 with Rayleigh Numbers up to 1011 – Part I: Numerical Methods and Time-Averaged Flow”. *International Journal of Heat and Mass Transfer*.

Vanpouille, D., B. Aupoix, and E. Laroche (2015). “Development of an Explicit Algebraic Turbulence Model for Buoyant Flows – Part 2: Model Development and Validation”. *International Journal of Heat and Fluid Flow*.

Van Rossum, Guido (1995). *Python Reference Manual*. CWI Report. Computer Science/Department of Algorithmics and Architecture.

Versteegh, T A M and F T M Nieuwstadt (1999). “A Direct Numerical Simulation of Natural Convection between Two Infinite Vertical Differentially Heated Walls Scaling Laws and Wall Functions”. *Int. J. Heat Mass Transfer*.

Viollet, P. L. (1987). “The Modelling of Turbulent Recirculating Flows for the Purpose of Reactor Thermal-Hydraulic Analysis”. *Nuclear Engineering and Design*.

Viollet, P. L. and J. Goussebaile (1983). *On the Modelling of Turbulent Flows under Strong Buoyancy Effects in Cavities with Curved Boundaries*.

Wilcox, David C. (1988). “Reassessment of the Scale-Determining Equation for Advanced Turbulence Models”. *AIAA Journal*.

Wilcox, David C. (2006). *Turbulence Modeling for CFD*. 3rd ed. DCW Industries.

Xin, Shihe and Patrick Le Quéré (2006). “Natural-Convection Flows in Air-Filled, Differentially Heated Cavities with Adiabatic Horizontal Walls”. *Numerical Heat Transfer, Part A: Applications*.

Xin, Shihe and Patrick Le Quéré (2012). “Stability of Two-Dimensional (2D) Natural Convection Flows in Air-Filled Differentially Heated Cavities: 2D/3D Disturbances”. *Fluid Dynamics Research*.

Zhang, Zheng et al. (2014). “Numerical Exploration of Turbulent Air Natural-Convection in a Differentially Heated Square Cavity at Ra = 5.33 × 109”. *Heat and Mass Transfer*.